International Journal of 3D Printing Technologies and Digital Industry

IJ3DPTDI

Print Turkey Org

Uluslararasi 3B Yazıcı Teknolojileri ve Dijital Endüstri Dergisi

Vol:8 Issue:2 2024 Cilt:8 Sayı:2

DergiPark AKADEMİK

TR DİZİN

https://3dprintturkey.org/

Sayın Yazarlar;

Dergimize 4 dilde (Türkçe Tr, İngilizce En, Rusça Ru ve Ukraynaca Ua) yazı kabul etmekteyiz. Türkçe, Rusça ve Ukraynaca yazılarda İngilizce özet yazılması zorunludur.

ULUSLARARASI 3B YAZICI TEKNOLOJİLERİ VE DİJİTAL ENDÜSTRİ dergisi,

IJ3DPTDI, Endüstri 4.0 – dijital endüstri teknolojileri, 3B yazıcı teknolojileri, katmanlı-eklemeli imalat teknolojileri ve uygulamaları yani mühendislik, bilim, teknoloji gibi tüm disiplinlerle ilgili araştırmaların sonuçlarını yaymak için açık, hakemli, disiplinlerarası, uluslararası, bilimsel, akademik, online bir dergidir. ij3dptdi, Mühendislik, Teknoloji ve Bilimin Endüstri 4.0 daki uygulamaları, tüm araştırmaları, gözden geçirme makalelerini, kısa bilgi paylaşımlarını ve önemli ilerlemeleri sunan teknik notları online yayınlamak için yazarları davet eder.

Endüstri 4.0, Dijital Endüstri, 3B Yazıcılar üzerine tüm bilimsel mühendislik araştırma ve teknoloji alanı konuları;

3B baskı için tıbbi uygulamalar; dokuların ve organların biyografik baskıları, 3B vaskülarize organların oluşturulmasında karşılaşılan zorluklar, özelleştirilmiş implantlar ve protezler, düşük maliyetli protez parçaları, cerrahi hazırlık için anatomik modeller, sentetik cilt, kafatası değişimi, tıbbi donatımı, kemik, özel üretilen sensörler, kişiselleştirilmiş ilaç dozu, benzersiz dozaj şekilleri, kompleks ilaç salınım profilleri v.d.

3B yazıcı uygulama alanları; tıbbi ve diş hekimliği uygulamaları, diş hekimliği uygulamaları ve materyalleri, yumuşak robotik sistemleri, robot tutucu sistemler, bina uygulamaları, kalıp / kalıp uygulamaları, mimarlık uygulamaları, model uygulamaları, hızlı prototip uygulamaları, görsel sanat uygulamaları, tekstil uygulamaları, dijital fabrikalar, mimari model uygulamaları ve malzemeleri, endüstriyel uygulamalar ve malzemeler, gıda uygulamaları ve malzemeleri, sanatsal uygulamalar ve malzemeler, tarama yöntemleri ve modelleme v.d.

Endüstri 4.0 ve dijital sanayi; büyük veri, yapay zeka, dijital yaşam döngüsü, sensör motorları, artırılmış gerçeklik, görselleştirme, sistem simülasyonu, kablosuz iletişim, BİT güvenlik, dijital iş, blok zinciri, veri Güvenliği, özerk robotlar, sistem entegrasyonu, nesnelerin interneti (IoTs), siber güvenlik, bulut bilişim, dijital fabrika v.d.

3B yazıcı tasarım, modelleme ve analiz; 3D yazıcı tasarımı, ekstruder tasarımı, 3B baskı için ürün geliştirme, seramik sistemleri tasarımı, gıda sistemleri tasarımı, elektronik bileşenleri, mekanik parçalar, standart bileşenler v.d.

3B yazıcı malzeme ve mekanik özellikleri; polimer malzemeler, esnek malzemeler, biyo malzemeler, metalik malzemeler, toz malzeme üretim yöntemleri, ağaç malzemeler, kompozit malzemeler v.d.

3B yazıcı program kontrol teknolojileri; kontrol programları, tasarım programları, 3D tarama teknolojileri, DMLS teknolojileri, SLA teknolojileri, SLS teknolojileri, FDM teknolojileri, dijital üretim teknolojileri, diğer 3B yazıcı teknolojileri v.d.

ij3dptdi, online yayınlanan bir dergidir ve yılda 3 defa yayınlanır.

1.periyot Ocak-Nisan
2.periyot Mayıs-Ağustos
3.periyot Eylül-Aralık

ISSN 2602-3350
web-site : http://dergipark.gov.tr/ij3dptdi
e-mail : korayozsoy32@gmail.com

Dear author,

Our Journal accepts articles in 4 languages (Turkish Tr, English En, Russian Ru and Ukrainian Ua). Articles in Turkish, Russian and Ukrainian must have an abstract in English.

International Journal of 3D Printing Technologies and Digital Industry
ij3dptdi, is an open access peer-reviewed, interdisciplinary international platform for disseminating results of relevant research related to all the disciplines of engineering, science, technology etc on Industry 4.0 - digital industry technologies, 3D printer technologies, additive manufacturing technologies and applications . ij3dptdi, invites all research, review articles, short communications & technical notes that describe significant advances research in the areas of Engineering, Technology, Science on Industry 4.0, Digital Industry, 3D Printers, additive manufacturing;

All scientific engineering research & technology area on Industry 4.0, Digital Industry and 3D printers;

Medical applications for 3D printing; bioprinting tissues and organs, challenges in building 3D vascularized organs, customized implants and prostheses, low–cost prosthetic parts, anatomical models for surgical preparation, synthetic skin, cranium replacement, medical equipment, bone, tailor-made sensors, personalized drug dosing, unique dosage forms, complex drug-release profiles ect.

Aplication fields; medical and dental applications, dental practices and materials, soft robotics systems, robot gripper systems, building applications, die/mold applications, architecture applications, models applications, rapid prototype applications, visual arts applications, textile applications, digital factories, architectural-model applications and materials, industrial applications and materials, food applications and materials, artistic practices and materials, scanning methods and modeling ect.

Digital industry; big data, artificial intelligence, digital life cycles, sensors actuators, augmented reality, visualization, system simulation, wireless communication, ICT security, digital business, block chain, data safety, autonomous robots, system integration, internet of things (IT's), cyber security, cloud computing, digital factory ect.

Design, modelling and analysis; 3D printer design, extruder design, product development, ceramic systems design, food systems design, table system design, electronics components, mechanic components, standard components ect.
Mechanical properties of filaments; polymer materials, flexible materials, bio materials, metallic materials, wood materials, composite materials ect.

Program – control technologies; control programs, design programs, 3D scanning technologies, DMLS technologies, SLA technologies, SLS technologies, FDM technologies, Digital production technologies, other 3D printer technologies ect.

ij3dptdi, Its publication frequency is 3 issues per year.

1.Period January-April
2.period May-August
3.period September-December

ISSN 2602-3350
Web-site: http://dergipark.gov.tr/ij3dptdi
E-mail: korayozsoy32@gmail.com

Уважаемый автор,

наш журнал принимает статьи на 4-х языках (турецком, английском, русском и украинском). Статьи на турецком, русском и украинском языках должны сопровождаться аннотацией на английском языке.

Международный журнал технологий 3D-печати и цифровой индустрии

IJ3DPTDI – это рецензируемое издание с открытым доступом, междисциплинарная международная платформа для обмена результатами исследований по инженерно-конструкторским разработкам, теоретическим исследованиям, усовершенствованию технологий Индустрии 4.0, в том числе – технологий цифровой промышленности, 3D-печати, аддитивного производства и разработки приложений. İJ3DPTDİ принимает исследовательские статьи, обзорные статьи, краткие сообщения и технические заметки, которые описывают значимые результаты исследований в области машиностроения, технологии, теоретической основы индустрии 4.0, цифровой промышленности, 3D печати, производства многокомпонентных материалов.

Тематика журнала включает все научно-технические исследования и обзор технологий Индустрии 4.0, цифровой промышленности и 3D печати.

Медицинские технологии 3D-печати: биопринтинг – воспроизведение объемных моделей тканей и органов, создание трехмерных васкуляризированных органов, индивидуализированных имплантатов и протезов, синтетической кожи, костей, замены частей черепа; удешевление технологии протезирования, разработка анатомических моделей для подготовки хирургов,тестовых хирургических операций, медицинского оборудования; изготовление датчиков с заданным набором характеристик, создание уникальных лекарственных препаратов с индивидуальными дозировками, сложных многокомпонентных лекарственных средств.

Области применения: материалы и оборудование для медицины и стоматологии, роботизированные системы на основе биологических прототипов, роботизированные захватные устройства, строительные материалы, пресс-формы, модели и прототипы в архитектуре, моделирование реальных объектов, прототипирование, сфера визуального искусства, текстильная промышленность, цифровые заводы, приложения и материалы для архитектурного моделирования, промышленные образцы и материалы, создание пищевых продуктов, технологии художественной обработки материалов, методы моделирования и сканирования и т.п.

Цифровая индустрия: большие данные, искусственный интеллект, жизненный цикл цифровых технологий, приводные механизмы датчиков, расширенная реальность, визуализация, моделирование систем, беспроводная связь, ИТ-безопасность, электронная коммерция, блокчейн технологии, безопасность данных, автономные роботы, системная интеграция, интернет вещей, кибербезопасность, облачные вычисления, цифровое производство.

Дизайн, моделирование и анализ: моделирование для 3D печати, экструдера; разработка разнообразных продуктов, проектирование систем керамического производства, усовершенствование технологии производства пищевых продуктов, проектирование предметов мебели, электронных компонентов, механических деталей, стандартных компонентов и т.п.

Механические свойства нитей: полимерные материалы, гибкие материалы, биоматериалы, изделия из металла и древесины, композиционные материалы.

Технологии управления приложениями: контрольные программы, проектные программы, технологии 3D-сканирования, технологии DMLS, SLA, SLS, FDM, цифровые технологии производства, другие технологии 3D-печати и т.п.

Периодичность выхода журнала – 3 раза в год:

1-й выпуск – январь-апрель;
2-й выпуск – май-август;
3-й выпуск – сентябрь-декабрь.

ISSN 2602-3350
Сайт журнала: http://dergipark.gov.tr/ij3dptdi
Электронная почта: korayozsoy32@gmail.com

Шановний авторе,

наш журнал приймає статті на 4-х мовах (турецькою, англійською, російською та українською). Статті турецькою, російською та українською мовою повинні супроводжуватися анотацією англійською мовою.

Міжнародний журнал технологій 3D-друку і цифрової індустрії

IJ3DPTDI – це рецензоване видання з відкритим доступом, міждисциплінарна міжнародна платформа для обміну результатами досліджень з інженерно-конструкторських розробок, теоретичних досліджень, удосконалення технологій Індустрії 4.0, в тому числі – технологій цифрової промисловості, 3D-друку, адитивного виробництва і розробки додатків. İJ3DPTDİ приймає дослідні статті, оглядові статті, короткі повідомлення і технічні записки, які містять значущі результати досліджень в галузі машинобудування, технології, теоретичній основі індустрії 4.0, цифровій промисловості, 3D друку, виробництва багатокомпонентних матеріалів.

Тематика журналу охоплює всі науково-технічні дослідження та огляд технологій Індустрії 4.0, цифрової промисловості і 3D друку.

Медичні технології 3D-друку: біопринтінг – відтворення об'ємних моделей тканин і органів, створення тривимірних васкуляризованих органів, індивідуалізованих імплантатів і протезів, синтетичної шкіри, кісток, заміни частин черепа; здешевлення технології протезування, розроблення анатомічних моделей для підготовки хірургів, тестових хірургічних операцій, медичного обладнання; виготовлення датчиків із заданим набором характеристик, створення унікальних лікарських препаратів із індивідуальними дозуваннями; складних багатокомпонентних лікарських засобів.

Сфери застосування: матеріали та обладнання для медицини і стоматології, роботизовані системи на основі біологічних прототипів, роботизовані захватні пристрої, будівельні матеріали, прес-форми, моделі і прототипи в архітектурі, моделювання реальних об'єктів, прототипування, сфера візуального мистецтва, текстильна промисловість, цифрові заводи, додатки та матеріали для архітектурного моделювання, промислові зразки і матеріали, створення харчових продуктів, технології художньої обробки матеріалів, методи моделювання та сканування і т.п.

Цифрова індустрія: великі дані, штучний інтелект, життєвий цикл цифрових технологій, приводні механізми датчиків, розширена реальність, візуалізація, моделювання систем, бездротовий зв'язок, IT-безпека, електронна комерція, блокчейн технології, безпека даних, автономні роботи, системна інтеграція, інтернет речей , кібербезпека, хмарні обчислення, цифрове виробництво.

Дизайн, моделювання і аналіз: моделювання для 3D друку, екструдера; розробка різноманітних продуктів, проектування систем керамічного виробництва, удосконалення технології виробництва харчових продуктів, проектування предметів меблів, електронних компонентів, механічних деталей, стандартних компонентів і т.п.

Механічні властивості ниток: полімерні матеріали, гнучкі матеріали, біоматеріали, вироби з металу і деревини, композиційні матеріали.
Технології управління додатками: контрольні програми, проектні програми, технології 3D-сканування, технології DMLS, SLA, SLS, FDM, цифрові технології виробництва, інші технології 3D-друку і т.п.

Періодичність виходу журналу – 3 рази на рік:
1-й випуск – січень-квітень;
2-й випуск – травень-серпень;
3-й випуск – вересень-грудень.

ISSN 2602-3350
Web-site: http://dergipark.gov.tr/ij3dptdi
E-mail: korayozsoy32@gmail.com

ULUSLARARASI 3B YAZICI TEKNOLOJİLERİ VE DİJİTAL ENDÜSTRİ DERGİSİ

Cilt:8 Sayı: 2 Yıl: 2024

INTERNATIONAL JOURNAL OF 3D PRINTING TECHNOLOGIES AND DIGITAL INDUSTRY

Volume:8 Number: 2 Year: 2024

ISSN: 2602-3350

---

http://dergipark.gov.tr/ij3dptdi

Uluslararası 3B Yazıcı Teknolojileri ve Dijital Endüstri Dergisi / International Journal of 3D Printing Technologies and Digital Industry

Vol: 8, No:2 (2024) **Cilt: 8, Sayı:2 (2024)**

ISSN 2602-3350

ULUSLARARASI 3B YAZICI TEKNOLOJİLERİ
VE DİJİTAL ENDÜSTRİ DERGİSİ

INTERNATIONAL JOURNAL OF 3D PRINTING
TECHNOLOGIES AND DIGITAL INDUSTRY

ISSN:2602-3350 (Online)

URL: https://dergipark.org.tr/ij3dptdi

FFF/FDM YÖNTEMİNDE TAGUCHİ DENEY TASARIMI İLE PARAMETRE OPTİMİZASYONU

PARAMETER OPTIMIZATION IN FFF/FDM METHOD USING TAGUCHI EXPERIMENTAL DESIGN

Yazarlar (Authors): Selin ALTUN, Zeynep KAYĞIN, Ali Fatih HALİLOĞLU, Rümeysa KOCA,Hasan BAŞ

Bu makaleye şu şekilde atıfta bulunabilirsiniz (To cite to this article): *Altun S., Kayğın Z., Haliloğlu A. F., Koca R., Baş H., "FFF/FDM Yönteminde Taguchi Deney Tasarımı ile Parametre Optimizasyonu" Int. J. of 3D Printing Tech. Dig. Ind., 8(2): 154-161, (2024).*

DOI: 10.46519/ij3dptdi.1321818

Araştırma Makale/ Research Article

Erişim Linki: (To link to this article): https://dergipark.org.tr/en/pub/ij3dptdi/archive

FFF/FDM YÖNTEMİNDE TAGUCHİ DENEY TASARIMI İLE PARAMETRE OPTİMİZASYONU

Selin ALTUN[a], Zeynep KAYĞIN[a], Ali Fatih HALİLOĞLU[a], Rümeysa KOCA[a], Hasan BAŞ[*a]

[a] Ondokuz Mayıs Üniversitesi, Mühendislik Fakültesi, Endüstri Mühendisliği Bölümü, TÜRKİYE

[*] *Sorumlu Yazar: hasan.bas@omu.edu.tr*

(**Geliş/Received:** 12.01.2024; **Düzeltme/Revised:** 07.06.2024; **Kabul/Accepted:** 10.07.2024)

ÖZ

Bu çalışmanın amacı eriyik yığma teknolojisinde (Fused Filament Fabrication (FFF) veya Fused Deposition Modeling (FDM)) baskı kalitesini artırmak ve baskı parametrelerinin etkilerini araştırmaktır. Bu kapsamda polilaktik asit (PLA) filament kullanılmış ve Taguchi parametre optimizasyonu ile katman kalınlığı, ekstrüder sıcaklığı, fan hızı, duvar baskı hızı ve geri çekme mesafesi gibi baskı parametreleri optimize edilmiştir. Taguchi deney tasarımı kullanılarak her bir faktör için 5 farklı seviyede toplam 25 numune üretilmiştir. Numuneler, sezgisel olarak kalite puanlaması yöntemiyle değerlendirilmiş ve her biri 1 ile 10 arasında puanlanmıştır. Baskı parametrelerinin ürün kalitesine etkileri detaylı bir şekilde analiz edilmiş olup, baskı esnasında karşılaşılan hatalar tanımlanarak çözüm önerileri sunulmuştur. Araştırma sonucunda, optimal baskı parametreleri olarak 0,24 mm katman kalınlığı, 200 °C ekstrüder sıcaklığı, 60 mm/s fan hızı, 24 mm/s duvar baskı hızı ve 0,6 mm/s geri çekme hızı belirlenmiştir. Ekstrüder sıcaklığının artması baskının genel kalitesini düşürürken diğer parametrelerin değişimi doğrusal bir ekti yaratmamıştır. Bu araştırma, FFF metoduyla üretilen parçaların genel kalitesini ve üretim süreçlerini optimize etmeyi hedeflemektedir. Çalışmada kullanılan metodolojinin endüstriyel uygulamalarda benimsenmesi, daha yüksek kalite ve verimlilik sağlanmasına ve FFF teknolojisinin daha geniş bir kullanım alanına sahip olmasına katkıda bulunabilir.

Anahtar Kelimeler: Eriyik Yığma Yöntemi, FFF, FDM, Taguchi, Deney Tasarımı.

PARAMETER OPTIMIZATION IN FFF/FDM METHOD USING TAGUCHI EXPERIMENTAL DESIGN

ABSTRACT

This study aims to enhance the print quality and investigate the effects of print parameters in Fused Filament Fabrication (FFF) or Fused Deposition Modeling (FDM) technology. In this context, polylactic acid (PLA) filament was used, and print parameters such as layer thickness, extruder temperature, fan speed, wall print speed, and retraction distance were optimized using the Taguchi parameter optimization method. A total of 25 samples were produced using the Taguchi experimental design, with five different levels for each factor. The samples were evaluated using an intuitive quality scoring method, with each sample being rated between 1 and 10. The effects of the print parameters on product quality were analyzed in detail, and errors encountered during printing were identified with proposed solutions. As a result of the research, the optimal print parameters were determined to be a layer thickness of 0.24 mm, an extruder temperature of 200 °C, a fan speed of 60 mm/s, a wall print speed of 24 mm/s, and a retraction speed of 0.6 mm/s. While increased extruder temperature generally decreased print quality, changes in the other parameters did not produce a linear effect. This study aims to optimize the quality and production processes of parts produced using the FFF method. If adopted in industrial applications, the methodology used in this study could contribute to higher quality and efficiency and a more comprehensive range of applications for FFF technology.

Keywords: Fused Deposition Modeling, FFF, FDM, Taguchi, Experimental Design.

1. GİRİŞ

FFF, nesnelerin 3 boyutlu (3D) model verilerinden katmanlar halinde üretildiği bir eklemeli imalat yöntemidir. Bu yöntem, karmaşık parçaların hızlı ve etkili bir şekilde üretilmesine olanak tanır. Ancak, FFF'in zayıf bir yönü, ürünlerin yüzey kalitesinin genellikle istenen düzeye ulaşamamasıdır. Bu nedenle, son ürünlerin kalitesini iyileştirmek ve beklentileri karşılamak için ayrıca bitirme işlemlerine ihtiyaç duyulabilir. Bu işlemler hem zaman alıcıdır hem de maliyetlidir. FFF yöntemi için kritik öneme sahip olan bir dizi parametre bulunmaktadır. Bu parametreler, FFF yönteminin sonuçlarını belirleyen ve kalitesini etkileyebilen faktörlerdir.

FFF yönteminde ürün kalitesini arttırmak için baskı parametrelerinin optimize edilmesi gerekmektedir. Taguchi metodu, parametre optimizasyonu için kullanılan etkili ve basit bir yöntem olup mühendislik uygulamalarında sıklıkla kullanılmaktadır [1-3]. Taguchi metodu eklemeli imalat çalışmalarında da kullanılmıştır [4-7]. Kartal [8] eriyik yığma yönteminde süreç parametrelerinin optimizasyonunu Taguchi metodolojisi kullanarak gerçekleştirmiştir. Kartal [8], PLA filament kullanarak ürettiği numunelerde katman kalınlığı ve raster genişliğinin yüzey kalitesini etkilediğini göstermiştir. Baş, Elevli and Yapıcı [9] çalışmasında, FFF tipi yazıcılardaki üretim süreçlerini hata ağacı analizi (FTA) ile incelemiş ve üretim sırasında meydana gelebilecek hataları detaylı bir şekilde ortaya koymuşlardır. Bacak, Varol ÖZkavak and Tatli [10] çalışmalarında, FFF yöntemiyle üretilen PLA numunelerin çekme dayanımını etkileyen işlem parametrelerini detaylı bir şekilde ele almıştır. Günay, Gündüz, Yilmaz, Yaşar and Kaçar [11], FFF baskı parametrelerini PLA numunelerin çekme dayanımı üzerinden incelemiş ve Taguchi L_{18} deney tasarımı ile bu parametrelerin etkilerini değerlendirmiştir. Bilgin [12] tarafından yürütülen çalışmada ise ABS malzeme ile üretilen parçalarda baskı parametrelerinin etkilerini inceleyerek optimum parametreleri belirlemiştir. Seçgin and Kahraman [13], PETG filament kullanarak yapılan parçalarda yüzey pürüzlülüğü üzerine parametre optimizasyonu yapmış ve katman kalınlığının en önemli parametre olduğunu bulmuşlardır. Sood, Ohdar and Mahapatra [14], FFF sürecindeki kritik parametrelerin boyutsal doğruluğa etkisini Taguchi ve gri Taguchi yöntemleriyle belirlemişlerdir. Zhang and Peng [15], FFF performansını belirleyen dört kritik süreç parametresini Taguchi ve bulanık kapsamlı değerlendirme ile optimize etmişlerdir. Bu örnek çalışmalar, FFF teknolojisinin çeşitli yönlerini keşfetme ve optimize etme çabalarını ortaya koymaktadır.

FFF yöntemi ile ilgili incelenmesi gereken birçok derleme makale de bulunmaktadır. Brenken, Barocio, Favaloro, Kunc and Pipes [16] fiberle güçlendirilmiş polimerlerin eriyik yığma yöntemiyle üretimine yönelik çalışmaları inceleyerek derleme bir makale yapmışlardır. Daminabo, Goel, Grammatikos, Nezhad and Thakur [17] ise polimer malzeme üretimini ve FFF tekniğini incelemiş ve FFF'nin ölçeklenebilirlik, maliyet etkinliği ve geniş malzeme işleme yeteneklerini vurgulamıştır. Sathies, Senthil and Anoop [18], polimer temelli eklemeli imalat süreçleri ve FFF uygulamalarındaki ilerlemeleri özetlemiş, FFF'nin konvansiyonel üretim sorunlarına çözüm sunduğunu belirtmiştir.

Bu çalışmada FFF yönteminde Taguchi deney tasarımını kullanarak parametre optimizasyonu yapılmıştır. Optimizasyon parametreleri olarak katman kalınlığı, ekstrüzyon sıcaklığı, soğutma fan hızı, duvar baskı hızı ve geri çekme hızı belirlenmiştir. Katman kalınlığı, baskı kalitesini etkileyen önemli bir parametredir; ince katmanlar daha pürüzsüz yüzeyler sunarken, kalın katmanlar hızlı baskı sağlar ancak yüzey kalitesini olumsuz etkileyebilir. Ekstrüzyon sıcaklığı, malzemenin akışkanlığını ve yapışkanlığını düzenlerken, fan hızı baskı sırasında soğutmayı kontrol eder. Baskı hızı, üretim hızını etkiler; daha yüksek hızlar hızlı üretimi sağlar ancak yüzey kalitesini olumsuz etkileyebilir. Geri çekme hızı filament akışını düzenler ve doğru ayarlandığında çekme ve deformasyonları önler.

Baskı parametrelerin doğru bir şekilde ayarlanması, 3D baskı ürünlerinin kalitesini arttırmak ve üretim süreçlerini yönetmek için kritik öneme sahiptir. Dolayısıyla, bu parametrelerin uygun bir şekilde optimize edilmesi, 3D baskı ürünlerinin kalitesini artırmakla kalmaz, aynı zamanda endüstriyel uygulamalarda daha etkili bir kullanımını da mümkün kılar. Bu, FFF teknolojisinin endüstriyel üretimde daha yaygın bir şekilde benimsenmesine katkı sağlayabilir ve ürünlerin

daha hızlı ve maliyet etkin bir şekilde üretilmesini teşvik edebilir.

2. MATERYAL VE METOD

2.1. Malzeme ve Ekipman

Numunelerin üretiminde Makerbot Replicator 5th Generation 3D yazıcı, malzeme olarak da PLA filament kullanılmıştır. Baskı modeli olarak 3B yazıcıların performansını denemede sıklıkla kullanılan 3DBenchy modeli seçilmiştir. Bu model yüzey kalitesi, model doğruluğu ve çarpılma gibi sorunları gözler önüne sererek 3D yazıcı performansını kapsamlı bir şekilde değerlendirmeyi sağlar [19]. 3D Benchy %80 ölçekli olarak dilimlenmiş olup X, Y, Z eksenlerinde sırasıyla 48 mm, 24,08 mm ve 37,4 mm ölçülere sahiptir (Şekil 1).

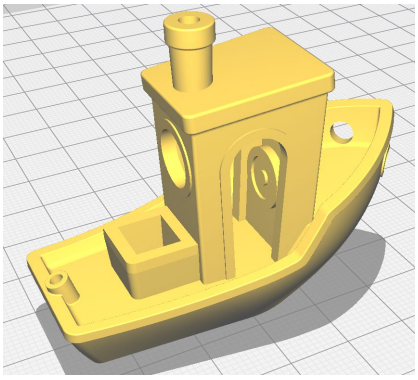

Şekil 1. #3DBenchy tasarımının üç boyutlu yazıcı programında yerleşim görüntüsü

2.2.FFF Metodu

Eklemeli imalat teknolojileri, konvansiyonel talaşlı imalat teknolojilerinden farklı olarak, üç boyutlu bilgisayar destekli (CAD) verilerden fiziksel parçaları katman katman oluşturma ve sadece ihtiyaç duyulduğu kadar malzeme kullanma prensibine dayanmaktadır [17]. Bu teknolojiler arasında yer alan malzeme ekstrüzyonu, ASTM standartlarına göre yedi farklı kategoride incelenen bir eklemeli imalat yöntemidir ve FFF, bu kategorideki malzeme ekstrüzyonu yöntemlerinden biri olarak bilinir [20]. Eriyik yığma teknolojisinde genellikle ince plastik tel veya filament kullanılır; ancak zaman zaman, hazneden beslenen plastik granül de tercih edilebilir. Plastik malzeme, nozul içindeki bir ısıtıcı tarafından ergime noktasının hemen üzerindeki bir sıcaklıkta tutularak ekstrüzyon işlemine tabi tutulur. Nozuldan çıkan eriyik plastik, tablaya ulaştığında anında sertleşir ve tablanın yüzeyine yapışır. Bir katman tamamlandığında platform aşağıya iner ve nozul diğer katmanı inşa eder. Katman kalınlığı ve düşey boyut hassasiyeti nozul çapına bağlıdır. FFF sisteminin çalışma prensibi Şekil 2'de gösterilmiştir.

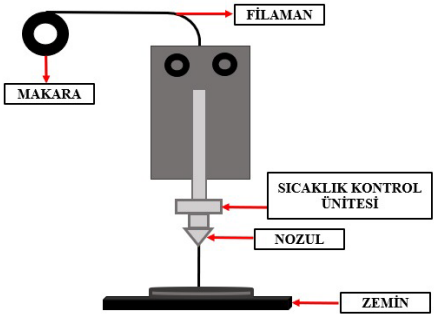

Şekil 2. FFF teknolojisinin şematik gösterimi

2.3. Taguchi Metodu Deney Tasarımı

Taguchi'nin deneysel tasarım yaklaşımı, ürün ve süreçteki değişkenliği en aza indirmek amacıyla kullanılır. Bu yaklaşım, değişkenliği oluşturan ve kontrol edilemeyen faktörlere karşı kontrol edilebilen faktörlerin düzeylerinin en uygun kombinasyonunu seçmeyi hedefler [21]. Taguchi metodu, ortogonal diziler olarak adlandırılan belirli sıralamaları kullanır. Bu standart diziler, performans parametrelerini etkileyen tüm faktörlerle ilgili en kapsamlı bilgiyi sağlamak ve en az sayıda deney yapmak için bir yöntem önermektedir [8].

Taguchi yöntemi, çok sayıda deneyi daha etkili bir şekilde yönetmek amacıyla geliştirilmiş bir optimizasyon yaklaşımıdır. Kalite iyileştirmeyi hedefleyen bu yöntem, deney tasarımı ve parametre optimizasyonu ile ürün veya süreç tasarımındaki faktörlerin etkilerini değerlendirir, böylece istenilen kalite seviyesine daha etkili bir şekilde ulaşılabilir. Taguchi yöntemi, faktörlerin etkileşimleri ve varyasyonun etkilerini göz önünde bulundurarak belirli faktörlerin sistemdeki önemini belirlemeyi amaçlar. Bu yöntem, süreçlerin daha etkin ve kararlı hale getirilmesinde önemli bir rol oynar.

Bu çalışma, FFF yöntemi kullanılarak PLA filament malzemeden üretilen numunelerin baskı kalitesinde işlem parametrelerinin etkisini belirlemeyi amaçlamıştır. Baskı deseni Diamond Fill (Fast) olarak belirlenmiştir. İç dolgu yoğunluğu %80, destek yoğunluğu %8 ve iç baskı hızı 90 mm/s olmak üzere sabit parametre; katman kalınlığı, ekstrüder sıcaklığı, fan hızı, duvar baskı hızı ve geri çekme

mesafesi parametreleri ise bağımsız değişken olarak seçilmiştir.

Belirlenen parametrelerin, FFF yöntemi ile üretilen parçaların baskı kalitesine göreceli katkısını değerlendirmek amacıyla bir Taguchi L_{25} deney yöntemi tasarlanmış ve uygulanmıştır. Deney tasarımında katmankalınlığı aralığı 0,16-0,20 mm, ekstrüder sıcaklık aralığı 200-220 ℃, Fan hızı %60-100, Duvar baskı hızı 12-28 mm/s ve geri çekme mesafesi 0,4-0,8 mm aralığında olacak şekilde belirlenmiştir (Çizelge 1).

2.4. Sezgisel Değerlendirme

Deneylerin değerlendirme sürecinde kullanılan kalite puanlaması, üretilen baskıların sezgisel bir puanlama yöntemi kullanılarak incelenmesine dayanmaktadır.

Bir baskı için puanlama yapılırken, söz konusu baskıda görülen hatalar 1 ile 10 arasında puanlamış ve her bir hatanın şiddeti eşit kabul edilmiştir. Bu puanlama yönteminde 1 yüksek kaliteyi temsil ederken, 10 düşük kaliteyi ifade etmektedir. Örneğin, sızıntı ve iplik hatası için baskının iç kısmını görmeye engel olacak kadar yoğun hata görülmüşse 10 puan, estetik görünüme engel olmayacak şekilde çok az rastlanmışsa 1 puan verilmiştir. Baskıda görülen hatalar 4 farklı gözlemci tarafından önem derecesine göre puanlandıktan sonra ortalamaları alınarak hata değerleri bulunmuştur. Sonuç olarak bir baskının sezgisel kalite puanı, baskıda görülen hata değerlerinin ortalaması alınarak bulunur.

Sezgisel puanlama süreci, gözlemcilerin kişisel deneyim ve estetik tercihlerine dayanmaktadır ve elde edilen sonuçlar makalenin sonuç bölümünde detaylı olarak ele alınmıştır. Bu şekilde, farklı parametre ayarlarının ürün kalitesine olan etkisi sistematik bir şekilde analiz edilerek, en uygun parametre kombinasyonunun belirlenmesi amaçlanmıştır.

3.DENEYSEL BULGULAR

3.1. FFF Yöntemin Görülen Hatalar

FFF'in aşamaları katı modellerin oluşturulması, dilimlenmesi, basılması ve temizleme olarak belirtilebilir. Bilgisayar destekli tasarım (CAD) programları ile oluşturulan model, evrensel STL formatında kaydedilir. Sonrasında dilimleme ve G-kod oluşturma işlemleri dilimleme programı ile gerçekleştirilir. Oluşturulan G-kod dosyası, 3D yazıcıya aktarılarak baskı süreci başlatılır. Baskı hataları dilimleme aşamasındaki kullanıcı ayarlarından da kaynaklanabilir. Bu nedenle, özellikle dilimleme aşamasında doğru ayarlamalar yapılmalıdır.

Baş, Elevli and Yapıcı [9] yaptıkları çalışmada FFF yönteminde oluşabilecek hataları detaylı bir şekilde açıklamışlardır. Bu hatalar arasında ekstrüzyon kesintileri, yan yüzeylerde bozulmalar, sarkmalar, boyutsal hatalar, küçük bölümlerin basılamaması, aşırı ısınma, üst yüzeyde çizikler, bükülme, destek problemleri, kıvrılmış kenarlar, delik ve boşluk problemleri, baskı başlangıç problemleri, fil ayağı ve görünür iç dolgu gibi çeşitli sorunlar bulunmaktadır. Bu hatalar, kullanıcıların yanlış dilimleme ayarları, mekanik sorunlar ve sıcaklık dalgalanmaları gibi çeşitli nedenlerden kaynaklanmaktadır. Bu hatalara sebep olan toplam 49 adet kök neden belirlemişlerdir. Mekanik sorunlar, sıcaklık ve kalibrasyon hatası gibi faktörler baskı sırasında modelin yanlış basılmasına neden olabilir. Bu çalışma kapsamında üretilen numunelerde literatürde belirtilen hataların bir kısmı tespit edilmiştir. Bu hatalar, deney numunelerinden alınan örnek görsellerle birlikte açıklanmıştır.

3.1.1. Yan Yüzeylerde Deformasyonlar

Yazdırma sırasında yüzey deformasyonları, damlacıklar, çizgiler ve dalgalı desenler gibi sorunlar ortaya çıkabilir. Bunlar genellikle geri çekilme, mekanik hatalar, sıcaklık dalgalanmaları veya düzensiz ekstrüzyon kaynaklıdır (Şekil 3).

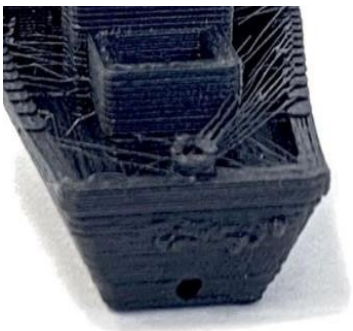

Şekil 3. Yan yüzeyde deformasyonlar

3.1.2. Sızıntı ve İplikler

Genellikle yanlış geri çekme mesafesi, düşük geri çekme hızı, aşırı yüksek sıcaklık veya uzun süreli ekstrüzyon olmadan yapılan hareketlerle ilgili

olarak tüylü veya saçlı görüntüler ortaya çıkabilir Geri çekme mesafesi sızıntıya neden olabilir; düşük geri çekme hızı plastik sızıntısına yol açar. Aşırı sıcaklık ise plastik akışkanlığını artırarak sızıntıya sebep olabilir (Şekil 4).

Şekil 4. Sızıntı ve İplikler

3.1.3. Üst Yüzeyde Çizikler

Aşırı ekstrüzyon ve düzensiz dikey kaldırma ayarları, baskının üst yüzeyinde çiziklere neden olabilir. Bu sorunu çözmek için uygun dikey kaldırma ayarlarını etkinleştirmek veya ekstrüzyon çarpanı ayarlarını düşürmek etkili olabilir (Şekil 5).

Şekil 5. Üst Yüzeyde Çizikler

3.1.4. Katman Kayması

Katman kayması (Şekil 6), 3D baskıda katmanların istenmeyen konumlarda olmasıdır. Mekanik sorunlar veya düşük tabaka yapışkanlığı nedeniyle gerçekleşebilir. Sorunu çözmek için mekanik kontrol ve düzenli bakım önemlidir. Doğru yatak sıcaklığı ve tabaka yapıştırıcı ayarları ile katman kayması önlenebilir, daha stabil baskılar elde edilebilir.

Şekil 6.Katman Kayması

3.1.5.Destek Nedeniyle Alt Yüzeyde Sorunlar

Destek (raft veya support) nedeniyle düşük yüzey kalitesi, etkisiz köprüleme veya çöken desteklerle ortaya çıkar. Yanlış dilimleme ayarları nedeniyle meydana gelen bu sorunları çözmek için katman kalınlığı ve destek doluluk yüzdesi ayarları kontrol edilmelidir. Çökme riskini azaltmak için ise yeterli doluluk oranı ve kaliteli filament kullanımına dikkat edilmelidir (Şekil 7).

Şekil 7. Destek nedeniyle alt yüzeyin pürüzlülüğü

3.1.6. Baskının Yatağa Yapışmaması

Baskının yatağa yapışmaması sorunu, düşük tabaka yapışkanlığı, düzensiz baskı platformu seviyesi veya yetersiz yatak sıcaklığı gibi nedenlere bağlıdır. Sorunu çözmek için doğru baskı yatağı sıcaklığına, uygun tabaka yapışkanlığına ve düzgün seviyelenmiş bir baskı platformuna dikkat etmek önemlidir.

3.2. Taguchi Deney Parametreleri ve Kalite Değerlendirmesi

Bu çalışmanın kapsamında, Taguchi deney düzenine göre belirlenen parametre ayarları sırasıyla uygulanmış ve toplamda 25 farklı deney gerçekleştirilmiştir. Deneyler, Çizelge 1'de sunulan Taguchi deney düzenine uygun olarak sistematik bir şekilde planlanmış ve uygulanmıştır. Bu deneylerin temel amacı, belirlenen parametrelerin çeşitli kombinasyonlarına bağlı olarak üretilen ürünlerin kalitesini değerlendirmektir.

Şekil 8, yürütülen analizde parametrelerin etkilerini ve seviyelerini gösteren ana etki

çizimini içermektedir. Analiz sürecinde, ortalama baskı kalitesi değerlerini belirlemek için "en küçük daha iyidir" kriteri benimsenmiştir. Bu kriter doğrultusunda, baskı hataları değerinin mümkün olduğunca düşük olması hedeflenmiş ve S/N oranları hesaplanmıştır. S/N oranının maksimize edilmesi, belirli bir performans ölçütünü en üst düzeye çıkarmayı hedefler. Bu durumda, S/N analizi ile en yüksek kalite değeri elde edilebilir. Taguchi analizinden elde edilen optimize edilmiş işlem parametreleri ve bunlara karşılık gelen sıralama Çizelge 2'te gösterilmiştir.

Çizelge 1. Taguchi deney düzeni ve sezgisel kalite değerleri

Deney Numarası	Katman Kalınlığı (mm)	Ekstrüder Sıcaklığı (°C)	Fan Hızı (%)	Duvar Baskı Hızı (mm/s)	Geri Çekme Mesafesi (mm)	Sezgisel Kalite Değerleri
1	0,16	200	60	12	0,4	1,468
2	0,16	205	70	16	0,5	2,250
3	0,16	210	80	20	0,6	2,031
4	0,16	215	90	24	0,7	1,625
5	0,16	220	100	28	0,8	2,625
6	0,18	200	70	20	0,7	2,750
7	0,18	205	80	24	0,8	2,250
8	0,18	210	90	28	0,4	2,937
9	0,18	215	100	12	0,5	2,593
10	0,18	220	60	16	0,6	2,781
11	0,20	200	80	28	0,5	1,500
12	0,20	205	90	12	0,6	1,875
13	0,20	210	100	16	0,7	2,218
14	0,20	215	60	20	0,8	2,250
15	0,20	220	70	24	0,4	2,468
16	0,22	200	90	16	0,8	1,500
17	0,22	205	100	20	0,4	1,437
18	0,22	210	60	24	0,5	1,812
19	0,22	215	70	28	0,6	2,218
20	0,22	220	80	12	0,7	3,062
21	0,24	200	100	24	0,6	0,968
22	0,24	205	60	28	0,7	0,843
23	0,24	210	70	12	0,8	1,437
24	0,24	215	80	16	0,4	1,781
25	0,24	220	90	20	0,5	2,875

Çizelge 2: S/N oranlarına ilişkin yanıt tablosu

Seviye	Katman Kalınlığı	Ekstrüder Sıcaklığı	Fan Hızı	Duvar Baskı Hızı	Geri Çekme Mesafesi
1	-5,82	-3,77	-4,58	-5,98	-5,74
2	-8,46	-4,24	-6,74	-6,27	-6,63
3	-6,15	-6,14	-6,29	-6,86	-5,42
4	-5,69	-6,29	-6,34	-4,79	-5,63
5	-3,11	-8,80	-5,28	-5,33	-5,82
Fark (maks–min)	5,35	5,02	2,16	2,06	1,20

Bu analitik süreç, üç boyutlu üretimde arzu edilen ve tercih edilen yüksek baskı kalitesini elde etmeyi amaçlamaktadır. Bu bağlamda, Çizelge 3'te en yüksek baskı kalitesi değerlerine ulaşmak için kullanılan optimum işlem parametreleri sunulmaktadır.

Çizelge 3: En yüksek baskı kalitesi değerleri için optimum işlem parametreleri

Katman Kalınlığı (mm)	Ekstrüder Sıcaklığı (°C)	Fan Hızı (%)	Duvar Baskı Hızı (mm/s)	Geri Çekme Mesafesi (mm)
0,24	200	60	24	0,6

4. SONUÇ

Bu çalışmada, FFF yöntemindeki baskı parametreleri Taguchi metoduyla optimize edilmiştir. Çalışmada katman kalınlığı, ekstrüder sıcaklığı, fan hızı, duvar baskı hızı ve geri çekme mesafesi parametreleri bağımsız değişken olarak seçilmiş ve bu parametrelerle ilgili olarak toplamda 25 adet örnek üretilmiştir. Üretilen numunelerin değerlendirme süreci, kalite puanlamasına dayanmaktadır. Bu puanlama sürecinde, belirli bir parametre kombinasyonuyla gerçekleştirilen baskılar,

gözlemcilerin kişisel deneyim ve estetik tercihlerine dayalı olarak sezgisel bir puanlama yöntemi kullanılarak incelenmiştir.

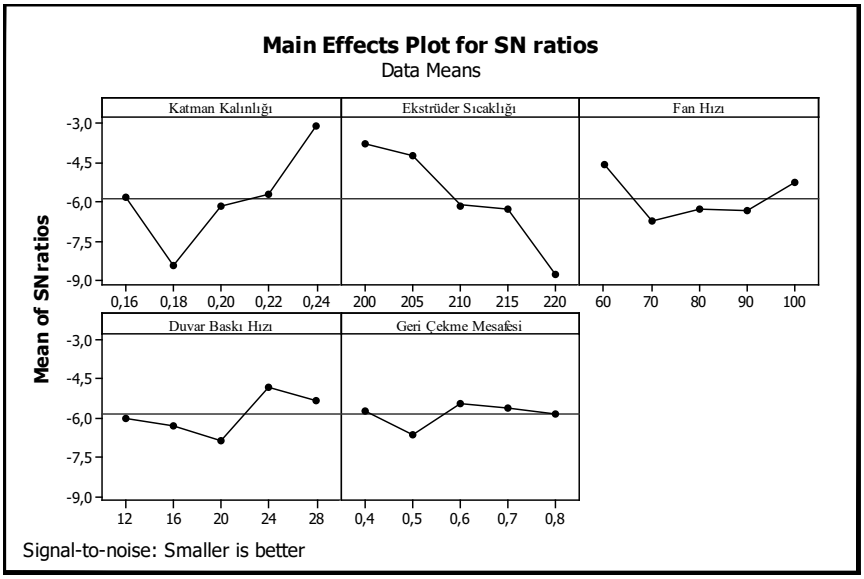

Şekil 8. Kalite değerleri için parametrelerin ana etkiler grafiği

Benchy modeli üzerinde meydana gelen hataların şiddeti eşit kabul edilerek, bu hatalar önem derecelerine göre 1 ile 10 arasında sezgisel olarak puanlanmıştır.

Yapılan deney numunelerinin incelenip sezgisel kalite puanlaması yöntemiyle değerlendirilmesi sonucunda, yan yüzeyde deformasyon hata türüne ait en yüksek hata değeri 20 numaralı numunede gözlemlenmiştir. Sızıntı-iplik ve üst yüzeyde çizik sorunları yine 20 numaralı numunede en çok gözlemlenmiştir. Katman kayması problemi en çok 25. numunede ortaya çıkmışken alt yüzey problemi ise en çok 9. numunede oluşmuştur.

Sezgisel puanlar üzerinden yapılan Taguchi analizi sonucunda optimum baskı parametreleri belirlenmiştir. Analiz sürecinde, "en küçük daha iyidir" kriteri benimsenmiş ve ortalama baskı kalitesi değerleri belirlenirken baskı hataları değerinin mümkün olduğunca düşük olması hedeflenmiştir. Bu kriter doğrultusunda, S/N oranları hesaplanmıştır. S/N oranının maksimize edilmesi, belirli bir performans ölçütünü en üst düzeye çıkarmayı hedefler. Bu bağlamda, S/N analizi ile en yüksek kalite değeri elde edilebilir. Elde edilen analiz sonuçlarına göre, optimal baskı parametreleri ve kalite değerleri şu şekildedir:

• Optimum parametreler 0,24 mm katman kalınlığı, 200 ºC ekstrüder sıcaklığı, 60 mm/s fan hızı, 24 mm/s duvar baskı hızı, 0,6 mm/s geri çekilme hızı olarak bulunmuştur. Fakat bulunan bu optimum değerler makine ve ortama göre değişkenlikler gösterebilir.

• Taguchi Analizi sonucunda en düşük kalite değeri 3,062 olarak 0,22 mm katman kalınlığı, 220 ºC ekstrüder sıcaklığı, 80 mm/s fan hızı, 12 mm/s duvar baskı hızı ve 0,7 mm/s geri çekme hızı parametrelerine sahip olan 20 numaralı numunede ortaya çıkmıştır.

• En yüksek kalite değeri ise 0,24 mm katman kalınlığı, 205 ºC ekstrüder sıcaklığı, 60 mm/s fan hızı, 28 mm/s duvar baskı hızı ve 0,7 mm/s geri çekilme hızı parametrelerine sahip olan 22 numaralı numunede 0,843 olarak bulunmuştur.

Sonuç olarak Taguchi yöntemi ile FFF metodunda parametre optimizasyonu başarılı bir şekilde gerçekleştirilmiştir. Bu çalışmada kullanılan deneysel yaklaşım, FFF yöntemiyle gerçekleştirilen 3D baskılarda kaliteyi artırmak ve istenmeyen hataları minimize etmek adına iyi bir örnek teşkil etmektedir.

KAYNAKLAR

1. Kara, F., Bulan, N., Akgün, M. and Köklü, U., "Multi-Objective Optimization of Process Parameters in Milling of 17-4 PH Stainless Steel using Taguchi-based Gray Relational Analysis", Engineered Science, Vol. 26, Pages 961, 2023.

2. Kara, F., Bayraktar, F., Savaş, F. and Özbek, O., "Experimental and statistical investigation of the effect of coating type on surface roughness, cutting temperature, vibration and noise in turning of mold steel", Journal of Materials and Manufacturing, Vol. 1, Pages 31-43, 2023

3. Nas, E., Özbek, O., Bayraktar, F. and Kara, F., "Experimental and Statistical Investigation of Machinability of AISI D2 Steel Using Electroerosion Machining Method in Different Machining Parameters", Advances in Materials Science and Engineering, Pages 1241797, 2021.

4. Baş, H., Yapıcı, F. and Ergün, E., "Effective use of adaptive slicing in binder jetting using Taguchi method and surface roughness measurement with image processing", Rapid Prototyping Journal ahead-of-print(ahead-of-print), 2024.

5. Giri, J., Sunheriya, N., Sathish, T., Kadu, Y., Chadge, R., Giri, P., Parthiban, A. and Mahatme, C., "Optimization of process parameters to improve mechanical properties of fused deposition method using taguchi method", Interactions Vol. 245, Issue 1, Pages 87, 2024.

6. Singh, T. K., Birru, A. K. and Singh, K. N., "Optimizing the printing parameters for dimensional accuracy of distal femur bone by using Taguchi's method", Journal of Engineering and Applied Science, Vol. 71, Issue, Pages 10, 2024.

7. Wambua, J. M., Mwema, F. M., Akinlabi, S., Birkett, M., Xu, B., Woo, W. L., Taverne, M., Ho, Y.-L. D. and Akinlabi, E., "Optimisation of printing parameters of fused filament fabrication and uniaxial compression failure analysis for four-point star-shaped structures", Rapid Prototyping Journal Vol. 30, Issue 5, Pages 885-903, 2024.

8. Kartal, F., "Optimization of fused deposition modeling process parameters", International Journal of 3D Printing Technologies and Digital Industry, Cilt 1, Sayı 1, Sayfa 49-56, 2017.

9. Baş, H., Elevli, S. and Yapıcı, F., "Fault tree analysis for fused filament fabrication type three-dimensional printers", Journal of Failure Analysis and Prevention, Vol. 19, Issues 5, Pages 1389-1400, 2019.

10. Bacak, S, Özkavak, H. V. ve Tatli, M., "FDM yöntemi ile üretilen PLA numunelerin çekme özelliklerine işlem parametrelerinin etkisinin incelenmesi", Mühendislik Bilimleri ve Tasarım Dergisi, Cilt 9, Sayı 1, Sayfa 209-216, 2021.

11. Günay, M., Gündüz, S., H. Yilmaz, Yaşar, N ve Kaçar, R., "PLA esaslı numunelerde çekme dayanımı için 3D baskı işlem parametrelerinin optimizasyonu", Politeknik Dergisi, Cilt, 23, Sayı 1, Sayfa 73-79, 2020.

12. Bilgin, M., "ABS Esasli Numunelerin 3d Yazici ile Üretilmesinde İşlem Parametrelerinin Optimizasyonu", International Journal of 3D Printing Technologies and Digital Industry, Cilt 6, Sayı 2, Sayfa 236-249, 2022.

13. Seçgin, Ö. ve Kahraman, H., "PETG materyali kullanılarak FDM yöntemiyle eklemeli imalat işleminde yüzey pürüzlülüğünün parametrik optimizasyonu", International Conference on Engineering, Natural and Social Sciences, Cilt 1, Sayfa 623-626, 2023.

14. Sood, A. K., Ohdar, R.K. and Mahapatra, S.S., "Improving dimensional accuracy of Fused Deposition Modelling processed part using grey Taguchi method", Materials and Design, Vol. 30, Issue 10, Pages 4243-4252, 2009.

5. Zhang, J.W. and Peng, A.H., "Process-Parameter optimization for fused deposition modeling based on Taguchi method", Advanced Materials Research, Vol., 538-541, Pages 444-447, 2012.

16. Brenken, B., Barocio, E., Favaloro, A., Kunc, V. and Pipes, R. B., "Fused filament fabrication of fiber-reinforced polymers: A review", Additive Manufacturing, Vol. 21, Pages 1-16, 2018.

17. Daminabo, S.C., Goel, S., Grammatikos, S.A., Nezhad, H.Y. and Thakur, V.K., "Fused deposition modeling-based additive manufacturing (3D printing): techniques for polymer material systems", Materials Today Chemistry, Vol. 16, Pages 100248, 2020.

18. Sathies, T., Senthil, P. and Anoop, M.S., "A review on advancements in applications of fused deposition modelling process", Rapid Prototyping Journal, Vol. 26, Issues 4, Pages 669-687, 2020.

19. Anonymous,"3D Benchy", https://www.3dbenchy.com/, October 24, 2023.

20. ASTM, "Standard terminology for additive manufacturing technologies", https://www.astm.org/f2792-12a.html, October 20, 2023.

21. Canıyılmaz, E., "Kalite geliştirmede Taguchi Metodu ve bir uygulama", Yüksek Lisans Tezi, Gazi Üniversitesi, Ankara, 2001

ULUSLARARASI 3B YAZICI TEKNOLOJİLERİ
VE DİJİTAL ENDÜSTRİ DERGİSİ

INTERNATIONAL JOURNAL OF 3D PRINTING TECHNOLOGIES AND DIGITAL INDUSTRY

ISSN:2602-3350 (Online)

URL: https://dergipark.org.tr/ij3dptdi

COMPARISON OF MECHANICAL DESIGN AND FLOW ANALYSIS OF QUADRUPED ROBOTS

Yazarlar (Authors): Enes UZUN*, Cengiz TEPE

Bu makaleye şu şekilde atıfta bulunabilirsiniz (To cite to this article): *Uzun E., Tepe C., "Comparison of Mechanical Design and Flow Analysis of Quadruped Robots" Int. J. of 3D Printing Tech. Dig. Ind., 8(2): 162-172, (2024).*

DOI: 10.46519/ij3dptdi.1437626

Araştırma Makale/ Research Article

Erişim Linki: (To link to this article): https://dergipark.org.tr/en/pub/ij3dptdi/archive

COMPARISON OF MECHANICAL DESIGN AND FLOW ANALYSIS OF QUADRUPED ROBOTS

Enes UZUN[a]*, Cengiz TEPE[b]

[a]Ondokuz Mayıs Üniversitesi, Mühendislik Fakültesi, Akıllı Sistemler Mühendisliği A.B.D., TÜRKİYE
[b]Ondokuz Mayıs Üniversitesi, Mühendislik Fakültesi Fakültesi, Elektrik Elektronik Mühendisliği Bölümü, TÜRKİYE

* *Sorumlu Yazar: enesuzunn@gmail.com*

(**Received:** 09.01.2024; **Revised:** 04.04.2024; **Accepted:** 16.04.2024)

ABSTRACT

In recent years, there has been a trend of developing innovative technologies inspired by living creatures in nature. Quadruped robots, in particular, have emerged as walking mobile systems with articulated leg structures that can skilfully perform dynamic movements that wheeled systems are limited to. These robots offer advantages in technical criteria such as manoeuvrability, cross-capability, controllability, terrain adaptability and stability. It is important to note that this evaluation is based on objective technical criteria rather than subjective opinions. This study compares the advantages and disadvantages of quadruped robots to wheeled systems. It highlights that quadruped robots outperform wheeled systems in manoeuvrability, obstacle overcoming, and speed, particularly in rough terrains. The study also suggests that designers of quadruped robots should consider aerodynamic factors, which are often overlooked. Flow analysis using the finite element method is crucial in robot design to enhance aerodynamic performance. This paper aims to comprehensively analyse the flow structure around quadruped robots using Computational Fluid Dynamics and investigate passive flow control methods to reduce the drag coefficient (Cd). The study examines four different robots, and the resulting Cd average percentage calculations are presented. The aerodynamic efficiency of Robot 4 compared to Robot 2 was found to be 95%. Similarly, the aerodynamic efficiency of Robot 3 was determined to be 28% compared to Robot 2. Additionally, it was determined that the aerodynamic efficiency of Robot 2 was 76% compared to Robot 1. These results provide an important comparison to understand the energy efficiency, differences in aerodynamic performance and relative effectiveness of quadruped robots.

Keywords: Aerodynamic, Computational Fluid Dynamics, Energy, Quadruped, Robot.

1. INTRODUCTION

Humanity has always strived to study living organisms in their natural habitats, generate novel ideas, and develop innovative technologies to enhance our daily lives. Such efforts are one of the most remarkable examples of recent years. A quadruped robot inspired by animals is capable of walking and performing dynamic movements [1]. Although wheeled vehicles have been in use for more than thousands of years, mountainous or desert terrain requires greater surface roughness than footed vehicles such as horses and mules. Over billions of years of evolution, the result of natural selection on the locomotion of land animals has fully demonstrated the adaptability, mobility and carrying capacity of four-legged mammals in rough terrain [2]. Wheeled robots move quickly but have poor manoeuvrability to navigate uneven ground or overcome obstacles such as stairs. Legged robots outperform wheeled robots in these terrain conditions [3]. Quadruped robots are walking locomotion systems with articulated leg structures and can also perform dynamic motions that are limited by wheeled systems. These robots are one of the most significant developments in the field of robotics [4]. Quadruped robot technology has developed rapidly since the 21st century. The robot's leg structure has been enhanced with bionic technology, improving its ability to adapt to various terrains. The manufacturing technology of power systems has led to the development of quadruped robots with

integrated power sources [2]. Each system has its own advantages and disadvantages. A detailed comparison of the technical criteria of legged and wheeled robots is shown in Table 1. As can be seen in Table 1, the development of legged locomotion on land has grown continuously over the last decade due to the fact that legged robots offer more advantages than wheeled robotic vehicles. The advantages of legged locomotion depend on the posture, the number of legs and the functionality of the leg. Although wheeled and tracked robots can operate on flat terrain, their ability to operate in most rough and difficult terrain conditions is poor [5].

Table 1. Comparison between wheeled and legged robots [5].

Technical Specifications	Wheeled robot	Legged Robot
Manoeuvrability	Poor	Good
Cross talent	Poor	Good
Controllability	Good	Poor
Terrain Compatibility	Poor	Good
Stability	Good	Poor
Cost-effective	Good	Poor
Navigating over obstacles	Poor	Good
Complexity	Poor	Good

Quadruped robot designs are widely used in various applications, from industrial to personal use. Their motion capabilities, adaptability, and capacity to perform a variety of tasks make them an ideal platform to increase the effectiveness of robotic systems. Robots are utilized in numerous manufacturing tasks, including painting, welding, assembly, soldering, handling, and conveying [1].

Mobile robots have a wide range of applications in various fields, including space exploration, military operations, and industrial use [5]. However, the design process of quadruped robots faces a fundamental problem in the form of aerodynamic factors, which are often overlooked. In particular, air resistance can pose a significant obstacle when these robots move at high speeds or operate in open spaces. Quadrupeds use a variety of gaits depending on their movement speed. At lower movement speeds, the robot uses a walking gait, which transitions to a sprint gait as the speed increases. At the highest range of movement speed, the robot uses a galloping gait [6]. To successfully design a legged robot, it is important to consider and optimize for aerodynamic challenges, as well as gait stability, robustness, speed, and practicality, including size, volume, weight, and energy efficiency [7]. Aerodynamic analyses are conducted using the finite element method to determine the optimal aerodynamic structure of robots. The finite element method simplifies complex engineering problems by dividing the solution domain into a large number of simple, interconnected sub-regions called finite elements. This means that it is possible to solve problems that are divided into parts connected by many nodes. The mesh method, which divides the surface into small parts and moves from the part to the whole, was used to perform airfoil flow analysis [8]. The aerodynamic performance of quadruped robots is often overlooked. This study aims to improve the aerodynamic performance of quadruped robot designs, increase their energy efficiency, and optimize their motion capabilities for industrial and research applications. To achieve this, a detailed analysis of the flow structure around the quadruped robots using Computational Fluid Dynamics (CFD) method will be conducted, and passive flow control methods for Cd reduction will be investigated.

2. MATERIAL AND METHOD

Modelling a quadruped robot requires creating an accurate representation of its physical properties and kinematics. Various methods for building such models have been studied in the literature.

Atique and Ahad [9] developed a quadruped robot controlled by the Android operating system. Inverse Kinematics Solutions and the Denavit Hartenberg rule were used to develop the structure. The movements were simulated using 3D software. An Android application was developed to control the robot via Bluetooth, allowing for six different movements. Yong et al. [10] investigated the optimisation of dynamic gait planning and stability control of quadruped robots under external disturbing forces. A quadruped walking robot platform with fourteen active degrees of freedom is designed. Subsequently, a forward kinematic joint model for quadruped robots is established based on the Denavit-Hartenberg (D-H) method. The inverse kinematic equations are solved to obtain joint values when the desired position and orientation are specified. Finally, a dynamic gait planning algorithm is proposed

and tested on a quadruped robot. Xiong [11] designed a mobile quadruped robot based on the bionic and simplified octopus structure. The single leg kinematics of the robot were analysed using the Denavit-Hartenberg system, and the kinematic equation was obtained. The joint angles were then calculated by solving the inverse kinematics with the method of separate variables. The joint angles of the vertical oscillation stance phase and the oscillation phase of the robot's walking motion were calculated and analysed using MATLAB. The experimental results confirmed the universality of robot motion. These are two basic examples of the mathematical and kinematic approaches used to construct quadruped robot models. The study analyses four different robot models using the k-Omega SST turbulence model and CFD analyses, presented under subheadings.

2.1. Trial Analysis

The performance of the quadruped robot model will be tested in various environments, and its effectiveness in real-world conditions will be evaluated based on multiple criteria.

To analyze the flow around the quadruped robot design, we will use CFD analysis, which involves mathematical modeling of fluid dynamics and solving it through computer simulations. CFD is a comprehensive research tool that allows us to understand and optimize various parameters. The analysis includes the steps shown in Figure 1.

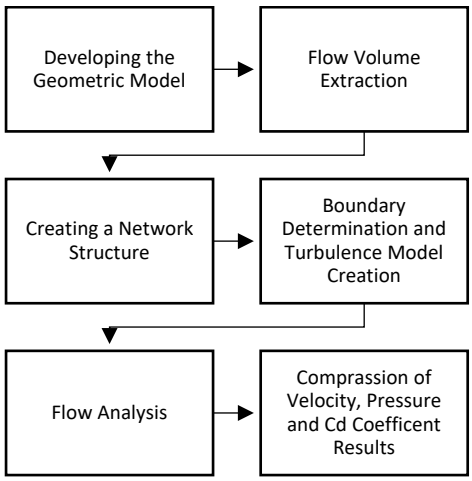

Figure 1. CFD analysis steps.

The study employed geometric modelling as the method for quadruped robot modelling. Other modelling methods include kinetic modelling, dynamic modelling, artificial neural networks, machine learning models, system identification methods, and simulation-based modelling.

2.1.1. Geometry Modelling

The task involves creating a detailed digital representation of the physical geometry of the quadruped robot in a computer environment.
Nowadays, mass production methods have evolved into mass-customised production, which requires the production of small quantities of similar but geometrically different parts. Therefore, it is necessary to rapidly design similar parts. The need for effective definition of design parameters has led to the development of design methods. Computer Aided Design (CAD) is a widely used method in all engineering fields. CAD refers to the computerised drawing of a part, a building or a map according to certain rules. In Mechanical Engineering, CAD is specifically used for part and mould design. Computer-aided systems are extensively used in design and manufacturing processes today. Worldwide, there are many CIS and Computer-Aided Manufacturing (CAD) programs with different features developed for this purpose [13]. These design techniques, known as parametric design, play a crucial role in fast and flexible design processes. Additionally, since a new construction involves design and stress calculations, designs are subject to frequent changes. They may require rapid reshaping of an existing product and design changes based on engineering analysis results. CIS systems are essential tools that aid engineers in the forming, detailing, fabrication, and assembly phases of design. Just as computers are crucial in the design phase of engineering systems, the use of CIS software is an inevitable necessity. The CIS system is designed to aid engineers in the design, detailing, manufacturing, and assembly phases. While computers are crucial in technical system design, the use of CIS software is also significant [12]. Figure 2 provides isometric views of the robots to be analyzed by CFD.

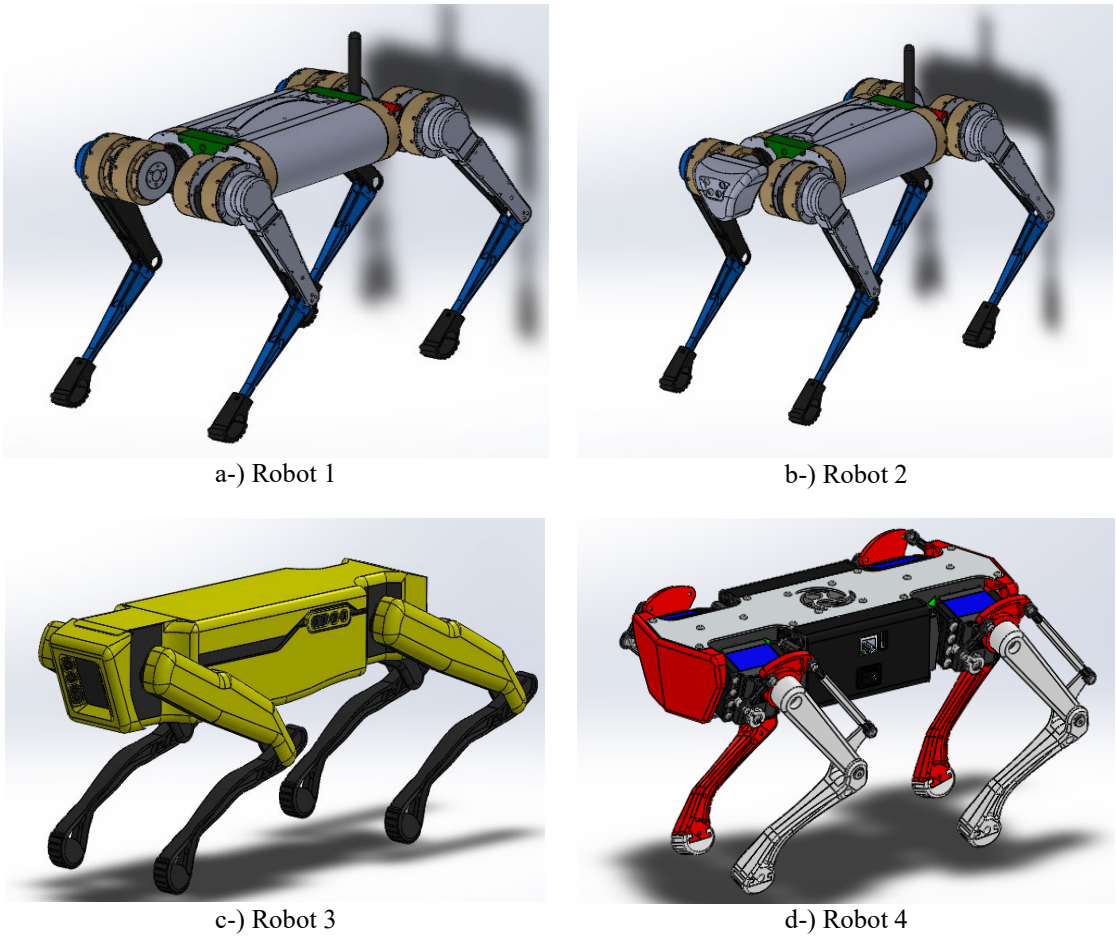

a-) Robot 1 b-) Robot 2

c-) Robot 3 d-) Robot 4

Figure 2. Isometric views of robots: a-) Robot 1, b-) Robot 2, c-) Robot 3 and d-) Robot.

2.1.2. Determining Flow Conditions

The analysis determined the flow conditions to be used, including parameters such as velocity, temperature, and pressure. The equations were numerically solved using the specified flow conditions and mathematical model through computers.

2.1.3. General Equations

The Fluent program uses finite volume methods to solve the integral equation that includes continuity, momentum, energy, and turbulence. Numerical methods are employed to solve these equations using the programs in the package. The continuity and momentum equations are analyzed using finite volume analysis with the aid of HAD. Solving these equations analytically is challenging in practice [14].

2.1.3.1. Continuity Equation

The continuity equation is a fundamental equation used in the field of fluid mechanics to express the conservation of mass. It is commonly applied in areas such as HAD. The equation defines the change in the amount of fluid mass in a control volume and states that the mass flow rate inside a control volume is equal to the mass flow rate across the control volume boundaries. Equation (1) illustrates the continuity equation.

$$\partial\bar{u}/\partial x + \partial\bar{v}/\partial y + \partial\bar{w}/\partial z = 0 \qquad (1)$$

Equation (1) demonstrates that the change in mass of a fluid in a control volume is due to the fluid moving in or out of this volume.

If the expression is satisfied, it shows that the fluid is continuous within the volume and satisfies the principle of mass conservation. The continuity equation, which is also used in HAD simulations, contributes to a better understanding of the fluid's motion and distribution. The equation expresses that the mass flow rate at a specific point is equal to the sum of the mass flow rates of all the fluids that combine or divide in that point.

2.1.3.2. Momentum Equation

The momentum equation is a fundamental equation that describes fluid motion. It is commonly used in applications such as HAD. In general, the momentum equation for a three-dimensional environment and a control volume is given by Equation (2)-(4). The equation is derived from Newton's second law of motion and specifies how the mass and velocity of a fluid change over time. The momentum equation for a three-dimensional environment and a control volume is typically expressed by Equation (2)-(4). It is important to maintain consistency in the use of this equation throughout the text.

$$\rho\frac{\mathrm{Du}}{\mathrm{Dt}} = \frac{\partial(-\mathrm{p}+\tau_{xx})}{\partial x} + \frac{\partial\tau_{yx}}{\sigma y} + \frac{\partial\tau_{zx}}{\sigma z} + S_{Mx} \qquad (2)$$

$$\rho\frac{\mathrm{Dv}}{\mathrm{Dt}} = \frac{\partial(-\mathrm{p}+\tau_{yy})}{\partial y} + \frac{\partial\tau_{xy}}{\sigma x} + \frac{\partial\tau_{zy}}{\sigma z} + S_{My} \qquad (3)$$

$$\rho\frac{\mathrm{Dw}}{\mathrm{Dt}} = \frac{\partial(-\mathrm{p}+\tau_{zz})}{\partial z} + \frac{\partial\tau_{xz}}{\sigma x} + \frac{\partial\tau_{yz}}{\sigma y} + S_{Mz} \qquad (4)$$

2.1.3.3. Navier – Stokes Equation

The Navier-Stokes equations are a set of fundamental differential equations used to describe fluid motion. Equations (5)-(7) below provide the most useful version of the Navier-Stokes equations for the development of finite volume methods [14].

$$\rho\frac{\mathrm{Du}}{\mathrm{Dt}} = -\frac{\partial\mathrm{p}}{\partial x} + div(\mu gradu) + S_{Mx} \qquad (5)$$

$$\rho\frac{\mathrm{Dv}}{\mathrm{Dt}} = -\frac{\partial\mathrm{p}}{\partial y} + div(\mu gradu) + S_{My} \qquad (6)$$

$$\rho\frac{\mathrm{Dw}}{\mathrm{Dt}} = -\frac{\partial\mathrm{p}}{\partial z} + div(\mu gradu) + S_{Mz} \qquad (7)$$

External flow problems refer to the hydrodynamic forces and moments that occur when a fluid moves over a stationary solid object or when a solid object moves within a stationary fluid [15]. The HAD method is a powerful tool for analyzing the flow around quadruped robot designs. Research in this field often focuses on unique solutions by examining specific designs and robot geometries.

The Finite Element Method is an engineering problem-solving approach that simplifies complex problems into possible solutions. It involves dividing the solution domain into numerous simple subdomains, called finite elements, which are connected to each other. This allows for the easy solution of problems that are divided into parts connected by numerous nodes and points. The surfaces of quadruped robots are divided into small pieces for flow analysis, and transitions are made from the pieces to the whole [16]. These examples represent general approaches used for CFD analysis of the flow around quadruped robot designs.

2.1.4. Passive Flow Control Methods

Passive flow control is a method of flow control that is achieved by changing the geometry of the aerodynamic structure, which is widely studied, within the system without consuming energy [14]. In a flowing medium, there is a certain flow structure around an object. The process of removing this flow structure from the normal flow structure is called flow control. There are two types of flow control methods. There are two types of flow control methods based on energy consumption in flow control: active flow control methods and passive flow control methods. Passive flow control is a flow control method that is generally achieved by changing the shape of the object being studied aerodynamically without expending energy on the system [17]. Aerodynamics is the branch of science that studies the movement of objects in the air and their interactions with air [14].

2.1.4.1. Optimising Body Geometry for Flow Control

Geometric modifications, particularly in studies on quadruped robot designs, can effectively direct the flow, reducing Cd and improving the robot's aerodynamic performance. Pipes or holes cut into the robot's surface can also reduce Cd by creating a specific effect on the fluid. There are two types of flow control schemes based on energy consumption: active flow control schemes and passive flow control schemes.

The Cd factor is a dimensionless value used to measure an object's air resistance. A lower value indicates less air resistance. Cd is influenced by the object's shape, position, fluid properties (such as fluid type, density, velocity, etc.), and angle of attack [18]. Reducing Cd results in decreased air resistance and improved aerodynamic performance. Lowering the Cd value can lead to increased

energy efficiency. Reducing the air resistance of an object can improve the energy efficiency of fast-moving vehicles, resulting in lower fuel consumption and energy costs.

The low Cd value of vehicles supports fuel savings, particularly in automobiles, and can also reduce emissions.

Additionally, lower air resistance is often associated with lower energy consumption, which can help to reduce environmental impacts. Reducing Cd offers several advantages, including the reduction of environmental impacts such as the use of fossil fuels and carbon emissions.

These methods can improve aerodynamic efficiency, which is particularly important for transportation vehicles and fast-moving systems. Passive flow control methods can be used to achieve this, and there are several general strategies available. However, the most effective strategies may vary depending on the specific application or design of the quadruped robot.

2.1.4.2. Volume Barriers and Surface Modifications

Geometric changes and surface modifications can reduce the drag coefficient (Cd) generated by the flow. For instance, adjusting the aerodynamic profile or adding volume barriers to specific regions on the body surface can improve flow steering and reduce Cd. Additionally, discrete holes or cavities placed on the surface of the robot can reduce Cd by inducing vortices as the flow passes over them. This type of passive control strategy can be effective for low-velocity flows. The Ansys Fluent program was used to perform flow analysis. A solid model was placed on the ground within an area of 700 mm x 1000 mm x 2000 mm, and a model cavity was created as shown in Figure 3. The Fluent program ensures convergence by balancing equations at each point in the solution set. The severity of the error in the solution for each fluid variable is indicated by the residual. The report predicts an area velocity of 0.7 m^2. The analysis employed a SIMPLE least squares cell-based, k-Omega SST turbulence model with k-Omega as the standard initialization. The walls were treated as standard. Technical abbreviations were explained when first used. The language is clear, objective, and value-neutral. The text is free from grammatical errors, spelling mistakes, and punctuation errors. The content of the improved text is as close as possible to the source text.

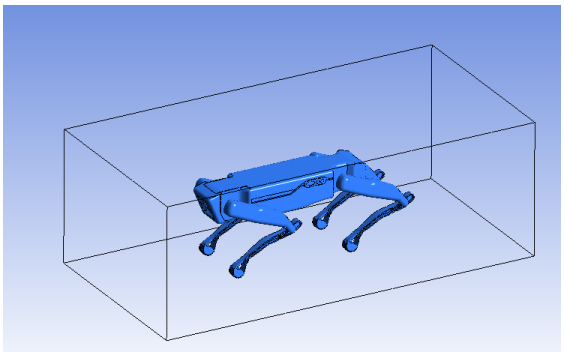

Figure 3. Model appearance in the "design modeler" interface and model space [14].

The Fluent® program was used to perform the analysis on a computer with an Intel(R) Core(TM) i7-4720HQ CPU @ 2.60GHz 2.59 GHz and 16 GB RAM.

3. RESULTS AND DISCUSSION

This study analysed the states of four quadruped robot models (named Robot (1)-(4) [14]) at different speeds, as shown in Figures (2)-(5) [19-21]. The results indicate that an increase in speed leads to an increase in pressure acting on the robots, particularly at the front and in the direction of the angle of attack of the fluid. Figures (4)-(7) present the velocity and velocity vector representations, revealing the direction of motion and speed of the robot. The analysis highlights the velocity drops observed at the joints of the robot, indicating a complex aerodynamic interaction in these regions.

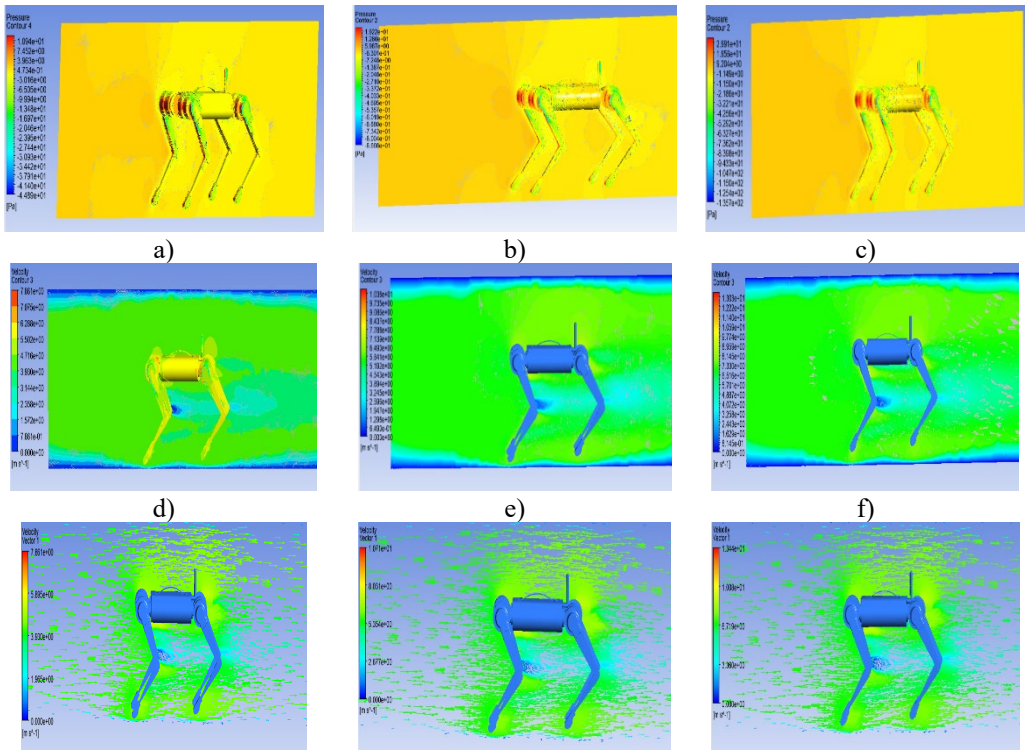

Figure 4. The CFD analysis of Robot 1 was conducted for speed variables of 15, 20, and 25 km/h (from left to right); The pressure results are shown in a), b), and c), while the speed results are shown in d), e), and f). The speed vector representations are shown in g), h), and i).

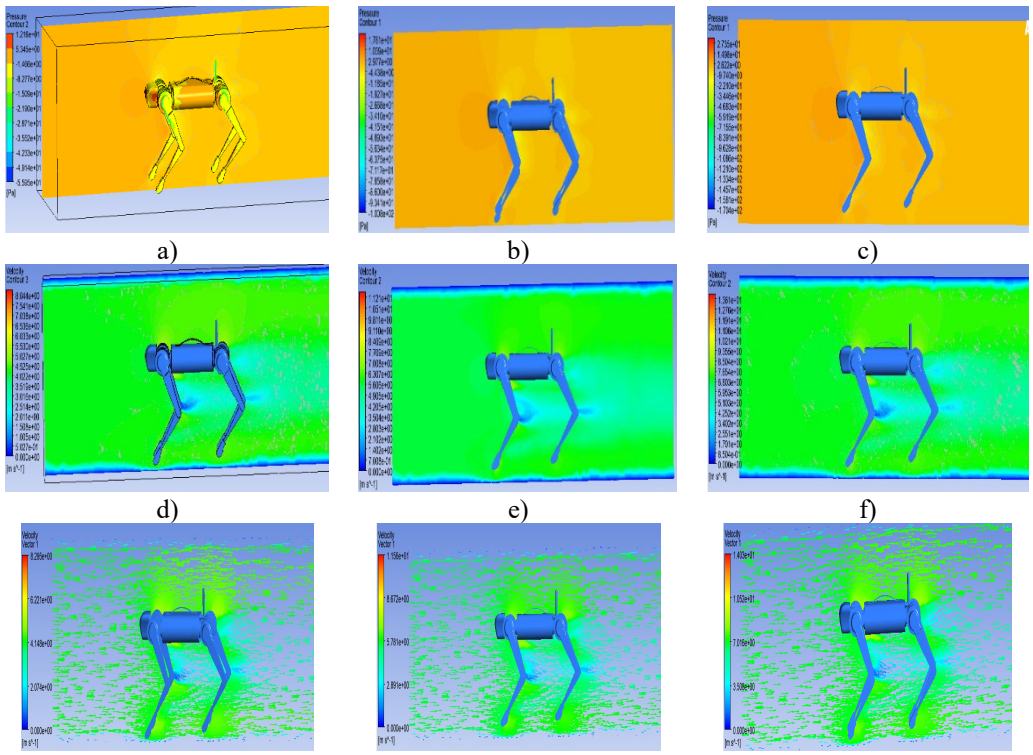

Figure 5. The CFD analysis of Robot 2 was conducted for speed variables of 15, 20, and 25 km/h (from left to right); The pressure results are shown in a), b), and c), while the speed results are shown in d), e), and f). The speed vector representations are shown in g), h), and i).

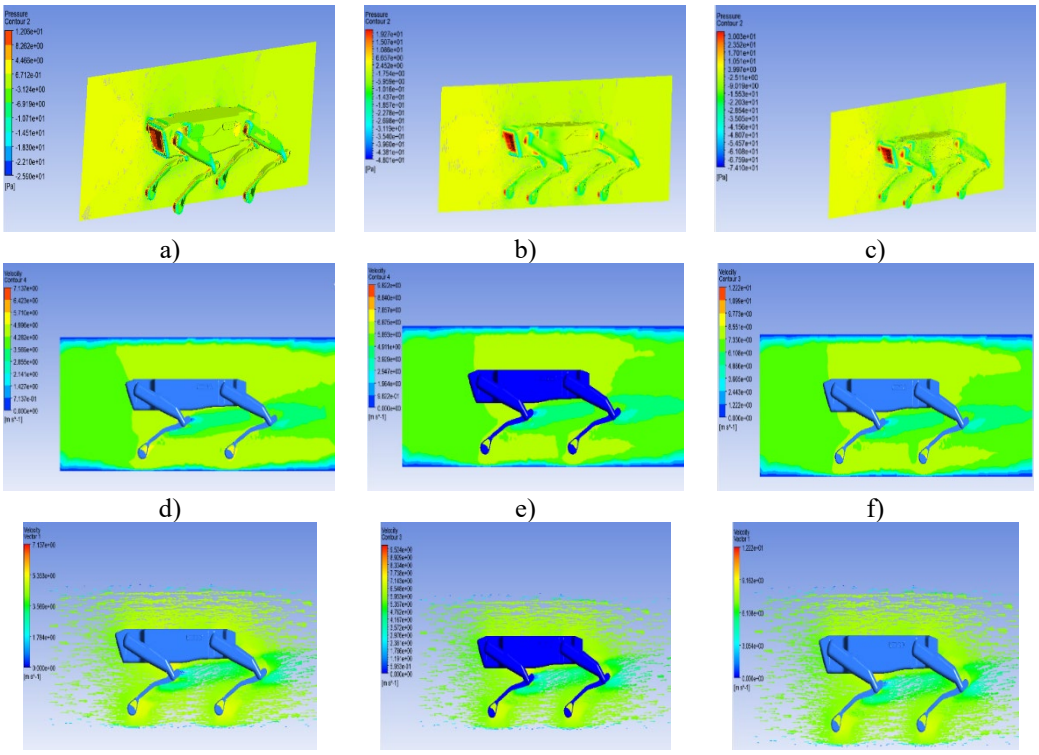

Figure 6. The CFD analysis of Robot 3 was conducted for speed variables of 15, 20, and 25 km/h (from left to right); The pressure results are shown in a), b), and c), while the speed results are shown in d), e), and f). The speed vector representations are shown in g), h), and i).

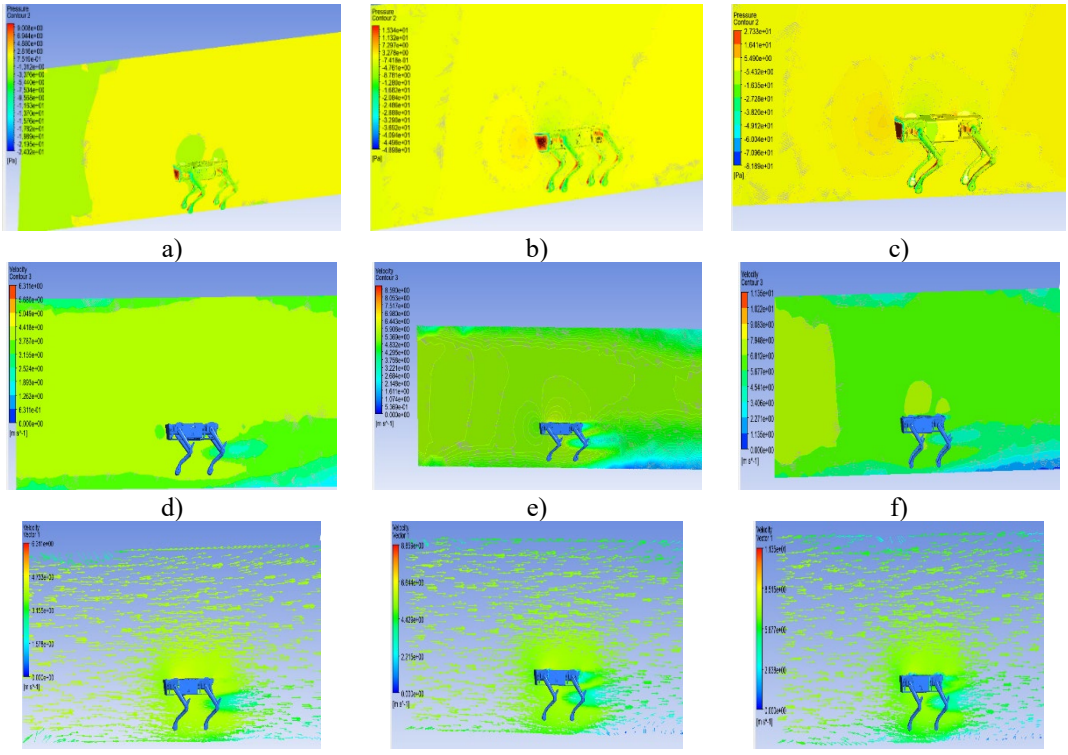

Figure 7. The CFD analysis of Robot 4 was conducted for speed variables of 15, 20, and 25 km/h (from left to right); The pressure results are shown in a), b), and c), while the speed results are shown in d), e), and f). The speed vector representations are shown in g), h), and i).

Figures (2)-(5) show the tight mesh structure of the regions that significantly affect the aerodynamic structure of the model. Boundary definitions were made, and the mesh file was sent to the setup department. The solution domain boundaries are defined as follows: the inlet has a constant velocity boundary condition where the fluid enters, the outlet has a constant pressure condition where the fluid exits, and the wall is the edge surface of the rectangular volume bounding the experimental area where the wall boundary condition is applied.

The analysis focused on the model space of the quadruped robot drawing data. The wall was defined as a boundary condition.

After performing 1000 iterations and using the Cd coefficients given in Table 2, the flow analysis yielded the Cd value that affects the quadruped robots. The aerodynamic Cd is provided in Equation (8) below. Here, the density (ρ) is a function of the free flow velocity (V) and the front view area (A_{front}) [14].

$$Cd = \frac{F_D}{1/2\rho V^2 A_{front}} \quad (8)$$

It concludes that Robot 4 has the lowest Cd value among Robot 1, Robot 2, and Robot 3, indicating higher aerodynamic efficiency. The paper evaluates the aerodynamic performance of quadruped robots at speeds of 15, 20, and 25 km/h by comparing their Cd values. According to the ranking, Robot 4 has the best aerodynamic performance with the lowest Cd value, indicating that it can increase energy efficiency by minimizing air resistance. Robot 3 follows in second place, while Robot 2 ranks third.

Robot 1 has the highest aerodynamic resistance compared to the other models' Cd values and ranks last in the analysis.

This ranking is a crucial step in objectively evaluating the aerodynamic performance of quadruped robots. Robot 4 stands out with the lowest Cd value, indicating an advantageous position in terms of energy efficiency and fast movement capabilities. This supports fuel savings and reduces environmental impact. However, it is important to consider these factors in the context of specific design and application, as the suitability of each robot for particular tasks may vary.

These analyses demonstrate that robots have the potential to enhance energy efficiency and optimize mobility. The analysis of the design and dimensional characteristics of the robots reveals that the aerodynamic structure has a significant impact. The study examines the aerodynamic properties of robots with different geometries and dimensions, as shown in Figure 8.

Table 2 shows the Cd average percentage calculations for Robots (1)-(4) following the examinations. Robot 4 demonstrated an aerodynamic efficiency of 95% compared to Robot 2. Robot 3's aerodynamic efficiency was found to be 28% according to Robot 2. Furthermore, Robot 2's aerodynamic efficiency was determined to be 76% compared to Robot 1.

The aerodynamic structure of the charged quadruped robots is a critical factor for long-term use, as inferred from these findings.

Table 2. Shows the Cd values and averages of robots at various speeds.

Speed	Cd value (xE-28)			
	Robot 1	**Robot 2**	**Robot 3**	**Robot 4**
15	5,57	4,49	3,23	2,45
20	3,14	2,53	1,82	1,38
25	2,01	1,62	1,16	8,83
Average	3,57	2,88	2,07	1,57
Average (%)	-24%	**Reference**	28%	95%

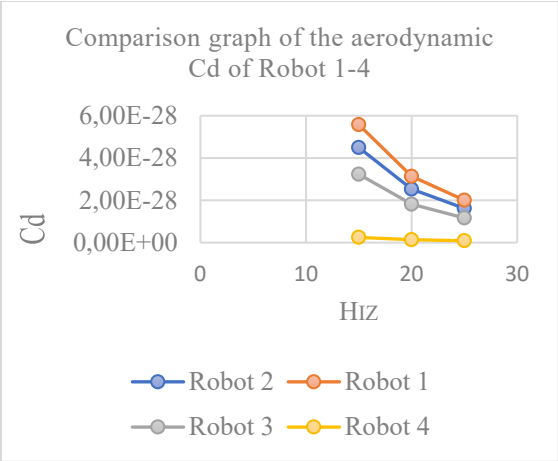

Figure 8. Comparison graph of the aerodynamic Cd of Robot (1)-(4).

4. CONCLUSIONS

This study concentrates on the design of quadruped robot technology, with a specific emphasis on their aerodynamic performance. The significance of aerodynamic factors in the design process has been emphasised, particularly in robots that move at high speeds, where these factors must be optimised.

Flow analysis using the CFD method enabled a detailed study of the flow structure around the quadruped robots. These analyses revealed the potential of passive flow control methods for reducing Cd. The study's findings demonstrate that these methods have the potential to enhance the energy efficiency of robots and optimize their motion capabilities.

One of the study's main focuses is the comparison of the aerodynamic characteristics of quadruped robots with varying geometries and dimensions. The investigation revealed that different designs have a significant impact on aerodynamic efficiency. The efficiency of the robots was found to be affected by air resistance due to their geometric dimensions. The efficiency of the robots was found to be affected by air resistance due to their geometric dimensions. Larger robots experience higher air resistance, resulting in lower energy efficiency. It is important to note that these observations are objective and based on the analysis of robot models. Conversely, smaller robots experience less air resistance and have higher energy efficiency.

Based on these results, it is concluded that considering the effect of geometric dimensions on drag is crucial for designing efficient and energy saving robots. This can lead to the creation of optimised structures and motion systems in future robot design processes. In particular, Robot 4 showed higher aerodynamic efficiency compared to the other models.

The study highlights the critical role of the aerodynamic structure in the long-term use of rechargeable quadruped robots. Optimising energy consumption through high aerodynamic efficiency enables robots to move longer and more effectively.

The aim of this study is to contribute to the development of more sustainable and aerodynamically efficient robotic systems by emphasising the importance of aerodynamic performance as a design parameter.

REFERENCES

1. Şen, M.A., Bakırcıoğlu, V. and Kalyoncu, M., “Three degree of freedom leg design for quadruped robots and fractional order pid (piλdμ) based control”, Konya Journal of Engineering Sciences, Vol. 8, Issue 2, Pages 237-247, 2020.

2. Chai, H., Li, Y., Song, R., Zhang, G., Zhang, Q., Liu, S., and Yang, Z., “A survey of the development of quadruped robots: Joint configuration, dynamic locomotion control method and mobile manipulation approach”, Biomimetic Intelligence and Robotics, Vol. 2, Issue 1, Pages 1-13, 2022.

3. Ekici, U. and Bilgin, N., “Design of a Quadruped Robot for Trajectory Planning and Obstacle Striding”, Fırat University Space and Defense Technologies Journal, Vol. 1, Issue 1, Pages 1-7, 2022.

4. Şen, M. A. and Kalyoncu, M., “A Literature Review on Modeling, Control and Walking on Rough Surfaces of Quadruped Robots”, Konya Journal of Engineering Sciences, Vol. 9, Issue 1, Pages 250-279, 2021.

5. Priyaranjan, B. and Prases, K.M., “Development of quadruped walking robots: A review”, Ain Shams Engineering Journal, Vol. 12, Issue 2, Pages 2017-2031, 2021.

6 Tanase, M., Ambe, Y., Aoi, S., and Matsuno, F., “A galloping quadruped model using left-right asymmetry in touchdown angles”, Journal of Biomechanics, Vol. 2, Issue 1, Pages 3383-3389, 2015.

7. Byeonghun, N. and Kyoungchul, K. "Design of a One Degree-of-Freedom Quadruped Robot Based on a Mechanical Link System: Cheetaroid-II", IFAC-PapersOnLine, Vol. 49, Issue 21, Pages 409-415, 2016.

8. Özden, M., Çelik, B., Genç, M. S. and Açikel, H., "Rüzgar Türbini kanadında akış kaynaklı deformasyonlarının sayısal ve deneysel incelenmesi", 3. İzmir Rüzgar Sempozyumu ve Sergisi, İzmir, Pages 113-125, 2015

9. Atique, M.M.U., Sarker, M.R.I. and Ahad, M.A.R., "Development of an 8DOF quadruped robot and implementation of Inverse Kinematics using Denavit-Hartenberg convention", Heliyon, Vol. 4, Issue 12, Pages 1-19, 2018.

10. Yong, S., Teng, C., Yanzhe, H., and Xiaoli, W., "Implementation and dynamic gait planning of a quadruped bionic robot", International Journal of Control, Automation and Systems, Vol. 15, Issue 6, Pages 2819-2828, 2017.

11. Xiong, W., "Structural Design and Motion Analysis of Universal Mobile Quadruped Robot", International Journal on Smart Sensing and Intelligent Systems, Vol. 9, Issue 3, Pages 1305-1322, 2016.

12. Halkacı, H. S.and Yiğit, O., "Parametrik tasarım ve Solidworks CAD programı ile bir uygulama", Mühendis ve Makine, Vol. 45 Issue 537, Pages 17-24, 2004.

13. Er, M. and Kayir, Y., "The Effect of The CAD Data Exchange on the Motion Analysis in the Solidworks CAD Program", Aksaray University Journal of Science and Engineering, Vol. 3, Issue 1, Pages 51-60, 2019.

14. Bayındırlı, C., Çelik, M. and Demiralp M., "The Investigation Of Flow Characteristic Around A Bus Model By CFD Method And Improvement of Drag Force By Passive Flow Control Method", Journal of Polytechnic, Vol. 21, Issue 4, Pages 785-795, 2018.

15. Yılmaz, G. and Yılmaz, S., "Analysis of Depth and Speed-Dependent Variation of Hydrodynamic Drift and Lift Forces in Unmanned Underwater Vehicles with CFD", International Journal of Engineering Research and Development, Vol. 14, Issue 1, Pages 72-83, 2022.

16. Vergün, T., Kurumu, T. H., Oztürk and S., Nikbay, M., "Kanatçık Açısının Insansız Hava Aracının Aeroelastik Davranışına Etkisinin İncelenmesi", 8. Ulusal Havacılık ve Uzay Konferansı, Ankara, Pages 137-140, 2020.

17. Akansu, Y.E., Bayındırli, C. and Seyhan, M., "The Improvement of Drag Force on a Truck Trailer Vehicle by Passive Flow Control Methods", Journal of Thermal Science and Technology, Vol. 36, Issue 1, Pages 133-141, 2016.

18. Yarın, T.G., "Farklı Taşıt Modellerinin Aerodinamik Yapısının Numerik Olarak İncelenmesi", Doktora Tezi, [Numerical Analysis of Aerodynamic Structure Of Different Vehicle Models], [Thesis in Turkish], Uludağ Üniversitesi, Bursa, 2019.

19. Belakaposki, J., "Cheetah Robot", https://grabcad.com/library/cheetah-robot-version-1-0-1, February 11, 2024.

20. Heulin, J., "Spot Boston Dynamics", https://grabcad.com/library/spot-bostondynamics-1, February 11, 2024.

21. Alp, B., "Diy Robot Dog: Kangal ", https://www.youtube.com/watch?v=ztCE2fqSIxo, February 11, 2024.

ULUSLARARASI 3B YAZICI TEKNOLOJİLERİ
VE DİJİTAL ENDÜSTRİ DERGİSİ

INTERNATIONAL JOURNAL OF 3D PRINTING TECHNOLOGIES AND DIGITAL INDUSTRY

ISSN:2602-3350 (Online)

URL: https://dergipark.org.tr/ij3dptdi

EVALUATION OF MECHANOBIOLOGICAL POTENTIAL OF 3D-PRINTED PLA BONE TISSUE SCAFFOLDS WITH DIFFERENT PORE ARCHITECTURES AND POROSITY RATIOS

Yazarlar (Authors): Safa ŞENAYSOY*, Hüseyin LEKESİZ

Bu makaleye şu şekilde atıfta bulunabilirsiniz (To cite to this article): *Şenaysoy S., Lekesiz H., "Evaluation of Mechanobiological Potential of 3D-Printed PLA Bone Tissue Scaffolds With Different Pore Architectures and Porosity Ratios" Int. J. of 3D Printing Tech. Dig. Ind., 8(2): 173-184, (2024).*

DOI: 10.46519/ij3dptdi.1449545

Araştırma Makale/ Research Article

Erişim Linki: (To link to this article): https://dergipark.org.tr/en/pub/ij3dptdi/archive

EVALUATION OF MECHANOBIOLOGICAL POTENTIAL OF 3D-PRINTED PLA BONE TISSUE SCAFFOLDS WITH DIFFERENT PORE ARCHITECTURES AND POROSITY RATIOS

Safa ŞENAYSOY[a]*, Hüseyin LEKESİZ[a]

[a]Bursa Technical University, Engineering and Nature Science Faculty, Mechanical Engineering Department, TÜRKİYE

* *Corresponding* safa.senaysoy@btu.edu.tr

(**Received:** 09.03.2024; **Revised:** 17.06.2024; **Accepted:** 12.08.2024)

ABSTRACT

Lattice structures are widely used in bone tissue scaffold designs due to interconnected porous structures that mimic the natural extracellular matrix (ECM) to treat large bone defects. This study investigated the mechanical behavior of scaffolds with different pore architectures and porosity ratios using experimental and numerical methods. In addition, mechanobiological potentials of scaffolds were evaluated in terms of the specific energy absorption and the specific surface area. Three different geometries were created by varying the combination of vertical, horizontal, and diagonal struts to evaluate the geometric factor and 50%, 62.5, and 75% porosity ratios are examined as potential permeabilities. Compression tests were performed to calculate stiffness values and energy absorptions of the scaffolds. Finite element simulations were used to obtain stiffness values of scaffolds. The specific energy absorptions of scaffolds were calculated under 4 N compressive load as a representative of potential body loads. According to the results, it was found that pore architectures and porosity ratios had crucial effects on stiffness values, energy absorption levels, specific energy absorption, and specific surface area which may lead to significant differences in bone remodeling. The highest specific energy absorption was observed in the scaffolds designed with only diagonal struts with 75% porosity. The highest specific surface area was observed in the scaffolds designed with the combination of vertical, horizontal, and diagonal struts with 75% porosity.

Keywords: Bone Tissue Scaffold, Mechanical Behavior, Mechanobiology, Bone Regeneration, Finite Element Analysis, Polylactic Acid (PLA)

1. INTRODUCTION

Bone tissue undergoes continuous remodeling processes that regulate bone formation and resorption throughout life [1-4]. The remodeling process allows bone tissue to regenerate, repair microdamage, and adapt to external mechanical loads [5-8]. Large defects in bone tissue can be caused by severe trauma or cancer, and they cannot be healed by remaining bone tissue. There are therapeutic methods to treat large bone defects, such as autograft, allograft, and xenograft. Nevertheless, these methods have some limitations in surgical operations due to insufficient tissue, the lack of donors, and immunity problems [9-12]. Tissue engineering has emerged as a promising alternative to traditional approaches for treating large bone defects [13-16, 20]. The tissue engineering approach uses different components such as cultured cells, scaffolds, and growth factors to facilitate tissue regeneration [17]. Bone tissue scaffolds replace extracellular matrix (ECM) that stimulates bone regeneration by mimicking the native tissue [18-19]. Since bone tissue scaffold plays a crucial role in bone tissue engineering, it should possess the following properties: porous structures to allow bone cell growth, vascularization, and diffusion of nutrients; mechanical strength to carry external loads during the bone-forming process; biocompatibility and biodegradation [20-24]. Moreover, bone remodeling is a mechanobiological phenomenon that can be affected by mechanical stimulation [1, 25-28]. Therefore, mechanical stimulation on scaffold

has an important effect on bone regeneration, and it can be adjusted by changing pore architecture and porosity ratio. Studies have demonstrated that pore architectures in scaffolds significantly determine mechanical properties, including strength, stiffness, and energy absorption [29-31]. In addition, the porosity ratio in the scaffold has essential effects on mechanical behavior, surface area, and interconnectivity, which are vital for bone regeneration [32]. In a study by Dawson et al., it was reported that the rate of bone tissue regeneration may increase with increasing scaffold porosity [33]. On the other hand, Buizer et al. explained that scaffolds with a high porosity ratio can show higher bone tissue ingrowth than scaffolds with a lower porosity ratio [34]. The reason is that the specific surface area of scaffolds increases with the porosity ratio and affects cell adhesion, growth, and nutrient-oxygen transportation.

The additive manufacturing technique, which has seen significant improvements in the last few decades, plays a pivotal role in scaffold production by allowing the creation of scaffolds with the desired pore architecture and porosity [35]. Lattice structures are well-known structures especially used in scaffold production which brings the advantage of controllability of manufacturing with Fused Deposition Modeling (FDM). The ability to create different pore architectures and porosity ratios in bone tissue scaffolds leads to different mechanical stimulation levels. As a result, the bone regeneration process can be controlled by changing pore architectures and porosity ratios with the help of flexible additive manufacturing methods. Polymers, particularly popular biomaterials used in tissue engineering, have many attractive properties, such as biocompatibility and biodegradability [36]. One of the most popular biomaterials used in bone tissue scaffolds is polylactic acid (PLA) due to its compressive strength and its high compatibility with additive manufacturing [37].

This study adopts a comprehensive approach to determine the mechanical behavior of bone tissue scaffolds with different pore architectures and porosity ratios. Three different pore architectures, Basic Cube (BC), Body-Centered Structure (BCS), and Body-Centered Cubic (BCC), were selected, and their designs were adjusted to achieve 50%, 62.5%, and 75% porosity ratios. The mechanical behavior of the scaffolds was determined using a combination of experimental and numerical methods. The experimental methods involved compressive tests, while the finite element method was used to predict the behavior of the scaffolds in the linear-elastic region. The mechanical properties of the scaffolds were also evaluated in terms of the specific energy absorption and the specific surface area under a 4 N load, forming the desired stress levels on the bone tissue scaffolds.

2. MATERIALS AND METHODS

2.1. Design and Printing of Bone Tissue Scaffolds

Three pore architectures and porosity ratios were chosen to design bone tissue scaffolds. These pore architectures were named Basic Cube (BC), Body-Centered Structure (BCS), and Body-Centered Cubic (BCC). The design of scaffolds, voxel meshed scaffolds, and 3D-printed scaffolds are illustrated in Figure 1.

The main reason for choosing these three designs is to create various combinations of axial and bending loadings so that the influence of different stresses can be investigated in detail. BC scaffolds present only struts in vertical and horizontal directions with major axial stress distribution. BCS scaffolds grant all bending loading with no axial support. On the other hand, the joints of all struts create a large surface area for bone cells to attach. BCC scaffolds combine axial and bending elements and therefore arise both stress types.

The well-known advantage of these three structures is that three-region (linear, plateau, and densification) force-displacement behavior can easily be controlled as suggested by Gibson [38]. However inconceivable disadvantages such as intense joint area along with possible printing deficiencies also need to be examined carefully. An auxiliary factor for choosing these specific lattice designs is that porosity can be assigned easily by changing basic parameters such as the length and cross-section of struts. The design parameters of the unit scaffold are shown in Figure 1a, and each unit scaffold was designed for 50%, 62.5%, and 75% porosity ratios. The naming of scaffolds is derived from combination their pore architectures and porosity ratios and is given in Table 1.

The unit scaffolds were patterned twice in the x, y, and z directions, and the periodic scaffolds were obtained. In addition, the specific surface

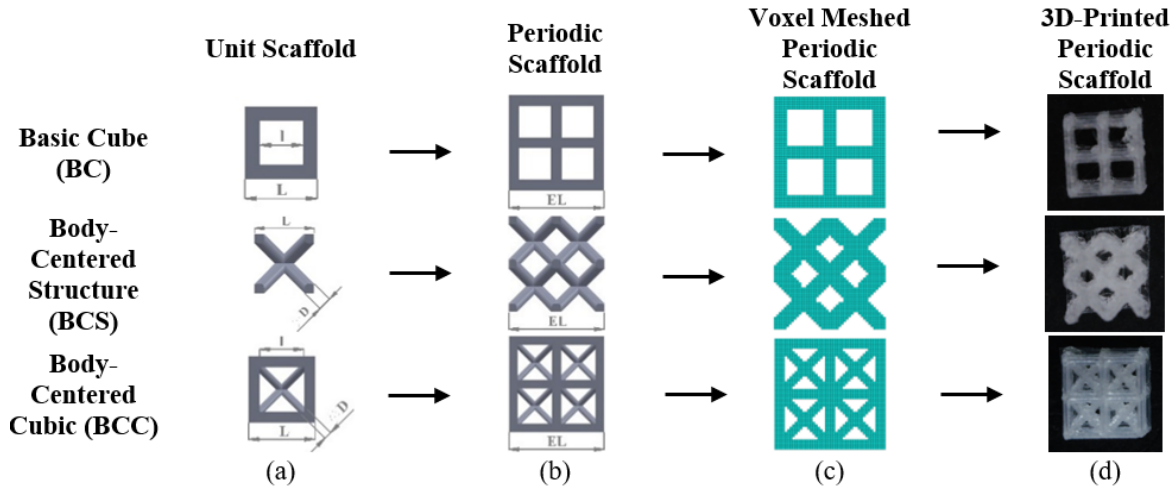

Figure 1. The Design of Scaffolds, Voxel Meshed Scaffolds, and 3D-Printed Images (a) Design of Unit Scaffolds (b) Design of Periodic Scaffolds (c) Voxel Meshed Scaffolds (d) 3D-Printed Scaffolds

Table 1. Design Parameters and Properties of Scaffolds

Scaffold	Length of Periodic Scaffold Edge (mm)	Length of Unit Scaffold Edge (L mm)	Length of Unit Scaffold Porous Edge (l mm)	Diameter of Rod (D mm)	Porosity Ratio (%)	Surface Area (mm^2)	Volume (mm^3)	Specific Surface Area (mm^{-1})	Mass (mg)
BC50	5.400	3	1.290	-	50.220	275.023	67.800	4.056	86.925
BC62.5	5.270	3	1.540	-	62.550	271.604	54.820	4.954	70.575
BC75	5.145	3	1.800	-	74.080	252.720	40.820	6.191	56.125
BCS50	5.390	3	-	1.000	51.640	254.724	75.430	3.377	94.600
BCS62.5	5.470	3	-	0.860	62.500	250.681	61.380	4.084	79.025
BCS75	5.580	3	-	0.690	74.630	233.096	44.070	5.289	54.475
BCC50	5.500	3	2.000	0.880	49.960	374.585	83.250	4.500	105.800
BCC62.5	5.500	3	2.000	0.660	62.450	369.320	62.470	5.912	75.900
BCC75	5.500	3	2.000	0.350	75.840	326.319	40.200	8.117	55.275

area of scaffolds was determined by dividing the surface area by volume. The design variables and properties of scaffolds are given in Table 1.

Table 2. Printing Parameters

Parameter	Value
Nozzle Temperature	200 ^{0}C
Nozzle Diameter	0.25 mm
Build Plate Temperature	60 ^{0}C
Printing Speed	30 mm/s
Layer Thickness	0.1 mm
Infill Density	100%

The designed periodic scaffolds were printed with Ultimaker 3 Extended 3D printer based on fused deposition modeling (FDM). Polylactic-acid (PLA) filament with 2.85 mm diameter was utilized to print periodic scaffolds. Printing parameters are given in Table 2.

PLA is approved by Food and Drug Administration (FDA) as biomaterial and therefore printing parameters are already well-characterized thank to its wide range of use. All scaffold geometries and all porosities are produced using the same parameters to avoid unexpected factors affecting consistency. Printing parameters such as infill, nozzle diameter, and temperature may also influence mechanical properties, therefore stable production is critical for proper evaluation of differences between designs, and this was made possible with the parameters given in Table 2.

2.2. Mechanical Behavior of Periodic Scaffolds

The mechanical behavior of periodic scaffolds with different pore architectures and porosity ratios were determined by compression test. Compression tests were performed using a universal test machine (Shimadzu AGS-X) at Bursa Technical University Mechanical Testing Laboratory. The universal test machine has 1 kN maximum load capacity. Compression test speed was selected as 0.3 mm/min. Compression tests were carried out up to 2.5 mm displacement for each scaffold, and force-displacement data was recorded using Trapezium X software. Stiffness values were calculated from the slope of the linear region of force-displacement curves for each scaffold. The total energy absorption value (E_T) for each scaffold was determined from the area under the force-displacement curve using Equation 1.

$$E_T = \int_0^{\delta} F d\delta \quad (1)$$

where δ is displacement and F is compression force. Moreover, each scaffold's specific energy absorption (SEA) value was calculated using Equation 2 [39].

$$SEA = {E_T}/{m} \quad (2)$$

where E_T is the total energy absorption and m is the mass of the scaffold. The mass of the scaffolds was measured by Radwag 220∓ 0.0001g analytical balance.

2.3. Finite Element Analysis of Periodic Scaffolds

Finite element analyses were performed on periodic scaffolds to obtain stiffness values, von mises stress, and equivalent strain distributions. The structure is meshed similar to voxel meshing with a length of 125 µm for all scaffolds. Each voxel mesh element had linear 8-node brick element properties [40]. Voxel meshed periodic scaffolds with three different pore architectures for 75% porosity ratio are given in Figure 1c. As boundary conditions, the bottom side of the scaffolds were fixed, and nodal displacement was applied perpendicular to the upper side of the scaffolds. The boundary conditions of scaffolds are illustrated in Figure 2.

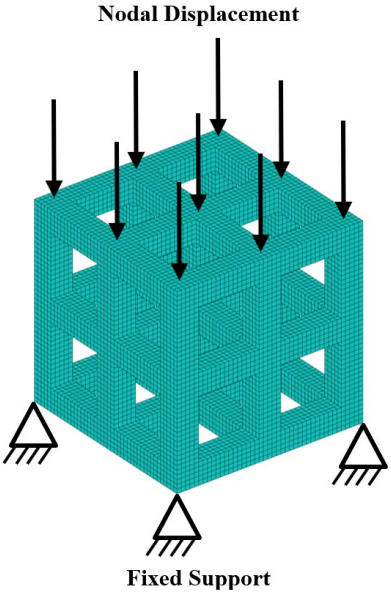

Figure 2. Boundary Conditions of Finite Element Analysis for Scaffold

The material properties of scaffolds were assumed to exhibit linear-elastic behavior in the finite element analysis. Young's modulus of scaffold material is taken as 1350 MPa. The porous nature and imperfections in structures due to FDM procedure are adjusted by equating experimental stiffness in linear region to stiffness obtained from FEM analysis of basic cube with 75%. This scaffold is chosen due to its high potential as the most robust scaffold. Elastic modulus obtained from this justification yields a good match for other geometries (Basic Cube and Body-Centered Cubic) and other porosities (50% and 62.5%).

Poisson's ratio of scaffold material was assumed to be 0.3 in the finite element analysis. The stiffness values of scaffolds were calculated from the slope of force-displacement curves obtained from linear finite element analysis. To obtain von Mises stress and equivalent strain distributions of scaffolds, 4 N load, which creates 1-2 MPa stress on scaffolds, was selected in the finite element analysis since 1-2 MPa stress in scaffolds is the desired stress level [41].
Post-yielding (plasticity and damage) behavior of the material is not considered in the analysis because excessive deformation is not acceptable for scaffolds. As mentioned previously, the stress level for optimum bone growth is significantly less than yielding stress. Furthermore, newly formed bone shares stress and stress decreases as the bone remodeling process continues, therefore, plasticity and damage are not involved in the process.

All linear-elastic finite element implementations are done using custom MATLAB coding written by authors.

3. RESULTS AND DISCUSSIONS

3.1. Stiffness Values of Periodic Scaffolds

The stiffness values obtained from the compression test and finite element analysis are given in Figure 3. As the porosity ratio of scaffolds increases, their stiffness values start to decrease in both compression tests and finite element analysis results. BC scaffold had the highest stiffness values for all porosity ratios since it consisted of thick vertical and horizontal struts rather than BCS and BCC scaffolds. Although the BCC scaffold had vertical and horizontal struts in addition to diagonal struts, the BCC scaffold's vertical and horizontal struts were thinner than the BC scaffold. Therefore, the BCC scaffolds had the second-highest stiffness values for all porosity, except in the finite element analysis, where 50% porosity ratio was observed. The BCS scaffolds had the lowest stiffness values for all porosity ratios in experimental results.

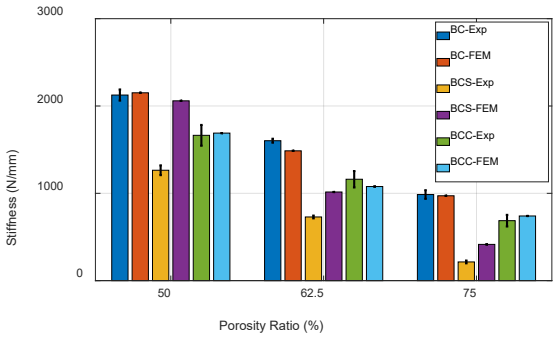

Figure 3. Stiffness Values of Periodic Scaffolds

When the experimental and finite element analysis results are compared, it is seen that they are close to each other except for the BCS results. BCS geometry involves only diagonal struts, and this leads mostly to bending loading which forces joints to rotate while joints are mostly modeled as fixed support in analytical models [38]. The length of the struts is also smaller, and this makes transverse shear comparable with flexural stress as in short beams. Furthermore, joints have the highest volume because the number of struts meeting at a common joint is also the highest. This leads to multiple concave surfaces around the joint and these surfaces may not be printed as modeled on the FE model. Therefore, a smooth joint with fixed support characteristics is not a valid assumption for these structures. On the other hand, transverse shear cannot be captured well in FEA. The mismatch can be attributed to these factors; however, printing deficiencies may also influence this mismatch. As indicated in the previous section, scaffolds were printed using fused deposition modeling (FDM). Printing parameters may affect the mechanical properties of scaffolds used in bone tissue engineering. Dimensional precision and accuracy in 3D printing are crucial for fabricating scaffolds with the desired mechanical properties. In addition, the 3D printing process can contain imperfections in the printed scaffolds, which can significantly affect the mechanical properties of scaffolds. These imperfections may be irregularities in the

printed layers, differences in material deposition, or incomplete fusion between layers, leading to variations from the desired pore geometry and mechanical properties of scaffolds, affecting their performance in bone tissue engineering. Differences between the experimental and finite element analysis results in BCS scaffolds may be related to the printing imperfections since BCS scaffolds consist of only diagonal struts, and printing diagonal struts are more complex than vertical struts.

3.2. Stress and Strain Distributions of Periodic Scaffolds

In bone tissue engineering applications, scaffolds are required to remain in the linear region under mechanical stimulation, and the desired stress levels on scaffolds under mechanical stimulation are approximately 1-2 MPa. Von Mises stress and equivalent strain distribution of scaffolds obtained from finite element analysis are illustrated in Figure 4. It was found that as the porosity of the scaffolds increased, the von Mises stress and equivalent strain values increased. The BCS75 scaffold

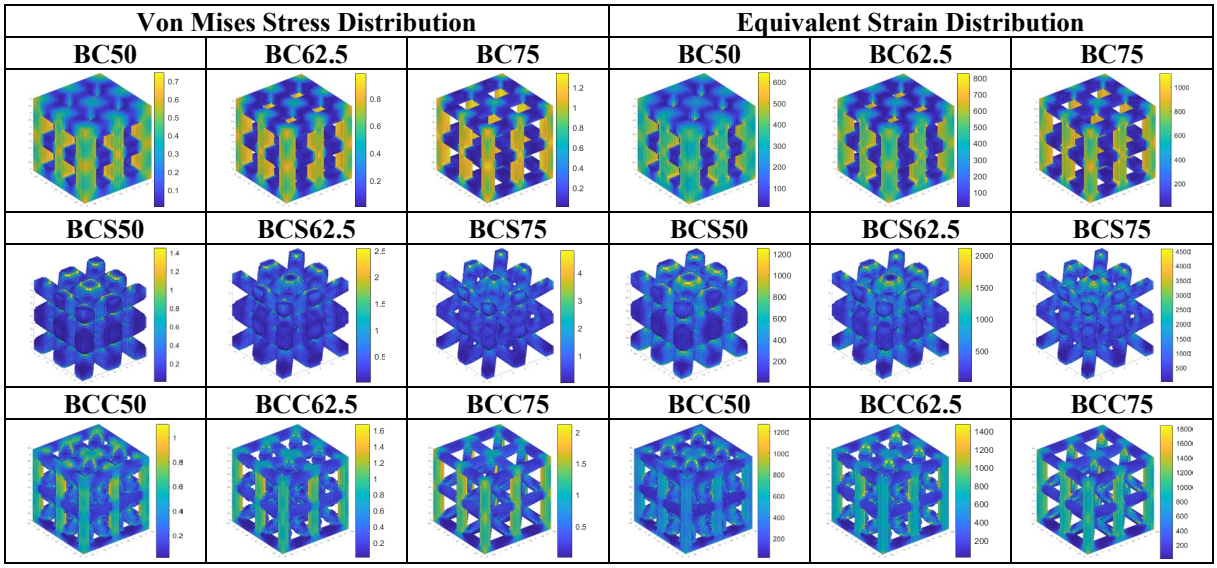

Figure 4. Von Mises Stress and Equivalent Strain Distributions for Scaffolds under 4 N Load

had the highest Von Mises stress and equivalent strain values. When Von Mises stress and equivalent strain values of scaffolds were compared with each other at the same porosity ratio, the BCS scaffolds had the highest values. The BCC scaffolds had the second-highest values, and the BC scaffolds had the lowest values. These results were consistent with the stiffness values of scaffolds. However, Von Mises' stress and equivalent strain values of the BCS75 scaffolds under 4 N load were approximately twice higher than those of other scaffolds. In bone tissue engineering applications, it should be taken into consideration that BCS75 scaffolds may fail due to their high Von Mises stress and equivalent strain values compared to other scaffolds.

3.3. Mechanical Behavior of Periodic Scaffolds under Compression Loading

Scaffolds under compression loading exhibit three different regions. These are elastic, plateau, and densification regions. Plateau region happens because of post-yielding behavior of PLA and densification occurs as a result of the failure of PLA. These three regions typically indicate the porous and cellular structure of scaffolds [38]. In the elastic region, struts of scaffolds exhibit linear behavior. After the elastic limits of scaffolds are exceeded, the plateau region starts. In this region, scaffold struts can exhibit elastoplastic or brittle behavior depending on the scaffold material [38]. Moreover, if the struts of scaffolds are slender enough, buckling in scaffold struts can be observed. Therefore, the force in the plateau region almost stays constant while displacement is increasing. After the plateau region, the scaffolds start to collapse in the densification region, and the struts of the scaffolds stack up

with each other [38]. Therefore, the force starts to increase. These regions have a crucial effect on the energy absorption behavior of scaffolds. The force-displacement behavior and the energy absorption behavior of periodic scaffolds obtained from compression tests are shown in Figure 5.

For scaffolds with 50% porosity, elastic and densification regions were more prominent up to 2.5 mm displacement while there was a gradual increase in stiffness between elastic and densification regions. Thick struts in 50% BCS create stacked and stiffer joints and therefore structure experiences a hardening as compression is sustained. This results in a shorter plateau region. On the contrary, slender struts in 75% porous scaffolds create more flexible joints and more chance of collapsing by buckling which means an extended plateau region.

For scaffolds with 62.5% porosity ratio, BCS scaffold reached the densification region first, therefore BCS62.5 scaffold had the highest force value at 2.5 mm displacement. By recalling that BCS involves only diagonal struts behaving mostly as beams, a possible explanation for this phenomenon is that short beams for 62.5% lead dominantly to shear loading and therefore fail prematurely. Beams

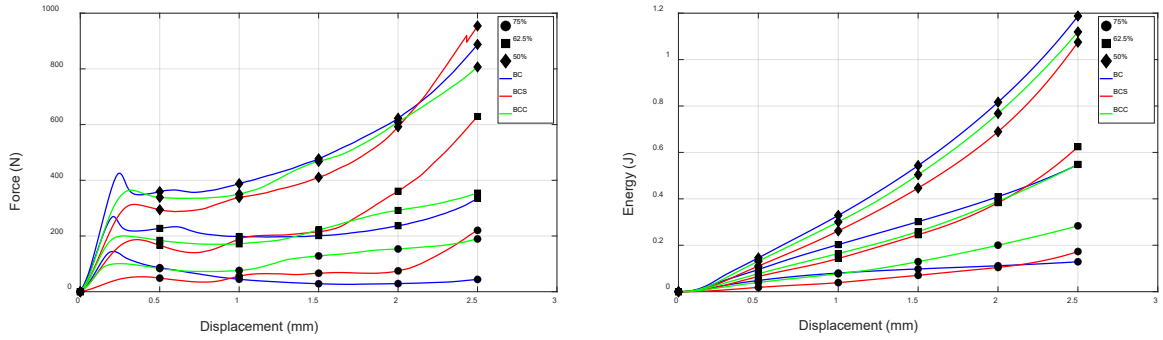

a) **b)**

Figure 5. Compression Test Results of Periodic Scaffolds **a)** Force-Displacement Graphics **b)** Energy-Displacement Graphic

are even shorter for 50% porous scaffolds; however, joint stiffness is also higher as explained in the previous paragraph and therefore, strut failure is less likely.

For 75%-porous scaffolds, only BCS75 reached the densification region, while BC75 scaffold remained in the plateau region. Therefore, BC75 scaffold had the lowest force value at 2.5 mm displacement.

When the energy absorption behavior of scaffolds in Figure 5b were examined, it was observed that as the porosity of the scaffolds increases, the amount of energy absorption also increases. In 50% porosity ratio, it was seen that the BC scaffold had the highest energy absorption amount at the end of 2.5 mm displacement. The BCC scaffold had the second-highest energy absorption amount, and the BCS scaffold had the lowest energy absorption amount. These results were proportional to the stiffness results of scaffolds. In the 62.5% porosity ratio, the energy absorption was proportional to the stiffness values of scaffolds up to 2 mm displacement. However, the BCS scaffold exhibited the highest energy absorption at 2.5 mm displacement. This changing behavior may be attributed to the compression behavior of scaffolds. The BCS62.5 scaffolds reached the densification region after 2 mm displacement, while the BC62.5 and BCC62.5 scaffolds were still in the plateau region. In the 75% porosity ratio, although the energy absorption amounts were proportional to the stiffness values of scaffolds up to 1 mm, the energy absorption behavior changed after 1 mm displacement. Finally, the BCC75 scaffolds had the highest energy absorption at 2.5 mm displacement. The BC75 scaffolds had the highest stiffness among 75% porosity scaffolds but it has the lowest energy absorption amount at the 2.5 mm displacement. Since the struts of BC scaffolds were slenderer than those of BCS and BCC scaffolds, they underwent buckling damage in the plateau region. Therefore, it couldn't carry

the load and had the lowest energy absorption amount at 2.5 mm displacement.

3.4. Evaluation of Mechanobiological Potentials of Periodic Scaffolds

The mechanical properties of bone tissue scaffolds play a crucial role in bone tissue regeneration. Since the bone regeneration process is a mechanobiological phenomenon, the strain energy distribution, especially on the bone tissue scaffold, critically impacts long-term bone regeneration [1-4, 43]. Therefore, different strain energy distributions in bone tissue scaffolds can lead to the formation of heterogeneous bone density [44]. In this study, the effect of strain energy on bone regeneration behavior in bone tissue scaffolds was evaluated by using compression test data up to 4 N loading for bone tissue scaffolds. The specific energy absorption was determined by dividing the total strain energy obtained up to 4 N loading by the mass of the scaffold. The specific energy absorption may be assumed as mechanical stimulation in the bone regeneration process, and higher mechanical stimulation on bone tissue scaffold may lead to higher bone regeneration. Therefore, the specific energy absorption amount is one of the vital mechanical properties in designing bone tissue scaffolds [44]. Furthermore, the specific surface area of bone tissue scaffolds is one of the important factors in bone tissue engineering since it affects bone tissue regeneration processes [45].

Cell adhesion, infiltration, and proliferation on 3-D scaffolds are already confusing topics that have not been investigated comprehensively in the literature. Therefore, geometry and mechanics relation to cell behavior is not clear yet. The continuum of this work will solely focus on these issues. On the other hand, it is already well known that bone cells are highly sensitive to mechanical stimulation via receptors in osteocyte-type cells. This sensitivity mostly results in complex procedures of bone regeneration which includes both formation and resorption. Based on preliminary work on in-vitro 3-D bone scaffolds, cells are sympathetic to both mechanical stimulation and largely curved surfaces [45].

The results of the specific energy absorption and the specific surface area for bone tissue scaffolds are depicted in Figure 6. According to the figure, the results of specific energy absorption were generally proportional to the stiffness values of bone tissue scaffolds, i.e., the stiffest structure BC50 has the lowest specific energy while the softest structure BCS75 has the highest specific energy. This is the result of the high deformation capacity of the overall scaffold rather than individual strut deformations. In other words, struts remain in the linear elastic region without reaching the yielding point even for higher overall deformations. This can be attributed to the fact that joints experience less resistance, and this leads joints to behave more like a pin joint rather than a fixed support resulting in a larger joint rotation. Larger rotation of joints means larger overall deformation without struts to reach yielding stress.

For scaffolds with the same pore architecture, the specific energy absorption of all scaffolds decreased as the porosity ratio increased. The BCS75 scaffold had the highest specific energy absorption amount under 4 N loading since it had the lowest stiffness value.

On the other hand, the BC50 scaffold had the lowest specific energy absorption since it had the highest stiffness value. When the specific surface areas of bone tissue scaffolds were examined, it was determined that the pore architecture of scaffolds had a significant effect on the specific surface area.

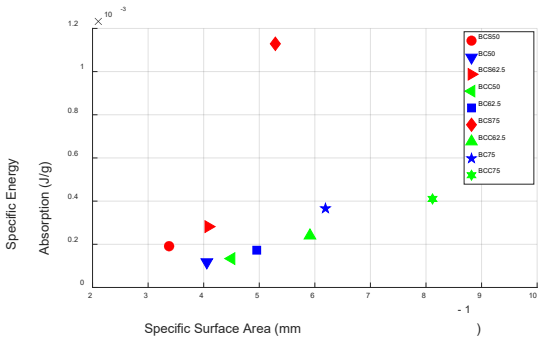

Figure 6. Specific Energy Absorption – Specific Surface Area Graph for Bone Tissue Scaffolds

Moreover, the specific surface area of all scaffolds increased as the porosity ratio increased in scaffolds with the same pore architecture. The highest specific surface area was observed in the BCC75 scaffold. However, the lowest specific surface area was found in the BCS50 scaffold. This means one can create more surface area for bone cells to attach for

BCC75 using less material and this creates efficiency while one needs to use more material to create surface area for BCS50 which is inefficient. However, surface area is not the only factor influencing cell growth and mechanical stimulation is also an important factor where specific energy becomes more critical.

Optimization algorithms can be utilized based on results produced in this work to evaluate how to change parameters for better bone remodeling. However, bone remodeling on 3-D scaffolds still requires extensive research to identify the procedure in detail. At first glance, a scaffold combining stimulation with the high specific surface area would lead to optimum design and therefore, some design between BCC 75 and BCS 75 seems the best option. This may be possible by joining diagonal struts in the middle of the adjacent strut rather than all at the center of the cube. However, these types of structures are projected to lead to several manufacturing issues.

4. CONCLUSION

This study aimed to evaluate the usage of scaffolds with different pore architectures and porosity ratios in bone tissue engineering in terms of mechanical properties using the compression test and finite element analysis. Basic Cube (BC), Body-Centered Structure (BCS), and Body-Centered Cubic (BCC) were chosen as pore architectures for bone tissue scaffolds. The porosity ratios of scaffolds were adjusted by changing the design parameters of the scaffolds. The stiffness values, energy absorption behaviors, and specific energy absorptions for bone tissue scaffolds were obtained from compression tests. The specific energy absorption was calculated under 4 N compressive loading, forming the desired stress level on the scaffold. The Von Mises stress, and equivalent strain distributions on scaffolds under 4 N loading were obtained from finite element analysis. Moreover, the stiffness values of scaffolds were calculated from finite element analysis. The compression test and finite element analysis results for scaffolds are summarized below.

- As the porosity ratios of all scaffolds increased, the stiffness values decreased in both experimental and finite element results.
- BC50 scaffold had the highest stiffness value since it had thicker vertical and horizontal struts than the other scaffolds. BCS75 scaffold had the lowest stiffness value since it only consisted of diagonal struts.
- The results of stiffness values obtained from the compression test and finite element analysis were found to be consistent with each other except for BCS scaffolds. Since the printing processes of diagonal struts were more complex than vertical and horizontal struts, these inconsistent results of BCS scaffolds may be related to the printing imperfections. As the printing imperfections have an essential effect on the stiffness values of scaffolds, they should be considered in the design and printing of scaffolds.
- The maximum Von Mises stress, and equivalent strain levels of the BCS75 scaffold were almost twice that of the other scaffolds. Therefore, BCS75 scaffolds may fail in usage.
- The energy absorption level increased as the porosity ratio decreased. BC50 scaffold had the highest energy absorption level, while the BC75 scaffold had the lowest. The energy absorption levels were proportional to the stiffness values of scaffolds at the 50% porosity ratio. However, the plateau region's behavior started to dominate the scaffolds' energy absorption levels at the 62.5% and 75% porosity ratios.
- BCS75 scaffold had the highest specific energy absorption level, while the lowest specific energy absorption level was observed in the BC50 scaffold. The specific energy absorption level increased as the porosity ratio increased in scaffolds with the same pore architecture.
- BCC75 scaffold had the highest specific surface area, while the lowest specific surface area was found in the BCS50 scaffold. It was determined that the specific surface area increased as the porosity ratio of scaffolds with the same pore architecture increased. It was also observed that pore architecture significantly impacted the specific surface area.

The specific energy absorption and surface area are essential properties of bone tissue scaffolds. BCS75 scaffold had the highest specific energy

absorption, while BCC75 scaffold had the highest specific surface area and the second highest specific energy absorption. Therefore, it is considered advantageous to use the BCC75 scaffold in bone tissue engineering.

ACKNOWLEDGMENTS

This study was supported by the Scientific and Technological Research Council of Turkey (TUBITAK) (Project No. 222M025)

REFERENCES

1. Li, J., Li, H., Shi, L., Fok, A. S., Ucer, C., Devlin, H., ... & Silikas, N., "A mathematical model for simulating the bone remodeling process under mechanical stimulus", Dental materials Vol. 13, Issue 9, Pages 1073-1078, 2007.

2. Zhao, Y., & Zhang, G., "A computational study of the dual effect of intermittent and continuous administration of parathyroid hormone on bone remodeling", Acta Biomaterialia, Vol. 93, Pages 200-209, 2019.

3. Cowin, S. C., & Hegedus, D., "Bone remodeling I: theory of adaptive elasticity", Journal of Elasticity, Vol. 6, Pages 313-326, 1976.

4. Pearce, C. J., "Efficient numerical analysis of bone remodelling", Journal of the Mechanical Behavior of Biomedical Materials, Vol. 4, Issue 6, Pages 858-867, 2011.

5. Zhang, Y., Zhang, C., Wang, J., Liu, H., & Wang, M., "Bone-Adipose Tissue Crosstalk: Role of Adipose Tissue Derived Extracellular Vesicles in Bone Diseases", Journal of Cellular Physiology, Vol. 236, Issue 11, Pages 7874-7886, 2021.

6. Shoji-Matsunaga, A., Ono, T., Hayashi, M., Takayanagi, H., Moriyama, K., & Nakashima, T., "Osteocyte regulation of orthodontic force-mediated tooth movement via RANKL expression", Scientific reports, Vol. 7 Issue 1, 8753, 2017.

7. Rémond, A., Naïli, S., & Lemaire, T., "Interstitial fluid flow in the osteon with spatial gradients of mechanical properties: a finite element study", Biomechanics and modeling in Mechanobiology, Vol. 7, Pages 487-495, 2008.

8. Smit, T. H., & Burger, E. H., "Is BMU-coupling a strain-regulated phenomenon? A finite element analysis", Journal of Bone and Mineral Research, Vol. 15, Issue 2, Pages 301-307, 2000.

9. Nwankwo, E. C., Chen, F., Nettles, D. L., & Adams, S. B., "Five-year follow-up of distal tibia bone and foot and ankle trauma treated with a 3D-printed titanium cage", Case Reports in Orthopedics, Vol. 2019, 2019.

10. Fernandes, M. B. C., Guimarães, J. A. M., Casado, P. L., Cavalcanti, A. D. S., Gonçalves, N. N., Ambrósio, C. E., ... & Duarte, M. E. L., "The effect of bone allografts combined with bone marrow stromal cells on the healing of segmental bone defects in a sheep model", BMC veterinary research, Vol. 10, Issue 1, Pages 1-12, 2014.

11. Long, T., Zhu, Z., Awad, H. A., Schwarz, E. M., Hilton, M. J., & Dong, Y., "The effect of mesenchymal stem cell sheets on structural allograft healing of critical sized femoral defects in mice", Biomaterials, Vol. 35, Issue 9, Pages 2752-2759, 2014.

12. Zhao, Z. H., Ma, X. L., Zhao, B., Tian, P., Ma, J. X., Kang, J. Y., ... & Sun, L., "Naringin-inlaid silk fibroin/hydroxyapatite scaffold enhances human umbilical cord-derived mesenchymal stem cell-based bone regeneration", Cell Proliferation, Vol. 54, Issue 7, e13043, 2021.

13. Carulli, C., Matassi, F., Civinini, R., & Innocenti, M., "Tissue engineering applications in the management of bone loss", Clinical cases in mineral and bone metabolism, Vol. 10, Issue 1, Pages 22-25, 2013.

14. Guilak, F., Butler, D. L., Goldstein, S. A., & Baaijens, F. P., "Biomechanics and mechanobiology in functional tissue engineering", Journal of biomechanics, Vol. 47, Issue 9, Pages 1933-1940, 2014.

15. Mi, H. Y., Jing, X., & Turng, L. S., "Fabrication of porous synthetic polymer scaffolds for tissue engineering", Journal of Cellular Plastics, Vol. 51, Issue 2, Pages 165-196, 2015.

16. Paladini, F., & Pollini, M., "Novel approaches and biomaterials for bone tissue engineering: a focus on silk fibroin", Materials, Vol. 15, Issue 19, 6952, 2022.

17. Kagami, H., Agata, H., & Tojo, A., "Bone marrow stromal cells (bone marrow-derived multipotent mesenchymal stromal cells) for bone tissue engineering: basic science to clinical translation", The international journal of biochemistry & cell biology, Vol. 43, Issue 3, Pages 286-289, 2011.

18. Thein-Han, W. W., & Misra, R. D. K., "Three-dimensional chitosan-nanohydroxyapatite composite scaffolds for bone tissue engineering", JOM, Vol. 61, Pages 41-44, 2009.

19. Shadjou, N., & Hasanzadeh, M., "Graphene and its nanostructure derivatives for use in bone tissue engineering: Recent advances", Journal of Biomedical Materials Research Part A, Vol. 104, Issue 5, Pages 1250-1275, 2016.

20. Lin, C. Y., & Kang, J. H., "Mechanical properties of compact bone defined by the stress-strain curve measured using uniaxial tensile test: a concise review and practical guide", Materials, Vol. 14, Issue 15, 4224, 2021.

21. Chen, J., "Recent development of biomaterials combined with mesenchymal stem cells as a strategy in cartilage regeneration", International Journal of Translational Medicine, Vol. 2, Issue 3, Pages 456-481, 2022.

22. Qu, H., Fu, H., Han, Z., & Sun, Y., "Biomaterials for bone tissue engineering scaffolds: A review", RSC advances, Vol. 9, Issue 45, Pages 26252-26262, 2019.

23. Collins, M. N., Ren, G., Young, K., Pina, S., Reis, R. L., & Oliveira, J. M., "Scaffold fabrication technologies and structure/function properties in bone tissue engineering", Advanced functional materials, Vol. 31, Issue 21, 210609, 2021.

24. Suamte, L., Tirkey, A., Barman, J., & Babu, P. J., "Various manufacturing methods and ideal properties of scaffolds for tissue engineering applications", Smart Materials in Manufacturing, Vol. 1, 100011, 2023.

25. Wang, L., You, X., Zhang, L., Zhang, C., & Zou, W., "Mechanical regulation of bone remodeling", Bone Research, Vol. 10, Issue 1, 16, 2022.

26. Shi, Q., Chen, Q., Pugno, N., & Li, Z. Y., "Effect of rehabilitation exercise durations on the dynamic bone repair process by coupling polymer scaffold degradation and bone formation", Biomechanics and Modeling in Mechanobiology, Vol. 17, Pages 763-775, 2018.

27. Sun, W., Li, Y., Li, J., Tan, Y., Yuan, X., Meng, H., ... & Li, Y., "Mechanical stimulation controls osteoclast function through the regulation of Ca2+-activated Cl− channel Anoctamin 1", Communications Biology, Vol. 6, Issue 1, 407, 2023.

28. Vatsa, A., Mizuno, D., Smit, T. H., Schmidt, C. F., MacKintosh, F. C., & Klein-Nulend, J., "Bio imaging of intracellular NO production in single bone cells after mechanical stimulation", Bone and Mineral Research, Vol. 21, Issue 11, Pages 1722-1728, 2006.

29. Onal, E., Frith, J. E., Jurg, M., Wu, X., & Molotnikov, A., "Mechanical properties and in vitro behavior of additively manufactured and functionally graded Ti6Al4V porous scaffolds", Metals, Vol. 8, Issue 4, 200, 2018.

30. Deng, F., Liu, L., Li, Z., & Liu, J., "3D printed Ti6Al4V bone scaffolds with different pore structure effects on bone ingrowth", Journal of biological engineering, Vol. 15, Pages 1-13, 2021.

31. Karaman, D., & Ghahramanzadeh Asl, H., "Biomechanical behavior of diamond lattice scaffolds obtained by two different design approaches with similar porosity; a numerical investigation with FEM and CFD analysis", Proceedings of the Institution of Mechanical Engineers, Part H: Journal of Engineering in Medicine, Vol. 236, Issue 6, Pages 794-810, 2022.

32. Zhang, X. Y., Fang, G., Xing, L. L., Liu, W., & Zhou, J., "Effect of porosity variation strategy on the performance of functionally graded Ti-6Al-4V scaffolds for bone tissue engineering", Materials & Design, Vol. 157, Pages 523-538, 2018.

33. Dawson, E. R., Suzuki, R. K., Samano, M. A., & Murphy, M. B., "Increased internal porosity and surface area of hydroxyapatite accelerates healing and compensates for low bone marrow mesenchymal stem cell concentrations in critically-sized bone defects", Applied Sciences, Vol. 8, Issue 8, 1366, 2018.

34. Buizer, A. T., Veldhuizen, A. G., Bulstra, S. K., & Kuijer, R., "Static versus vacuum cell seeding on high and low porosity ceramic scaffolds", Journal of biomaterials applications, Vol. 29, Issue 1, Pages 3-13, 2014.

35. Kontogianni, G. I., Loukelis, K., Bonatti, A. F., Batoni, E., De Maria, C., Naseem, R., ... & Chatzinikolaidou, M., "Effect of Uniaxial Compression Frequency on Osteogenic Cell Responses in Dynamic 3D Cultures", Bioengineering, Vol. 10, Issue 5, 532, 2023.

36. Narayanan, G., Vernekar, V. N., Kuyinu, E. L., & Laurencin, C. T., "Poly (lactic acid)-based biomaterials for orthopaedic regenerative engineering", Advanced drug delivery reviews, Vol. 107, Pages 247-276, 2016.

37. Alavi, M. S., Memarpour, S., Pazhohan-Nezhad, H., Salimi Asl, A., Moghbeli, M., Shadmanfar, S., & Saburi, E., "Applications of poly (lactic acid) in bone tissue engineering: A review article", Artificial Organs, Vol. 47, Issue 9, Pages 1423-1430, 2023.

38. Gibson, L. J., "Cellular solids", Pages 93-172, Mrs Bulletin, Cambridge, 2003.

39. Demirci E., Şenaysoy S., Tuğcu S. E., "The Effect of Nozzle Diameter and Layer Thickness on Mechanical Behavior of 3D Printed PLA Lattice Structures Under Quasi-Static Loading", Int. J. of 3D Printing Tech. Dig. Ind., Vol. 7, Issue 1, Pages 105-113, 2023.

40. T. Chandrupatla and A. Belegundu, "Introduction to Finite Elements in Engineering", Pages 214-258, Cambridge University Press, Cambridge, 2022.

41. Gorriz, C., Ribeiro, F., Guedes, J. M., Folgado, J., & Fernandes, P. R., "A Biomechanical Approach for Bone Regeneration Inside Scaffolds Embedded with BMP-2", New Developments in Tissue Engineering and Regeneration, Vol. 51, Pages 67-86, 2019.

42. Li, J. J., Dunstan, C. R., Entezari, A., Li, Q., Steck, R., Saifzadeh, S., ... & Zreiqat, H., "A novel bone substitute with high bioactivity, strength, and porosity for repairing large and load-bearing bone defects", Advanced healthcare materials, Vol. 8, Issue 8, 1801298, 2019.

43. Milan, J. L., Planell, J. A., & Lacroix, D., "Simulation of bone tissue formation within a porous scaffold under dynamic compression", Biomechanics and modeling in mechanobiology, Vol. 9, Pages 583-596, 2010.

44. Shi, Q., Chen, Q., Pugno, N., & Li, Z. Y., "Effect of rehabilitation exercise durations on the dynamic bone repair process by coupling polymer scaffold degradation and bone formation", Biomechanics and Modeling in Mechanobiology, Vol. 17, Pages 763-775, 2018.

45. Tovar, N., Witek, L., Atria, P., Sobieraj, M., Bowers, M., Lopez, C. D., ... & Coelho, P. G., "Form and functional repair of long bone using 3D-printed bioactive scaffolds", Journal of tissue engineering and regenerative medicine, Vol. 12, Issue 9, Pages 1986-1999, 2018.

ULUSLARARASI 3B YAZICI TEKNOLOJİLERİ
VE DİJİTAL ENDÜSTRİ DERGİSİ
INTERNATIONAL JOURNAL OF 3D PRINTING
TECHNOLOGIES AND DIGITAL INDUSTRY

ISSN:2602-3350 (Online)
URL: https://dergipark.org.tr/ij3dptdi

OPTIMIZATION OF ANNEALING AND 3D PRINTING PROCESS PARAMETERS OF PLA PARTS

Yazarlar (Authors): Mhd Usama Alabd*, Abdurrahim Temiz

Bu makaleye şu şekilde atıfta bulunabilirsiniz (To cite to this article): *Alabd M. U., Temiz A., "Optimization of Annealing and 3D Printing Process Parameters of Pla Parts" Int. J. of 3D Printing Tech. Dig. Ind., 8(2): 185-201, (2024).*

DOI: 10.46519/ij3dptdi.1451666

Araştırma Makale/ Research Article

Erişim Linki: (To link to this article): https://dergipark.org.tr/en/pub/ij3dptdi/archive

OPTIMIZATION OF ANNEALING AND 3D PRINTING PROCESS PARAMETERS OF PLA PARTS

Mhd Usama Alabd[a]*, Abdurrahim Temiz[a]

[a]Karabük University, Technology Faculty, Industrial Design Engineering Department, TURKEY

* *Corresponding Author:* osama.alabd9994@gmail.com

(**Received:** 12.03.24; **Revised:** 24.06.24; **Accepted:** 09.08.24)

ABSTRACT

Fused Filament Fabrication (FFF) has gained significant popularity as the prevalent additive manufacturing method due to its ability to reduce production time and expenses. However, the constraints of limited dimensional precision, poor surface quality, and relatively low Ultimate Tensile Strength (UTS) hinder compliance with the stringent regulatory norms of conventional manufacturing, necessitating post-processing for enhancement. In this investigation, the response surface method was used to optimize annealing and specific printing parameters to enhance the quality of PLA parts produced by FFF. Tensile specimens were printed with varying production parameters and annealed at varying heat treatment parameters. The following parameters are specified: layer height (0.1, 0.2, and 0.3 mm), build orientation (0°, 22.5°, 45°, 67.5°, and 90°), annealing temperature (70, 90, 110, and 130 ºC), and annealing time (60, 120, 180, and 240 min). The optimization technique aimed to enhance the UTS and match the CAD dimensions while minimizing surface roughness. The RSM optimization analysis identified the optimal parameters as layer height of 0.1 mm, build orientation at 0 degrees, annealing temperature of 110 degrees, and annealing time of 180 min. The consistent achievement of high levels of agreement between estimated and experimental response values substantiates the proposed models. A composite desirability value of 0.80 was derived for the variables due to the optimization investigation.

Keywords: Additive manufacturing, Annealing, Response surface method, Optimization, 3D printing.

1. INTRODUTION

The novel technological process of additive manufacturing makes physical objects from digital 3D models generated through computer-aided design (CAD) [1]. The FFF is a highly prevalent approach in 3D printing fields. It involves the sequential deposition of layers to fabricate three-dimensional structures, utilizing thermoplastic materials as the primary medium [2-3]. The FFF technique has demonstrated its utility not only in the realm of prototype but also in the domain of industrial production, establishing itself as a multifaceted and invaluable way of manufacturing [4]. The precision, consistency, and range of materials utilized in 3D printing techniques, such as FFF, have advanced to a level suitable for implementation in industrial manufacturing technology [5]. The materials employed in FFF commonly consist of polylactic acid (PLA) [6]. This technique is renowned for its capacity to manufacture end-use components, rather than solely prototypes [6-7]. Nevertheless, the FFF technique is a multifaceted procedure that is subject to numerous factors that might impact the overall quality of the printed output [8-9].

The layer height in FFF has a notable impact on the printed parts' ultimate tensile strength, surface roughness, and dimensional accuracy. The effect of layer height on the mechanical characteristics of FFF-printed components has been the subject of several investigations. For instance, Rajpurohit and Dave varied the line width and height of the layers to study their effect on the tensile strength of PLA-printed parts. It was found that the layer height and line width substantially affected the tensile strength of the printed parts [10]. Similarly, Magri et al. highlighted that process settings, including

raster orientation, printing speed, and layer height significantly affect the tensile strength of FFF printed parts [11]. Furthermore, Vyavahare et al. concluded that as the height of a layer increases, its tensile strength diminishes, indicating a clear relationship between layer height and mechanical properties [12]. In addition to tensile strength, the layer height also influences surface roughness and dimensional accuracy. Hua et al. noted that FFF parts printed with lower layer heights exhibit better mechanical performance [13]. Moreover, Vyavahare et al. identified layer height and print speed as significant parameters for the dimensional accuracy of FFF parts [14]. Furthermore, Chohan & Singh found that electroplating on FFF parts enhanced tensile strength and surface finish, indicating the interplay between layer thickness and surface characteristics [15].

The build orientation in FFF also significantly influences the printed parts' surface roughness, mechanical characteristics, and dimensional accuracy. Several studies have investigated the impact of build orientation on the characteristics of FFF-printed parts. For instance, Syrlybayev et al. extensively reviewed the effects of various process settings, including build orientation, on the mechanical characteristics of FFF-printed parts. Their review highlighted the critical influence of build orientation on the strength properties of FFF-printed parts [16]. Similarly, Dey & Yodo found that specific build orientations and raster orientations were crucial for achieving optimum surface roughness in FFF-printed parts [17]. Furthermore, Singh et al. revealed that build orientation significantly impacts the ultimate tensile properties of the printed parts [18]. This underscores the importance of considering build orientation when optimizing the mechanical characteristics of FFF-printed parts. Additionally, Huang et al. emphasized build orientation as a critical factor affecting the quality of the part [19]. In addition to mechanical properties, build orientation also affects surface roughness and dimensional accuracy. Hervan et al. highlighted that part build orientation and other settings affect the flexural, tensile, and impact strength of FFF-printed parts [20]. Moreover, Eryildiz demonstrated that build orientation substantially impacted the printing time and tensile properties of FFF-printed parts [21]. This further emphasizes the multifaceted influence of build orientation on the overall quality of FFF-printed parts.

Furthermore, research has shown that adding heat treatment can influence FFF printed parts mechanical strength [22]. The process of annealing in FFF has a noticeably impact on the surface roughness, mechanical characteristics, and dimensional precision of the printed parts. Akhoundi et al. investigated the impact of annealing and nozzle temperature on the mechanical characteristics of high temperature PLA in FFF. Their study provides the impact of annealing on the mechanical behavior of FFF parts [23]. Torres et al. explored the effects of annealing on the roughness of the surface and tensile characteristics of FFF-printed ABS components. The study emphasized the critical aspects of concern pertaining to the annealing treatment, particularly focusing on time and temperature and its influence on quality of the printed parts [24]. Additionally, Shbanah et al. found that heat treatment, specifically annealing, led to a significant increase in the ultimate tensile strength (UTS) of FFF-printed PLA polymer specimens, highlighting the positive effect of annealing on mechanical properties [25]. Furthermore, Rane et al. investigated the effects of annealing on the UTS of parts printed using FFF. Their research sheds light on the impact of thermal annealing on the mechanical properties of FFF-printed parts, offering significant perspectives on the role of annealing in enhancing the mechanical performance of printed components [26]. Overall, annealing, layer height, and build orientation in FFF play an important role in determining the printed parts' ultimate tensile strength, roughness of the surface, and dimensional precision. Understanding the impact of annealing, layer height, and build orientation on these properties is essential for optimizing the FFF process parameters to attain the intended mechanical and dimensional characteristics of the parts.

The response surface methodology (RSM) can be utilized to optimize printing parameters and annealing conditions, aiming to boost the quality of printed parts [3]. Elkaseer et al. (2020) examined the impact of process parameters and their interrelationships on the resource efficiency and quality of the FFF printing method. The authors highlighted the possible utility of RSM in the optimization of

3D printing parameter values [27]. Magri et al. (2020) presented a three-dimensional response surface to figure out the target response values and comprehend the interplay of printing settings, demonstrating the efficacy of RSM in optimizing printing parameters [28]. Additionally, Ouassil et al. utilized RSM to optimize FFF parameters to boost mechanical characteristics, highlighting the role of RSM in enhancing the mechanical performance of can ultimately gain valuable insights into the complex interactions between printing parameters and annealing conditions. Leading to the enhancement of printing processes and the quality of printed components.

This study aims to assess the impact of various printing parameters, including layer height and structure orientation, as well as annealing heat treatment parameters, including annealing temperature and annealing time, on the printed parts [29]. Furthermore, Tho employed RSM to identify the ideal settings for FFF printed parts, showcasing the versatility of RSM in optimizing various aspects of the 3D printing process [30]. The application of RSM for 3D printing process parameters and annealing parameters offers a systematic and efficient approach to optimize the quality, mechanical properties, and resource efficiency of 3D-printed parts. By leveraging RSM, researchers mechanical characteristic, surface roughness, and dimensional precision of PLA components printed using FFF. The RSM was employed to optimize the experimental settings, while the Analysis of Variance (ANOVA) test was utilized to examine the results. The study's originality is shown by its evaluation of printer process parameters in conjunction with annealing heat treatment parameters and optimization of these parameters using RSM.

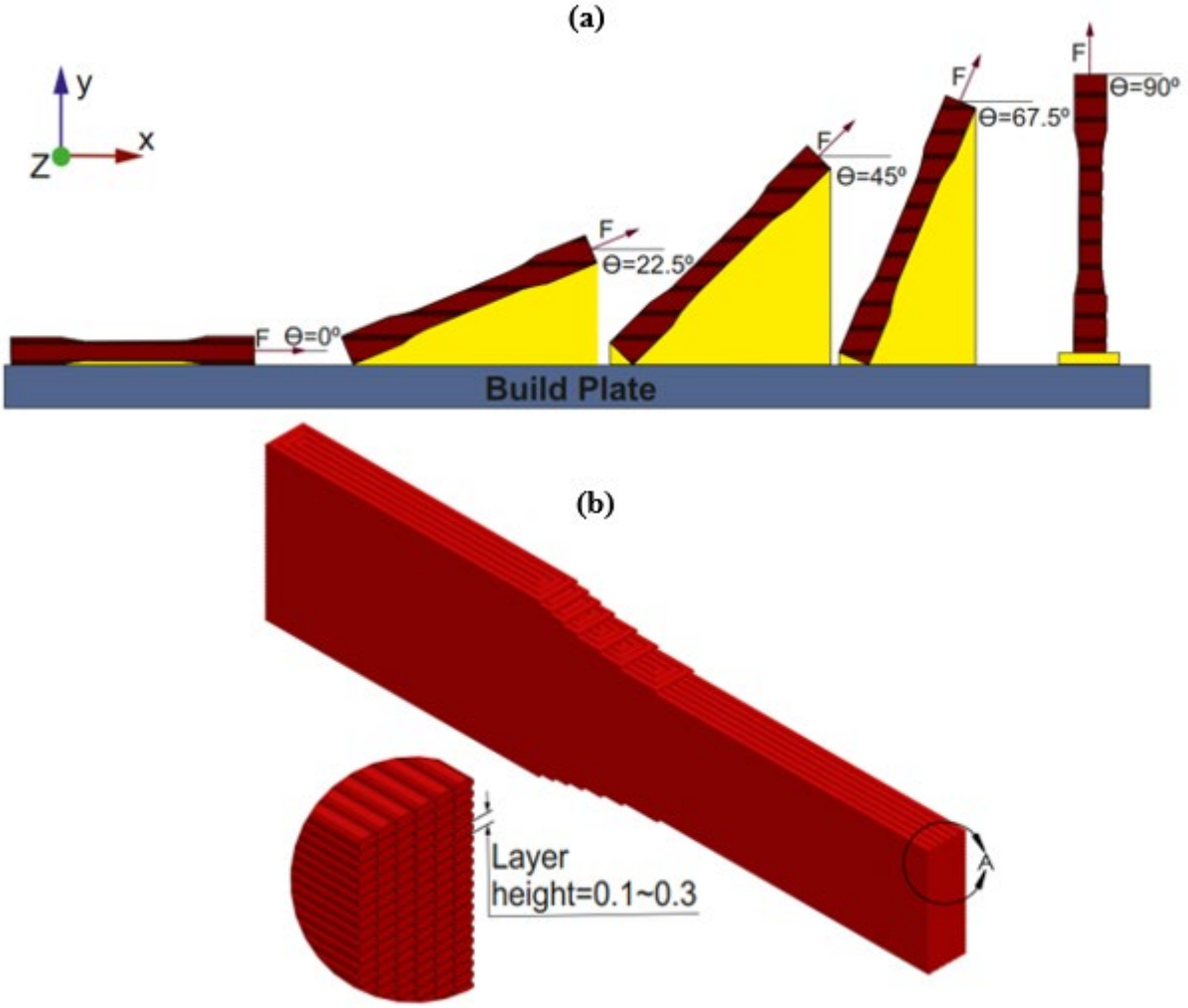

Figure 1. (a) The build orientations of the test specimens, and (b) the height of the layers.

2. MATERIALS AND METHODS

2.1. Specifications for printing and printers

All of the specimens utilized in this research were manufactured from PLA material by the FFF method, printed with a build volume of 200 × 200 × 220 mm on a cartesian type Zaxe X1 FFF 3D printer. The following 3D printing settings were utilized during the research: nozzle diameter of 0.4 mm, nozzle temperature of 215 °C, print speed of 70 mm/s, infill density of 100%, and bed temperature of 60 °C. A dog bone-shaped specimen was created to perform a tensile test with the purpose of assessing the tensile characteristics, dimensional precision, and surface roughness of plastic materials. Specimen dimensions were settled upon by consulting the ASTM Type I model [31], and the CAD model was created within the SolidWorks software environment. The print parameters used in this study were kept constant excluding the build orientation and layer height. The doge-bone tensile specimens were printed using various angles (0°, 22.5°, 45°, 67.5°, and 90°) and three-layer heights (1 mm, 2 mm, and 3 mm), as displayed in Figure 1. The entirety of the printed components was made with a density of 100% infill. The procedure makes use of a number of materials, although PLA is among the most used [6-7]. The PLA filament, with its properties clearly documented in [9], produced by ESUN, was used.

2.2. Annealing

Following the printing of the specimens, annealing is performed in accordance with the experimental design matrix. The processes of thermal annealing were carried out in a hot air oven. Four distinct temperatures (70, 90, 110, and 130 ◦C) and four distinct periods (60, 120, 180, and 240 min) were taken into account for the annealing process. Following the completion of the annealing procedure, the specimen remains within the oven until it reaches the ambient temperature.

2.3. Mechanical testing

The application of various criteria obtained from the DOE resulted in the effective production of a total of twenty-six distinct samples. A tensile test was conducted using the AG-50 kN Shimadzu Autograph. The test was carried out under standardized conditions, with a crosshead speed of 5 mm/min and at ambient temperature. Tensile testing was conducted following the recommendations presented in ASTM D638 [31]. The specimens underwent tensile testing until they reached the point of fracture. To minimize the influence of fluctuations and unpredictable inaccuracies, every recorded value in the dataset is based on a minimum of three valid tests. Throughout the experiment, no instances were observed where the samples exhibited any additional peaks in strength. Consequently, the UTS was identified as the highest stress value ever recorded.

2.4. Dimensional accuracy

The gauge section of the dog-bone tensile test specimen is of the utmost significance. Measurements were performed on dog bone samples at specified locations, including both ends and the middle (a total of three positions), as depicted in Figure 2 using digital vernier caliper. The objective was to independently assess the accuracy and precision of both thickness (h) and width (b). Therefore, in order to assess the precision, it was necessary to compare the produced dimensions with the original CAD design. Through the use of the standard deviation calculations, the precision (consistency) was defined. The weight of all samples was measured, and their accuracy was confirmed as well.

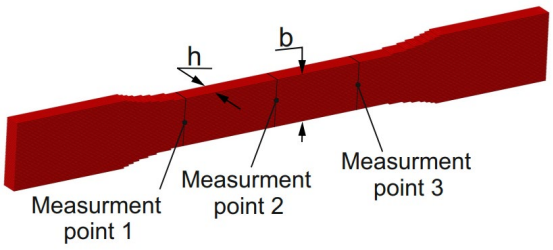

Figure 2. The schematic representation of measurement sites for width (b) and thickness (h) on the gauge section of the dog-bone specimen.

2.5. Surface Roughness

The surface finish quality of a component is related to its measured roughness. Roughness refers to the extent to which the chosen process parameters result in the appearance of surface irregularities on the printed object. Prior research has shown that components generated using the FFF process exhibit increased surface

roughness values, indicating a below-average surface quality [32]. Determining the effect of various printing settings on the surface roughness of the samples is a complex and challenging task. As a result, measurements were performed in two separate directions, specifically Vertical and Horizontal, relative to the tensile direction of the test specimen utilized in the tensile test. This is illustrated in figure 3, which serves as a schematic representation of the surface roughness measurements. The inability to measure perpendicular to the printing direction solely arises from the fact that the printing direction serves as a printing parameter, causing a shift in the orientation of each sample. The roughness measurements were performed using the Mitutoyo Surftest SJ-210, a needle-tipped inductive roughness device. The Mitutoyo SJ-210 table surface tester, equipped with a 20-millimeter-long probe, allows for effortless inspection of surfaces. The tester's stylus tip has a radius of 2 µm, while its detecting force amounts to 4 mN. The measurement of surface roughness was conducted with a "cut-off length" of 0.8 mm in the Z-axis orientation. Every evaluation condition was executed a minimum of five times on distinct areas of the FFF 3D printed objects' surfaces to ensure that the results obtained can be replicated. In order to properly evaluate the results, just one result was obtained by calculating the arithmetic mean.

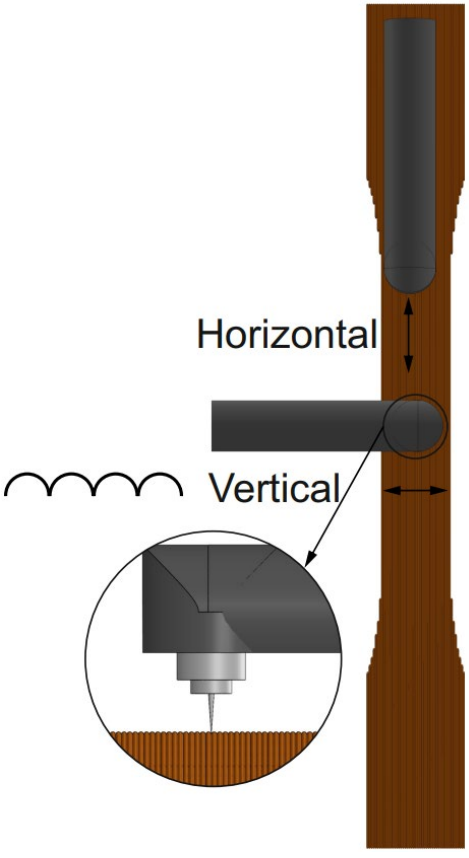

Figure 3. A schematic representation of the surface roughness measurements.

2.6. Response Surface Method

The printed components are affected by several processing parameters, such as layer height and build orientation [15,16]. The quality of components is affected by a number of variables, including the annealing parameters and the printing parameters. Specifically, the annealing temperature and the exposure period to this temperature perform a key role in deciding the components' quality [21,23]. The criteria for factor selection are established based on the extant literature and the corresponding degrees of importance attributed to each. The aim of this investigation was to assess the printing and annealing parameters of FFF-printed items. An insufficient amount of scholarly research has been devoted to the comprehensive evaluation of surface roughness, mechanical properties, and dimensional precision of heat-treated objects produced via FFF technology. This situation requires a substantial amount of tests. The objective of optimization is to optimize specific variables by either maximizing, minimizing, or reaching a target value, while also adhering to stated constraints, in order to get the most optimal outcomes. The utilization of RSM, a widely used technique, appears to offer benefits in the creation of an effective approximation method [33]. RSM is a powerful optimization tool that combines mathematical statistics to model both input and output parameters. As a result, one can determine the important elements and their respective amounts while also determining the best experimental conditions [34]. The use of RSM in this study is justified because several input and output factors are present.

A primary goal of optimization is to enhance the UTS while also minimizing surface roughness and achieving the desired CAD dimensions. The purpose of this optimization is illustrated in figure 4

Response	Goal	Lower	Target	Upper	Weight	Importance
Ra(V) (µm)	Minimize	1,04	1,04	24,35633333333	1	1
Ra(H) (µm)	Minimize	0,837666666666	0,837666666666	23,18	1	1
b (mm)	Target	12,64444444444	13	13,90444444444	1	1
h (mm)	Target	3,166666666666	3,2	3,707777777777	1	1
UTS (Mpa)	Maximize	9,3149	58,6939	58,6939	1	1

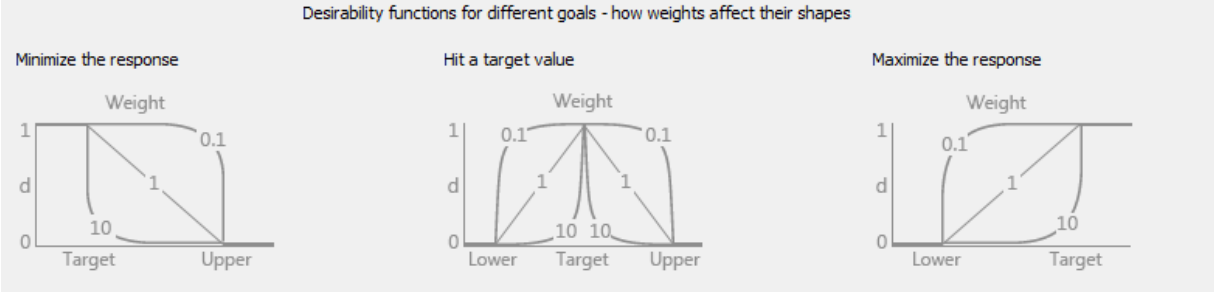

Figure 4. Different optimization goals and objectives correspond to distinct desirable functions.

The relevant experimental study was developed using Minitab, an RSM-based program. Each input parameter is assumed to be calculable and can be expressed as follows within the context of RSM [35].

$$y = F(x_1, x_2, \dots, x_m) \quad (1)$$

In the above situation, the variables x_1, x_2, ..., x_m, and y indicate the input and output factors, respectively. Within the framework of RSM, the primary phase entails establishing a robust connection between the two variables. The connection is clarified by employing a model based on second-order equations [35].

$$y = b_0 + \sum_{i=1}^{m} b_i x_i + \sum_{i=1}^{m-1} \sum_{j \geq i}^{m} b_{ij} x_i x_j + \sum_{i=1}^{m} b_{ii} x_i^2 + \varepsilon \quad (2)$$

The equation provided indicates the linear coefficient (i), the coefficient for the second order term (j), the regression coefficient (b), the total number of parameters (m), and the error associated with the response variable (ε). It is recommended to utilize RSM to investigate three dependent responses and three independent variables (one of which is a categorical factor and two of which are continuous factors) with a total of 26 experiments. Surface roughness, dimensional accuracy, and UTS are the output factors chosen for the settled RSM model. However, considering the model is configured with the following input parameters: build orientation, layer height, and annealing parameters (temperature and time). The annealing parameters, time and temperature are interdependent categorical factors. On the other hand, the printing parameters, layer height, and build orientation are continuous parameters. All other printing and post-processing factors that could affect printed component quality are kept constant.

3.RESULTS AND DISCUSSIONS

The present part examines and analyzes the outcomes of tensile testing, specifically focusing on the impact of layer height, build orientation, and annealing process parameters (time and temperature) on ultimate tensile strength (UTS). Table 1 presents the design table, which contains data from 26 tests and their corresponding responses.

Table 1. The values of the experimental response variable and the experimental design matrix.

Run Order	Layer Height, mm	Build Orient-ation, °	Temperature,°C -Time, min	UTS, Mpa (± SD)	h, mm (± SD)	b, mm (± SD)	Ra(H), µm (± SD)	Ra(V), µm (± SD)
1	0.1	0	0-0	54.65±0.7	3.17±0.02	13.43±0.04	0.95±0.16	7.46±0.3
2	0.1	22.5	70-60	46.31±0.7	3.28±0.02	13.54±0.14	8.04±0.15	8.41±0.24
3	0.1	67.5	110-240	18.96±1.4	3.34±0.03	12.78±0.08	8.71±0.77	7.72±1.04
4	0.1	90	130-120	10.99±1.1	3.28±0.03	12.64±0.08	9.16±1.07	2.60±1.7
5	0.1	0	70-240	58.69±0.5	3.17±0.01	13.90±0.04	1.16±0.27	10.57±0.4
6	0.1	22.5	130-60	45.78±1.6	3.35±0.04	13.51±0.09	8.20±0.13	9.99±1.26
7	0.1	67.5	90-240	19.64±1.8	3.27±0.04	12.78±0.07	8.13±0.27	7.74±0.03
8	0.1	90	0-0	38.65±2	3.28±0.03	12.96±0.02	7.88±0.28	2.29±0.12
9	0.2	0	90-120	52.88±0.4	3.25±0.03	13.62±0.05	1.11±0.25	14.87±0.42
10	0.2	22.5	110-240	37.52±6.9	3.44±0.06	13.43±0.2	11.74±0.84	14.41±0.99
11	0.2	45	0-0	38.76±1.6	3.54±0.03	13.39±0.07	14.94±0.39	14.56±0.46
12	0.2	67.5	130-180	24.93±1	3.53±0.05	13.10±0.12	14.94±0.53	12.04±0.8
13	0.2	0	110-60	53.89±0.2	3.31±0.04	13.66±0.06	1.22±0.29	14.86±0.29
14	0.2	22.5	0-0	50.42±1	3.38±0.02	13.46±0.09	12.31±1.44	14.85±0.28
15	0.2	45	70-120	28.43±2.9	3.47±0.03	13.33±0.04	14.62±0.19	14.53±0.19
16	0.2	67.5	130-240	18.53±1.4	3.46±0.04	13.10±0.05	14.55±0.18	11.67±0.46
17	0.2	90	90-120	32.13±0.3	3.56±0.06	13.17±0.06	14.98±0.19	1.81±0.32
18	0.3	0	130-180	42.28±2.3	3.27±0.03	13.45±0.09	1.87±0.45	24.36±0.56
19	0.3	22.5	90-60	45.03±2.1	3.50±0.04	13.68±0.07	12.58±2.08	22.87±1.82
20	0.3	90	110-120	9.31±1.9	3.70±0.07	13.28±0.06	22.95±0.46	1.25±0.22
21	0.3	0	90-180	43.61±1.3	3.24±0.04	13.51±0.07	0.84±0.11	24.13±1.37
22	0.3	22.5	0-0	41.88±3.83	3.42±0.03	13.45±0.03	13.11±1.3	22.85±0.58
23	0.3	45	130-60	26.81±0.9	3.61±0.07	13.56±0.12	20.89±0.49	19.91±0.35
24	0.3	67.5	70-240	24.52±0.6	3.71±0.05	13.29±0.05	22.88±0.72	12.92±1.33
25	0.3	90	130-240	16.7±3.1	3.67±0.07	13.32±0.05	23.18±0.8	1.04±0.31
26	0.3	0	110-180	50.92±1	3.37±0.02	13.48±0.01	1.08±0.32	22.54±0.63

It also analyzes the influence of these factors on surface roughness and dimensional precision. Variance analysis can be employed to derive numerical data pertaining to the probability value. ANOVA can accurately predict the optimal combination of process variables and identify the main contributing factors. Models with a p-value larger than 0.05 are widely regarded as insignificant. The resulting model is significantly influenced when a factor's p-value is less than 0.05 [33]. The ANOVA results in Table 2 indicate that all of the p-values for the linear coefficients of the build orientation are below 0.05. All the p-values for the linear coefficients of layer height are below 0.05, except for UTS. All p-values for the linear coefficients of the categorical factor temperature-time are greater than 0.05 for dimensional precision and surface roughness measured in the vertical direction. However, p-values are less than 0.05 for UTS and surface roughness measured in the horizontal direction. The p-values for layer height and build orientation, in relation to UTS and surface roughness, are less than 0.05, except for surface roughness measured vertically. However, the p-values for layer height and build orientation are greater than 0.05 for dimensional precision and surface roughness measured horizontally. In the case of 2-way Interaction, the p value is over 0.05 for UTS and b, and below 0.05 for surface roughness and h. The significance of the term in the proposed correlations of response becomes more pronounced as the p value decreases and f value increases. The primary factor that significantly affects all responses is the build

orientation, as evidenced by the ANOVA table. Furthermore, it is seen that the categorical variable of time-temperature has a greater impact on the UTS compared to the layer height. Conversely, the opposite holds true for surface roughness and dimensional correctness.

Table 2. Results of ANOVA include the p value, f value, and R2 value.

	UTS (MPa)		h (mm)		b (mm)		Ra(H)		Ra(V)	
	F value	P value	F value	P value	F value	P value	F value	P value	F value	P value
Model	22.90	0.001	28.05	0.001	6.87	0.021	161.00	0.000	39.84	0.000
Linear	25.48	0.001	26.39	0.001	6.98	0.021	129.60	0.000	34.77	0.000
X-Layer height	1.77	0.241	93.04	0.000	6.68	0.049	420.41	0.000	31.86	0.002
Y-Build orientation	62.12	0.001	126.36	0.000	19.86	0.007	690.26	0.000	166.30	0.000
CT-Temperature-Time	5.88	0.030	1.84	0.260	1.25	0.433	5.74	0.032	1.13	0.484
Square	5.96	0.047	12.56	0.011	2.38	0.188	59.02	0.000	18.82	0.005
X^2	6.99	0.046	2.72	0.160	4.31	0.093	15.89	0.010	0.69	0.443
Y^2	11.90	0.018	2.56	0.170	4.21	0.096	9.33	0.028	19.25	0.007
2-Way Interaction	0.36	0.576	25.47	0.004	0.68	0.446	91.30	0.000	35.04	0.002
X*Y	0.36	0.576	25.47	0.004	0.68	0.446	91.30	0.000	35.04	0.002
R^2, %	98.92%		99.12%		96.49%		99.84%		99.38%	
Adj. R^2, %	94.60%		95.58%		82.44%		99.22%		96.88%	

The influence of printer parameters (specifically, build direction and thickness of layers) in conjunction with annealing process parameters on the UTS result is illustrated in Figure 5. The results indicated a negative relationship between the UTS and the increase in layer thickness without any post-processing. The decrease in UTS found when the thickness of layers in 3D printed parts increases, without any post-processing, can be due to many variables that have been explained in the existing literature. An extensive study has been conducted on the correlation between layer height and the UTS of 3D printed components. Hua et al. (2023) noted that FFF specimens printed with lower layer heights exhibit better mechanical performance [13]. Choudhary et al. [36] also discovered an inverse interaction between layer thickness and the decrease in UTS. Furthermore, it was noted that decreasing the layer height resulted in a higher level of bonding, perhaps leading to an enhanced UTS [37]. It is observed that the UTS value exhibits a decreasing trend initially and subsequently rises with increasing layer thickness, owing to the thermal diffusion features [38]. These findings indicate that the thermal characteristics related to varying layer thicknesses can impact the bonding between layers and the overall structural strength of the printed objects. Grasso et al. [39] revealed a significant correlation between stiffness and strength, which was influenced by the infill orientation and temperature values. This indicates that the mechanical characteristic are affected by the printing parameters. Figure 5 demonstrates that in the samples without post-processing, the UTS initially drops and subsequently stabilizes as the structural orientation increases. The stability of the UTS can also be influenced by the variability in the height of each layer. The scholarly literature provides clarification on the phenomenon under consideration by employing the terms interlayer fracture and intralayer fracture [40]. The UTS results of annealed heat-treated samples varied depending on the printing parameters. Upon analysis of the sample with a layer thickness of 0.1 mm and a printing angle of 0°, it was seen that the sample, which underwent heat treatment at 70° C for 240 minutes, had a tensile strength roughly 10% higher than the untreated sample. The value shown represents the maximum UTS achieved in the experiments. A decrease in UTS is observed, particularly at a construct orientation of 90°, despite alterations to the annealing process parameters, as indicated by the graph. The UTS is significantly decreased by the

annealing heat treatment at 130°, and this reduction becomes more noticeable with longer durations. During the annealing heat treatment process at temperatures of 90° and 70°, it can be observed that the ultimate tensile strength (UTS) generally increases with longer durations. Nevertheless, establishing a universal correlation is not possible because to variations in layer thickness and build orientation. The ultimate tensile strength (UTS) of samples produced by FFF printing is influenced by the level of crystallinity in the printed object. The non-linear changes in UTS values can be attributed to the temperature-dependent modification of crystallinity during the printing process [41].

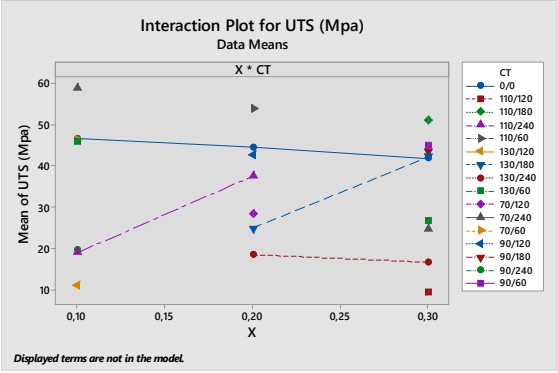

(a)

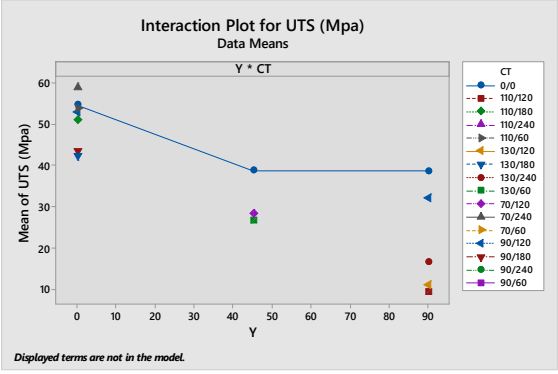

(b)

Figure 5. The surface roughness interaction plot with layer height, build orientation, and annealing parameters.

The correlation between printer parameters and annealing process parameters as they pertain to the surface roughness outcome is visually represented in Figure 6. Consistent with expectations, the samples utilizing the identical direction of printing and measurement exhibited the lowest surface roughness values. Conversely, as the angle between the printing orientation and the direction of measurement increased, the surface roughness value increased as well, reaching its maximum value in the fully perpendicular measurement. As mentioned in the literature [16,18], it was found that specific build orientations and raster orientations were crucial for achieving optimum surface roughness in FFF-printed parts. As expected, the graphs clearly indicate that altering the height of the layers has no effect on the roughness of the surface when the direction of measurement and the direction of printing are identical. However, when the orientation of printing and the direction of measurement were at at 90 degrees to each other, the roughness exhibited an upward trend with increasing layer height. This rise is roughly similar to the rate of increase in layer height. Several studies have highlighted the effect of layer height on roughness of the surface in FFF-printed parts. Several investigations have emphasized the influence of layer height on the surface roughness of objects produced using FFF printing. For instance, Mushtaq et al. highlighted the importance of layer thickness in determining surface roughness [42]. Similarly, Singh et al. [43] conducted investigations using an orthogonal array and concluded that layer height was the most dominant factor influencing roughness of the surface. Furthermore, Garg et al. [44] studied the effect of layer height and part deposition orientation on roughness of the surface using an artificial neural network, further emphasizing the importance of layer thickness. Consistent with findings in some existing literature [45,46], the surface roughness positively correlated with both the temperature and time of the annealing heat treatment. On the other hand, Novotný et al. reported that thermal annealing maintained the complicated three-dimensional structure of PLA produced through 3D printing, suggesting a multifaceted connection between annealing and surface roughness [47]. The annealing process, layer height, and build orientation are all critical factors in defining the roughness of the surface of parts in FFF technology.

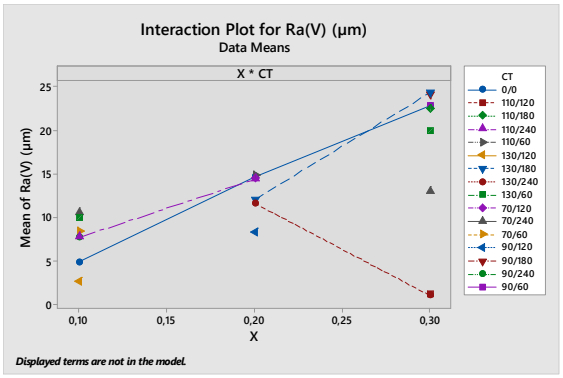

(a)

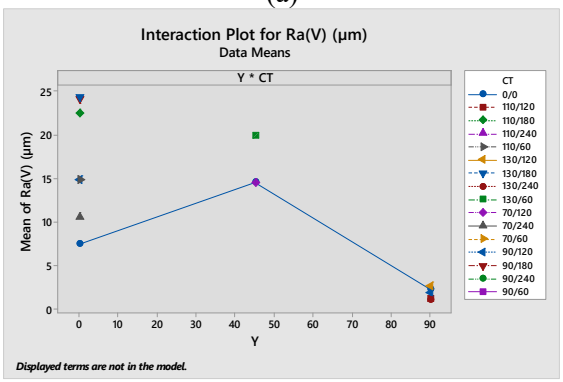

(b)

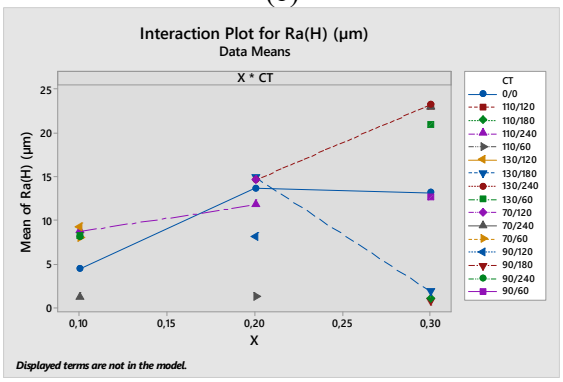

(c)

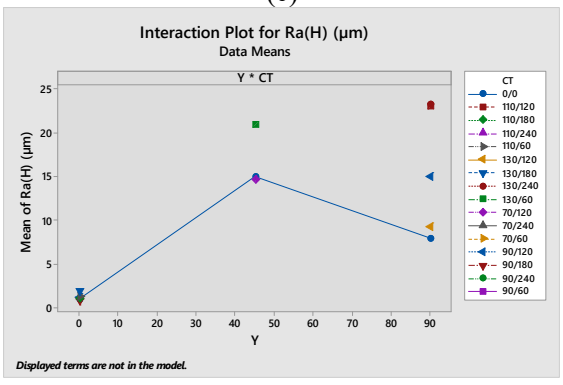

(d)

Figure 6. The surface roughness interaction plot with layer height, build orientation, and annealing parameters.

The dimensional accuracy of the dog bone tensile test specimen was determined by the proximity of the thickness and width values in a gauge zone to the CAD dimensions and the actual dimensions of the specimen. Based on the CAD measurements, the value of b should be 13 mm and the value of h should be 3.2 mm. The interaction plots demonstrating the influence of printing and annealing parameters on the values of b and h are shown in Figure 7. When analyzing the graphs, it becomes evident that the b value exhibits more dimensional precision when the build orientation is set at 90°, whereas the h value demonstrates higher dimensional accuracy at 0°. The natural tendency of molten matter to flow downward explains this phenomenon. Cojocaru et al. [48] highlight that the accuracy of 3D-printed PLA parts can be affected by alterations in material volume and the presence of residual stress resulting from PLA crystallinity. The graphs also clearly indicate that there is a greater level of dimensional precision when the layer thickness is smaller. While the annealing process parameters generally have an adverse impact on dimensional accuracy, the impact of these variables on precision in dimensions does not exhibit a linear rise. The ANOVA results also confirm this.

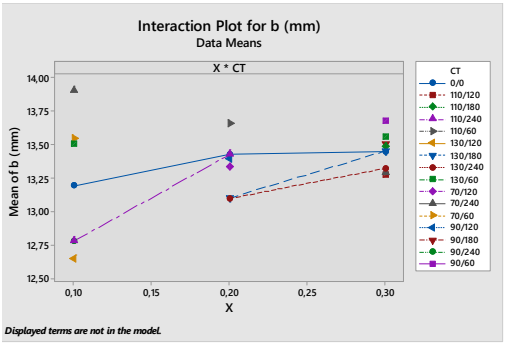

(a)

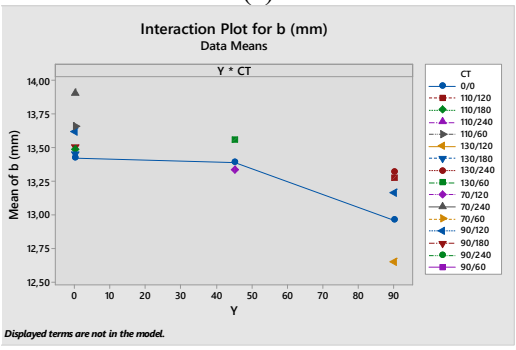

(b)

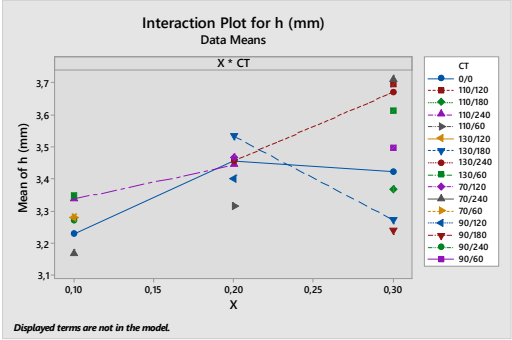

(c)

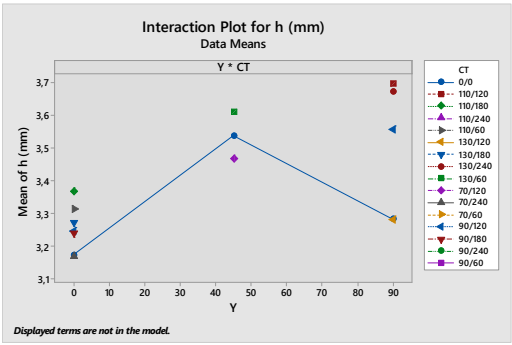

(d)

Figure 7. The dimensional accuracy interaction plot with layer height, build orientation, and annealing parameters.

The Insize ISM-PM200SA digital microscope was used to obtain macroscopic pictures of after tensile fractures, along with the previous findings. Figure 8 displays several images taken of the post-fracture specimens. Although the build orientation and layer heights are same between run 1 and run 5, the annealing process produces noticeable differences in the two samples. The sample that underwent annealing shows greater uniformity in its structure. Results from samples run 4, 8, and 17 indicate that the 90° build orientation performs better at lower layer thicknesses and lower annealing temperatures. The best results are achieved without any annealing. Furthermore, an intralayer fracture is seen on the fracture surface of sample number 4. This result indicates that the printing temperature and other printing settings for the filament are suitable. When comparing all angles, it is evident that the results improve as the angles approach zero. It becomes less effective as it nears a 90° angle. When samples with low build orientations are analyzed, samples at run 5, 9, and 13 exhibited the highest shape integrity with minimal gap between layers in low build orientations. As the building angles of the samples approach 0º, the tension in the tensile test will align with the layers of the sample being formed. Rupture occurs when the tensile stresses increase as the cross-sectional area of the layer decreases. The layers are created by stretching fibers in the direction of a pulling force and then breaking them into chopped layers.

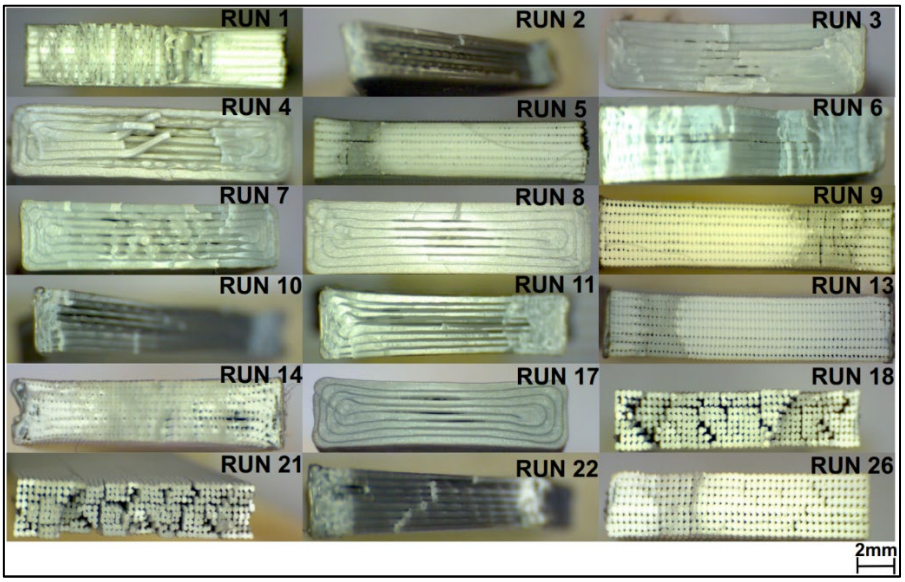

Figure 8. Microstructure of tensile specimen rupture surfaces.

An analysis of the results obtained from RSM-based multipurpose optimization is conducted as part of this investigation. The guiding principle of the optimization procedure is to minimize or maximize the output responses, which include dimensional accuracy, surface

irregularity, and UTS. The basics of optimization involve achieving dimensional accuracy, approaching the desired size, minimizing surface roughness (specifically Ra(V) and Ra(H)), and simultaneously maximizing the UTS. The RSM optimization study, shown in Figure 9 (a), determined the ideal values for the layer height, build orientation, annealing temperature, and annealing time as follows: 0.1 mm for the layer height, 0 degrees for the build orientation, 110 degrees for the annealing temperature, and 180 dk mm for the annealing time. The values of Ra(V), Ra(H), b, h, and the UTS are determined to be 7.19 µm, -2.99 µm, 13.32 mm, 3.28 mm, and 52.40 MPa, respectively, given the specified optimal variable conditions. Desirability quantifies how well a process or product metric complies with specifications using a standardized scale. The weighted geometric mean may then be used to aggregate the individual desirability evaluations into a multiresponse composite desirability score. This index gives a single numerical value for requirement conformity, making it easy to evaluate options and improve the design of a process or product.

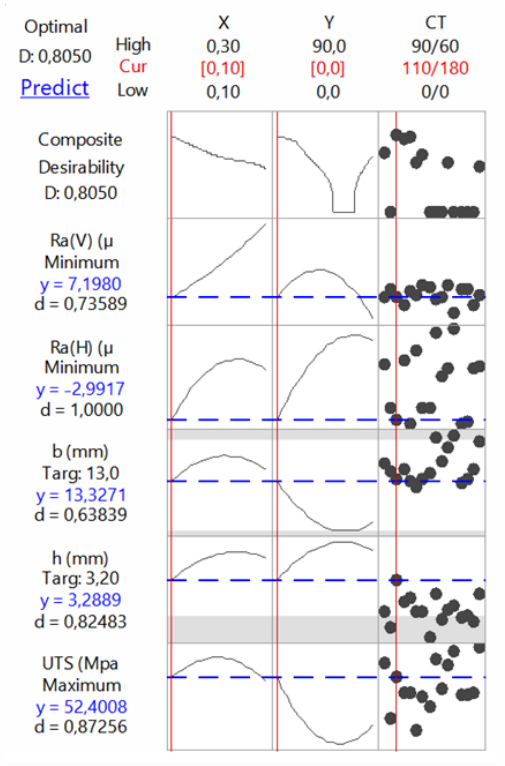

Figure 9. Predicted responses based on the best parameters for optimal results

The determined desirability levels for each response and the composite desirability are also displayed in Figure 9. The optimization investigation resulted in a composite desirability value of 0.80 for the variables. The maximum level of desirability assigned to Ra(H) is 1.0, while the minimum level of desirability assigned to b is 0.64. The corresponding levels of desirability for h, Ra(V), and UTS are 0.82, 0.73, and 0.87.Figure 10 displays surface plots illustrating the UTS, dimensional accuracy, and surface roughness based on the optimal annealing conditions.As illustrated in Figure 10, the UTS value reaches its maximum across all construction orientations when the layer height approaches 0.2 mm in the optimal annealing parameters. The parts manufactured with a 0.3 mm layer height have a minimum UTS. Additionally, the maximal UTS is observed in the 0° build direction; as the build direction increases, the UTS initially decreases and then rises around 90°. Lowering layer heights improves dimensional precision and reduces surface roughness. In accordance with the anticipated relationship, roughness of the surface is greater when measured in a direction perpendicular to the printing orientation.

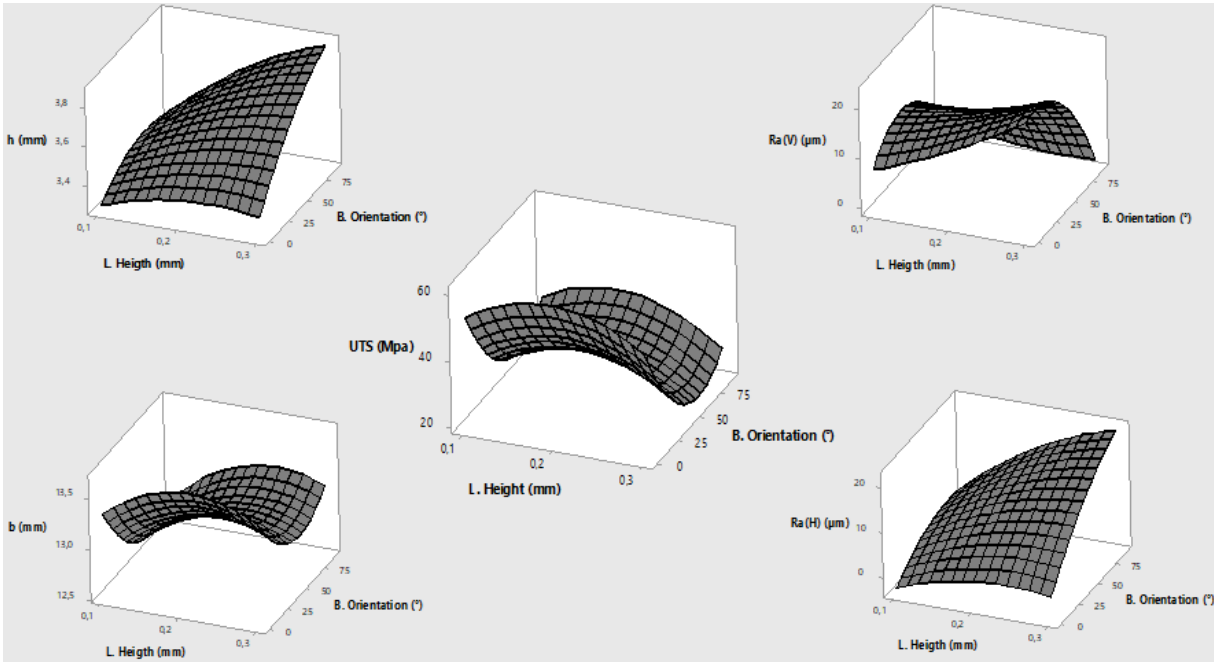

Figure 10. Surface plots displaying UTS, dimensional accuracy, and surface roughness.

The anticipated optimal results of this study were in comparison to the actual results, and the discrepancies between the two were determined. The objective of this procedure was to validate the precision and efficacy of the optimized results. Additionally, validation research was implemented in order to verify the confidence of the optimization results. The dataset for validation is presented in tabular format in Table 3. Subsequently, a comparison was performed between the experimental results acquired and the input variables' optimal values obtained through the optimization procedure. The error rates for dimensional accuracy (b and h) and UTS are notably low among all the recorded responses, falling precisely below 5%. Regarding surface roughness, the error rate in the vertical direction is 4.03%, while the error rate in the horizontal direction is considerably higher at 151.50%, suggesting a comparatively decreased degree of dependability.

Table 3 The validation results for the expected and observed values.

Build orient-ation, °	Layer height, mm	Annealing Temperature, °C	Annea-ling Time, min	Value	UTS, MPa	Ra(V)	Ra(H)	b	h
0	0.1	110	180	Anticipated	52.40	7.19	-2.99	13.32	3.28
0	0.1	110	180	Experimental	51.18	7.48	1.54	13.46	3.12
-	-	-		Error (%)	2.33	4.03	151.50	1.04	4.87

4. CONCLUSIONS

This research investigated the impact of annealing heat treatment parameters, build orientation, thickness of layers, and FFF 3D printed PLA samples on dimensional precision, mechanical characteristics, and surface roughness. The parameters for the annealing and printing were optimized by means of the response surface method. The following conclusions could be derived from the outcomes of those experiments:

- The RSM optimization resulted in an overall desirability number of 0.80, leading to optimal values for printing and annealing variables: 0° for build orientation, 0.1 mm for layer height, 110°C for annealing temperature, and 180 minutes for annealing time. The optimal variable values resulted in

responses of 7.19 μm for Ra(V), 2.99 μm for Ra(H), 13.32 mm for b, 3.28 mm for h, and 52.40 MPa for the UTS.

- The validation investigation showed that the maximum error percentage between the optimal and experimental values for UTS and dimensional accuracy was less than 5%, utilizing the printing and annealing variables determined through RSM optimization. The maximum percentage error between the optimal and experimental values exceeded 5% for surface roughness. This model's consistency with experimental data demonstrates the reliability and strong predictive capability of the established models for UTS and dimensional accuracy.
- The R2 and adjusted R2 values for each response were 96.49% and 82.44%, respectively, indicating that the model produces statistically significant results.
- The factor that has the most significant impact on all responses is the build orientation. Annealing parameters have a greater impact on the UTS compared to the layer height parameter. Annealing factors have the least influence on dimensional precision and surface roughness.
- The sample that underwent annealing exhibits not only a greater UTS value but also greater structural homogeneity and reduced volumes of voids.
- The samples with a 90° build orientation exhibit improved performance at decreasing layer thicknesses and annealing temperatures, reaching their peak performance without annealing. This occurs due to the printing temperature being ideal for this filament, resulting in strong interlayer adhesion.
- Positive outcomes were observed throughout the annealing process in samples oriented at a 0° build angle, whereas negative outcomes were noted when increasing the layer thickness. The most favorable results were attained with a thickness of 0.1 mm. Comparing all angles reveals that the closer they are to zero, the more favorable the outcomes. It becomes less effective as it nears a 90° angle.

ACKNOWLEDGMENTS AND FUNDING INFORMATION

Scientific Research Projects Coordination Unit of Karabuk University provided funding for this study. KBÜBAP-23-YL-149 is the project number. We appreciate the support.

Potential Conflicts of Interest Statement

Not a single conflict of interest exists, according to the authors.

REFERENCES

1. Ligon, S. C., Liska, R., Stampfl, J., Gurr, M., and Mülhaupt, R., "Polymers for 3D Printing and Customized Additive Manufacturing", Chemical Reviews, Vol. 117, Issue 15, Pages 10212–10290, 2017.

2. Ellson, G., Carrier, X., Walton, J., Mahmood, S. F., Yang, K., Salazar, J., and Voit, W. E., "Tough thiourethane thermoplastics for fused filament fabrication", Journal of Applied Polymer Science, Vol. 135, Issue 6, Pages 1-7, 2018.

3. El Magri, A., El Mabrouk, K., Vaudreuil, S., Chibane, H., and Touhami, M. E., "Optimization of printing parameters for improvement of mechanical and thermal performances of 3D printed poly(ether ether ketone) parts", Journal of Applied Polymer Science, Vol. 137, Issue 37, Pages 1-14, 2020.

4. Floor, J., Van Deursen, B., and Tempelman, E., "Tensile strength of 3D printed materials: Review and reassessment of test parameters", Materials Testing, Vol. 60, Issue 8, Pages 679-686, 2018.

5. Mahmood, A., Akram, T., Chen, H., and Chen, S., "On the Evolution of Additive Manufacturing (3D/4D Printing) Technologies: Materials, Applications, and Challenges", Polymers, Vol. 135, Issue 6, Pages 1-31, 2018.

6. Öz, Ö., Öztürk, F. H., and Güleç, C., "Effect of fiber content and plasticizer on mechanical and joint properties of carbon fiber powder reinforced PLA manufactured by 3D printing process", Journal of Adhesion Science And Technology, Vol. 37, Issue 15, Pages 2208-2231, 2023.

7. Çakan, B. G., "Effects of raster angle on tensile and surface roughness properties of various FDM filaments", Journal of Mechanical Science and

Technology, Vol. 35, Issue 8, Pages 3347-3353, 2021.

8. Eryildiz, M., "Comparison of notch fabrication methods on the impact strength of FDM-3D-printed PLA specimens", Materials Testing, Vol. 65, Issue 3, Pages 423-430, 2023.

9. Demir, S., Temiz, A., and Pehlivan, F., "The investigation of printing parameters effect on tensile characteristics for triply periodic minimal surface designs by TAGUCHI", Polymer Engineering & Science, Vol. 64, Issue 3, Pages 1209-1221, 2024.

10. Rajpurohit, S. R. and Dave, H. K., "Effect of process parameters on tensile strength of FDM printed PLA part", Rapid Prototyping Journal, Vol. 24, Issue 8, Pages 1317-1324, 2018.

11. Magri, A. E., El Mabrouk, K., Vaudreuil, S., and Touhami, M. E., "Mechanical properties of CF-reinforced PLA parts manufactured by fused deposition modeling", Journal of Thermoplastic Composite Materials, Vol. 34, Issue 5, Pages 581-595, 2021.

12. Vyavahare, S., Teraiya, S., Panghal, D., and Kumar, S., "Fused deposition modelling: a review", Rapid Prototyping Journal, Vol. 26, Issue 1, Pages 176-201, 2020.

13. Hua, L., Wang, X., Ding, L., Zeng, S., Liu, J., and Wu, Z., "Effects of fabrication parameters on the mechanical properties of short basalt-fiber-reinforced thermoplastic composites for fused deposition modeling-based 3D printing", Polymer Composites, Vol. 44, Issue 6, Pages 3341-3357, 2023.

14. Vyavahare, S., Kumar, S., and Panghal, D., "Experimental study of surface roughness, dimensional accuracy and time of fabrication of parts produced by fused deposition modelling", Rapid Prototyping Journal, Vol. 26, Issue 9, Pages 1535-1554, 2020.

15. Chohan, J. S. and Singh, R., "Pre and post processing techniques to improve surface characteristics of FDM parts: a state of art review and future applications", Rapid Prototyping Journal, Vol. 23, Issue 3, Pages 495-513, 2017.

16. Syrlybayev, D., Zharylkassyn, B., Seisekulova, A., Akhmetov, M., Perveen, A., and Talamona, D., "Optimisation of Strength Properties of FDM Printed Parts—A Critical Review", Polymers, Vol. 13, Issue 10, Pages 1-35, 2021.

17. Dey, A. and Yodo, N., "A Systematic Survey of FDM Process Parameter Optimization and Their Influence on Part Characteristics", Journal of Manufacturing and Materials Processing, Vol. 3, Issue 3, Pages 1-30, 2019.

18. Singh, J., Goyal, K. K., Kumar, R., and Gupta, V., "Development of artificial intelligence-based neural network prediction model for responses of additive manufactured polylactic acid parts", Polymer Composites, Vol. 43, Issue 8, Pages 5623-5639, 2022.

19. Huang, M., Zheng, N., Qin, Y., Tang, Z., Zhang, H., Fan, B., and Qin, L., "Description Logic Ontology-Supported Part Orientation for Fused Deposition Modelling", Processes, Vol. 10, Issue 7, Pages 1-20, 2022.

20. Zhiani Hervan, S., Altınkaynak, A., and Parlar, Z., "Hardness, friction and wear characteristics of 3D-printed PLA polymer", Proceedings Of The Institution Of Mechanical Engineers, Part J: Journal of Engineering Tribology, Vol. 235, Issue 8, Pages 1590-1598, 2021.

21. Eryildiz, M., "Effect of Build Orientation on Mechanical Behaviour and Build Time of FDM 3D-Printed PLA Parts: An Experimental Investigation", European Mechanical Science, Vol. 5, Issue 3, Pages 116-120, 2021.

22. Yilmaz, M. and Yilmaz, N. F., "Effects of raster angle in single- and multi-oriented layers for the production of polyetherimide (PEI/ULTEM 1010) parts with fused deposition modelling", Materials Testing, Vol. 64, Issue 11, Pages 1651-1661, 2022.

23. Akhoundi, B., Nabipour, M., Hajami, F., and Shakoori, D., "An Experimental Study of Nozzle Temperature and Heat Treatment (Annealing) Effects on Mechanical Properties of High-Temperature Polylactic Acid in Fused Deposition Modeling", Polymer Engineering & Science, Vol. 60, Issue 5, Pages 979-987, 2020.

24. Torres, J., Abo, E., and Sugar, A. J., "Effects of annealing and acetone vapor smoothing on the tensile properties and surface roughness of FDM printed ABS components", Rapid Prototyping Journal, Vol. 29, Issue 5, Pages 921-934, 2023.

25. Shbanah, M., Jordanov, M., Nyikes, Z., Tóth, L., and Kovács, T. A., "The Effect of Heat Treatment on a 3D-Printed PLA Polymer's Mechanical Properties", Polymers, Vol. 15, Issue 6, Pages 1-12, 2023.

26. Rane, R., Kulkarni, A., Prajapati, H., Taylor, R., Jain, A., and Chen, V., "Post-Process Effects of Isothermal Annealing and Initially Applied Static Uniaxial Loading on the Ultimate Tensile Strength

of Fused Filament Fabrication Parts", Materials, Vol. 13, Issue 2, Pages 1-18, 2020.

27. Elkaseer, A., Schneider, S., and Scholz, S. G., "Experiment-Based Process Modeling and Optimization for High-Quality and Resource-Efficient FFF 3D Printing", Applied Sciences, Vol. 10, Issue 8, Pages 1-18, 2020.

28. El Magri, A., El Mabrouk, K., Vaudreuil, S., and Ebn Touhami, M., "Experimental investigation and optimization of printing parameters of 3D printed polyphenylene sulfide through response surface methodology", Journal of Applied Polymer Science, Vol. 138, Issue 1, Pages 1-13, 2021.

29. Ouassil, S., El Magri, A., Vanaei, H. R., and Vaudreuil, S., "Investigating the effect of printing conditions and annealing on the porosity and tensile behavior of 3D -printed polyetherimide material in Z -direction", Journal of Applied Polymer Science, Vol. 140, Issue 4, Pages 1-16, 2023.

30. Tho, N. H., "Application of box-behnken, ann, and anfis techniques for identification of the optimum processing parameters for fdm 3d printing parts", Journal of Industrial Engineering and Halal Industries, Vol. 3, Issue 1, Pages 64-86, 2022.

31. I. ASTM, Standard Test Method for Tensile Properties of Plastics ,2022.

32. Hashmi, A. W., Mali, H. S., and Meena, A., "A comprehensive review on surface quality improvement methods for additively manufactured parts", Rapid Prototyping Journal, Vol. 29, Issue 3, Pages 504-557, 2023.

33. Temiz, A., "The Effects of Process Parameters on Tensile Characteristics and Printing Time for Masked Stereolithography Components, Analyzed Using the Response Surface Method", Journal of Materials Engineering and Performance, Vol. 1, Issue 1, Pages 1-10, 2023.

34. Cotabarren, I., Palla, C. A., McCue, C. T., and Hart, A. J., "An assessment of the dimensional accuracy and geometry-resolution limit of desktop stereolithography using response surface methodology", Rapid Prototyping Journal, Vol. 25, Issue 7, Pages 1169-1186, 2019.

35. Wang, K., Lam, F. "Quadratic RSM Models of Processing Parameters for Three-Layer Oriented Flakeboards", Wood Fiber Sci. Vol. 31, Issue 2, Pages 173-186, 1999.

36. Choudhary, N., Sharma, V., and Kumar, P., "Polylactic acid-based composite using fused filament fabrication: Process optimization and biomedical application", Polymer Composites, Vol. 44, Issue 1, Pages 69-88, 2023.

37. Moreno, R., Carou, D., Carazo-Álvarez, D., and Gupta, M. K., "Statistical models for the mechanical properties of 3D printed external medical aids", Rapid Prototyping Journal, Vol. 27, Issue 1, Pages 176-186, 2021.

38. Lanzotti, A., Grasso, M., Staiano, G., and Martorelli, M., "The impact of process parameters on mechanical properties of parts fabricated in PLA with an open-source 3-D printer", Rapid Prototyping Journal, Vol. 21, Issue 5, Pages 604-617, 2015.

39. Grasso, M., Azzouz, L., Ruiz-Hincapie, P., Zarrelli, M., and Ren, G., "Effect of temperature on the mechanical properties of 3D-printed PLA tensile specimens", Rapid Prototyping Journal, Vol. 24, Issue 8, Pages 1337-1346, 2018.

40. Wang, S., Ma, Y., Deng, Z., Zhang, S., and Cai, J., "Effects of fused deposition modeling process parameters on tensile, dynamic mechanical properties of 3D printed polylactic acid materials", Polymer Testing, Vol. 86, Issue 1, Pages 1-8, 2020.

41. Frunzaverde, D., Cojocaru, V., Ciubotariu, C.-R., Miclosina, C.-O., Ardeljan, D. D., Ignat, E. F., and Marginean, G., "The Influence of the Printing Temperature and the Filament Color on the Dimensional Accuracy, Tensile Strength, and Friction Performance of FFF-Printed PLA Specimens", Polymers, Vol. 14, Issue 10, Pages 1-15, 2022.

42. Mushtaq, R. T., Iqbal, A., Wang, Y., Cheok, Q., and Abbas, S., "Parametric Effects of Fused Filament Fabrication Approach on Surface Roughness of Acrylonitrile Butadiene Styrene and Nylon-6 Polymer", Materials, Vol. 15, Issue 15, Pages 1-25, 2022.

43. Singh, J., Singh, R., and Singh, H., "Investigations for improving the surface finish of FDM based ABS replicas by chemical vapor smoothing process: a case study", Assembly Automation, Vol. 37, Issue 1, Pages 13-21, 2017.

44. Garg, A., Bhattacharya, A., and Batish, A., "On Surface Finish and Dimensional Accuracy of FDM Parts after Cold Vapor Treatment", Materials and Manufacturing Processes, Vol. 31, Issue 4, Pages 522-529, 2016.

45. Wang, S., Daelemans, L., Fiorio, R., Gou, M., D'hooge, D. R., De Clerck, K., and Cardon, L., "Improving Mechanical Properties for Extrusion-Based Additive Manufacturing of Poly(Lactic Acid)

by Annealing and Blending with Poly(3-Hydroxybutyrate)", Polymers, Vol. 11, Issue 9, Pages 1-13, 2019.

46. Park, S.-S., Lee, Y.-S., Lee, S.-W., Repo, E., Kim, T.-H., Park, Y., and Hwang, Y., "Facile Surface Treatment of 3D-Printed PLA Filter for Enhanced Graphene Oxide Doping and Effective Removal of Cationic Dyes", Polymers, Vol. 15, Issue 2, Pages 1-19, 2023.

47. Novotný, F., Urbanová, V., Plutnar, J., and Pumera, M., "Preserving Fine Structure Details and Dramatically Enhancing Electron Transfer Rates in Graphene 3D-Printed Electrodes via Thermal Annealing: Toward Nitroaromatic Explosives Sensing", ACS Applied Materials & Interfaces, Vol. 11, Issue 38, Pages 35371-35375, 2019.

48. Cojocaru, V., Frunzaverde, D., Miclosina, C.-O., and Marginean, G., "The Influence of the Process Parameters on the Mechanical Properties of PLA Specimens Produced by Fused Filament Fabrication—A Review", Polymers, Vol. 14, Issue 5, Pages 1-23, 2022.

ULUSLARARASI 3B YAZICI TEKNOLOJİLERİ
VE DİJİTAL ENDÜSTRİ DERGİSİ
INTERNATIONAL JOURNAL OF 3D PRINTING
TECHNOLOGIES AND DIGITAL INDUSTRY

ISSN:2602-3350 (Online)
URL: https://dergipark.org.tr/ij3dptdi

BİR KİRAL KAFES YAPININ TASARIM VE OPTİMİZASYONU

DESIGN AND OPTIMISATION OF A CHIRAL LATTICE STRUCTURE

Yazarlar (Authors): Yusuf Bostancıoğlu, İlyas Kacar

Bu makaleye şu şekilde atıfta bulunabilirsiniz (To cite to this article): *Bostancıoğlu Y., Kacar İ., "Bir Kiral Kafes Yapının Tasarım ve Optimizasyonu" Int. J. of 3D Printing Tech. Dig. Ind., 8(2): 202-213, (2024).*

DOI: 10.46519/ij3dptdi.1452986

Araştırma Makale/ Research Article

Erişim Linki: (To link to this article): https://dergipark.org.tr/en/pub/ij3dptdi/archive

BİR KİRAL KAFES YAPININ TASARIM VE OPTİMİZASYONU

Yusuf Bostancıoğlu[a], İlyas Kacar[a]

[a]Niğde Ömer Halisdemir Üniversitesi, Mühendislik Fakültesi, Mekatronik Mühendisliği Bölümü, Niğde, TÜRKİYE

[*]*Sorumlu Yazar: ikacar@gmail.com*

(**Geliş/Received:** 14.03.2024; **Düzeltme/Revised:** 06.07.2024; **Kabul/Accepted:** 17.07.2024)

ÖZ

Kiral kafes yapıları zikzak şeklinde kübik hücrelerin üst üste ve yan yana çoğaltılmasıyla oluşturulan ökzetik davranışa sahip yapılardır. Bu çalışmada bir kiral kafes yapının tasarımı ve optimizasyonu yapılmıştır. Malzeme Ti-6Al-4V titanyum alaşımıdır. Kafes yapının ayrıt kesiti daireseldir. Yapısal analiz için sonlu eleman esaslı simülasyon yapılmıştır. Simülasyonda yapı bir ucundan ankastre bağlantı ile mesnetlenmiştir. Yük olarak da yapının serbest ucuna eksenel yer değiştirme uygulanmıştır. Simülasyon sonunda gerilme, deformasyon, enerji, Poisson oranı elde edilmiştir. Bu parametreler ve kafesin boyutları, uygulanan yük değerleri genetik algoritma esaslı optimizasyona tabii tutulmuştur. Optimizasyonda minimum boyut ile maksimum dayanımın elde edilmesi amaçlanmıştır. Sonuç olarak optimum değerler elde edilmiş ve parametrelerin birbirleri ile ilişiklerini veren cevap yüzey fonksiyonları sunulmuştur. Buna göre ayrıt kesitin yarıçapı 1 mm olduğunda yapı 0,12 mm yer değiştirmeye dayanmaktadır. Bu durumda yapı içerisinde 266,05 MPa değerinde çekme ve 233,34 MPa değerinde basma gerilmeleri oluşmaktadır. Bu değerler yapının akma dayanımının altındadır. Bu hâli ile yapının kütlesi 0,4549 g değerindedir.

Anahtar Kelimeler: Sonlu Elaman Simülasyonu, Kompozit Panel, 3D Kiral Ökzetik Çekirdek, Optimizasyon, Yapısal Analiz

DESIGN AND OPTIMISATION OF A CHIRAL LATTICE STRUCTURE

ABSTRACT

Chiral lattice structures have euxetic behaviour, which are manufactured by replicating zigzag-shaped cubic cells on top of each other and side by side. In this study, a chiral lattice structure is designed and optimised. The material is Ti-6Al-4V titanium alloy. The cross-section of the lattice structure is circular. Finite element based simulation is used for structural analysis. In the simulation, the structure is fix-supported at one end. As load, axial displacement is applied to the free end. Stress, deformation, energy, and Poisson's ratio are obtained at the end of the simulation. These parameters, lattice dimensions, and the applied load are subjected to genetic algorithm-based optimisation. In the optimisation, it is aimed to obtain maximum strength with minimum size. As a result, optimum values are obtained and response surfaces giving the relationship between the parameters are presented. When the cross-section radius is 1 mm, the structure withstands a displacement of 0.12 mm. In this case, tensile stresses of 266.05 MPa and compressive stresses of 233.34 MPa occur in the structure. These values are below the yield strength of the structure. In this state, the mass of the structure is 0.4549 g.

Keywords: Finite Element Simulation, Composite Panel, 3D Chiral Euxetic Core, Optimization, Structural Analysis

1. GİRİŞ

Tasarım konusunda karşılaşılan en büyük zorluklardan biri, yüksek verimli ve düşük maliyetli titreşim sönümleme sistemleri geliştirmektir. Mevcut malzemelerin sönümleyebileceği frekans aralığı geniş değil ayrıca yüksek sönümleme performansı da gösterememektedir.

Bu probleme bir çözüm olarak, yapı içerisine iyi titreşim dayanımı özelliğine sahip katkı malzemeleri eklenmektedir. Kiral kafes yapılar sadece moleküler kimyada karşılaşılan bir konu olmayıp mekanik tasarım esnasında da kullanılan yapılardır. Meriam sözlüğüne göre "ayna görüntüsü üzerine bindirilemeyen bir moleküle ait veya onunla ilgili" olarak tarif edilmiştir [1]. Kiralite türüne göre çeşitli zikzak yapılar mevcuttur [2]. Dolayısıyla yukarıda bahsedilen problemi ortadan kaldırılmak için kiral kafes yapılardan yararlanmak bir çözümdür [3]. Ökzetik kelimesi ise negatif Poisson oranı anlamına gelmektedir. Kiral kafes yapılar ökzetik davranabilmektedir. Bu özellikleri sayesinde Kiral yapılar, istenen deformasyon özelliklerine sahip olacak biçimde tasarlanabilmektedir.

Kiral yapıların deneme yanılma yolu ile seçimleri zahmetli, maliyetli ve zaman alıcı bir işlemdir. Artan rekabetçi piyasada üretim sektörü için optimum faydayı yakalamak önemlidir. Bu nedenle tasarım alanında optimizasyon kullanılması, optimizasyonların sonlu eleman simülasyonları ile birlikte yapılması bir yaygın mühendislik pratiğidir. Optimizasyon, tasarımcı tarafından belirlenen amaç ve ceza fonksiyonlarını sağlayan değişkenleri tespit etme sürecidir [4]. Bu bağlamda sıklıkla sonlu eleman yöntemi esaslı yapısal simülasyonlar kullanılmaktadır. Statik analiz, cisimlerin statik yük altındaki davranışlarını, oluşan gerilmeleri ve deformasyonları incelemektedir. Statik, fizik biliminin dengede duran mekanik sistemlerle ilgilenen dalıdır [5]. Statik analiz, mühendislerin veya tasarımcıların, bir ekipmanın veya yapının, dayanması beklenen yükler altında güvenli olduğundan emin olmalarını sağlamaktadır [6]. Simülasyon, Latince kökenli bir kelime olup "taklit, benzer" anlamına gelmektedir [7]. Statik yapısal simülasyon sayesinde, herhangi bir yapının üzerine binmiş yükün sonucunda yapının durumu elde edilebilmektedir [8].

Ha ve ark. (2016) kiral üç boyutlu kübik kafesleri, rijit kübik modüller halinde oluşturmuş ve sonlu elemanlar yöntemi ile analiz etmişlerdir. Kafesler, geometriye bağlı olarak negatif değerler alabilen Poisson oranına sahiptirler. Poisson oranı, küpler birbirinden uzaklaştıkça sıfıra doğru yaklaşmaktadır. Kafeslerde eksenel gerilme neticesinde eğilme deformasyonu oluşmaktadır. Bu tür bir durum klasik sürekli ortam mekaniğinde meydana gelememekte ancak kiral bir Cosserat katısında meydana gelebilmektedir [9]. Barad ve ark. (2023) havacılık uygulamaları için mekanik yapıların tasarımında dayanım-ağırlık oranını en üst düzeye çıkarmayı ve yapının titreşim cevabını mümkün olduğunca azaltmayı, böylece gerilmelerin dayanıklılık sınırının çok altında olmasını amaçlamışlardır. Kiral kafes yapılarındaki önceden ayarlanabilen deformasyon şekilleri sayesinde yapıdaki sönümleme artırılabilmiştir. Bu sayede söz konusu yapılar, yararlanıldıkları sahada yapının genel titreşim tepkisini azaltmak için bir titreşim emici olarak kullanılmıştır. İçerisinde kiral bir kafes bulunan basit bir konsol kiriş ele alınarak titreşim tepki karakteristiğini anlamak amacıyla geometrik tasarım, parametrik hale getirilmiştir. Optimizasyon sayesinde uygun boyutlar tespit edilmiştir [10].

Yukarıda verilen literatür taramasından anlaşılacağı üzere, sağladıkları yararlar nedeniyle kiral kafes sistemleri yapısal tasarım alanında kullanılmaktadır. Optimizasyon ise tasarımcıların vazgeçilmez araçlarından biridir. Ancak kiral yapıların optimizasyonu ile ilgili çalışmaların sayısının az olduğu görülmüştür. Bu çalışmanın amacı, bir burkulma moduna karşılık gelen şekle sahip kübik birim hücrelerden oluşan bir kiral kafes yapının optimum boyutlarının, sonlu eleman analizi esaslı yapısal simülasyon ve genetik algoritma esaslı optimizasyon ile belirlenmesidir. Cevap yüzey fonksiyonu, parametrelerin birbiri ile olan ilişkilerini veren fonksiyon olup bu çalışmada tek gizli katmanlı, üç hücreli yapay sinir ağı yöntemi ile tespit edilmiştir. Cevap yüzey fonksiyonu sayesinde de parametreler arası lokal ilişkiler tespit edilmiştir. Tasarım noktalar kümesi Latin hiperküp ve cevap yüzey fonksiyonu ise Kriging yöntemleri ile oluşturulmuştur.

Bu çalışmanın literatüre katkısı şöyledir: Kiral kafes yapının optimum boyutları tespit edilmiş ve parametrelerin birbirleri ile olan ilişiklerini veren cevap yüzey fonksiyonları sunulmuştur. Çalışmanın özgün yönü, bir yapısal kiral kafes yapı tasarımıdır. Bu konu ile ilgili olarak açık Türkçe literatürde çok az makale mevcuttur. Bu makale ile Türkçe literatüre kiral yapı tasarımına ilişkin yöntemler sunulmaktadır.

2. MATERYAL ve METOD

Şekil 1 (*a*)'da bu çalışmada kullanılan kiral kafes geometrisi gösterilmiştir. Bu tür kiral kafes biçimlerine, kübik kafes yapı denmektedir. Kiral hücresel yapıya sahip ökzetik bu yapının birim hücresinin şekli, Körner ve Liebold-Ribeiro (2015) tarafından ilk olarak tanıtılan ve Warmuth ve Körner (2015), Wormser vd. (2017), ve Warmuth vd. (2017) tarafından daha ayrıntılı olarak incelenen bir düzenli kübik birim hücrenin 10. burkulma moduna karşılık gelmektedir [11-14]. Eleman, yapının ayrıklaştırılması sonucunda oluşan birim parçaya verilen addır. Düğüm noktası ise oluşan her elementin köşe noktalarıdır. Birim hücre geometrisi Şekil 1 (*b*)'de tanımlanmıştır.

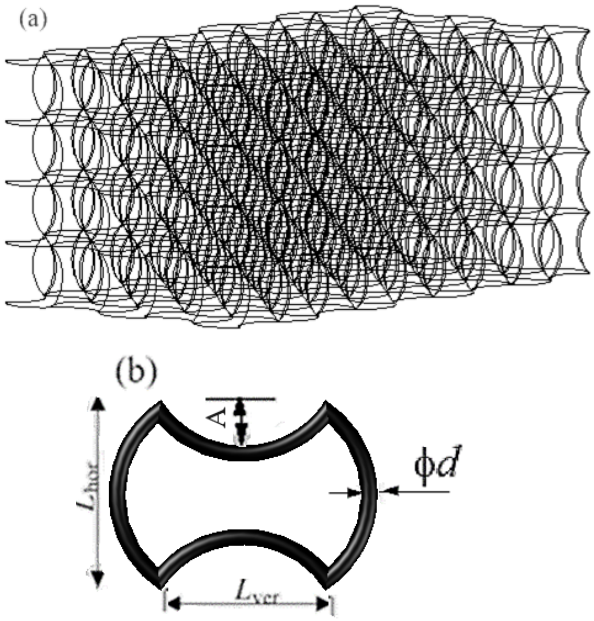

Şekil 1. Çalışmada kullanılan (*a*) kiral kafes yapı ve (*b*) birim hücre boyutları.

Kafesteki eğrisel çubuklar, düğüm noktalarında birleşen sinüs dalgası biçimindedir. Birim hücre geometrik parametreleri şu şekildedir: Dikey (L_{ver}) ve yatay (L_{hor}) yönlerde ardışık iki düğüm arası mesafe, eğri biçimli çubuğun genliği (A) ve kesit çapı (d) olmak üzere tüm yapı 9×4×5 adet birim hücreli olup $L_{ver} = L_{hor} = 2$ mm, $A = 0{,}5$ mm değerindendir. Katmanlar arası mesafe 2 mm değerindedir. Başlangıçta $d = 0{,}6$ mm olup bu hali ile tüm yapı 886,14 mm³ hacme ve 4,094 g kütleye sahiptir. Malzeme olarak Ti-6Al-4V alaşımı kullanılmıştır. Malzemeye ait mekanik özellikler Çizelge 1'de verilmiştir.

Çizelge 1. Ti-6Al-4V alaşımının mekanik özellikleri.

Özellikler	Değer
Yoğunluk (kg/m^3)	4620
Termal genleşme katsayısı (1/°C)	9,4e-006
Özgül ısı (J/kg°C)	522
Termal iletkenlik (W/m°C)	21,9
Direnç (ohm.m)	1,7
Basmadaki maksimum dayanım (MPa)	1070
Basmadaki akma dayanımı (MPa)	930
Çekmedeki akma dayanımı (MPa)	930
Çekmedeki maksimum dayanım (MPa)	1070
Elastisite modülü (GPa)	96
Poisson oranı	0,36
Bulk modülü (GPa)	11,429
Kayma modülü (GPa)	35,294

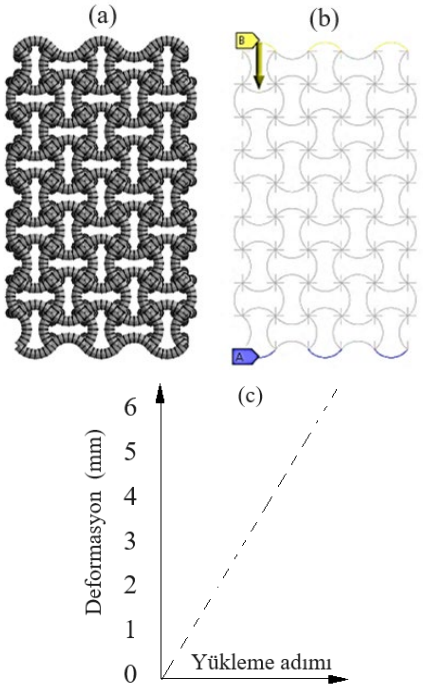

Şekil 2. Yapının (*a*) FE modeli ve (*b*) uygulanan yük ve sınır şartları (*c*) 0-6mm arasında rampa şeklinde yer değiştirme.

Simülasyonlar ANSYS© programı kullanılarak yapılmıştır [15]. Oluşturulan geometriye uygulanan yük, sınır şartları ve cismin sonlu eleman modeli, eleman ağı sonunda kiral yapının dairesel kesitli hâli Şekil 2'de görülmektedir. Yük olarak deplasman ve sınır şartı olarak ankastre mesnet uygulanmıştır. Son

olarak da eleman ağı oluşturmak üzere ayrıklaştırma işlemi gerçekleştirilmiştir. Ayrıklaştırma için lineer şekil fonksiyonuna sahip tam integrasyon formüllü kiriş elemanlar kullanılmıştır. En uygun bölüntüleme sayısını (minimum elaman ile maksimum hassasiyetin elde edildiği kritik sayıyı) belirlemek üzere ağdan bağımsızlık analizi yapılmıştır. Buna göre 10816 adet eleman sayısı optimum olarak tespit edilmiştir. Bu eleman sayısında yapıda 20580 adet düğüm noktası oluşmaktadır.

Ağın kalite ölçütlerden biri çarpıklık olup maksimum ve ortalama değerleri sıfır olmuştur. Ortogonal kalite ise 1'dir. Korkmaz ve Kacar (2022) kalite ölçütlerini şu biçimde tariflemiştir [16]: "Çarpıklık (skewness) değeri [0,1] arasında değişir. Max skewness<0,90…0,94 olması gerekir. Bu değer ne kadar küçük olursa veya sıfıra ne kadar yakın ise ağ kalitesi açısından o kadar iyidir. Kalite aralığı ideal ağ elemanı geometrisinden sapma ölçüsü olarak değerlendirilir. Ortogonal kalite, ağ elemanı yüzeylerinin orta noktasının merkezine olan uzaklığının, komşu mesh eleman yüzeylerinin orta noktalarında birbirine olan uzaklığa oranıdır. En küçük değerine bakılarak değerlendirme yapılır. En küçük değer > 0,1…0,15 olması istenir. En/boy oranı ise ağ elemanı uzun kenar uzunluğunun kısa kenar uzunluğuna oranıdır. İdeal bir ağ elemanında bu oran 1 dir. Bu orandan uzaklaştıkça ağ kalitesi düşer. En büyük en/boy oranına göre kalite değerlendirmesi yapılır. Bu değerin 20' den büyük olması istenmez."

Optimizasyon için ise sırasıyla şu adımlar takip edilmiştir. Öncelikle değişkenler parametrik hâle getirilmek üzere program içerisinde seçilmiştir. Giriş ve çıkış değişkenleri olmak üzere iki farklı değişken türü mevcuttur. Değişkenler parametrik hâle getirildikten sonra kullanıcı tarafından değiştirilememekte, ancak parametrelerin alt üst sınırları belirtilerek bu aralık içerisinde istenen adette tasarım noktası (DP) oluşturulabilmektedir. Giriş değişkenlerinin başlangıçtaki alt ve üst sınır değerleri ile çıkış değişkenleri Çizelge 2 'de verilmiştir. Çizelgede, çıkış değişkenlerinin sadece hangileri olduğu belirtilmiştir. Ancak bunlar, giriş değişkenlerinin değerlerine göre hesaplanacak olan değerlerdir. Giriş değişkenleri ise tek değer olmayıp, her biri, birer aralıkta değiştiği için, karşılık gelen çıkış değişkenleri de farklı farklı olacaktır. Çıkışların neler olacağı, hangi aralıkta olacağı, henüz optimizasyon yapılmadan bilinememektedir. Optimizasyon sonunda elde edilecek bilgilerden biridir. Bu nedenle Çizelge 2 içerisinde verilememiştir. Çıkış değişkenlerinin değerleri (aralığı) Şekil 6'daki cevap yüzey fonksiyonunda verilmiştir.

Çizelge 2. Parametrelerin alt ve üst sınırları.

Giriş değişkenleri	**Başlangıç**	**Alt sınır**	**Üst sınır**
Çap (mm)	0,6	0,1	1,0
Yer değiştirme (mm)	6,0	-6,0	6,0
Çıkış değişkenleri			
Gerilme (MPa)	--	--	--
Poisson oranı	--	--	--
Yanal daralma (mm)	--	--	--

DP noktaları oluşturulması için Latin hiperküp örnekleme yöntemi kullanılmış ve 200 adet DP oluşturulması sağlanmıştır. Bütün DP noktalarının çözülebildiği görülmüştür. Cevap yüzey fonksiyonu tek gizli katmanlı, üç hücreli yapay sinir ağı sayesinde tespit edilmiştir. Cevap yüzeyi fonksiyonu eğri uydurma esaslı fonksiyonlar olup değişkenlerin birbiri ile ilişkilerini vermektedir. Amaç fonksiyonu olarak minimum ayrıt kesit ve maksimum dayanım şartları girilmiştir. Optimizasyon için çok amaçlı çok kısıtlı genetik algoritma (MOGA) yöntemi kullanılmıştır. MOGA yöntemi kontrollü elitizm kavramlarına dayanan popüler NSGA-II'nin (Non-dominated Sorted Genetic Algorithm-II) bir çeşididir. Çoklu hedefleri, kısıtlamaları desteklemekte ve global optimumun bulunmasını amaçlamaktadır. Her iterasyonda 400 örnek olmak üzere 2000 örnek üretilmiş ve maksimum 8 iterasyon sonunda 3 aday bulunmuştur. 4039 değerlendirmeden sonra yakınsama gerçekleşmiştir. Yakınsama grafiği Şekil 3'te verilmiştir.

Optimizasyonda temel amaç(lar), hafif ve dayanıklı bir yapı elde etmektir. Bu çalışma içerisinde yer yer "minimum boyut", "minimum yarıçap" ve "minimum kafes boyutu" ifadeleri kullanılmıştır. Bunların hepsi "hafif bir yapı" amacına götüren tek bir parametreye işaret etmektedir. O da çap değeridir. Zira bu çalışmada kafes boyutlarından sadece "çap" değeri parametrik hâle getirilmiştir.

Benzer olarak, "dayanım sınırını aşmadan deformasyonu artırmak", "maksimum dayanım" ve "gerilmenin akma sınırının altında kalması" ifadelerinin tamamı da "dayanıklı bir yapı" amacına hizmet eden tek bir parametredir, o da "yer değiştirme" parametresidir. Zira bu çalışmada "dayanım-gerilme-yük" ile ilişkili tek parametrik değişken "yer değiştirme" değeridir. Yer değiştirme arttıkça yapıda gerilme artmaya başlar ve bir sınır değerde hasar başlar. Hasar başlamadan önce, gerilmenin çıkabileceği en yüksek değere ulaşmak için uygulanacak en fazla yer değiştirme elde edilirse, o zaman "dayanıklı bir yapı" amacına ulaşılmış olacaktır.

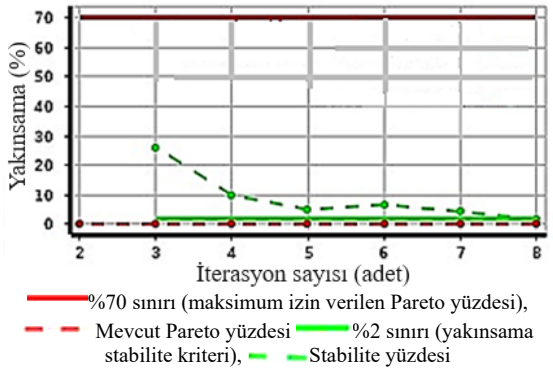

Şekil 3. Optimizasyon esnasında genetik algoritmanın yakınsama grafiği.

3. BULGULAR VE TARTIŞMA

3.1. Gerilme Deformasyon sonuçları

Başlangıçta kiral yapının bir ucu ankastre mesnetlenirken diğer ucundan Z ekseni doğrultusunda 6 mm değerinde basma türünde yer değiştirme (deplasman) uygulanmıştır. Yer değiştirme rampa şeklinde 0-6 mm arasında uygulanmaktadır. Her bir analiz 20 GB RAM ve 1,3 GHz 8 çekirdekli bir bilgisayar ile 14 sn sürmüştür. Hesaplamaya dair istatistiki bilgiler Çizelge 3'te verilmiştir.

Çizelge 3. Çözüme dair hesaplama bilgileri.

Özellikler	Değer
Hesaplama süresi (s)	14
Kullanılan bellek (MB)	623
Sonuç dosyası boyutu (MB)	23,875

Henüz optimizasyon yapılmadan önce başlangıç değerleri kullanılarak gerçekleştirilen simülasyon sonucunda eksenel doğrultuda 6 mm basma yer değiştirmesi uygulanmıştır. Başlangıç değerleri ile yapılan analiz sonucunda eksenel doğrultuda 6,0185 mm toplam deformasyon oluşmuştur. Yanal deformasyon ise -0,62728 mm olarak elde edilmiştir. Yanal daralmanın ölçüldüğü nokta ve daralmış geometri Şekil 4'te verilmiştir. Eksenel doğrultuda basma uygulandığında, yanal doğrultuda şişme beklenirken daralma olması, ökzetik davranış nedeniyledir.

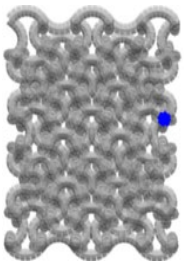

Şekil 4. Poisson oranı nedeni ile oluşan yanal deformasyonun ölçüm noktası.

Poisson oranı Denklem (1) kullanılarak hesaplanmaktadır.

$$\nu = -\frac{\varepsilon_{yanal}}{\varepsilon_{eksenel}} \tag{1}$$

Burada ν Poisson oranı olup birimsizdir. ε_{yanal} ve $\varepsilon_{eksenel}$ ise sırasıyla yanal ve eksenel doğrultulardaki şekil değiştirmelerdir. Denklem (2) ile hesaplanmaktadır. Birimsizdir.

$$\varepsilon_{yanal} = \frac{L_{son}-L_{ilk}}{L_{ilk}} \tag{2-a}$$

$$\varepsilon_{eksenel} = \frac{H_{son}-H_{ilk}}{H_{ilk}} \tag{2-b}$$

Burada L_{ilk} ilk genişlik, L_{son} genişlik, H_{ilk} tüm yapının ilk boy ve H_{son} ise son boydur. Uzunluk birimindedir.

Kafes yapıda ölçüm yapılan noktadaki yanal ilk genişlik $10{,}198\ mm$ olup tüm yapının eksenel genişliği ise $19{,}002\ mm$'dir. Bu durumda yanal şekil değiştirme $\varepsilon_{yanal} = \frac{-0{,}62728\ mm}{10{,}198\ mm} = -0{,}0615101$ olmaktadır. Eksenel şekil değiştirme ise $\varepsilon_{eksenel} = \frac{-6\ mm}{19{,}002\ mm} = -0{,}31576$ olmaktadır. Sonuçta Poisson oranı $\nu = -\frac{\varepsilon_{yanal}}{\varepsilon_{eksenel}} = -\frac{-0{,}0615101}{-0{,}31576} = -0{,}1948$ olmaktadır. Poisson oranının negatif çıkması, yapının ökzetik davrandığını göstermektedir.

Şekil 5'ten görüldüğü gibi yapıda -3700,4 MPa basma gerilmesi ve 1296,5 MPa çekme gerilmesi oluştuğu görülmektedir. Basma gerilmelerinin dikey çubuklarda çokça oluştuğu, yatay çubuklarda ise çekme gerilmelerinin oluştuğu görülmektedir. Yapıya eksenel basma yer değiştirmesi uygulanmasına rağmen yer yer basma veya çekme gerilmesinin

oluşması kiral yapıdan beklenen bir durumdur. Kullanılmış olan malzeme titanyum alaşımı olup basmadaki akma gerilmesi 930 MPa, çekmedeki akma gerilmesi 930 MPa ve maksimum akma gerilmesi 1070 MPa değerlerine sahiptir. Analizde malzeme davranışı lineerdir. Bu nedenle gerilmenin maksimum değeri, akma sınırını geçmiştir. Akma sınırının altında kalacak en büyük gerilme değerinin tespiti amacıyla optimizasyon yapılmıştır.

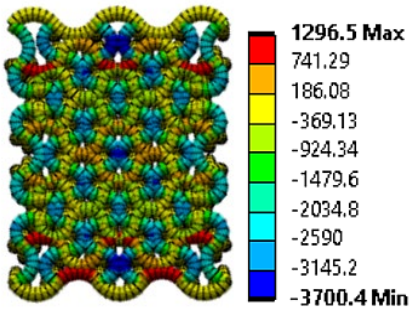

Şekil 5. Eksenel gerilme değerleri (MPa).

3.2. Parametreler arasındaki ilişkiler

Kiral kafes yapıların tasarımında parametrelerin birbirleriyle ilişkileri önemlidir. Yapılan tasarımda bu ilişkiler cevap yüzey fonksiyonu ile elde edilmiş ve Şekil 6'da her bir giriş parametresinin, çıkış değişkenleri üzerindeki etkisi verilmiştir.

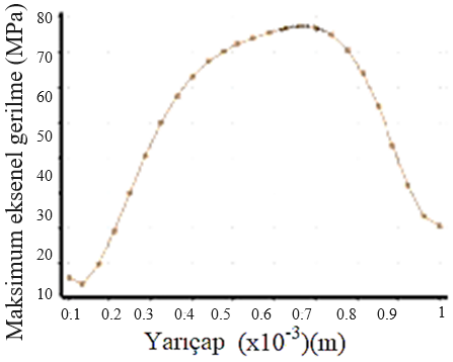

(*a*)

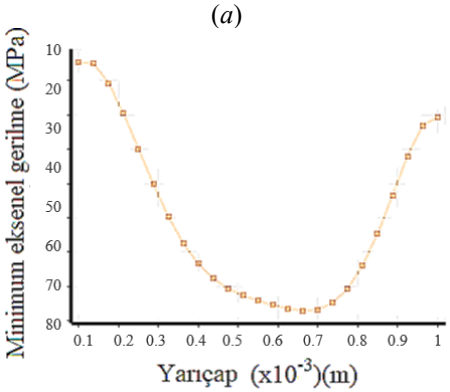

(*b*)

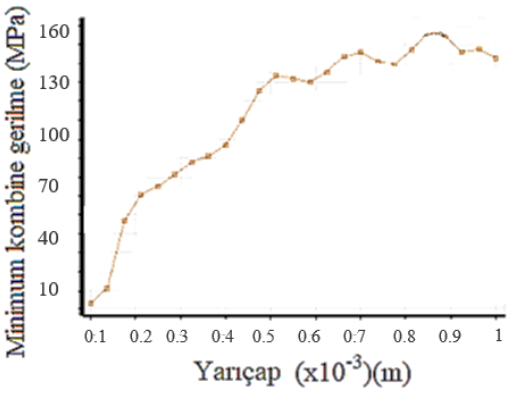

(*c*)

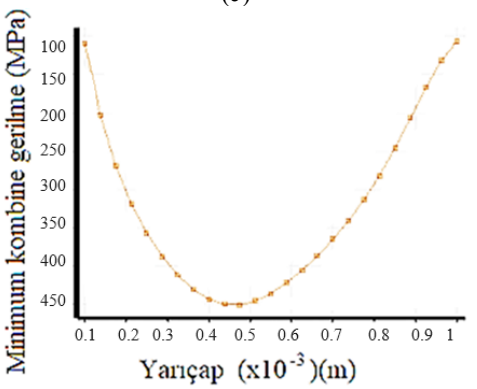

(*d*)

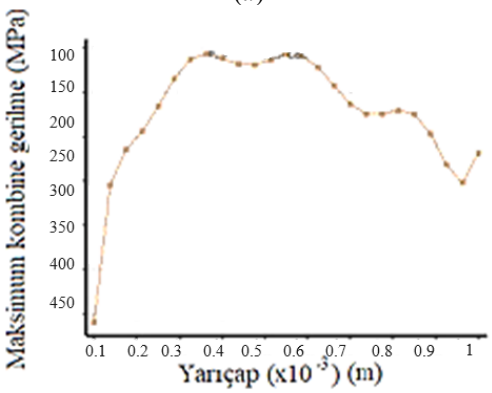

(*e*)

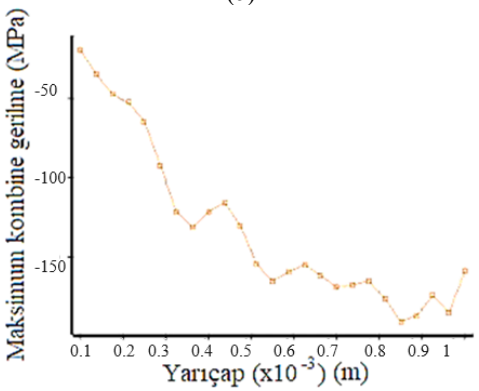

(*f*)

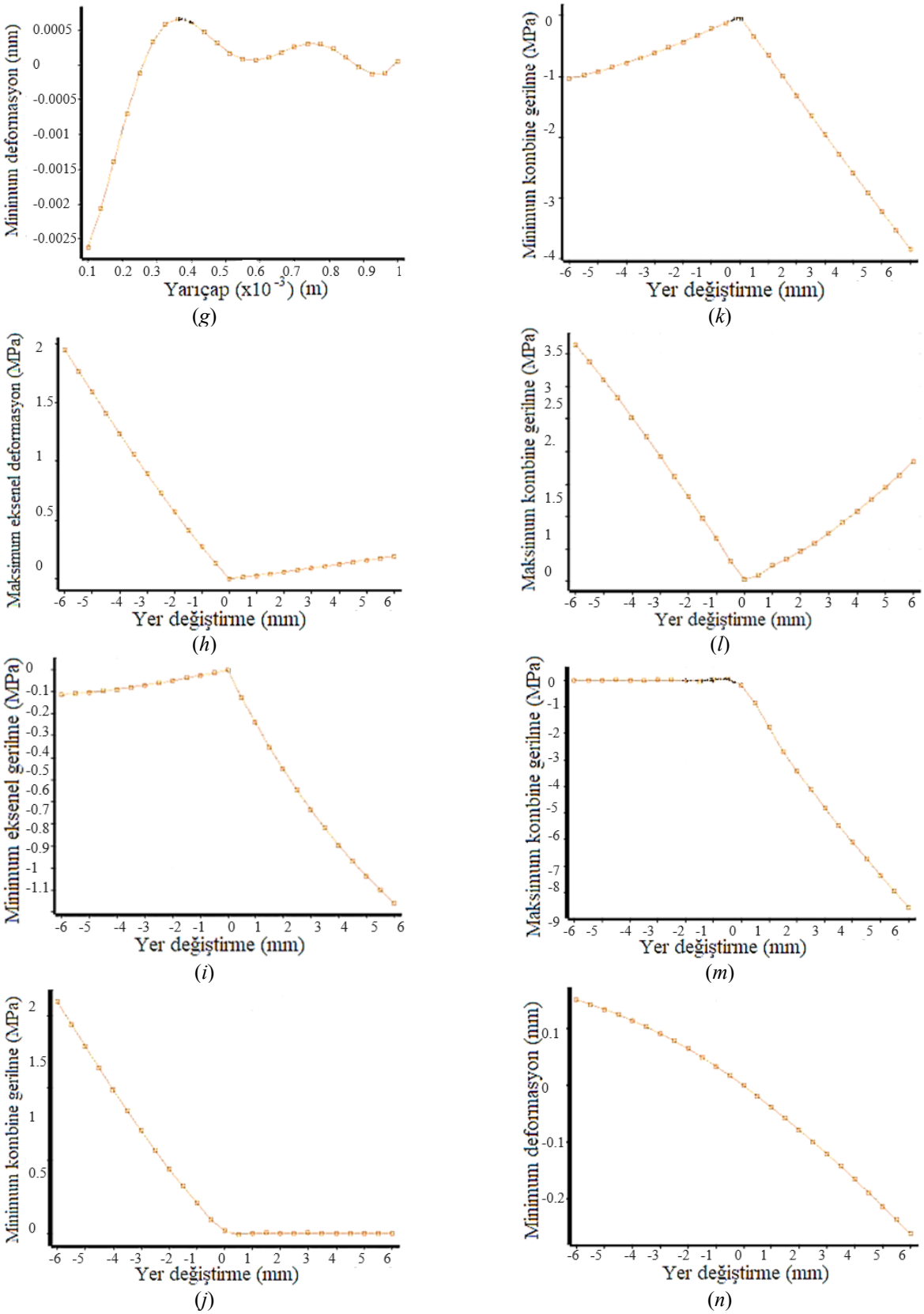

Şekil 6. Cevap yüzey fonksiyonundan elde edilen parametrik ilişkiler.

Şekil 6*a* ve 6*b*'de görüldüğü üzere yarıçap değeri 0,65 mm olduğunda gerilme değeri 80 MPa değerine ulaşmakta 0-0,65 mm aralığında yükselişte, 0,65-1 mm aralığında azalıştadır. Şekil 6*c*'de minimum kombine gerilmenin maksimum değeri görülmektedir. Yarıçap [0,1-1] mm arasında 160 MPa değerine ulaşmaktadır. Genel olarak arttığı görülmektedir. Şekil 6*d*'de minimum kombine gerilmenin minimum değerine ait eğri görülmektedir. Yarıçap değeri [0,1-0,45] mm arasında -100 MPa ile -450 MPa gerilme değişimine yol açmaktadır. [0,45-1] mm değerleri arasında yükseliş görülmektedir. Şekil 6*e*'de maksimum kombine gerilmenin maksimum değerine ilişkin grafik görülmektedir. Maksimum gerilme değeri 700 MPa olup başlangıçta artış izleyen bu değer 0,6 mm yarıçap değerinden sonra düşüşe başlamaktadır. Şekil 6*f*'de maksimum kombine gerilmenin minimum değerine ait grafik görülmektedir. Minimum gerilme değerinin -200 MPa değerine yaklaşmış olduğu görülmektedir. Şekil 6*g*'de minimum deformasyon değerinin 0,35 mm yarıçap değerine kadar bir artış izlediği daha sonra yavaş yavaş bir denge noktasına doğru dalgalanma yaptığı görülmektedir. Şekil 6*h* maksimum eksenel gerilme-yer değiştirme grafiğidir. Yer değiştirme -6 ile 6 mm arasında değişkenlik gösterirken, gerilme değeri -6 mm ile 0 mm arasında 2 MPa ile 0 MPa arasında düşüş göstermektedir. 0 mm ile 6 mm arasında gerilme yaklaşık olarak 0,25 MPa değerine kadar ulaşmaktadır. Şekil 6*i*'de minimum eksenel gerilme-yer değiştirme grafiği görülmektedir. Bir önceki grafiğin benzeridir. Şekil 6*j*'de minimum kombine gerilme-yer değiştirme grafiği ve Şekil 6*m*'de maksimum kombine gerilme-yer değiştirme grafiği görülmektedir. Minimum kombine gerilme grafiğinde -6 mm ile 0 mm arasında bir düşüş yaşanırken 0 mm ile 6 mm arasında gerilme değeri 0 MPa olarak sabit kaldığı görülmektedir. Maksimum kombine gerilme grafiği ise -6 mm ile 0 mm arasında sabit 0 MPa olarak sabit kalırken 0 mm ile 6 mm arasında -8 MPa değerine kadar düşüş olduğu görülmektedir. Şekil 6*k*'da minimum kombine gerilme-yer değiştirme ve Şekil 6*l*'de maksimum kombine gerilme–yer değiştirme grafikleri görülmektedir. Minimum kombine gerilme -6 mm ile 0 mm arasında -1 MPa ile 0 MPa arasında yükselmekte olup 0 mm ile 6 mm arasında -4 MPa değerine kadar düşüş görülmektedir. Maksimum kombine gerilme -6 mm ile 0 mm arasında 3,5 MPa ile 0 MPa arasında düşüş izlerken 0 mm ile 6 mm arasında 2 MPa değerine kadar yükseldiği görülmektedir. Şekil 6*n*'de minimum deformasyon-yer değiştirme grafiği görülmektedir. Eklsenel deformasyon -6 mm ile 6 mm arasında iken yanal deformasyon 0,2 mm ile -0,2 mm arasındadır. Gerilmelerdeki (-) işareti basma ve (+) ise çekme gerilmelerini ifade etmektedir.

Cevap yüzey fonksiyonunun iyilik derecesini ifade etmek için hata ölçütleri ve korelasyon katsayısı, determinant katsayısı kullanılmaktadır [17, 18]. Ek sık kullanılan hata ölçütleri şunlardır: MSE hataların karelerinin ortalaması, RMSE değeri MSE'nin karekökü, MAE mutlak hatanın ortalaması ve MAPE ise mutlak hatanın ortalamasının yüzdesidir. MSE (birim^2), RMSE (birim), MAE (birim) ve MAPE (birim) değerlerinin sıfıra yakın olması hata değerlerinin azlığını göstermektedir. Ayrıca regresyon analizleri de modellerin iyiliklerini belirleme araçlarından biridir. R^2 ise determinat katsayısı olup [1,-1] arasında değerler alabilmektedir, birimi yoktur. R (veya R^2) değerlerinin pozitif 1'e yakın olması, fonksiyon kestirimi ile ham veri arasında yüksek doğrusal bir ilişki olduğunu göstermektedir. Negatif 1'e yakın değerler yüksek doğrusal ters bir ilişki olduğunu göstermektedir. Sıfıra yakın değerler ise herhangi bir ilişki olmadığı anlamına gelmektedir. İyilik değerleri Çizelge 4'te verilmiştir. Çizelgeden görüleceği üzere oluşturulan cevap yüzey fonksiyonu, çok yüksek pozitif korelasyona sahiptir. Fonksiyon ile veri arasındaki hata ise oldukça ufaktır. Her iki durum da cevap yüzey fonksiyonunun tahminlerinin güvenilir olacağına işaret etmektedir [18].

Çizelge 4. Cevap yüzey fonksiyonunun iyiliği.

Parametreler	R^2	**RMSE (birim)**	**MAE (birim)**
Toplam deformasyon (mm)	0,99995	0,002395	8,5094e-3
Gerilme (MPa)	0,9999	70,097e-6	4,7587e-6

3.3. Optimum değerler

Optimizasyon modülü, Çizelge 5'te gösterildiği gibi üç optimumu, aday nokta olarak önermiştir.

Çizelge 5. Önerilen üç optimum aday nokta.

Değişkenler	Aday nokta 1	Aday nokta 2	Aday nokta 3
Yarıçap (mm)	0,99348	0,99331	0,99157
Eksenel yer değiştirme (mm)	-0,1068	-0,1142	-0,1195
Gerilme (MPa)	-282,23	-290,62	-299,92
Poisson oranı	-0,181	-0,181	-0,187
Yanal daralma (mm)	-0,0116	-0,0117	-0,012

Optimizasyon ile tespit edilen aday noktalar aslında cevap yüzeyindeki fonksiyon kullanılarak elde edilen değerlerdir. Ayrıca, simülasyonda yeniden analiz edilerek doğrulanmışlardır. Doğrulamaları Çizelge 6'da gösterilmiştir.

Çizelge 6. Aday noktaların doğrulanması.

Değişkenler	Aday nokta 1	Aday nokta 2	Aday nokta 3
Yarıçap (mm)	0,99348	0,99331	0,99157
Eksenel yer değiştirme (mm)	0,10688	0,11421	0,11959
Gerilme (MPa)	-208,02	-222,17	-232,33
Poisson oranı	-0,184	-0,186	-0,187
Yanal daralma (mm)	-0,0118	-0,0119	-0,012

Optimizasyonla hesaplanan geometrik boyutlar, mevcut geleneksel imalat makinelerinin tolerans aralığının dışında kalan 0,99157 mm gibi pek çok küsurat içermektedir. Bu nedenle bunların üretimi günümüz imalat yöntemleri ile mümkün değildir. Üretilebilir değerler, küsuratı azaltmak için boyutların üst değerlere yuvarlanmasıyla elde edilmektedir. Bu bağlamda 1 mm değerine sahip bir yarıçapın üretilmesi mümkündür. Doğrulanmış değerlerden üç numaralı aday seçilmiş ve bunların üretilebilir değerleri Çizelge 7'de verilmiştir. 3 numaralı aday ile 1 numaralı adayın hafiflik açısından bir farkı yoktur zira her ikisi de 1 mm yarıçapa sahiptir. Ancak 3 numaralı durumda -232.33 MPa değeri ile 1 numaradan daha fazla gerilme oluşmaktadır. Bu durumda 1 numaralı adayın seçilmesi beklenebilirdi. Bununla birlikte mutlak değerce daha büyük Poisson oranına sahip olan aday, 3 numaralı olandır. Daha büyük Poisson oranı, birbirine eşit şartlar altında, yapının daha fazla yanal daralma yapabileceğinin göstergesidir.

Çizelge 7. Doğrulanmış değerlerin üretilebilir değerleri.

Değişkenler	Aday nokta 3
Yarıçap (mm)	1
Eksenel yer değiştirme (mm)	0,11959
Gerilme (MPa)	-232,33
Poisson oranı	-0,187
Yanal daralma (mm)	-0,012

Bu değerle sahip kafes yapının eksenel yer değiştirmesi 0,11959 mm olduğunda yanal daralma değeri de 0,0041581 mm olmaktadır. Şekil 7 seçilen noktanın yeniden analiz edilmesiyle elde edilen deformasyon, gerilme sonuçlarını göstermektedir. Beklendiği gibi, ankastre mesnetlenen bölgede herhangi bir deformasyon yoktur. Ancak, yapının kenar kısımları maksimum deformasyona sahiptir. Maksimum gerilme 266,05 MPa olup 930 MPa olan akma dayanımının oldukça altındadır.

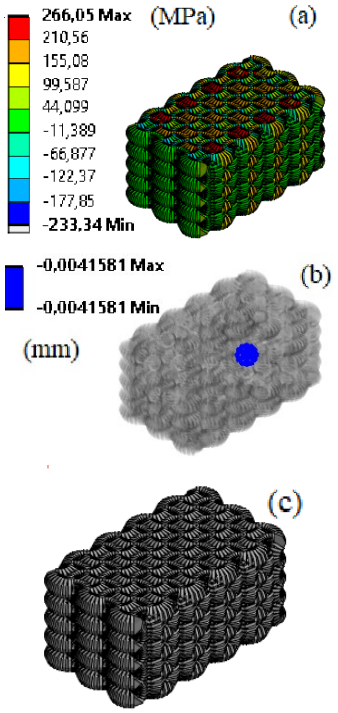

Şekil 7. (*a*) Seçilen noktalar için gerilme, (*b*) yanal deformasyon ve (*c*) ağ görüntüsü.

Şekil 8'de Spearman'ın korelasyon matrisi verilmiş olup parametreler arasındaki ilişkilerin tespiti için kullanılan bir araçtır. P5 (minimum kombine gerilmenin maksimumu), P8 (maksimum kombine gerilmenin minimumu) ve P12 (yanal daralma) kalınlıkları P13 (eksenel

yer değiştirme) ile ters orantılıdır. P5, P6, P7, P8, P12 ve P13 P11 ile aralarında bir orantı olmadığı görülmektedir. P3 (maksimum gerilme) ile P7 (maksimum kombine gerilmenin maksimumu) ve P4 (minimum gerilme) ile P6 (minimum kombine gerilmenin minimumu) arasında doğru orantı olduğu görülmektedir.

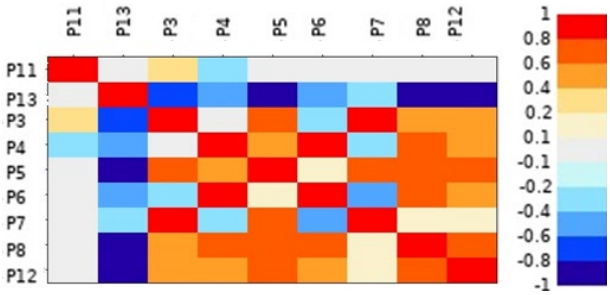

Şekil 8. Spearman'ın korelasyon matrisi, P3-maksimum gerilme, P11-yarıçap, P4- minimum gerilme, P12-yanal daralma, P5-minimum kombine gerilmenin maksimumu, P13-eksenel yer değiştirme, P6- minimum kombine gerilmenin minimumu, P7- maksimum kombine gerilmenin maksimumu, P8- maksimum kombine gerilmenin minimumu.

3.4. Tartışma

Bu çalışmada, eksenel yük uygulaması sonunda yapıda eğilme oluştuğu belirtilmiş ve eğilme nedeniyle oluşan çekme ve basma gerilmeleri hesaplanmıştır. Eksenel yük neticesinde yapıda eğilme oluşması hâli, Vigliotti ve Pasini (2013) tarafından da ifade edilmiştir [19]. Mikro boşlukların, kesitin atalet momentinde belirgin bir azaltma yapmadığı, ancak makro ölçekte malzemenin akma mukavemetini azaltan gerilme yığılmaları ürettiğini raporlamışlardır. Gülcan vd. (2021) kiral kafes yapı tasarımında topoloji optimizasyon yöntemlerinin verimli bir şekilde kullanıldığına dikkat çekmektedir [20]. 3 × 3 × 3 (20 mm × 20 mm × 20 mm) dizi desenine sahip basit kübik, oktahedron, kesik küp ve kesik oktahedron tabanlı kafes yapıların en iyi eksenel basınç dayanımı özelliklerini gösterdiği ifade edilmiştir [21-22]. Bu bağlamda mevcut çalışmada sunulan 9×4×5 kafes yapısı optimum şekle sahip değildir. Ancak ultra hafiflik açısından dikkate değer hafifliğe sahiptir. 3 × 3 × 3 dizilimdeki titanyum alaşımından yapılan kafes yapıdan (Ti-6Al-4V) 1125.0 MPa akma dayanımı, 1200.0 MPa çekme dayanımı ve 0.34 Poisson oranı elde edilmiştir [21].

Uçaklardaki geleneksel taban-kanat tasarımına kıyasla kafes dolgulu tasarımlarda önemli bir ağırlık azalması rapor edilmiştir. Geleneksel kanada kıyasla tüm kafes yapılar arasında en yüksek ağırlık tasarrufu %9,5 ile Kelvin yapısı sağlamıştır [23]. Mevcut çalışmada ise 4,094 g başlangıç kütlesi 0,4549 g kütleye inerek %900 ağırlık azaltımı sağlamıştır. Kiral kafesler ultra hafiflik avantajlarıyla dikkat çekmektedir.

4. SONUÇLAR

Bu çalışmada kübik birim hücreye sahip bir kiral kafes yapının tasarımı ve optimizasyonu gerçekleştirilmiştir. Sonuçta ulaşılan temel çıkarımlar aşağıdaki gibidir:

- Kafes boyutları, genetik algoritma yöntemi kullanılarak deformasyonu artırmak ve dayanım sınırını aşmamak için optimize edilmiştir. Optimum değerler ile yapılan analiz sonunda, yapının ayrıt kesitinin yarıçapı 1 mm olduğunda yapı 0,12 mm yer değiştirmeye dayanmaktadır. Bu durumda yapı içerisinde 266,05 MPa değerinde çekme ve 233,34 MPa değerinde basma gerilmeleri oluşmaktadır. Bu değerler yapının akma dayanımının altındadır.
- Başlangıçta 4,094 g olan kütle, optimizasyon neticesinde 0,45489 g değerine düşmektedir. Daha küçük ve daha hafif yapı, daha düşük enerji tüketimi açısından tercih edilmektedir. Oldukça hafif ve dayanaklı bir yapı elde edilmiştir. Kullanılacak olan malzemenin hacmi az olduğundan maliyet açısından bu yapı geleneksel malzemelere iyi bir alternatiftir.
- Cevap yüzey fonksiyonu sayesinde tasarımda kullanılan değişkenlerin birbirleri ile olan ilişkileri tespit edilmiştir.
- Müteakip çalışma olarak yapının titreşim cevabının elde edilmesine yönelik serbest ve zorlanmış titreşim analizlerinin yapılması mümkündür.

ÇIKAR ÇATIŞMASI BEYANI

Yazarlar arasında çıkar çatışması bulunmamaktadır.

TEŞEKKÜR

Bu çalışmanın inceleme ve değerlendirme aşamasında yapmış oldukları değerli katkılardan dolayı editör, hakem ve emeği geçenlere içten teşekkür ederim.

YAZARLARIN KATKILARI

Y. B.: Kavramsallaştırma, yöntem, yazılım, doğrulama, formel analiz, araştırma, kaynaklar, yazı yazma - orijinal taslak hazırlama.
İ.K.: Yöntem, yazılım, doğrulama, araştırma, kaynaklar, yazı yazma - gözden geçirme ve düzenleme.

REKABETÇİ MENFAAT BEYANI

Yazarlar rakip bir finansal çıkar beyan etmemektedir.

FİNANSMAN KAYNAKLARI

Bu araştırma, kamu, ticari veya kâr amacı gütmeyen sektörlerdeki finansman kuruluşlarından herhangi bir özel hibe almamıştır.

KAYNAKLAR

1. Merriam Webster, "chiral", in Merriam Webster America, Encyclopaedia Britannica, 2024.

2. Darroudi, M., Nazari, S. E., Kesharwani, P., Rezayi, M., Khazaei, M., and Sahebkar, A., "Background of carbon nanotubes for drug delivery systems", in Emerging Applications of Carbon Nanotubes in Drug and Gene Delivery, Woodhead Publishing Series in Biomaterials, Pages 1-35, Woodhead Publishing, Sawston, Cambridge, 2023.

3. Abdeljaber, O., Avci, O., Inman, D. J., "Optimization of chiral lattice based metastructures for broadband vibration suppression using genetic algorithms", Journal of Sound and Vibration, Vol. 369, Issue 50, Pages 13-44, 2016.

4. Bakir, D., and Savaş, S., "Çarpma yükü etkisinde sandviç plakların şekil optimizasyonu", Bitlis Eren Üniversitesi Fen Bilimleri Dergisi, Cilt 10, Sayı 1, Sayfa 113-127, 2021.

5. Toğan, V., DaloğLu, A., "Genetik algoritma ile üç boyutlu kafes sistemlerin şekil ve boyut optimizasyonu", Teknik Dergi, Cilt 17, Sayı 82, Sayfa 3809-3824, 2006.

6. Doğanalp, S., Turgut, B., "Statik ve kinematik modelde deformasyon analizi", Selçuk Üniversitesi Mühendislik, Bilim ve Teknoloji Dergisi, Cilt 24, Sayı 2, Sayfa 31-49, 2009.

7. Küçükönder, M., Uçar, M., "Üretim etkinliğinde simülasyon", Kahramanmaraş Sütçü İmam Üniversitesi İktisadi ve İdari Bilimler Fakültesi Dergisi, Cilt 5, Sayı 1, Sayı 117-129, 2015.

8. Erdem, M., Gök, K., Tümsek, M., Gök, A., "Bir bisiklet gövdesinin sonlu elemanlar yöntemiyle statik analizi", Bilecik Şeyh Edebali Üniversitesi Fen Bilimleri Dergisi, Cilt 6, Sayı 2, Sayı 605-632, 2019.

9. Ha, C. S., Plesha, M. E., Lakes, R. S., "Chiral three-dimensional lattices with tunable Poisson's ratio", Smart Materials and Structures, Vol 25, Issue 5, Pages 054005-050076, 2016.

10. Barad, R. S., Nagesh, B. K., Barad, S., Suresh, T. N., "Influence of chiral lattice on modal characteristics of structures", in Gullapalli Sivaramakrishna, S. Kishore Kumar and B. N. Raghunandan Singapore, editors, Proceedings of the National Aerospace Propulsion Conference, Springer Nature Pages 209-230, Singapore, 2023.

11. Körner, C., Liebold-Ribeiro, Y., "A systematic approach to identify cellular auxetic materials", Smart Materials and Structures, Vol. 24, Issue 1, 2015.

12. Warmuth, F., Körner, C., "Phononic band gaps in 2D quadratic and 3D cubic cellular structures", Materials (Basel), Vol. 8, Issue 12, Pages 8327-8353, 2015.

13. Wormser, M., Warmuth, F., Körner, C., "Evolution of full phononic band gaps in periodic cellular structures", Applied Physics A, Vol. 123, Issue 10, Pages 661-689, 2017.

14. Warmuth, F., Osmanlic, F., Adler, L., Lodes, M. A., Körner, C., "Fabrication and characterisation of a fully auxetic 3D lattice structure via selective electron beam melting", Smart Materials and Structures, Vol. 26, Issue 2, Pages 025013-025056, 2017.

15. Ansys, "Theory Manual Version 9.0", Canonsburg, PA, USA., ANSYS Inc., 2004.

16. Korkmaz, C., Kacar, İ., "Hesaplamalı akışkanlar dinamiği simülasyonları için optimum ağ elemanı yapısının belirlenmesi", In Osman Gökdoğan Deniz Yılmaz, Önder Uysal, Mehmet Emin Gökduman, Ahmet Süslü editörler, Tarımsal mekanizasyon ve enerji üzerine güncel araştırmalar, Sayfa 109-125, Akademisyen Yayinevi, Ankara, 2021.

17. Kacar, İ., Korkmaz, C., "Determination of drying kinetics of a N25P5K5 type new generation plant food by regression and machine learning methods", Cukurova University Journal of the Faculty of Engineering, Vol. 37, Issue 4, Pages 989-1024, 2022.

18. Kacar, İ., Korkmaz, C., "Prediction of agricultural drying using multi-layer perceptron network, long short-term memory network and regression methods", Gümüşhane University Journal

of Science and Technology Institute, Vol 12, Issue 4, Pages 1188-1205, 2022.

19. Vigliotti, A., Pasini, D., "Mechanical properties of hierarchical lattices", Mechanics of Materials, Vol. 62, Pages 32-43, 2013.

20. Gülcan, O., Simsek, U., Kavas, B., "Eklemeli İmalatla üretilen işlevsel olarak derecelendirilmiş metal yapılar", Mühendis ve Makina, Cilt. 62, Sayı 702, Sayfa 1-12, 2021.

21. Park, K.-M., Min, K.-S., Roh, Y.-S., "Design optimization of lattice structures under compression: study of unit cell types and cell arrangements", Materials, Vol. 15, Issue 1, Pages 97-102, 2022.

22. Fernandes, R. R., Tamijani, A. Y., "Design optimization of lattice structures with stress constraints", Materials and Design, Vol. 210, Issue 110026, 2021.

23. Khan, N., Acanfora, V., "Non-Conventional wing structure design with lattice infilled through design for additive manufacturing", Vol. 17, Issue 7, Pages 1470-1478, 2024.

ULUSLARARASI 3B YAZICI TEKNOLOJİLERİ
VE DİJİTAL ENDÜSTRİ DERGİSİ

INTERNATIONAL JOURNAL OF 3D PRINTING
TECHNOLOGIES AND DIGITAL INDUSTRY

ISSN:2602-3350 (Online)

URL: https://dergipark.org.tr/ij3dptdi

DEVELOPMENT OF PREDICTION MODELS FOR COMPRESSIVE STRENGTH IN CEMENT MORTAR WITH BENTONITE USING MACHINE LEARNING TECHNIQUES

Yazarlar (Authors): Yusuf Tahir Altuncı, Kemal Saplıoğlu

Bu makaleye şu şekilde atıfta bulunabilirsiniz (To cite to this article): *Altuncı Y. T., Saplıoğlu K., "Development of Prediction Models for Compressive Strength in Cement Mortar with Bentonite Using Machine Learning Techniques" Int. J. of 3D Printing Tech. Dig. Ind., 8(2): 214-224, (2024).*

DOI: 10.46519/ij3dptdi.1469238

Araştırma Makale/ Research Article

Erişim Linki: (To link to this article): https://dergipark.org.tr/en/pub/ij3dptdi/archive

DEVELOPMENT OF PREDICTION MODELS FOR COMPRESSIVE STRENGTH IN CEMENT MORTAR WITH BENTONITE USING MACHINE LEARNING TECHNIQUES

Yusuf Tahir Altuncı[a]*, Kemal Saplıoğlu[b]

[a]Isparta University of Applied Sciences, Vocational School of Techn. Sciences, Constr. Techn. Dept., TURKEY
[b] Süleyman Demirel University, Faculty of Engr. and Natural Sciences, Dept. of Civil Engr., TURKEY

* *Corresponding Author: yusufaltunci@isparta.edu.tr*

(**Received:** 16.04.2024; **Revised:** 09.06.2024; **Accepted:** 06.07.2024)

ABSTRACT

In this study, the effects of bentonite-substituted cement mortar, cement compressive strength, cement quantity, spread values, water absorption percentages by weight, and porosity values on the 28-day compressive strength were investigated using Multiple Regression, Adaptive Neuro-Fuzzy Inference System and the intuitive optimization method known as Particle Swarm Optimization. Based on the results obtained from 18 data points, with 4 of them used for testing and 14 for training, effective and ineffective input parameters were identified in comparison to Multiple Regression. Subsequently, Particle Swarm Optimization and Adaptive Neuro-Fuzzy Inference System main models were designed according to the obtained results. As a result of the study, it was determined that cement compressive strength, cement quantity and water absorption parameters have a higher impact on compressive strength compared to other parameters. It was found that the best accuracy model was achieved with the Particle Swarm Optimization model, and the results of the Multiple Regression model can also be used in predicting outcomes.

Keywords: Bentonite-Substituted Cement Mortar, Cement Compressive Strength, Multiple Regression, Particle Swarm Optimization.

1. INTRODUCTION

Due to its porous structure, concrete absorbs water, leading to permeability within the concrete. Various mineral and chemical additives are used to mitigate the water permeability of concrete. One of these mineral additives is bentonite. Bentonite is a type of montmorillonite mineral formed through the weathering of volcanic ash deposits over millions of years [1]. Bentonites are classified into three groups: sodium bentonite, calcium bentonite, and active sodium-calcium Bentonite [2]. Bentonite finds applications in civil engineering, pelletizing iron ores, clarifying wine and fruit juices, animal feed, pharmaceuticals, rubber industry, paper industry, ceramic industry, petroleum refining, wastewater treatment, paint industry, fire extinguishers, fertilizer production, soil improvement, and drilling operations. One of the most significant characteristics of bentonite is its high silica content, which imparts its binding properties.

When bentonite undergoes hydration, it swells, creating a gel-like structure, and this condition imparts excellent water absorption and water retention properties to Bentonite [3]. Due to this property, bentonite can be used in the construction industry to create impermeable surfaces. Yang et al. [1], observed that by substituting natural sodium bentonite at a rate of 8% by weight in cement, after drying it in an oven at 105°C for 6 hours, it exhibited superior performance in terms of compressive strength, flexural strength, and impermeability compared to the reference sample. Wei et al. [4], have indicated that metakaolin and bentonite-substituted cements can effectively reduce concrete deterioration caused by ASR (Alkali-Silica Reaction). Memon et al. [5], found that bentonite-substituted cements perform effectively on surfaces exposed to acidity.

In addition, there is a need for the use of applications that predict concrete properties to ensure the safe utilization of materials incorporated into concrete mixtures [6]. In the literature, various studies exist where concrete's compressive strength [6–11], flexural strength [12], service life [13], workability [14] and creep behavior [15] have been predicted using different methods.

The most common methods among these include ANN (Artificial Neural Network) [16–30], SVM (Support Vector Machine) [31–37], GPR (Gaussian Process Regression) [38–44], RSM (Response Surface Methodology) [16, 18, 45], ANFIS (Adaptive Neuro-Fuzzy Inference System) [46–55] FL **(**Fuzzy Logic) [56–65] and also statistical methods such as [7, 32, 53, 66–72] and others.

In this context, the mechanical property of compressive strength of bentonite-substituted cement mortar was attempted to be determined in the study. Parameters such as cement type and substitution rate, as well as fresh property represented by the spread diameter and physical properties including hardened density, porosity, and water absorption by weight were considered. Among these properties, the significant ones were identified, and models were created using both these significant properties and all the properties combined. Models used for prediction were generated using MR (Multiple Regression), ANFIS, and the heuristic optimization method known as PSO (Particle Swarm Optimization). The prediction values obtained from these models were compared using R^2 and RMS (Root Mean Square), and the model that predicted the compressive strength of bentonite-substituted cement mortar without conducting destructive testing such as a compressive strength test was determined.

2. MATERIAL AND METHOD

2.1. Material

In the study, materials such as water, CEN standard sand, and cement types CEM I 42.5 R and CEM I 52.5 R, along with the cement substitute material bentonite, were used. The bentonites used in the preparation of bentonite-substituted cement mortar samples were ground and sieved. In order to determine the physical properties of the mixtures, sieve analysis, specific gravity, and specific surface area (Blaine fineness) tests were conducted according to the EN 196-6 standard. Subsequently, chemical analyses were carried out. Chemical data for the binding materials used in cement production are provided in Table 1, while physical data can be found in Table 2.

Table 1. Chemical properties of binding materials

Components	CEM I 42.5 R (%)	CEM I 52.5 R (%)	Bentonite (%)
SiO_2 (S)	21.12	20.57	63.2
Al_2O_3 (A)	6.03	4,6	14.27
Fe_2O_3 (F)	3.2	2.5	0,55
CaO	62.11	64.8	3.91
MgO	2.2	1.28	4.02
SO_3	2.69	3.25	-
Na_2O	0.35	0.21	0.17
K_2O	1.1	0.36	0,61
Cl^-	0.0068	0.01	-
TiO_2	-	-	0.03
LOI	2.79	3.18	14.46
S+A+F	30.35	27.67	78.02

Table 2. Physical properties of binding materials

Materials	Grain size (plus sieve) >40μm	>90μm (%)	Specific gravity (g/cm^3)	Specific surface (Blaine) (cm^2/g)
CEMI 42.5	15.6	7.9	3.08	3526
CEMI 52.5	1	0.1	3.11	4480
Bentonite	1.2	0.1	2.80	4700

Bentonite was substituted in bentonite-substituted cement mortar in proportions of 0%, 2.5%, 5%, 7.5%, 10%, 12.5%, 15%, 17.5%, 20%, 22.5%, 25%, 27.5%, and 30%, instead of CEM I 42.5 R and CEM I 52.5 R type cements. The codes and mixture information of bentonite-substituted cement mortar samples are provided in Table 3.

Table 3. Codes and mixture ınformation of mortar samples

Mixture code	Water (g)	CEM I 42.5 (g)	CEM I 52.5 (g)	Bentonite (g)	Standard sand (g)
A0		450.00	-	-	
A2.5		438.75	-	11.25	
A5		427.50	-	22.50	
A7.5		416.25	-	33.75	
A10		405.00	-	45.00	
A12.5		393.75	-	56.25	
A15		382.50	-	67.50	
A17.5		371.25	-	78.75	
A20	225.00	360.00	-	90.00	1350.00
B0		-	450.00	-	
B2.5		-	438.75	11.25	
B5		-	427.50	22.50	
B7.5		-	416.25	33.75	
B10		-	405.00	45.00	
B12.5		-	393.75	56.25	
B15		-	382.50	67.50	
B17.5		-	371.25	78.75	
B20		-	360.00	90.00	

The statistical analysis of the training parameters used in the model is provided in Table 4, while the statistical analysis of the test parameters used in the model is presented in Table 5.

Table 4. Statistical analysis of the training parameters used in the model

	Cement strength (MPa)	Cement amount (g)	Spread (cm)	Water absorption (%)	Porosity (%)	Density (g/cm^3)	Compressive strength (MPa)
Average	47,50	405,00	16,72	7,70	15,20	2,17	49,38
Standard error	1,39	8,75	0,19	0,16	0,31	0,00	1,53
Median	47,50	405,00	16,60	7,67	15,21	2,17	49,95
Standard deviation	5,19	32,72	0,72	0,60	1,18	0,01	5,73
Sample variance	26,92	1070,91	0,52	0,35	1,38	0,00	32,87
Kurtosis	-2,36	-1,48	0,24	-0,76	-1,62	-0,63	-0,75
Skewness	0,00	0,00	0,88	0,45	0,09	-0,08	-0,35
Range	10,00	90,00	2,41	1,87	3,37	0,04	17,95
Minimum	42,50	360,00	15,80	6,95	13,62	2,15	39,20
Maximum	52,50	450,00	18,21	8,82	16,99	2,19	57,15
Confidence level (95,0%)	3,00	18,89	0,42	0,34	0,68	0,01	3,31

Table 5. Statistical analysis of the test parameters used in the model

	Cement strength (MPa)	Cement amount (g)	Spread (cm)	Water absorption (%)	Porosity (%)	Density (g/cm^3)	Compressive strength (MPa)
Average	47,50	405,00	16,58	7,61	15,33	2,17	49,81
Standard error	2,89	10,27	0,21	0,21	0,54	0,01	2,99
Median	47,50	405,00	16,55	7,57	15,41	2,17	49,91
Standard deviation	5,77	20,54	0,41	0,42	1,09	0,02	5,97
Sample variance	33,33	421,88	0,17	0,18	1,19	0,00	35,66
Kurtosis	-6,00	-3,30	1,28	0,56	-0,95	-3,90	-3,79
Skewness	0,00	0,00	0,36	0,57	-0,34	-0,37	-0,06
Range	10,00	45,00	1,00	1,01	2,53	0,03	12,84
Minimum	42,50	382,50	16,10	7,15	13,99	2,15	43,28
Maximum	52,50	427,50	17,10	8,16	16,52	2,18	56,12
Confidence level (95,0%)	9,19	32,68	0,65	0,68	1,73	0,02	9,50

2.2. Methods

2.2.1. Production Method

In the Hobart mixer's bowl, water, binding material (cement with bentonite admixture), and CEN standard sand were sequentially added, and the device was operated until the mixture became homogeneous. Then, the device was stopped, and the portion that was not well mixed under the bowl and adhered to the mixer blade was scraped into the bowl to ensure homogeneity. The mixture was then operated for a sufficient duration. After the mortar was subjected to the spread test, hardened mortar specimens were produced in 4x4x16 cm molds. The specimens were removed from the molds 24 hours after production and placed in a curing tank. After a curing period of 28 days, physical tests (water absorption, porosity, and density) and mechanical tests (compressive strength) of the specimens were completed.

2.2.2. Multiple Regression

MR is used to predict or model a dependent variable (output) using one or more independent variables (input).

MR is expressed as a linear function, as specified in Equation 1 [73]. (In the equation; Y represents the dependent variable, A represents the constant coefficient, B represents the regression coefficients, X represents the independent variables, and n represents the number of inputs.)

$$Y = A + B_1X_1 + B_2X_2 + B_3X_3 + \ldots + B_nX_n \quad (1)$$

2.2.3. Particle Swarm Optimization

PSO is a metaheuristic optimization algorithm used for the purpose of optimizing a problem, based on the movement of birds flying in flocks. In PSO, the position of each particle in the swarm (Equation 2), the velocity of each particle in the swarm (Equation 3), and the velocities of all particles are updated based on their fitness within the boundary values of particles (Equation 4) (Equation 5). The obtained velocity is then updated by adding it to the previous particle position (Equation 6), and in this way, an optimization algorithm is formed [74]. (In the equations, the symbol X_{id} represents the position, V_{id} represents the velocity, W represents the inertia weight, and C_1 and C_2 represent the scaling factors.)

$$\begin{matrix} X_{11}' & X_{12}' & X_{1n}' \\ X_{m1} & X_{m2} & X_{mn} \end{matrix} \quad (2)$$

$$\begin{matrix} V_{11}' & V_{12}' & V_{1n}' \\ V_{m1} & V_{m2} & V_{mn} \end{matrix} \quad (3)$$

$$\begin{pmatrix} f(1) = & f(X_{11}, X_{12} \ldots\ldots X_{1n}) \\ f(m) = & f(X_{m1}, X_{m2} \ldots X_{mn}) \end{pmatrix} \quad (4)$$

$$V_{id} = W * V_{id} + C_1\, x\, rand * (pbest_{id} - X_{id}) + C_2 * rand * (gbest - X_{id}) \quad (5)$$

$$X_{id} = X_{id} * V_{id} \quad (6)$$

2.2.4. Adaptive Neuro-Fuzzy Inference System

ANFIS is an artificial intelligence model designed for solving prediction problems by combining fuzzy logic and artificial neural networks, enabling data-driven and optimized inference.

The ANFIS model consists of five layers (fuzzification rule normalization fuzzyfication sum) and If-then rules are applied as in Equation 7 and Equation 8 [75-78]. (In the equations, the symbols x and y represent input parameters, A_1, A_2, B_1, and B_2 represent fuzzy sets, p_1, p_2, q_1, q_2, r_1, and r_2 represent output parameters, and f represents the output parameter of the ANFIS model.)

$$Rule\ 1: if\ x\ is\ A_1\ and\ y\ is\ B_1, then\ f_1 = p_{1x} + q_{1y} + r_1 \quad (7)$$

$$Rule\ 2: if\ x\ is\ A_2\ and\ y\ is\ B_2, then\ f_2 = p_{2x} + q_{2y} + r_2 \quad (8)$$

2.2.5. The Wilcoxon Test

The Wilcoxon test is a statistical method used to compare data when the normal distribution assumption is not met or when the data does not follow a normal distribution. To achieve this objective, the absolute values are computed using Equation (10), while the discrepancies between quasi-observations are determined based on Equation (9) [79]. T^+ represents the sum of rows marked with plus signs, while T^- represents the sum of rows marked with minus signs (Equation 11) [80].

$$D_i = X_i - Y_i \quad (9)$$

$$|D_i| = |X_i - Y_i| \quad (10)$$

$$T = T^+ - T^- \quad (11)$$

The difference between the first half of the data, Xi, and the second half, Yi, is represented by the value Di, which serves as the test statistic for Wilcoxon, defining the trend conditions, indicated by Zw Zα/2 value in Equation (12) (for two tails) [80]. The numerical mean is denoted by μT, and the standard deviation is denoted by μT, both assumed to be zero [81]. $T^+ = T^-$, indicating that the amount of difference between trial outcomes, both good and bad, is equal [80].

$$Z_W = \frac{T-\mu_T}{\sigma_T} = \frac{T}{\sigma_T} \quad (12)$$

3. RESULTS AND DISCUSSION

In the experimental results, out of the 18 values obtained from the samples, four were set aside for testing, and the remaining 14 were used for training. In the study, first, an MR model was created. Based on the results obtained from this model, PSO and ANFIS main models were designed.

Based on the available training data, an MR model was constructed, and adjusted R^2 values were examined at each stage (Table 6). Consequently, effective and ineffective input parameters were determined relative to MR. While R^2 values may increase with each new parameter, adjusted R^2 values can remain constant or decrease. Parameters associated with a constant or decreasing value can be considered as having no effect. In this study, based on this analysis, both MR, ANFIS, and PSO models including all input parameters were created, and models excluding parameters based on adjusted R^2 values were also constructed. In a single-input, single-output model, the input parameter was chosen as cement strength, and an adjusted R^2 value of 0.598 was found. Then, when the cement quantity was added, it was observed that this value increased to 0.983. However, with the addition of the third parameter, due to the decrease in the adjusted R^2 value to 0.982, it was determined that the spread table value might not be used in the model. The water absorption value was introduced in the fourth step, and because it raised the value to 0.989, it was concluded that this parameter is significant. Subsequently, the inclusion of porosity and density in the following step was found to have no effect on the results.

Table 6. The contributions of the parameters included in the model to R^2 and adjusted R^2

Model	Added	R^2	adjusted R^2
Cement strength	Cement strength	0.629	0.598
Cement strength + cement amount	Cement amount	0.986	0.983
Cement strength + cement amount + spread	Spread	0.986	0.982
Cement strength + cement amount + spread + water absorption	Water absorption	0.993	0.989
Cement strength + cement amount + spread + water absorption + porosity	Porosity	0.993	0.988
Cement strength + cement amount + spread + water absorption + porosity + density	Density	0.993	0.987

Due to the results of the adjusted R^2 values, it was determined that cement strength, cement quantity, and water absorption were more important among the 6 input parameters. Therefore, in both MR, PSO, and ANFIS, models were created with both 6-parameters and 3-parameters. The formulas for the models created with MR were determined as shown in Equation 13 and Equation 14.

$$BD = 0.714X_1 + 0.019X_2 - 0.126X_3 - 4.138X_4 - 0.273X_5 + 26.127X_6 - 17.88 \quad (13)$$

$$BD = 0.789X_1 + 0.034X_2 - 4.032X_4 + 29.004 \quad (14)$$

Table 7. The comparison of MR models

Model	Training R^2	Error (%)	Test R^2	Error (%)
3-parameter MR	0.9925	0.84	0.9987	0.88
6-parameter MR	0.9881	2.62	0.9931	2.36

When examining the R^2 values and error values in both models, it was observed that the 3-parameter regression model yielded better results (Table 7). As seen in this model as well, instead of using all available parameters in the model, conducting a preliminary evaluation to identify effective parameters is crucial.

In the second part of the study, models created with PSO were developed. In these models, a six-input model was used, and a three-input model was created based on the adjusted R^2 value (Equation 15-16).

$$BD = 0.838X_1 + 0.059X_2 - 0.298X_3 - 3.11X_4 + 0.085X_5 + 3.76X_6 + 4.85 \quad (15)$$

$$BD = 0.79X_1 + 0.033X_2 - 4.189X_4 + 29.294 \quad (16)$$

Table 8. The comparison of PSO models

Model	Training R^2	Error (%)	Test R^2	Error (%)
3-parameter PSO	0.9925	0.75	0.9987	0.78
6-parameter PSO	0.9925	0.84	0.9931	0.85

When Table 8 is examined, it is observed that there is not a significant difference between both the 3-parameter and 6-parameter PSO models. Therefore, it is considered that both models can be used. The proximity of the results indicates that predictions can be made with fewer parameters, which is important both in terms of time and cost.

Finally, in the study, ANFIS models were constructed by varying the cluster numbers of input parameters, and these models are summarized in Table 9. In addition to the 6-parameter models for ANFIS, 3-parameter models were also constructed (determined based on adjusted R^2 values in MR). A common characteristic of all ANFIS models is that the training results come out close to perfection. However, in the test results, it has been revealed that most ANFIS models tend to memorize and cannot generalize. In ANFIS models, having a large number of subsets and parameters does not necessarily imply a more accurate model. In the study, it is important to identify the ideal parameters and models divided into subsets. It can be said that in the study, the model with 2-4-3 subsets, using cement strength, cement quantity, and water absorption parameters in that order, is the most suitable among ANFIS models.

Table 9. The comparison of ANFIS models

Number of clusters	Training R^2	Error (%)	Test R^2	Error (%)
2,3,3	1	0.0005	0.8213	3.7063
2,3,4	1	0.0002	0.5899	6.6289
2,3,5	1	0.0002	0.6729	14.9330
2,4,3	1	0.0002	0.9946	2.4057
2,4,4	1	0.0002	0.7800	5.0333
2,4,5	1	0.0001	0.7383	10.4069
2,5,3	1	0.0001	0.4493	9,7674
2,5,4	1	0.0001	0.1302	13,4016
2,5,5	1	0.0001	0.1847	25,0392
2,7,7	1	0.0001	0.1045	66.4502
2,3,4,3,3,3	1	0.0005	0.3019	15.3642
2,3,5,3,3,4	1	0.0005	0.3019	15.3642
2,4,3,3,3,5	1	0.0004	0.8279	15.1278
2,5,4,3,3,3	1	0.0005	0.1439	23.0605

In the study, the best results obtained in all models were compared in Table 10 and Figure 1. When examining the results, it is observed that the 3-parameter PSO model is better than all other models, but it is also possible to achieve very close results when the MR model is used. The results of the ANFIS model also approach the truth (Figure 1), but it is seen that there is a significant deviation when the correct ANFIS model cannot be established (Table 9). In addition, Wilcoxon values were also examined for the best results of each model in Table 10. According to these values, all results were found to be significant.

Table 10. The comparison of the best models

Model	Training R^2	Error (%)	Z_W	Test R^2	Error (%)	Z_W
3-parameter MR	0.9925	0.84	-1.16	0.9987	0.88	-0.73
3-parameter PSO	0.9925	0.75	-0.09	0.9987	0.78	0.01
ANFIS (2,4,3)	1	0.0002	-1.44	0.9946	2.4057	-1.83

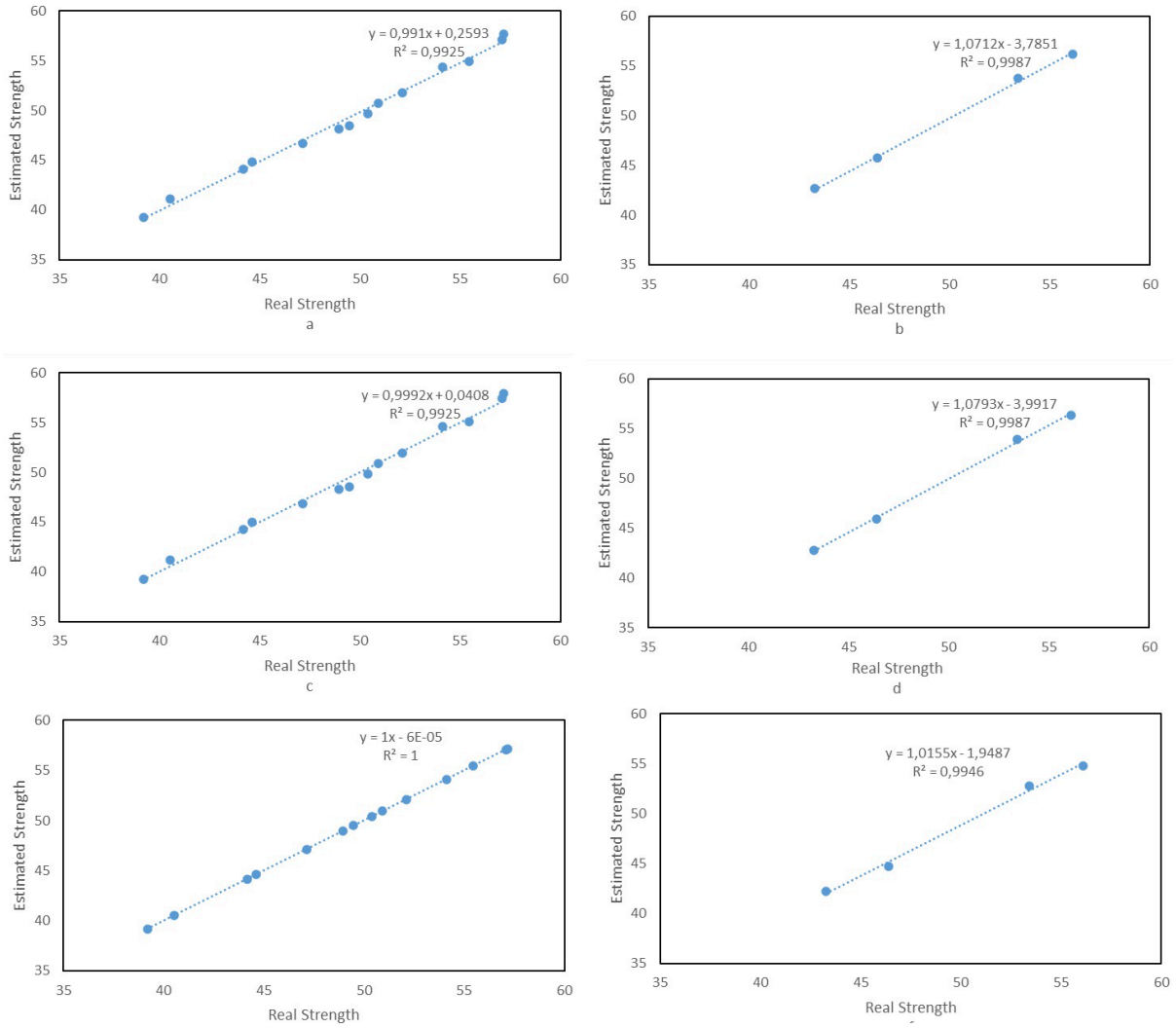

Figure 1. Comparison of scatter plots of prediction models (a-3-parameter MR training b-3-parameter MR test c-3-parameter PSO training d-3-parameter PSO test e-ANFIS (2-4-3) training f-ANFIS (2-4-3) test)

4. CONCLUSION

In this study, three models, namely MR, ANFIS, and PSO were employed to predict the compressive strength of bentonite-substituted cement mortar. The input parameters used in the models were cement strength, cement quantity, spread, water absorption, porosity, and density. The results obtained from the models indicated that both PSO and MR models could be used to predict the outcomes. However, it can be stated that cement strength, cement quantity, and water absorption parameters have a greater influence on compressive strength compared to other parameters. The results also demonstrated that PSO provided the highest accuracy in predicting the compressive strength of bentonite-substituted cement mortar. The developed PSO model can serve as a valuable database to facilitate the design of cement mortar mixtures.

Acknowledgement
ChatGPT 3.5 was utilized for translating the manuscript into English and for proofreading.

REFERENCES

1. Yang, H., Long, D., Zhenyu, L., et al. 'Effects of bentonite on pore structure and permeability of cement mortar', Constr Build Mater., Vol. 224, Pages 276-283, 2019.

2. Muhammad, N. and Siddiqua, S., 'Calcium bentonite vs sodium bentonite: The potential of calcium bentonite for soil foundation', Mater Today Proc., Vol. 48, Pages 822-827, 2022.

3. Dimirkou, A., Ioannou, A. and Doula, M., 'Preparation, characterization and sorption properties for phosphates of hematite, bentonite and bentonite–hematite systems', Adv Colloid Interface Sci., Vol. 97, Issue 1-3, Pages 37-61, 2002.

4. Wei, J., Gencturk, B., Jain, A. ans Hanifehzadeh, M., 'Mitigating alkali-silica reaction induced concrete degradation through cement substitution by metakaolin and bentonite', Appl Clay Sci., Vol. 182, Pages 105257, 2019.

5. Memon, S. A., Arsalan, R., Khan, S. and Lo, T. Y., 'Utilization of Pakistani bentonite as partial replacement of cement in concrete', Constr Build Mater., Vol. 30, Pages 237-242, 2012.

6. Tam, V. W. Y., Butera, A., Le, K. N., Silva, L. C. F. D. and Evangelista, A. C. J., 'A prediction model for compressive strength of CO_2 concrete using regression analysis and artificial neural networks', Constr Build Mater., Vol. 324, Pages 126689, 2022.

7. Nazari, A. and Sanjayan, J. G., 'Modelling of compressive strength of geopolymer paste, mortar and concrete by optimized support vector machine', Ceram Int., Vol. 41, Issue 9, Pages 12164-12177, 2015.

8. Akkurt, S., Ozdemir, S., Tayfur, G. and Akyol, B., 'The use of GA–ANNs in the modelling of compressive strength of cement mortar', Cem Concr Res., Vol. 33, Issue 7, Pages 973-979, 2003.

9. Zhou, X. Q. and Hao, H., 'Modelling of compressive behaviour of concrete-like materials at high strain rate', Int J Solids Struct., Vol. 45, Issue 17, Pages 4648-4661, 2008.

10. Zhang, J., Ma, G., Huang, Y,, Sun, J., Aslani, F. and Nener, B., 'Modelling uniaxial compressive strength of lightweight self-compacting concrete using random forest regression', Constr Build Mater., Vol. 210, Pages 713-719, 2019.

11. Mousavi, S. M., Aminian, P., Gandomi, A. H., Alavi, A. H. and Bolandi, H., 'A new predictive model for compressive strength of HPC using gene expression programming', Adv Eng Softw., Vol. 45, Issue 1, Pages 105-114, 2012.

12. Shishegaran, A., Khalili, M. R., Karami, B., Rabczuk, T. and Shishegaran, A., 'Computational predictions for estimating the maximum deflection of reinforced concrete panels subjected to the blast load', Int J Impact Eng., Vol. 139, Pages 103527, 2020.

13. Alexander, M. and Beushausen, H., 'Durability, service life prediction, and modelling for reinforced concrete structures – review and critique', Cem Concr Res., Vol. 122, Pages 17-29, 2019.

14. Bai, J., Wild, S., Ware, J. A. and Sabir, B. B., 'Using neural networks to predict workability of concrete incorporating metakaolin and fly ash', Adv Eng Softw, Vol. 34, Issue 11-12, Pages 663-669, 2003.

15. Liang, M., Chang, Z., Wan, Z., Gan, Y., Schlangen, E. and Šavija, B., 'Interpretable Ensemble-Machine-Learning models for predicting creep behavior of concrete', Cem Concr Compos. Vol. 125, Pages 104295, 2022.

16. Ray, S., Haque, M., Ahmed, T. and Nahin, T. T., 'Comparison of artificial neural network (ANN) and response surface methodology (RSM) in predicting the compressive and splitting tensile strength of concrete prepared with glass waste and tin (Sn) can fiber', J King Saud Univ - Eng Sci., Vol. 35, Issue 3, Pages 185-199, 2023.

17. Moradi, M. J., Daneshvar, K., Ghazi-nader, D. and Hajiloo, H., 'The prediction of fire performance of concrete-filled steel tubes (CFST) using artificial neural network', Thin-Walled Struct., Vol. 161, Pages 107499, 2021.

18. Hammoudi, A., Moussaceb, K., Belebchouche, C. and Dahmoune, F., 'Comparison of artificial neural network (ANN) and response surface methodology (RSM) prediction in compressive strength of recycled concrete aggregates', Constr Build Mater., Vol. 209, Pages 425-436, 2019.

19. Congro, M,, Monteiro, V. M., De, A., Brandão, A. L. T., Santos, B. F., Roehl, D. and Silva, F. A., 'Prediction of the residual flexural strength of fiber reinforced concrete using artificial neural networks', Constr Build Mater., Vol. 303, Pages 124502, 2021.

20. Ramkumar, K. B., Rajkumar, P. R, Noor, A. S. and Jegan, M., 'A Review on Performance of Self-Compacting Concrete – Use of Mineral Admixtures

and Steel Fibres with Artificial Neural Network Application', Constr Build Mater., Vol. 261, Pages 120215, 2020.

21. Felix, E. F, Carrazedo, R. and Possan, E., 'Carbonation model for fly ash concrete based on artificial neural network: Development and parametric analysis', Constr Build Mater., Vol. 266, Pages 121050, 2021.

22. Xu, J., Chen, Y., Xie, T., Zhao, X., Xiong, B. and Chen, Z., 'Prediction of triaxial behavior of recycled aggregate concrete using multivariable regression and artificial neural network techniques' Constr Build Mater., Vol. 226, Pages 534-554, 2019.

23. Xi, X., Yin, Z., Yang, S. and Li, C.Q., 'Using artificial neural network to predict the fracture properties of the interfacial transition zone of concrete at the meso-scale', Eng Fract Mech., Vol. 242, Pages 104788, 2021.

24. Xu, J., Zhao, X., Yu, Y., Xie, T., Yang, G. and Xue, J.i 'Parametric sensitivity analysis and modelling of mechanical properties of normal- and high-strength recycled aggregate concrete using grey theory, multiple nonlinear regression and artificial neural networks', Constr Build Mater., Vol. 211, Pages 479-491, 2019.

25. Zhao, Y., Hu, H., Song, C. and Wang, Z., 'Predicting compressive strength of manufactured-sand concrete using conventional and metaheuristic-tuned artificial neural network', Measurement. Vol. 194, Pages 110993, 2022.

26. Liu, Q., Iqbal, M. F., Yang, J., Lu, X., Zhang, P. and Rauf, M., 'Prediction of chloride diffusivity in concrete using artificial neural network: Modelling and performance evaluation', Constr Build Mater., Vol. 268, Pages 121082, 2021.

27. Shahmansouri, A. A., Yazdani, M., Ghanbari, S., Akbarzadeh, H., Jafari, A. and Farrokh, H., 'Artificial neural network model to predict the compressive strength of eco-friendly geopolymer concrete incorporating silica fume and natural zeolite', J Clean Prod., Vol. 279, Pages 123697, 2021.

28. Mukherjee, A. and Biswas, S. N., 'Artificial neural networks in prediction of mechanical behavior of concrete at high temperature', Nucl Eng Des., Vol. 178, Issue 1, Pages 1-11, 1997.

29. Yeh, I. C., 'Modeling of strength of high-performance concrete using artificial neural networks', Cem Concr Res., Vol. 28, Issue 12, Pages 1797-1808, 1998.

30. Lee, S. C., 'Prediction of concrete strength using artificial neural networks', Eng Struct., Vol. 25, Issue 7, Pages 849-857, 2003.

31. Wen, L., Li, Y., Zhao, W., Cao, W. and Zhang, H., 'Predicting the deformation behaviour of concrete face rockfill dams by combining support vector machine and AdaBoost ensemble algorithm', Comput Geotech. Vol. 161, Pages 105611, 2023.

32. Jiang, W., Xie, Y., Li, W., Wu, J. and Long, G., 'Prediction of the splitting tensile strength of the bonding interface by combining the support vector machine with the particle swarm optimization algorithm', Eng Struct., Vol. 230, Pages 111696, 2021.

33. Fan, Z., Chiong, R., Hu, Z. and Lin, Y., 'A fuzzy weighted relative error support vector machine for reverse prediction of concrete components', Comput Struct., Vol. 2020, Pages 106171, 2020.

34. Luo, H. and Paal, S. G., 'Metaheuristic least squares support vector machine-based lateral strength modelling of reinforced concrete columns subjected to earthquake loads', Structures. Vol. 33, Pages 748-758, 2021.

35. Zhou, Y., Zhang, Y., Pang, R. and Xu, B., 'Seismic fragility analysis of high concrete faced rockfill dams based on plastic failure with support vector machine', Soil Dyn Earthq Eng., Vol. 144, Pages 106587, 2021.

36. Jueyendah, S., Lezgy-Nazargah, M., Eskandari-Naddaf, H. and Emamian, S. A., 'Predicting the mechanical properties of cement mortar using the support vector machine approach', Constr Build Mater., Vol. 291, Pages 123396, 2021.

37. Ling, H., Qian, C., Kang, W., Liang, C. and Chen, H., 'Combination of Support Vector Machine and K-Fold cross validation to predict compressive strength of concrete in marine environment', Constr Build Mater., Vol. 206, Pages 355-363, 2019.

38. Basaran, B., Kalkan, I., Bergil, E. and Erdal, E., 'Estimation of the FRP-concrete bond strength with code formulations and machine learning algorithms', Compos Struct., Vol. 268, Pages 113972, 2021.

39. Saleh, E., Tarawneh, A., Naser, M. Z., Abedi, M. and Almasabha, G., 'You only design once (YODO): Gaussian Process-Batch Bayesian optimization framework for mixture design of ultra high performance concrete', Constr Build Mater., Vol. 330, Pages 127270, 2022.

40. Ziyad, B. H., Ziyad, B.F., Kumar, P, et al., 'Feasibility analysis for predicting the compressive

and tensile strength of concrete using machine learning algorithms' Case Stud Constr Mater., Vol. 18, Pages e01893, 2023.

41. Fu, W., Sun, B., Wan, H. P., Luo, Y. and Zhao, W., 'A Gaussian processes-based approach for damage detection of concrete structure using temperature-induced strain', Eng Struct., Vol. 268, Pages 114740, 2022.

42. Pereira, D. P., Bhagya, J. L. and Waldmann, D., 'Machine learning in mix design of Miscanthus lightweight concrete', Constr Build Mater., Vol. 302, Pages 124191, 2021.

43. Asteris, P. G., Skentou, A. D., Bardhan, A., Samui, P. and Pilakoutas, K., 'Predicting concrete compressive strength using hybrid ensembling of surrogate machine learning models', Cem Concr Res., Vol. 145, Pages 106449, 2021.

44. Kaloop, M. R., Kumar, D., Samui, P., Hu, J. W. and Kim, D., 'Compressive strength prediction of high-performance concrete using gradient tree boosting machine', Constr Build Mater., Vol. 264, Pages 120198, 2020.

45. Altunci, Y. T. and Özkan, Ş., 'Design Optimization and Statistical Modeling of Compressive Strtength of Cement Mortars Containing Recycled Waste Brick Dust Using Response Surface Methodology', Int J Sustain Eng Technol., Vol. 2, Issue 7, Pages 88-97, 2023.

46. Yuan, Z., Wang, L. N. and Ji, X., 'Prediction of concrete compressive strength: Research on hybrid models genetic based algorithms and ANFIS', Adv Eng Softw., Vol. 67, Pages 156-163, 2014.

47. Sobhani, J., Najimi, M., Pourkhorshidi, A. R. and Parhizkar, T., 'Prediction of the compressive strength of no-slump concrete: A comparative study of regression, neural network and ANFIS models', Constr Build Mater., Vol. 24, Issue 5, Pages 709-718, 2010.

48. Sadrmomtazi, A., Sobhani, J. and Mirgozar, M. A., 'Modeling compressive strength of EPS lightweight concrete using regression, neural network and ANFIS', Constr Build Mater., Vol. 42, Pages 205-216, 2013.

49. Ahmadi-Nedushan, B., 'Prediction of elastic modulus of normal and high strength concrete using ANFIS and optimal nonlinear regression models', Constr Build Mater., Vol. 36, Pages 665-673, 2012.

50. Madandoust, R., Bungey, J. H. and Ghavidel, R., 'Prediction of the concrete compressive strength by means of core testing using GMDH-type neural network and ANFIS models', Comput Mater Sci., Vol. 51, Issue 1, Pages 261-272, 2012.

51. Kumar, A., Arora, H. C., Kumar, K. and Garg, H., 'Performance prognosis of FRCM-to-concrete bond strength using ANFIS-based fuzzy algorithm', Expert Syst Appl., Vol. 216, Pages 119497, 2023.

52. Pei, Z. and Wei, Y., 'Prediction of the bond strength of FRP-to-concrete under direct tension by ACO-based ANFIS approach', Compos Struct., Vol. 282, Pages 115070, 2022.

53. Li, J., Yan, G., Abbud, L. H., et al., 'Predicting the shear strength of concrete beam through ANFIS-GA–PSO hybrid modeling', Adv Eng Softw., Vol. 181, Pages 103475, 2023.

54. Vakhshouri, B. and Nejadi, S., 'Prediction of compressive strength of self-compacting concrete by ANFIS models', Neurocomputing. Vol. 280, Pages 13-22, 2018.

55. Emiroğlu, M., Beycioğlu, A. and Yildiz, S., 'ANFIS and statistical based approach to prediction the peak pressure load of concrete pipes including glass fiber', Expert Syst Appl., Vol. 39, Issue 3, Pages 2877-2883, 2012.

56. Akkurt, I., Başyigit, C., Kilincarslan, S. and Beycioglu, A., 'Prediction of photon attenuation coefficients of heavy concrete by fuzzy logic', J Franklin Inst., Vol. 347, Issue 9, Pages 1589-1597, 2010.

57. Moon, J., Kim, J. J., Lee, T. H. and Lee, H. E., 'Prediction of axial load capacity of stub circular concrete-filled steel tube using fuzzy logic', J Constr Steel Res., Vol. 101, Pages 184-191, 2014.

58. Güler, K., Demir, F. and Pakdamar, F., 'Stress–strain modelling of high strength concrete by fuzzy logic approach', Constr Build Mater., Vol. 37, Pages 680-684, 2012.

59. Tanyildizi, H., 'Fuzzy logic model for prediction of mechanical properties of lightweight concrete exposed to high temperature', Mater Des., Vol. 30, Issue 6, Pages 2205-2210, 2009.

60. Golafshani, E. M., Rahai, A., Sebt, M. H. and Akbarpour, H., 'Prediction of bond strength of spliced steel bars in concrete using artificial neural network and fuzzy logic', Constr Build Mater., Vol. 36, Pages 411-418, 2012.

61. Özcan, F., Atiş, C. D., Karahan, O., Uncuoğlu, E. and Tanyildizi, H., 'Comparison of artificial neural network and fuzzy logic models for prediction of long-term compressive strength of silica fume

concrete', Adv Eng Softw., Vol. 40, Issue 9, Pages 856-863, 2009.

62. Saridemir, M., Topçu, I. B., Özcan, F. and Severcan, M. H., 'Prediction of long-term effects of GGBFS on compressive strength of concrete by artificial neural networks and fuzzy logic', Constr Build Mater., Vol. 23, Issue 3, Pages 1279-1286, 2009.

63. Topçu, I. B. and Saridemir, M., 'Prediction of rubberized concrete properties using artificial neural network and fuzzy logic', Constr Build Mater. Vol. 22, Issue 4, Pages 532-540, 2008.

64. Topçu, I. B. and Saridemir, M., 'Prediction of compressive strength of concrete containing fly ash using artificial neural networks and fuzzy logic', Comput Mater Sci., Vol. 41, Issue 3, Pages 305-311, 2008.

65. Cao, Y., Zandi, Y., Rahimi, A., et al., 'Evaluation and monitoring of impact resistance of fiber reinforced concrete by adaptive neuro fuzzy algorithm', Structures. Vol. 34, Pages 3750-3756, 2021.

66. Qi, C,. Fourie, A. and Chen, Q., 'Neural network and particle swarm optimization for predicting the unconfined compressive strength of cemented paste backfill', Constr Build Mater., Vol. 159, Pages 473-478, 2018.

67. Kaplanvural, İ., 'Volumetric water content estimation of concrete by particle swarm optimization of GPR data', Constr Build Mater., Vol. 375, Pages 130995, 2023.

68. Hanoon, A. N., Jaafar, M. S., Hejazi, F. and Aziz F. N. A. A., 'Strut-and-tie model for externally bonded CFRP-strengthened reinforced concrete deep beams based on particle swarm optimization algorithm: CFRP debonding and rupture', Constr Build Mater., Vol. 147, Pages 428-447, 2017.

69. Jiang, G., Keller, J., Bond, P. L. and Yuan, Z., 'Predicting concrete corrosion of sewers using artificial neural network', Water Res., Vol. 92, Pages 52-60, 2016.

70. Wen, Z., Zhou, R. and Su, H., 'MR and stacked GRUs neural network combined model and its application for deformation prediction of concrete dam', Expert Syst Appl., Vol. 201, Pages 117272, 2022.

71. Yilmaz, I. and Yuksek, G., 'Prediction of the strength and elasticity modulus of gypsum using multiple regression, ANN, and ANFIS models', Int J Rock Mech Min Sci., Vol. 46, Issue 4, Pages 803-810, 2009.

72. Yilmaz, I. and Kaynar, O., 'Multiple regression, ANN (RBF, MLP) and ANFIS models for prediction of swell potential of clayey soils', Expert Syst Appl., Vol. 38, Issue 5, Pages 5958-5966, 2011.

73. Gaya, M. S. A., Abdu, A. M. T., Abubakar, I. S., Mubarak, A. E. P. and Wahab, N. A., 'Estimation of water quality index using artificial intelligence approaches and multi-linear regression', Int J Artif Intell., Vol. 9, Issue 1, Pages 126-134, 2020.

74. Uzundurukan, S. and Saplıoğlu, K., 'Konsol İstinat Duvarlarında Yükseklik Maliyet İlişkisinin Parçacık Sürü Algoritması İle İncelenmesi' Düzce Üniversitesi Bilim ve Teknol Derg., Vol. 8, Issue 4, Pages 2544-2554, 2020.

75. Acar, R. and Saplıoğlu, K., 'Etkili Girdi Parametrelerinin Çoklu Regresyon ile Belirlendiği Su Sertliğinin ANFIS Yöntemi ile Tahmin Edilmesi', Afyon Kocatepe Üniversitesi Fen Ve Mühendislik Bilim Derg., Vol. 22, Issue 6, Pages 1413-1424, 2022.

76. Al-Adhaileh, M. H. and Alsaade, F. W., 'Modelling and Prediction of Water Quality by Using Artificial Intelligence', Sustainability. Vol. 13, Issue 8, Pages 4259, 2021.

77. Acar, R. and Saplıoğlu, K., 'Akarsulardaki Sediment Taşınımının Yapay Sinir Ağları Ve Anfıs Yöntemleri Kullanılarak Tespiti', Niğde Ömer Halisdemir Üniversitesi Mühendislik Bilimleri Dergisi, Vol. 9, Issue 1, Pages 437-450, 2020.

78. Acar, R. and Saplioglu, K., 'Using the Particle Swarm Optimization (PSO) Algorithm for Baseflow Separation and Determining the Trends for the Yesilirmak River (North Turkey)', Russian Meteorology and Hydrology., Vol. 49, Issue 1, Pages 40-51, 2024.

79. Lee, H. and Kang, K., 'Interpolation of Missing Precipitation Data Using Kernel Estimations for Hydrologic Modeling', Hindawi Publishing Corporation Advances in Meteorology., Vol. 2015, Article ID 935868, 12 Pages, 2015.

80. Acar, R., 'A comparison of the performance of different innovative trend assessment approaches for air temperature and precipitation data: an application to Elazığ Province (Turkey)', Journal of Water and Climate Change, Volume 15, Issue 3, Pages 1417-1437, 2024

81. Wilcoxon F., 'Individual comparisons by ranking methods. In: Breakthroughs in Statistics: Methodology and Distribution New York' (Kotz, S. & Johnson, N. L., eds.). Springer, New York, Pages 196–202, 1992.

ULUSLARARASI 3B YAZICI TEKNOLOJİLERİ
VE DİJİTAL ENDÜSTRİ DERGİSİ

INTERNATIONAL JOURNAL OF 3D PRINTING
TECHNOLOGIES AND DIGITAL INDUSTRY

ISSN:2602-3350 (Online)

URL: https://dergipark.org.tr/ij3dptdi

DIŞ ÇEPERLİ ARŞİMET POMPANIN MONTAJ EĞİMİNE GÖRE KOVA HACMİ PERFORMANSININ İNCELENMESİ

INVESTIGATION OF THE BUCKET VOLUME PERFORMANCE OF THE OUTER WALLED ARCHIMEDEAN PUMP ACCORDING TO THE MOUNTING ANGLE

Yazarlar (Authors): Fatih UYSAL, Zebo AKPARALİEVA

Bu makaleye şu şekilde atıfta bulunabilirsiniz (To cite to this article): *Uysal F., Akparalieva Z., "Dış Çeperli Arşimet Pompanın Montaj Eğimine Göre Kova Hacmi Performansının İncelenmesi" Int. J. of 3D Printing Tech. Dig. Ind., 8(2): 225-236, (2024).*

DOI: 10.46519/ij3dptdi.1469903

Araştırma Makale/ Research Article

Erişim Linki: (To link to this article): https://dergipark.org.tr/en/pub/ij3dptdi/archive

DIŞ ÇEPERLİ ARŞİMET POMPANIN MONTAJ EĞİMİNE GÖRE KOVA HACMİ PERFORMANSININ İNCELENMESİ

Fatih UYSAL[a], Zebo AKPARALİEVA[a,b]

[a] Sakarya Uygulamalı Bilimler Üniversitesi, Teknoloji Fakültesi, Makine Mühendisliği Bölümü, TÜRKİYE
[b] FADA Mühendislik ve Makine Sanayi ve Ticaret A.Ş., TÜRKİYE

[*]*Sorumlu Yazar: fatihuysal@subu.edu.tr*

(**Geliş/Received:** 17.04.2024; **Düzeltme/Revised:** 15.06.2024; **Kabul/Accepted:** 23.07.2024)

ÖZ

Su, insan hayatının vazgeçilmezi olup yerleşim yerlerinde temiz suyun temini ve atık suyun uzaklaştırılması zorunlu ihtiyaçtır. Bu zorunlu ihtiyaç gelişen teknoloji ile birlikte farklı yöntemlerle karşılanmaktadır. Arşimet pompalar da su temini ve atık suyun uzaklaştırılmasında kullanılan en eski akım makineleridir. Bu çalışmada Klasik Arşimet Pompa'ya alternatif olarak geliştirilmiş olan Dış Çeperli Arşimet pompanın performansı ve kova doldurma performansı incelenmiştir. Tasarımı yapılan dış çeperli Arşimet pompanın basma yüksekliği 6 metre, basma açısı 30° olacak gerçek boyutlarının 1/20 ölçeği referans alınarak tasarlanmıştır. Tasarımın farklı basma açılarındaki performansını değerlendirmek için 20°, 30°, 40° basma açılarında analizler ve deneyler yapılmıştır. Hesaplama ile elde edilen kova hacimleri geometrik analiz ile elde edilen hacimlerinden %15 daha büyüktür. Ancak deneysel olarak elde edilen kova hacimleri hesaplama ile elde edilen hacimlerin azami %37'sine karşılık gelmektedir. Bu durum dış çeperli Arşimet pompa tasarımında memba tarafının suya batma miktarının kova doldurma oranını doğrudan etkilediğini göstermektedir. Ayrıca kova hacmi hesaplamalarında CAD modeli üzerinden yapılan hacimsel analizler Arşimet pompaların kova hacimlerini daha net bir şekilde hesaplayabilmektedir.

Anahtar Kelimeler: Arşimet Pompa, Pompa Verimi, Hesaplamalı Akışkanlar Dinamiği (HAD), Pompa Performansı, Vidalı Pompa.

INVESTIGATION OF THE BUCKET VOLUME PERFORMANCE OF THE OUTER WALLED ARCHIMEDEAN PUMP ACCORDING TO THE MOUNTING ANGLE

ABSTRACT

Water is indispensable for human life and supply of clean water and removal of waste water in settlements is a compulsory need. This compulsory need is met by different methods with the developing technology. Archimedes pumps are the oldest current machines used in water supply and waste water removal. In this study, the performance and bucket filling performance of the outer wall Archimedes pump, which has been developed as an alternative to the classical Archimedes pump, has been investigated. The design of the outer wall Archimedes pump with a head of 6 m and a discharge angle of 30° is based on 1/20 scale of the actual dimensions. In order to evaluate the performance of the design at different discharge angles, analyses and experiments were performed at 20°, 30°, 40° discharge angles. The bucket volumes obtained by calculation are 15% larger than the volumes obtained by geometrical analysis. However, the experimentally obtained bucket volumes correspond to a maximum of 37% of the volumes obtained by calculation. This shows that the amount of submergence of the upstream side in the outer wall Archimedes pump design directly affects the bucket filling rate. In addition, volumetric analyses made on the CAD model in bucket volume calculations can calculate the bucket volumes of Archimedes pumps more clearly.

Keywords: Archimedes Pump, Pump Efficiency, CFD (Computational Fluid Dynamics) Analysis, Pump Performance, Screw Pump.

1. GİRİŞ

Arşimet pompaları, Arşimet tarafından Antik Yunan döneminde keşfedilen ve suyu yukarıya doğru taşımak için kullanılan basit makineler olup dairesel bir tüp içinde dönen bir vida veya helisel pervane ile çalışan hacimsel pompalardır [1]. Klasik arşimet pompa (KAP), bir silindir üzerine sarılan helislerin yarım dairesel bir yuva içersine yerleştirilerek iki ucundan yataklanması ile oluşturulur (Şekil 1). Ayrıca arşimet pompaları antik dönemden günümüze içmesuyu temininde, zirai sulama işlerinde, atık suların yerleşim yerlerinden uzaklaştırılmasında, maden ocakların-dan su tahliyesinde vb. işlerde kullanılmıştır ve kullanımı devam etmektedir [2]. Arşimet vidalar su pompalamanın haricinde taneli katıların taşınmasında [3], kara araçları tahrikinde [4], kan pompalamada [5] vb. işlerde de kullanılmaktadır.

Şekil 1. Klasik Arşimet pompa.

Arşimet pompaların tasarımında kullanılan helis sayısı ve montaj eğim açısı, pompa verimine doğrudan etkili olup optimize edilmesi gereklidir [6]. Klasik Arşimet pompalarındaki helezon ile yatak arasındaki zorunlu boşluktan kaynaklanan hidrolik kayıpların analizi ve hesaplaması zor bir problemdir [7-8]. Ayrıca pompanın giriş ve çıkış kısımlarındaki su seviyesi de verimi doğrudan etkilemektedir [9]. Giriş su seviyesinin artışı verimi arttırırken çıkış seviyesinin minimumda olması gerekir [10-11]. Giriş suyu seviyesi kova hacmi doldurma miktarını etkilediği için Arşimet pompa verimimi de doğrudan etkilemektedir [12]. Giriş suyu seviyesi belli bir değeri aşarsa Arşimet pompa veriminin düşmesine sebep olmaktadır [13]. Arşimet vidalı türbinlerde devir artarken moment ve verim düşmekte, debi artarken moment azalmaktadır. Debi artışına bağlı olarak mekanik verim klasik pompalar ile benzer şekilde debi arttıkça artan ve belli devirden sonraya azalmaya başlayan bir parabol oluşturmaktadır [14].

Günümüzde gelişen teknoloji ile birlikte santrifüj pompaların kullanımı artsa da Arşimet pompaların pompa ve türbin olarak kullanımı az düşülü yüksek debili yerlerde yaygın şekilde devam etmektedir. Ovalardaki yerleşimlerde 160 cm derinlikten inşaatına başlanan kanalizasyon hatları 6 m derinliğe ulaştığı zaman üretimleri ekonomik olmaktan çıkmaktadır. Bu durumda kurulan terfi istasyonları ile kanalizasyon suyu tekrar 160 cm derinliğe çıkartılarak kanalizasyon inşaatına devam edilmektedir. Bu terfi merkezlerinde verimleri kısmen düşük olsa da atık su içindeki yabancı cisimleri taşıma kabiliyetleri ve suyu havalandırma yeteneklerinden dolayı Arşimet Pompalar yaygın şekilde kullanılmaya devam etmektedir. Atık su içerisindeki yabancı cisimler yüksek devirlerde çalışan eksenel ve santrifüj pompaların millerine sarılarak arızalara sebep olmaktadır. Düşük devirleri ve geniş geçiş yolları ile dere üzerinde yüksek setler gerektirmeden kurulumu yapılabilen Arşimet pompalar, balık geçişlerine müsaade eden çevreci özellikleri ile de ön plana çıkmaktadır [15].

Montaj eğim açısı, Arşimet pompaların verimine etki eden önemli bir parametredir. Bu konuda yapılan literatür araştırmaları, araştırmacıların Arşimet pompalarının verimlerini artırmak için montaj eğim açısını optimize etme ihtiyacını vurgulamaktadır

[6,16]. Farklı montaj eğim açıları için pompaların verimlerini belirlemek amacıyla yapılan deneysel çalışmalar belirli bir montaj eğim açısının, Arşimet pompaların ve türbinlerin hidrolik verimini etkileyerek su taşıma kapasitesini ve enerji tüketimini değiştirdiğini göstermektedir [7-8,10,17-18].
Arşimet pompalarında kullanılan günümüz yataklama sistemleri maliyet, kullanım ömrü ve çevre açısından sorun teşkil etmektedir. Pompanın yataklama sorunu vidayı aşağıdan yataklayan yapının suyun içinde kalmasıdır. Gres beslemeli kaymalı yatak veya konik makaralı rulman kullanılan yataklar suyun içinde çalışmak zorunda olduğunda sızdırmazlığın uzun süre sağlanama-ması problem oluşturmaktadır. Su zamanla yatağın kaymasını sağlayan yağ filmini deforme eder ve sürtünmeleri arttırır. Bu da sürtünmelerin artmasına müteakip tahrik motorunun zorla-nmasına ve yatak sarması gibi problemlerin oluşmasına sebep olur. Bu durumlar bakım maliyetlerini büyük ölçüde arttırır (Şekil 2).

Şekil 2. Arşimet pompanın yataklama probleminden dolayı kırılan alt yatak flanşı.

Bu çalışmada, Arşimet pompalarındaki (veya türbinlerindeki) yataklama sorununa çözüm olarak vida çeperi dıştan kapatılarak çeper dışından makaralı yataklı bir Arşimet Pompa tasarlanmıştır. Tasarlanan sistemde hesaplanan kova hacimlerinin doluluk oranları ANSYS FLUENT programı ile analiz edilmiş ve deneysel olarak incelenmiş, tasarımın kova hacmi katı model programı ile geometrik olarak ölçülmüş ve sonuçlar karşılaş-tırılmıştır.

2. MATERYAL ve METOD

2.1. Model Tasarımı

Arşimet pompaları, az düşü ve yüksek debi için tasarlanan hacimsel pompalar olduğu için büyük gövdeye ve çok geniş montaj alanına sahiptir. Bu yüzden üretim süreçlerinde işlenebilmeleri büyük tezgahlar gerektirmektedir. Büyük tezgahlardaki işleme zorluğu ve toleranslardaki artıştan dolayı KAP'ın sabit silindirik gövdesi ile helis kanatları arasındaki boşluklar artmakta ve dolayısı ile hidrolik verimi azalmaktadır. Ayrıca helis, vidanın sadece alt ve üst taraflardan yataklanma zorunluluğu, su içinde kalan yatağın işletme zorluğunu ve maliyetlerini de arttırmaktadır. Alt yatağın aşırı kirliliğe maruz kalmaması için yatak kotunun aşağıya düşürülememesinden dolayı da memba kotu da aşağıya düşürülememektedir. Bu durum özellikle kanalizasyon terfi merkezlerinde kullanılan KAP'lardan dolayı su kotunun kanal içinde belli bir seviyede bırakılmasını zorunlu hale getirmektedir. Bu durum kanalizasyon hatları içindeki teresubat birikimini arttırmaktadır. Yapılan çalışmada bu olumsuzlukların önüne geçebilecek farklı bir tasarım olan Dış Çeperli Arşimet Pompanın (DAP) eğime bağlı verimi ve kova hacmi performansı (KHP)incelenmiştir.
Bu sistemin avantajlarını şu şekilde sıralanabilir;

1. Yataklarda kullanılan yağ suya karışmaz, çevreyi kirletmez
2. Yataklar suyun altında çalışmadığı için kullanım ömürleri daha uzun ve periyodik bakım maliyetleri daha düşüktür.
3. Pompanın yatağa monte ve demonte işlemi daha basittir.
4. Pompanın mil tasarımı daha sade şekilde yapılabilmektedir. Pompa dış çeperler üzerinden yataklanabilmektedir.
5. Dış çeperler ile helis arasında boşluk oluşmadığı için hidrolik verim artar.
6. Alt yatak su içinde kalmadığı için memba tarafındaki su seviyesi aşağıya düşürülerek kanallardaki teresubat birikimini azaltıla-bilir.
7. Pompada gövde dış çeperi ile sızdırmazlık sağlandığı için sabit gövdeyi taşıyacak büyük yapılara gerek kalmaz.

8. Dış çeper üzerinden yapılabilecek tahrik sistemi ile redüktör ihtiyacı ortadan kalkar.

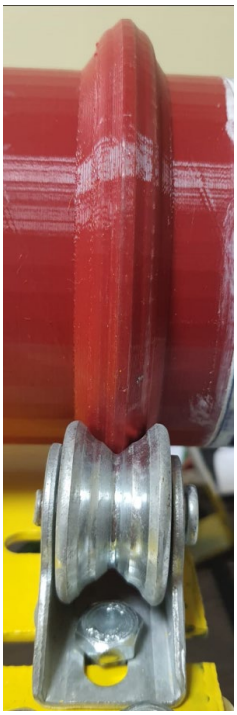

Şekil 3. DAP üzerindeki rip ve yatak.

DAP'ın helisleri üzerine dış çeper sarılarak DAP'ınn gövdesi oluşturulmuştur. Bu gövde üzerine yataklama için yatak yuvasına uygun ripler yapılmıştır (Şekil 3). Bu ripleri yataklayacak 2 adet yatak, zemin üzerine yerleştirilmiştir. Bu şekilde oluşturulan iki adet rip dört yatak tarafından yataklanarak DAP'ın yataklama işlemi gerçekleştirilmiştir. Ayrıca DAP'ın gövdesi kapalı olduğundan redüktör maliyetinden kaçınmak üzere gövdeye kayış yuvaları açılmıştır. DAP'ı tahrik edecek olan elektrik motoru üzerinde tasarlanan kasnak ile gövde arasındaki kasnak arasında 1/10 tahrik oranı oluşturarak kayış-kasnak sistemi tasarlanmıştır (Şekil 4).

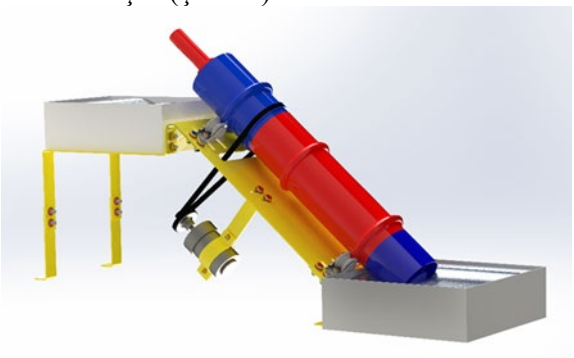

Şekil 4. DAP modeli.

Arşimet pompasının deneyleri montaj eğim açısına bağlı olduğu için prototip üretim aşamasında eğim açısını ayarlamak önemli bir kriterdir. Faklı montaj açılarını ayarlamak üzere farklı yüksekliklerde ve açılarda saç ayaklar kesilerek bükülmüştür (Şekil 5). Deney aşamasında eğim açısına göre büküm parçaları değiştirilerek, montajda DAP'a gerekli eğim verilmiştir (Şekil 6).

Şekil 5. Pompa yataklama sistemi açılı bükümlü saclar.

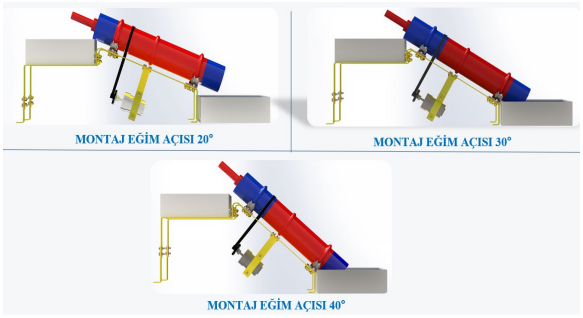

Şekil 6. Pompa montaj eğim açıları.

2.2. Helis (Kanat) Tasarımı

Helis tasarımı, pompaların su veya sıvıyı taşıma etkinliği üzerinde doğrudan etkilidir. Arşimet pompasının tasarım kriterlerini belirlemek için farklı helis açıları ve kanat sayıları ile hesaplamalar yapılarak verim üzerindeki etkiler incelenmektedir. Çizelge 1, MATLAB analizlerine dayanan 1'den 25'e kadar helisli KAP'lar için optimum hatve-yarıçap oranlarını ve buna karşılık gelen devir başına optimum hacim ve hacim oranlarını göstermektedir [19].

Çizelge 1. Farklı kanat sayısına göre Arşimet vidasının optimum oran parametreleri [19].

Kanat sayısı N*	Optimum yarıçap oranı: p*	Optimum adım oranı: λ*	Optimum hacim oranı v(N,p*,h*)
1	0.5358	0.1285	0.2811
2	0.5369	0.1863	0.2747
3	0.5357	0.2217	0.2697
4	0.5353	0.2456	0.2667
5	0.5352	0.263	0.2647
6	0.5353	0.2763	0.2631
7	0.5354	0.2869	0.2619
8	0.5354	0.2957	0.2609
9	0.5356	0.3029	0.2601
10	0.5356	0.3092	0.2592
11	0.5358	0.3145	0.2586
12	0.536	0.3193	0.258
13	0.536	0.3234	0.2574
14	0.536	0.327	0.2571
15	0.5364	0.3303	0.2567
16	0.5362	0.3333	0.2562
17	0.5362	0.3364	0.2556
18	0.5368	0.338	0.2559
19	0.5364	0.3404	0.2555
20	0.5365	0.3426	0.2551
21	0.537	0.344	0.2553
22	0.5365	0.3465	0.2544
23	0.5369	0.3481	0.2543
24	0.5367	0.35	0.2538
25	0.5371	0.3507	0.2542
.	.	.	.
∞	0.5394	0.3953	0.2471

Çizelge 1'in son satırında ise kanat sayısının sonsuza yaklaştıkça bu değerlerin de limit değerine yaklaştığı gösterilmektedir. Bu şekilde kanat sayısı (N) arttıkça hacmin devire oranı monoton bir şekilde arttığından, bir devirde kaldırılabilecek su miktarı için bir üst sınır sağlanmaktadır [19].

Çizelge 1'de ayrıca N değeri birden sonsuza doğru arttıkça optimum hacim oranı ($v(N, p^*, \lambda^*)$)'nin 0,2811'den 0,2471'e düştüğü görülmektedir. Böylece, kanat sayısı arttıkça su hacmi azalmaktadır. Şekil 7'de 1, 2, 3 veya 4 kanatlı vidanın bir kova hacmin kesit görünümünü göstermektedir. Bu şekilde, 1 veya 2 kanatlı vida kesiti için su hacmi tek hacim olarak görünmektedir. Ancak 3 veya 4 kanatlı bir vida için iki hacme bölünmektedir. Su hacmi tek olduğunda, vida tamamen su geçirmez bir dış silindire sahiptir ve vidanın üstünden altına kadar net bir hava geçişi vardır. Bununla birlikte, su hacmi iç silindir tarafından ikiye bölündüğünde, su kovaları kanalları kapatır ve böylece herhangi bir oluktaki kovalar arasındaki boşluklarda hava kalmamakta-dır. Bu da pompa verimini etkilemektedir [20].

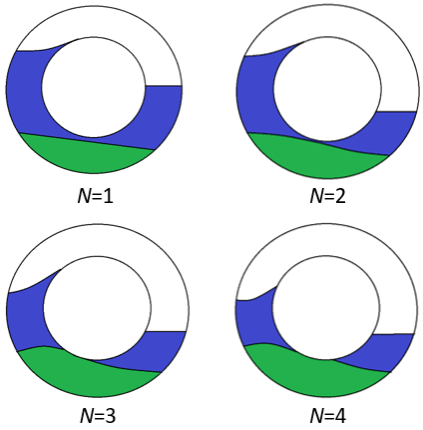

Şekil 7. 1, 2, 3 ve 4 kanatlı vidanın bir kova hacmin kesiti. (Mavi alan suyun yatay yüzeyidir. Yeşil alan kova hacminin kanat ile temas noktasını göstermektedir) [19].

Arşimet pompaların su taşıma kapasitesini belirleyen temel unsur kova hacmidir. Kova hac-minin hesaplanabilmesi için bazı parametrelerin önceden belirlenmesi gerekir. Dış parametreler adını verdiğimiz bu kıstaslar, montaj yeri, basma yüksekliği ve debi göz önüne alınarak önceden belirlenmelidir. Arşimet vidasının dış parametre-leri şu şekildedir:

R_d = vidanın dış silindirinin yarıçapı (m)
L = toplam vida uzunluğu (m)
K = vidanın eğimi (boyutsuz)

Dış parametreler genellikle pompanın kullanıla-cağı yere göre tasarım öncesi belirlenir. Bu çalışmada dış parametreler su pompasının 6 metrelik basma yüksekliğine göre seçilmiştir. Dış parametrelere ek olarak, vidanın geometrisini tamamen belirtmek için aşağıdaki iç parametrelere de ihtiyaç vardır;

R_i = vidanın iç silindirinin yarıçapı (m) ($\theta \leq R_i \leq R_d$)
Λ = bir kanat aralığı (veya adımı) (m) ($\theta \leq \Lambda \leq \frac{2\pi R_d}{K}$)
N = kanat sayısı (adet), N = 1, 2, . . . ∞

Çizelge 1'de kanat sayısına göre optimum yarıçap oranı (p) belirlenebilir. Bundan sonra dış yarıçap imalat şartları ve mevcut uygulamalara göre belirlendikten sonra iç yarıçap aşağıdaki formüle göre belirlenebilir [19].

$$p = \frac{R_i}{R_d} \quad (1)$$

Benzer şekilde Çizelge 1'de 3 kanat sayısına göre optimum adım oranı 0.2217'dir. Buna göre kanat aralığı bulunabilir. Bunun için öncelikle montaj eğiminin belirlenmesi gerekir:

$$K = \tan\theta \quad (2)$$

Daha sonra aşağıdaki formüle göre adım uzunluğu (Λ) belirlenir. Bunu için öncelikle Çizelge 1'den optimum adım oranının (λ) belirlenmesi gerekir.

$$\lambda = \frac{K\Lambda}{2\pi R_d} \quad , (0 \leq \lambda \leq 1) \quad (3)$$

2.3. Hidrolik Model

Arşimet pompanın kova hacmini optimize etmek için vidanın bir devirdeki kova hacminin (V_T) vidanın bir devirde toplam hacmine ($\pi R_0^2 \Lambda$) oranı olarak, (ν) boyutsuz bir parametrenin tanımlanması ile başlanır. Pompanın debisini hesaplayabilmek için ilk önce iki kanat arasındaki oluşan kova hacmini bulmamız gerekmektedir. Kova hacmi pompa eğim açısına bağlı olarak değişmektedir, aynı zamanda kanat sayısına ve vida adımına da bağlıdır. Aşağıdaki Denklem (4) ve Denklem (5)'e göre Çizelge 1 verilerini kullanarak 3 kanatlı Arşimet Pompa için V_T hesaplanabilir [19]:

$$\nu = \frac{V_T}{\pi R_0^2 \Lambda} \quad (4)$$

$$V_T = \left(\frac{2\pi^2 R_0^3}{K}\right) \lambda v(N, p, \lambda) \quad (5)$$

Pompanın bir devirde süpürdüğü kova hacmini V_T hesaplandıktan sonra, Arşimet pompanın maksimum debi değeri ($\dot{Q}$) aşağıdaki formülle hesaplanır [19]:

$$\dot{Q} = V_T \frac{n}{60} \quad (6)$$

Pompanın hidrolik gücü (P_h) sıvı yoğunluğuna (ρ), yerçekimi ivmesine (g), debiye ($\dot{Q}$) ve basma yüksekliğine (H) bağlı olarak şu şekilde hesaplanır:

$$P_h = \rho g \dot{Q} H \quad (7)$$

Motorun çektiği akım (I) ve gerilim (V) değerleri ölçülerek pompaya verilen güç hesaplanabilir. Bu durumda elektrik motorunun verimi ihmal edilmiş olacaktır.

$$P_e = VI \quad (8)$$

Sonuç olarak motor ve pompanın toplam verimi şu (η_t) şekilde hesaplanabilir:

$$\eta_t = \frac{P_h}{P_e} \quad (9)$$

2.4. Malzeme Seçimi ve Prototip Üretimi

Arşimet pompa üretimi helisin açılı yapısından dolayı zor bir üretimdir. Ayrıca helis vida üzerinin ilave bir boru ile kapatılması üretimi daha da zorlaştırmaktadır. Normal boyutlarında üretilecek bir Arşimet pompanın yatakları arasındaki eksen kaçıklıklarının azaltılarak pompanın kullanılabilir seviyeye getirilmesi ise büyük talaşlı imalat makinaları gerektirmektedir. Bu çalışmada tasarlanan Arşimet pompa 1/20 ölçeğinde prototip olarak üç boyutlu yazıcıda üretilmiştir. Prototip modellerin üç boyutlu yazıcıda üretilmesi, hızlı prototipleme sürecinde sıkça kullanılan bir yöntemdir [21]. Üretim malzemesi suya dayanıklı olması bakımından polietilen tereftalat glikol (PET-G) olarak seçilmiştir. PET-G, polietilen tereftalatın geliştirilmiş bir versiyonudur ve çeşitli endüstriyel uygulamalarda yaygın olarak kullanı-lan bir plastik malzemedir. Malzeme özellikleri Çizelge 1'de gösterilmiştir.

Çizelge 2. PET-G malzemesinin mekanik özellikleri.

Özelllik	Birim	Değer
Young Modülü	GPa	2,95
Yoğunluk	kg/m^3	1375
Poissons's Oranı	MPa	0,33
Çekme Gerilimi	-	53
Baskı Gerilimi	MPa	55
Akma Dayanımı	MPa	47,9

Arşimet pompanın tahriki için 12 V_{DC}, 100 W 150 d/d motor kullanılmıştır. Sisteme güç 12 V_{DC} 60 Ah akü ile sağlanmıştır. Motor hızını kontrol eden DC sürücü, motor tarafı 12 V_{DC} ile çalışırken kontrol kartı kısmında enerjinin DC-DC regülatör ile 7 volta düşürülmüş enerji ile çalışmaktadır. Motor sürücüsüne potansiyometre üzerinden verilen analog değer ile motorun hızı kontrol edilmektedir. Hız sensörü ile motorun dakikada yaptığı devir sayısı ölçülebilmektedir. Ölçülen tur sayısı LCD ekran üzerinden kullanıcıya yansıtılmıştır (Şekil 8). Pompanın alt ve üst tarafına havuzlar yerleştirilerek su giriş çıkışı kontrollü şekilde sağlanmıştır (Şekil 9).

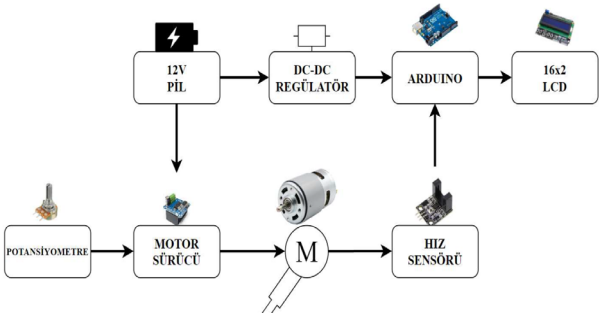

Şekil 8. Tahrik ve kontrol sistemi blok diyagramı.

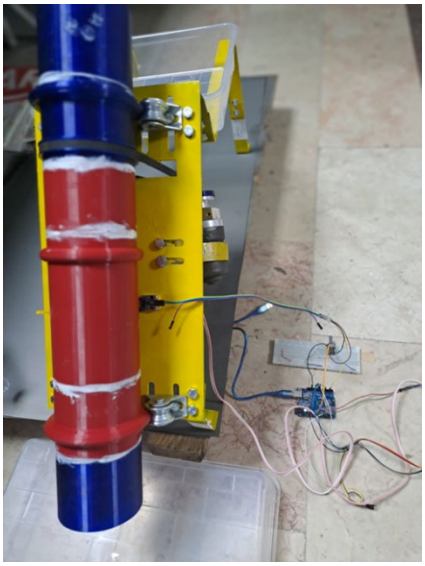

Şekil 9. Arşimet pompası deney düzeneği.

2.5. Hesaplamalı Akışkanlar Dinamiği Analizleri

HAD analizleri, bilgisayar tabanlı simülasyon yazılımları aracılığıyla gerçekleştirilmiştir ve bu yöntemle pompanın içinden geçen suyun akış miktarı, basınç dağılımını ve diğer hidrolik parametreleri analiz edebilir. Bu analizler, kompleks akışkan dinamiklerini ve etkileşimlerini simüle ederek pompanın performansının daha iyi anlaşılmasına yardımcı olur. Arşimet pompasının geometri modeli bir katı model programında çizilmiş (Şekil 10) ve HAD analizi için bu geometri modeli, HAD yazılımına yüklenmiştir. HAD yazalım programı olarak ANSYS Fluent seçilmiştir. Pompanın HAD analizi 3 farklı eğim açısına göre yapılmıştır (20º, 30 º ve 40 º).

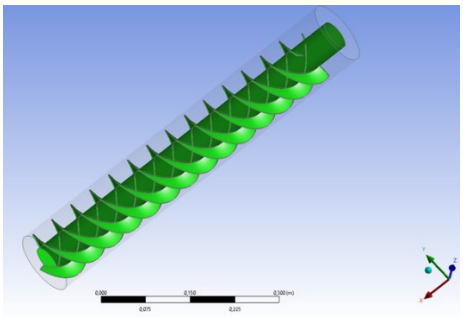

Şekil 10. DAP'ın geometri modeli.

Mesh işlemi için 0.0675 m'lik bir tetrahedral eleman boyutuna sahip ağ kullanılmıştır ve sonuç olarak Şekil 11'de görüldüğü gibi, 507788 elemandan ve 101044 düğümden oluşan bir ağ elde edilmiştir.

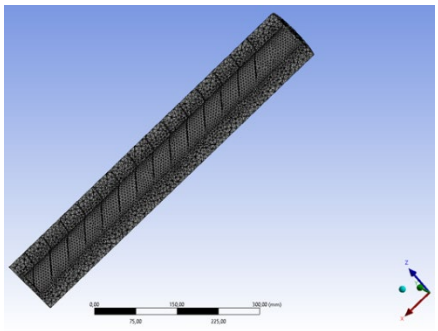

Şekil 11. Mesh işlemin kesit görüntüsü.

Mesh hesaplama süresi ile sonuçların doğruluğu arasındaki ilişkiyi optimize etmek amacıyla mesh yapısı bu şekilde oluşturulmuştur. Çok fazla eleman içeren oldukça detaylı bir mesh oluşturulmuş olsaydı, hesaplama süresi önemli ölçüde artacaktı. Üç milyon elemana kadar olan meshler denenmiş olsa da simülasyonun hesaplanması çok uzun sürmüştür. Bu nedenle, farklı ağlarla yapılan birkaç testten sonra, yaklaşık yarım milyon elemandan oluşan bir meshin yeterli olduğuna karar verilmiştir.

Yapılan çalışmada belirsizlik analizi Akılcı Yaklaşıma göre yapılarak elde edilen sonuçlar çizelgel 3'te verilmiştir. Belirsizlik analizinde elde edilen sonuçlar verilerin tutarlı şekilde değerlendi-rilebileceğini göstermektedir.

Çizelge 3. Belirsizlikler

Parametre	**Belirsizlik, ±**
Yükseklik, m	0,001
İç çap- Dış çap, m	0,001
Kova hacmi, l	0,001
Gerilim , V	0,05
Akım , A	0,05
Kova hacmi, l	0,0005
Hız(devir) , d/d	0,5
Parametre	**Toplam belirsizlik, %**
Su gücü, W	0,43
Elektriksel güç, W	0,98

3. BULGULAR ve DEĞERLENDİRMELER

DAP tasarımı için kullanımda olan bir KAP'ın ölçüleri referans alınmıştır. Buna göre dış parametreler R_d= 1 m ve basma yüksekliğini = 6m ve eğim açısı θ=30º'de verecek şekilde olan vida boyu L =12 m olarak belirlenmiştir. Referans alınan KAP'ın helis sayısı N=3 olduğundan bu çalışmada da aynı şekilde kullanılmıştır. Çizelge 1'e göre 3 helis için p=0,5357 olarak alınmıştır. Denklem (1)'e göre Ri = 0,5357 m olması gerekir. Ancak ölçü ve üretim kolaylığı açısından p= 0,5 alınarak Ri = 0,5 m hesaplanmıştır. Büyük boyutlarda bir DAP'ın üretim ve testi büyük mekan, hidrolik ve güç sistemleri gerektirmektedir. Deneylerimizi ve ölçümlerimizi laboratuvar ortamında yapmak için tasarlanan DAP'ın 1/20 ölçekli bir modeli üretilmiştir. Hesapların 1/1 ölçek üzerinden yapılması ile 1/20 ölçekli bir model üzerinden yapılması arasında bir fark bulunmadığı için bundan sonraki yapılan hesaplamalar model üzerinden Denklem (1)-(5)'e göre yapılarak sonuçları Çizelge 4'de verilmiştir.

Çizelge 4. DAP için seçilen ve hesaplanan değerler.

θ	**20º**	**30º**	**40º**
R_d (cm)	10	10	10
L (cm)	60	60	60
K	0,364	0,577	0,839
Λ (cm)	20	12	8,3
N	3	3	3
p	0,5	0,5	0,5
λ	0,2217	0,2217	0,2217
ν	0,2697	0,2697	0,2697
V_T	0,405	0,255	0,176
V_B	0,135	0,085	0,0586

Simülasyon sonuçları, pompadan geçen suyun debisini gösterir. Bu, pompanın ne kadar suyu taşıyabildiğini ve verimini belirlemek için önemli bir parametredir. Bu veriler ve sonuçlar, Arşimet pompa tasarımı ve performansının değerlendirilmesi için önemlidir. Simülasyonlar, farklı tasarım seçeneklerinin karşılaştırılması, optimum parametrelerin belirlenmesi ve pompanın performansının iyileştirilmesi için kullanılabilir. Bu çalışmada kova hacimlerinin hesaplanan değerleri ile üretim değerlerinin karşılaştırılması için bir CAD programında Geometrik Analiz yapılmıştır.

DAP'ın eğime göre monta edilmesi durumunda kova hacimlerinin katı modellerinde karşımıza üç önemli yüzey çıkmaktadır. Bunlar hava ile temas eden yüzey (kırmızı renkli), üst helis ile temas eden yüzey (gri renkli) ve iç silindir yüzeyi ile temas eden yüzeylerdir (yeşil renkli) (Şekil 12). Dış silindir ve alt helis yüzeyleri, diğer yüzeylere göre şekil alan ve kova hacminin oluşması için gereken yüzeylerdir.

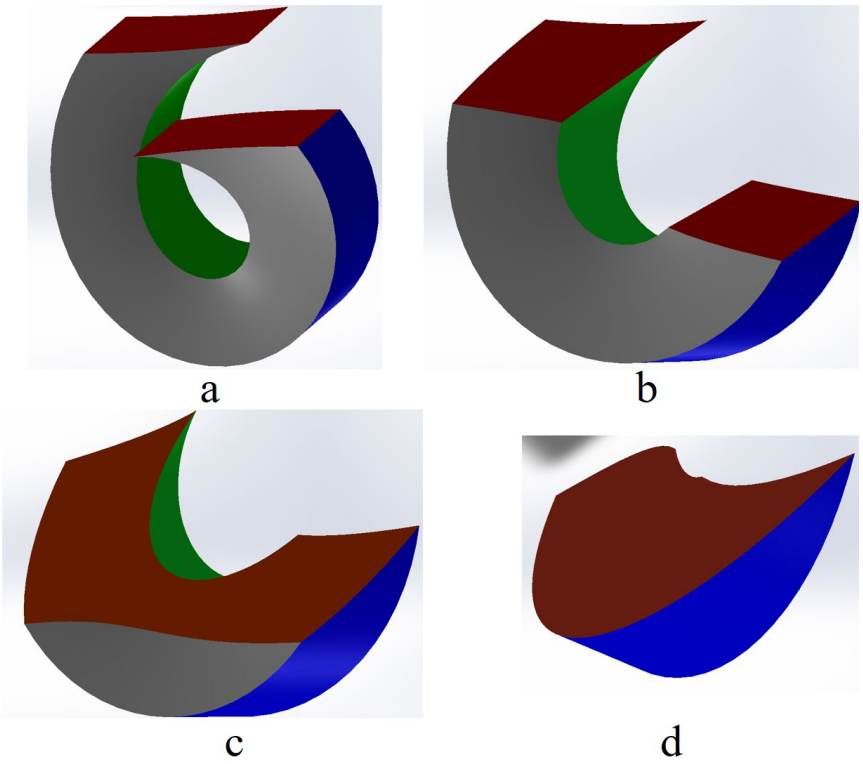

Şekil 12. Katı model üzerinden oluşturulan kova hacimleri; a: 0º pompa eğimi için, b: 20º pompa eğimi için, c: 30º pompa eğimi için, d: 40º pompa eğimi için.

Montaj açısının 0º olması durumunda azami kova hacmi elde edilmekte olup helisin sağ ve sol taraflarında hava ile aynı kotta yüzeyler oluşturmaktadır (Şekil 12-a). Suyun yukarıya doğru en kısa mesafeden taşınması ve DAP boyunun asgari olması için mümkün olan en yüksek eğitimin kullanılması gereklidir. Montaj eğimi arttıkça sol taraftaki serbest yüzeyin alanı belirgin bir şekilde artarken sağ tarafta azalma meydana gelmektedir (Şekil 12-b). Bu durum montaj eğimi arttıkça kova hacminin azaldığını açıkça göstermektedir. Montaj eğimi artarak 30º'ye çıktıkça sağ ve sol tarafın serbest yüzeyleri birleşmekte ve iç çap ile olan temas azalmaktadır (Şekil 12-c). Montaj açısı 40º'ye ulaştığında kova hacminin, iç çap ile irtibatı kalmayacak derece küçülmüş durumdadır (Şekil 12-d). Bu durum montaj eğim açısı arttıkça DAP tasarımında hatvenin azaltılması ve/veya kanat sayısının arttırılması gerektiğini ortaya koymaktadır. Böylece bir helisteki kova hacmi azalırken bir devirde süpürülen kova hacminin azalmasının önüne geçilebilir.

Bir devirde süpürülen kova hacmi (V_T) metot kısmında belirtilen yöntemle hesaplanmıştır. Hesaplanan değerlerin doğruluğunu karşılaştırmak için öncelikle tasarım üzerinde yapılan çalışma ile her montaj açısı için oluşan kova hacminin hacimsel modeli elde edilmiş (Şekil 12) ve elde edilen modelin hacmi tasarım programında hesaplanmıştır. Daha sonra modeli üretile DAP her montaj açısı için ayrı ayrı monte edilerek manuel olarak çalıştırılmış, toplam 10 devirde elde edilen su hacmi ölçülmüş ve buradan bir turdaki toplam kova hacmi deneysel olarak bulunmuştur. V_T'nin deneysel olarak belirlenmesi esnasında memba tarafındaki su kotu sabit tutulmuştur. Bu sonuçlar kıyaslandığında DAP modeli üzerinden alınan hacimlerden elde edilen V_T değerinin hesaplama ile elde edilen VT'den %15 civarında daha düşük olduğu görülmektedir (Şekil 13). Bu durum hesaplamanın referans alındığı kaynakta kullanılan hacim hesaplama yönteminden (simpson kuralı) kaynaklanır. Bu yöntem belli hacmi belli sayıda küplere böldüğü ve ortalama küp hacmi üzerinden hareket ettiği için sonuçlarda hatalar ortaya çıkmaktadır. Ayrıca hesaplama yönteminde helis cidar kalınlıklarının hesaplanmaması da hatayı arttırmaktadır.

Arşimet pompaların performansını belirleyen temel parametrelerden birisi bir devirdeki kova hacmidir (V_T). Bu kova hacmi başlangıçta hesaplanarak bir geometri ortaya çıkartılabilir.

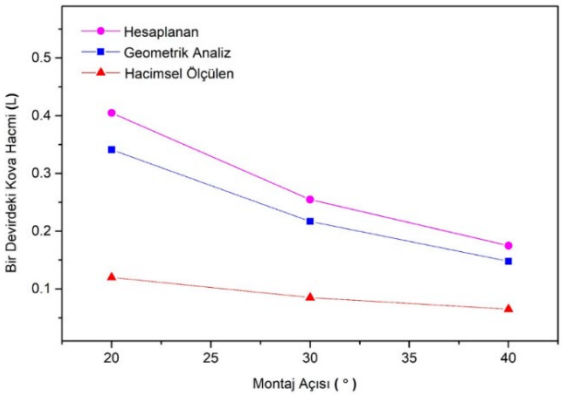

Şekil 13. Bir devirdeki kova hacmi.

Ancak ortaya çıkartılan geometrinin çalışma şartları ile uyumlu olabilmesi tasarımın başarısını göstermektedir. Bu yüzden V_T üç farklı şekilde değerlendirilmiştir. Geometrik analiz ile elde edilen hacimler hesaplama ile elde edilen hacimlerin %85'ine denk gelmektedir. Bu durum hesaplama yöntemindeki hatanın miktarını göstermektedir. Çünkü geometrik analiz sonuçları hesaplama yöntemine göre daha net sonuçlardır. Hacimsel ölçüm sonuçları ise 20°, 30° ve 40°'de sırasıyla hesaplamanın %29, %33 ve %37'sine denk gelmektedir. Deney sonuçları da hacimsel ölçüm sonuçlarına benzer şekilde hesaplanan hacimlerin %28, %31 ve %35'ine denk gelmektedir. Ölçüm sonuçları ile deney sonuçlarının birbirine yakın olması ve hesaplanan hacmin 1/3'üne denk gelmesi giriş su hacmi seviyesinin düşük kalmasından kaynaklanmak-tadır. Lyons vd.'nin elde ettiği sonuçlar ile bu çalışmanın sonuçları örtüşmektedir [22]. DAP yatakları giriş su hacminin seviyesinin yükseltilmesini kısıtlamaktadır. Bu durumda kova hacimleri girişte dolmadığı için yeterli seviyeye ulaşamamaktadır. Bunun için DAP'ın giriş seviyesinin yükseltilmesi gerekir. Bu durumda da basma yüksekliği azalacaktır. Dikkat çeken başka bir konu ise montaj eğim açısı arttıkça kovanın dolma oranının artmasıdır. Buna göre yüksek eğimlerde Arşimet Pompaların kovalarının dolması girişteki su seviyesi az olsa bile artmaktadır. Yani giriş su seviyesinin düşük olduğu yerlerde montaj eğim açısı yüksek tutularak tasarım yapılabilir. Ancak bu durumda Arşimet pompaların devrinin artırılması gerekir. Ancak Arşimet pompaların devirlerinin kısıtlı olduğu gözden kaçırılmamalıdır [2,6,13]. Pompanın dönme hızı devir ölçü sensörü ile okunmuştur. Devir ölçü sensörü, bir sistemdeki dönme hareketini algılayan ve bu hareketin hızını veya frekansını ölçen bir sensör olarak tasarlanmıştır. Pompanın dönme hızını istenilen devirde döndürerek sabit deney sonuçları elde edilmiştir. Deneyler nominal çalışma devrine yakın bir devir olan 70 d/d'da yapılmıştır.

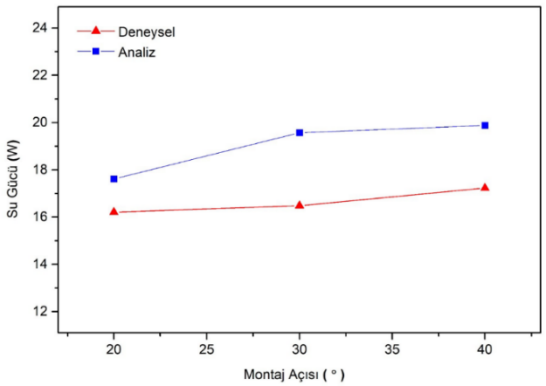

Şekil 14. Montaj açısına bağlı olarak su gücünün değişimi.

Deneylerde, model DAP'ın montaj açısı 20º, 30º ve 40º'ye ayarlandıkça basma yüksekliği de 0,20, 0,3 ve 0,386 m olmuştur. Debi değerleri eğim arttıkça %30-44 oranında azalmasına rağmen basma yüksekliğindeki %46-88 'lik artışlar su gücünde önemli bir değişikliğe sebep olmamıştır. Analizde ise eğim açısı arttıkça su gücünde %11 civarında bir artış olmuştur (Şekil 14). Bu durum DAP modelinin 3D yazıcı ile imalatı esnasında ortaya çıkan yüzey pürüzlülüğünün fazlalığından (kanatların yüzey pürüzlülüğü 350µm'den büyüktür) kaynaklanmaktadır. Helislerin üretimi esnasında ortaya çıkan desteklerden ve eğimli imalattan dolayı yüzeylerde gözle görülebilir derin izler içeren yüzey pürüzlülükleri gözlemlenmiştir. Yüzey pürüzlülüğü su ile yüzeyler arasındaki adhezyon kuvvetlerini arttırdığı için deneysel verim ile analiz verimi arasındaki fark da artmıştır.

Bir devirde süpürülen su hacminin montaj açısına göre değişimi incelendiğinde 20º 'de deneysel değer ile simülasyon değeri arasında %8'lik bir fark olduğu görülmektedir. 30º 'de bu fark %16 seviyesine çıkarken 40º 'de %13 seviyesine gerilemektedir (Şekil 15). Bir devirde süpürülen su hacminin montaj açısı arttıkça azalması, DAP tasarımlarında montaj açısı arttıkça adım sayısının da azaltılması veya helis sayısının arttırılması gerektiğini ortaya koymaktadır. Tasarımda artan ve optimize edilmesi gereken parametre sayısı DAP tasarımında sadece matematiksel modellerle yapılan tasarımların istenilen performansı

ortaya koymakta zorlanacağını göstermektedir. Bu yüzden CAD modelleri üzerinden Geometrik Analiz yapmak da uygulama öncesi tasarımcılara yardımcı olacaktır.

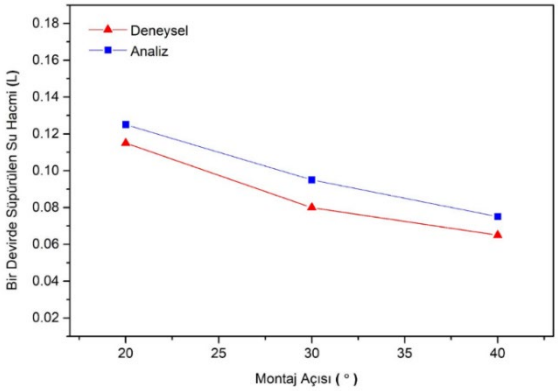

Şekil 15. Bir devirde süpürülen su hacminin (V_T) montaj açısına göre değişimi.

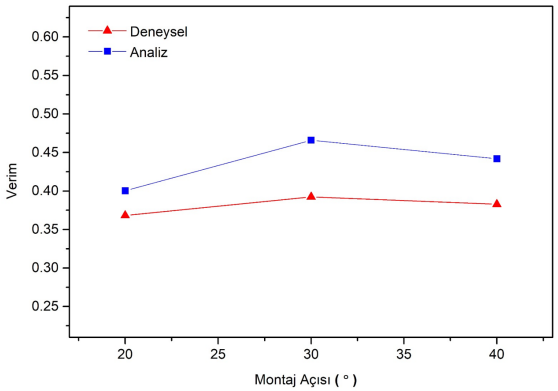

Şekil 16. Montaj açısına göre verim değişimi.

Verim eğrisi klasik bir santrifüj pompanın verimi ile benzerlik göstermektedir. Montaj açısı 20º iken deneysel verim analize göre %2,4 düşükken, montaj açısı 30º 'de en yüksek değerine ulaşıp montaj açısı yükseldiğinde tekrar %3 civarında [15,17] düşmektedir (Şekil 16). DAP'da düşük montaj açısında büyük V_T değerinde daha az düşü varken montaj açısı yükseldikçe daha düşük V_T ve daha yüksek düşüde çalışmasına rağmen verim değerinde çok büyük değişimler olmamaktadır. Bu durum Arşimet pompaların hacimsel olarak çalışmasından ve DAP'ın KAP'a göre sızıntı kaybı oluşturmamasından kaynaklanmaktadır.

4. SONUÇ VE ÖNERİLER

Bu çalışmada KAP'ların bir alternatifi olarak DAP geliştirilmiş, kova hacmi doldurma performansı ve pompa performansı montaj açısına göre değerlendirilmiştir. Arşimet pompalarının montaj açıları azaldıkça memba tarafının suya batma yüksekliğinin artması gerekir. Bu da Arşimet pompalarının montaj açıları azaldıkça boyunun daha uzun olmasını gerektirmekte ve dolayısı ile maliyetleri de artmaktadır. Tam tersi bir durum da şu şekilde ortaya çıkmaktadır; Arşimet pompaların montaj açıları azaldıkça kova hacimleri artmaktadır. Dolayısı ile daha uzun adımlarda daha az helis ile Arşimet pompalar üretilmektedir. Montaj açısı arttıkça kova hacmi küçüldüğü için helis adımlarının azaltılması ve/veya helis sayısının arttırılması gerekmektedir. Bu durumlar Arşimet pompa tasarımında optimizasyonu ve dolayısı ile analizi zorunlu hale getirmektedir. HAD analizleri ile DAP'ların performansları %1'e düşen hata ile hesaplanabilmektedir. Geometrik Analiz ile Arşimet pompaların kova hacimleri %100 doğrulukta hesaplanabilmektedir. Bu durum Arşimet Pompaların tasarımın CAD programları ile optimize edilebileceğini göstermektedir.
Gelecek çalışmalarda DAP'ların çalışma devrine ve montaj açısına bağlı debi değişimleri incele-nerek kova doldurma performansını ve dolayısı ile debisini arttırıcı tasarımsal yenilikler geliştirilecek-tir.

TEŞEKKÜR

Bu çalışma, 1919B012109877 numaralı proje kapsamında TÜBİTAK tarafından desteklenmiştir.

KAYNAKLAR

1. Monserrat J., Ortiz RG., Cots L., Barragán J., "Energy Saving in a Variable-Inclination Archimedes Screw", Irrigation & Drainage Systems Engineering, Vol. 4 Issue 1, Pages 1-4, 2016.

2. Nagel, G., "Archimedian Screw Pump Handbook", Pages 10-13, RITZ Pumpenfabrik OHG, Schwäbisch Gmünd, 1968.

3. Askari Asli-Ardeh E, Mohsenimanesh A., "Determination of effective factors on power requirement and conveying capacity of a screw conveyor under three paddy grain varieties", The ScientificWorld Journal, Vol 2012, Issue 1, Pages 1-5, 2012.

4. Villacrés J, Barczyk M, Lipsett M., "Literature review on Archimedean screw propulsion for off-road vehicles", Journal of Terramechanics, Vol. 108. Issue 1, pages 47–57, 2023.

5. Yu H, Janiga G, Thévenin D. "Computational Fluid Dynamics-Based Design Optimization Method for Archimedes Screw Blood Pumps Artif Organs"; Vol. 40, Issue 1 pages 341–52, 2016

6. Dellinger G, Simmons S., Lubitz WD., Garambois PA., Dellinger N., "Effect of slope and number of blades on Archimedes screw generator power output", Renewable Energy, Vol. 136 Issue 1, Pages 896-908, 2019.

7. Dellinger G., Garambois PA., Dellinger N., Dufresne M., Terfous A., Vazquez J., Ghnaim A., "Computational fluid dynamics modeling for the design of Archimedes Screw Generator", Renewable Energy, Vol. 118, Issue 1, Pages 847-857, 2018.

8. Dellinger G., Terfous A., Garambois PA., Ghenaim A., "Experimental investigation and performance analysis of Archimedes screw generator", Journal of Hydraulic Research, Vol. 54, Issue 2, Pages 197-209, 2016.

9. Khan A., Simmons S., Lyons M., Lubitz W., "Inlet Channel Effects On Archimedes Screw Generators ", CSME International Congress, Pages 1-5, Toronto, 2018.

10. Simmons S, Songin K, Lubitz W., "Experimental investigation of the factors affecting Archimedes screw generator power output ", HYDRO 2017, Pages 1-12, Seville, 2017.

11. Lyons M., Lubitz WD., "Archimedes screws for microhydro power generation", Proceedings of the ASME 2013 7th International Conference on Energy Sustainability, Pages 1-8, Minneapolis, 2013.

12. Simmons S, Dellinger G, Mendes CE, Lubitz W. "Development of a Computational Fluid Dynamics Model for Archimedes Screw Pumps" Canadian Society for Civil Engineering International Congress, Pages 1-22, Moncton, 2023.

13. Simmons S, Miller L, Saudagar MF, Mendes C, Yoosefdoost A, Lubitz W. "An experimental study of archimedes screw pump efficiency" , Proceedings of the Canadian Society for Mechanical Engineering International Congress, Pages 1-7, Sherbrooke, 2023.

14. Rohmer J., Knittel D., Sturtzer G., Flieller D., Renaud J., "Modeling and experimental results of an Archimedes screw turbine", Renewable Energy, Vol. 94 Issue 1, Pages 136-146, 2016.

15. Waters S., Aggidis GA., "Over 2000 years in review: Revival of the Archimedes Screw from Pump to Turbine", Renewable and Sustainable Energy Reviews, Vol. 51 Issue 1, Pages 497-505, 2015.

16. Chan WL, Jamaludin UK, Azahari NS., "Archimedes Screw Pump Efficiency Based on Three Design Parameters using Computational Fluid Dynamics Software - Ansys CFX", 7th International Conference on Mechanical Engineering Research, Phys Conf Ser. Kuantan, Pahang, Pages 1-11, 2024

17. Erinofiardi, Nuramal A., Bismantolo P., Date A., Akbarzadeh A., Mainil AK., Suryono A.F., "Experimental Study of Screw Turbine Performance based on Different Angle of Inclination", Energy Procedia, Vol. 110 Issue 1, Pages 8-13, 2017.

18. Shimomura M., Takano M., "Modeling and Performance Analysis of Archimedes Screw Hydro Turbine Using Moving Particle Semi-Implicit Method", Journal of Computational Science and Technology, Vol. 7, Issue 2, Pages 338-353, 2013.

19. Rorres C., "The Turn of the Screw: Optimal Design of an Archimedes Screw", Journal of Hydraulic Engineering, Vol 126, Issue 1, Pages 72-81, 2000.

20. Nuernbergk DM., Rorres C., "Analytical Model for Water Inflow of an Archimedes Screw Used in Hydropower Generation.", Journal of Hydraulic Engineering, Vol 139, Issue 2, Pages 213-220, 2013.

21. Yermurat B., Seçgin Ö., Taşdemir V., "Multi-material additive manufacturing: investigation of the combined use of ABS and PLA in the same structure" Material Testing, Vol 65, Issue 7, Pages 1119-1126, 2023.

22. Lyons M., Simmons S., Fisher M., Williams JS., Lubitz WD., "Experimental Investigation of Archimedes Screw Pump.", Journal of Hydraulic Engineering, Vol 146, Issue 8, Pages 1-10, 2020.

ULUSLARARASI 3B YAZICI TEKNOLOJİLERİ
VE DİJİTAL ENDÜSTRİ DERGİSİ

INTERNATIONAL JOURNAL OF 3D PRINTING
TECHNOLOGIES AND DIGITAL INDUSTRY

ISSN:2602-3350 (Online)

URL: https://dergipark.org.tr/ij3dptdi

USING 3-DIMENSIONAL MODELS AS TEACHING TOOLS IN SCIENCE EDUCATION FOR PRIMARY SCHOOL STUDENTS

Yazarlar (Authors): Ayşegül ASLAN, Sinem Gül AVCI, Melike Şeyma GÖKÇÜ

Bu makaleye şu şekilde atıfta bulunabilirsiniz (To cite to this article): *Aslan A., Avcı S. G., Gökçü M. Ş., "Using 3-Dimensional Models as Teaching Tools in Science Education for Primary School Students" Int. J. of 3D Printing Tech. Dig. Ind., 8(2): 237-254, (2024).*

DOI: 10.46519/ij3dptdi.1473140

Araştırma Makale/ Research Article

Erişim Linki: (To link to this article): https://dergipark.org.tr/en/pub/ij3dptdi/archive

USING 3-DIMENSIONAL MODELS AS TEACHING TOOLS IN SCIENCE EDUCATION FOR PRIMARY SCHOOL STUDENTS

Ayşegül ASLAN[a]*, Sinem Gül AVCI[b], Melike Şeyma GÖKÇÜ[b]

[a]Trabzon University, Fatih Faculty of Education, Secondary Science and Math Education Department, TÜRKİYE
[b]Trabzon University, Fatih Faculty of Education, Primary Education Department, TÜRKİYE

* *Corresponding Author: :aysegulaslan@trabzon.edu.tr*

(**Received:** 26.04.2024; **Revised:** 25.07.2024; **Accepted:** 20.08.2024)

ABSTRACT

This research aims to identify the concepts that elementary school students struggle to understand in their science classes and to overcome these difficulties by utilizing a design thinking model. Specifically, the impact of instructional methods based on the use of 3D models on students' academic achievements has been examined. The study adopted a mixed method approach. The sample of the research consists of 3rd grade (N=31) and 4th grade (N=29) students attending an elementary school in Trabzon. This study used a mixed-method research design. Before using the final 3D models in the lessons, a "Concept Achievement Test" consisting of 10 questions each was administered as a pre-test to the students. One week after the pre-tests were administered, lessons were given using the final 3D models developed by the researchers. These models were used interactively with the students in the classroom environment for two class hours. Three days after this interactive lesson process using the models, post-tests were administered to evaluate the learning levels of the students. Comparison of the pre-test and post-test results revealed a statistically significant improvement in favor of the post-test for both 3rd grade ($t_{(sd)}$=-5.005; $p<.05$) and 4th grade ($t_{(sd)}$=-2.813; $p<.05$) students. In analyzing the data, a dependent samples t-test was used on the students' test results. In addition, in the qualitative dimension of the study, semi-structured interviews with students and teachers and classroom observations were also conducted. The results of the research demonstrate that the design thinking approach and three-dimensional models enhance understanding and comprehension levels in elementary school science classes. These findings can serve as an important resource for educators and policymakers in developing teaching methods that support active learning processes and encourage conceptual understanding.

Keywords: Science Education, 3D Model, Teaching Material, Primary School Students.

1. INTRODUCTION

The challenges in primary school science education are multifaceted, encompassing various aspects that affect both teachers and students. Primary teachers' attitudes, competence and self-efficacy towards science teaching are critical for effective science teaching [1]. Limited science pedagogical content knowledge among primary school teachers can lead to heavy reliance on activities that may not effectively support scientific conceptual awareness or learning [2]. Addition, challenges affecting learner performance in science include the medium of instruction, lack of adequate teaching and learning resources, overcrowded classrooms and learner indiscipline [3]. Despite reported increases in primary teachers' knowledge of science and confidence in teaching, difficulties remain, particularly in the area of physical science and uncertainty about higher-level scientific ideas [4].

Furthermore, primary school teachers' self-efficacy in teaching science is of great importance and can significantly impact students' interest and success in science-related subjects at higher education levels [5-7]. The influence of higher-order thinking and metacognitive skills on hands-on teaching in

science among primary school teachers is also a critical aspect to consider [8]. Moreover, the hesitance of primary school teachers to teach science can be discouraging and may contribute to gaps in science education in the foundation phase [9]. Implementing innovative approaches, such as using multimedia boards for visualization and conducting pedagogical discussions, can enhance science teaching in primary schools [10]. Additionally, exploring the feasibility of implementing experimental inquiry approaches in primary schools is crucial for promoting effective science teaching and learning [11]. Addressing challenges encountered in the teaching and learning of natural sciences in rural schools is also essential for ensuring equitable access to quality science education [12]. Overcoming challenges in primary science teaching requires a comprehensive approach that takes into account teacher attitudes, competencies and self-efficacy, as well as available resources and innovative teaching approaches [13]. By addressing these challenges, it is possible to improve the quality of science education at the primary school level, thereby laying a strong foundation for students' future academic and professional success. Based on the provided references, the concept of "Student-Centered Design-Focused Learning" can be comprehensively understood through the integration of design thinking principles and student-centered learning approaches [14].

Lee and Hannafin [14], present a design framework that enhances engagement in student-centered learning by emphasizing ownership, active learning, and knowledge sharing. This framework aligns with the principles of student-centered design-focused learning, as it promotes students' active involvement in their learning process and encourages them to take ownership of their educational journey. Moreover, Morel [15] discusses the combination of constructivist, constructionist, and self-determination theories to address student-centered learning, highlighting the importance of contextualizing the learning experience. This approach resonates with the idea of student-centered design-focused learning, as it emphasizes the need to tailor the learning experience to the individual needs and interests of students, thereby fostering a more personalized and engaging educational environment. Additionally, [16] explore the pedagogic sense of design thinking in higher education, particularly in the context of problem-based learning and autonomous student decision-making. This aligns with the principles of student-centered design-focused learning, as it emphasizes the importance of empowering students to make autonomous decisions and take an active role in their learning process. Furthermore, the work of [17] emphasizes the significance of student-centered learning in acknowledging students' voices as central to the learning experience. This is consistent with the fundamental principles of student-centered, design-focused learning, which emphasize the active participation and input of students in shaping their educational experiences.

The implementation of 3D models in primary science instruction has been internationally recognized for enhancing students' grasp of scientific concepts. Educational studies across various countries have demonstrated that these innovative tools bolster engagement and facilitate a deeper understanding of complex principles. For instance, 3D printing has been identified as an excellent method for fabricating 3D models of molecules and extended solids, which has been shown to enhance students' comprehension of chemistry concepts [18]. Additionally, the use of 3D models has been found to facilitate the learning of material in chemistry education, as reported in student surveys [19]. Furthermore, the incorporation of 3D models in science education has been supported by research, particularly for teaching spatial concepts such as atomic orbitals and molecules [20].

In addition to their impact on student learning, 3D models have also been recognized for their potential in various fields. For instance, 3D technology has revolutionized the field of Health Sciences by facilitating low-cost manufacturing and custom surgical devices, 3D models for use in preoperative planning, and fabricated biomaterials [21]. Furthermore, the availability of 3D models on the internet is rapidly expanding, providing valuable resources for both students and educators [22]. The integration of 3D printing technology in education has been driven by the concepts of Science, Technology, Engineering, and Mathematics (STEM), emphasizing the broader implications of 3D models beyond science

instruction [23]. Three-dimensional models presented to students play an important role in the learning of science concepts. These models enable students to visualize events they cannot observe, such as cell division, gene expression, heat transfer, etc. [24]. Moreover, the use of dynamic visualizations helps students to process information better, prevents misunderstandings (conceptual misconceptions), and reduces cognitive load [24]. Anđić, et. al. [25] aimed to determine the pre and post-implementation knowledge of primary school students on plant and animal cells and their views on the use of 3D models in biology education. The results of the study have shown that 3D models contribute to the learning of the students by improving their ability to count, identify, and visualize the cell and its parts, as well as correcting some of their misconceptions and enhancing communication in the classroom. In conclusion, the utilization of 3D models in primary science teaching offers a promising avenue for enhancing science education by providing students with interactive and visually stimulating learning experiences. This approach aligns with the broader trends in educational technology and instructional design, emphasizing the importance of technology-based learning and innovative instructional strategies in primary science education [26].

1.1. Purpose of the Study

This study aims to identify the topics that primary school students have difficulty in understanding in the science course and to overcome these difficulties by using the design thinking model. In particular, the effect of teaching methods based on using 3D models in science teaching on students' academic achievement was examined. In addition, students' opinions on the use of 3-dimensional solid models in science lessons were also taken. In line with this general purpose, answers to the following questions were sought:

- What are the opinions of primary school teachers about the topics that students have difficulty in understanding in science course units?
- What is the effect of using the teaching method based on using 3D models in science lessons on students' academic achievement?
- What are the opinions of the students about the use of 3D models in the lessons?

2. METHOD

2.1. Research Design, Research Variables and Ethics

This research adopted a mixed-method design, which is essentially an approach where data is gathered using multiple methods to bolster their reliability and validity, effectively mitigating the drawbacks of both qualitative and quantitative data [27.] Specifically, a sequential explanatory mixed model was employed, with a predominant emphasis on quantitative methodologies. The impact of the practice was gauged using quantitative data collection instruments, while the perspectives of the experimental group on the practice were elicited through the concurrent use of both qualitative and quantitative approaches. The study was conducted after permission had been obtained from the Social and Humanities Scientific Research and Publication Ethics Committee of Trabzon University (dated 17.11.2023 and numbered E-81614018-000-2300063426).

In the mixed methods research design, quantitative data from pre- and post-tests were rigorously integrated with qualitative insights from interviews and observations. This approach allows not only to measure progress in students' understanding of science concepts, but also to explore the subtle ways in which 3D models facilitate learning. In particular, it offers a holistic view of learning outcomes by examining how students' interactions with these models contribute to their conceptual understanding. A stratified random sampling technique was used to ensure a representative sample. This involved categorising the population according to key demographic characteristics and then randomly selecting participants from each category, thereby maximising the diversity and representativeness of the sample. Such a methodological approach strengthens the validity of the findings by providing a sound basis for both quantitative and qualitative analyses.

2.2. Research Group

The study group consisted of 31 3rd grade and 29 4th grade students randomly selected from a primary school in Akçaabat district of Trabzon

province and 20 classroom teachers working in different schools in Trabzon province.

2.3. Data Collection Tools and Data Collection Process

Within the scope of the study, two different data collection tools were used for students and teachers. In the data collection tool prepared for teachers, a form including the units and subject areas in the 3rd and 4th grade science curriculum was created. Teachers were asked to fill out "Teacher Opinion Form" with the subjects that their students struggled to understand and that they were unable to embody in the teaching process. As the second data collection tool, "Concept Achievement Tests" consisting of ten questions on the related subjects of the science course were created separately for 3rd and 4th grade students. In addition, in the Concept Achievement Test, students were also asked (after implementation) their opinions on the use of 3D models in science lessons with three open-ended questions. The open-ended questions asked to students in the post-test were respectively: "What did teaching this course using the 3D model contribute to your learning? Can you explain?", "Did teaching this course using a 3D model facilitate your learning? Can you explain?" and "Which other subjects would you like to be taught using 3D models? Mark (x) in the table below and write why". The achievement tests were administered to the students as pre-test and post-test. In the preparation of the achievement tests, the "Attainment Comprehension Tests" published by the Republic of Türkiye Ministry of National Education were utilized. In the development of the data collection tools, "Teacher Opinion Form" and "Concept Achievement Tests", a rigorous process was carried out to ensure their validity and reliability. These instruments were designed in consultation with science education experts to accurately measure educators' perceptions and students' conceptual understanding and views. The data collection tools used in the study and the data collection process are shown in Figure 1.

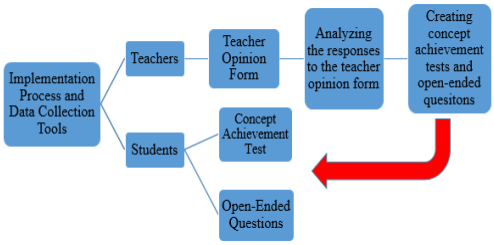

Figure 1. Data Collection Tools and Process

Within the scope of the study, first of all, based on the design thinking model, in the "Empathy" stage, the opinions of 20 classroom teachers were obtained by using the "Teacher Opinion Form" prepared by the researchers about the subjects that primary school students have difficulty in understanding in the science course units. Afterwards, statistical and descriptive analyses of the teachers' responses were conducted and it was determined that "The Structure of the Earth" for the 3rd grade level and "The Structure of the Earth's Crust" for the 4th grade level were the topics that students had difficulty in understanding. In the "Define the Problem" and "Generate Ideas" stages of the Design Thinking Model (DTM), the researchers decided what kind of 3D models (Figure 2) could be designed for teaching these topics.

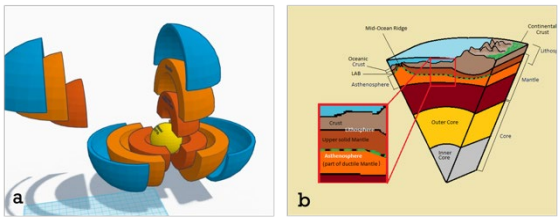

Figure 2. (a) An Exploded View of the Different Layers of Earth, **(b)** The Structural View of the Earth's Crust

After deciding how the 3D models would be, 2D drawings were made and designs were made by the researchers in the "Prototype Development" stage using 3D pens. The preliminary designs of the models were drawn on the computer and printed out on 3D printers (Figure 3, Figure 4).

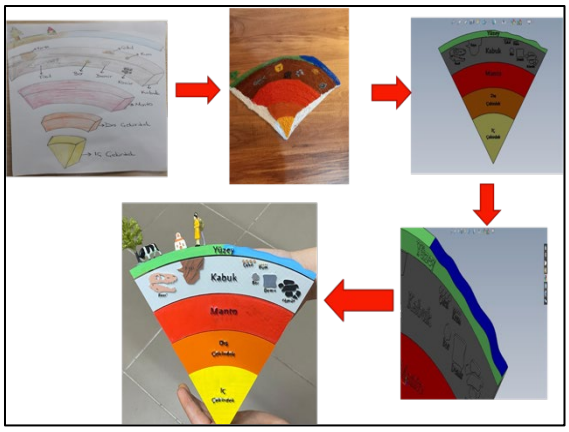

Figure 3. 3D Model Design Stages of the Structure of the Earth's Crust (4th Grade Students)

Figure 3 shows the 2D drawing of the Structure of the Earth Crust model, the drawing made using a 3D pen, and finally the image of the model designed in the drawing program and printed out using a 3D printer. In Figure 4, the 2D drawing of the Structure of the Earth model, the drawing made using a 3D pencil, and finally the image of the 3D printer output of the model designed in the drawing program are shared.

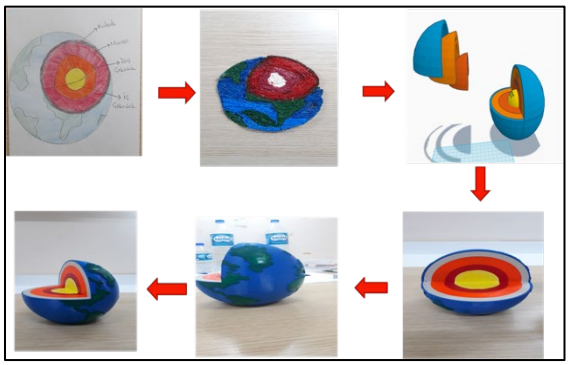

Figure 4. 3D Model Design Stages of the Structure of the Earth (3rd Grade Students)

Before the use of the final models in the lessons, the "Concept Achievement Test" consisting of 10 questions was applied to the students as a pre-test. One week after the pre-test implementation, the use of the final models in the teaching process was realized by the researchers. One week after the interactive use of 3D models in the lesson, post-tests were applied. In the post-test, students were also asked their opinions about the use of 3D models in science lessons with three open-ended questions. Some photos from the implementation are shared on Figure 5.

Figure 5. Photos from the implementation process

2.4. Data Analysis

This study employed a mixed-method research design to investigate the effectiveness of using 3D models in primary science education. The analysis involved both quantitative and qualitative data to identify the subjects that are difficult in primary school science learning and to offer a comprehensive understanding of the impact of 3D models on students' learning. The quantitative data obtained from the teacher opinion form were transformed into a frequency table. Qualitative data were analyzed descriptively. Other quantitative data were obtained from the pre and post-test scores obtained from the Concept Achievement Test administered to 3rd and 4th grade students. SPSS program was used to analyze the quantitative data. Comparative t-test was preferred due to the normal distribution of the data obtained. Content analysis was preferred to analyze the qualitative data obtained from the Concept Achievement Test.

In the qualitative analysis, a detailed method of content analysis was used to examine the transcripts of the interviews and the notes of the observations. Initially, two researchers independently examined a subset of the data, developing a preliminary codebook and providing a grounded approach to the data itself. Regular meetings were held to discuss and refine these codes, aiming for inter-coder reliability. The collected data was compared by the researchers at that point, and coding and categorization made by each of them were examined. Once consensus was reached, the final codebook was applied to the entire dataset. Using the formula developed by Miles and Huberman (1994), the percentage of agreement

between the three researchers was determined to be 0.93. During the qualitative data analysis, 3rd grade students were coded as S_3 and 4th grade students were coded as S_4.

3. RESULTS

In the presentation of the findings, the implementation steps carried out in two stages were taken into consideration. First, the findings obtained from the analysis of teacher responses were presented, and then the findings of the achievement test and semi-structured interview form applied to the students were presented.

3.1. Results of the First Sub-question

Table 1 shows the frequency distributions of the 3rd grade science course units, topics and subject areas and the frequency distributions of the responses of the teachers regarding the learning difficulties of these units and subject areas for students.

Table 1. Frequency Table of the Difficulties Experienced for The Units and Subject Areas for the 3rd Grade Science Course

Units	Subject Areas	(f)
F.3.1. Let's Know Our Planet/ Earth and Universe	The Shape of the Earth	7
	Structure of the Earth	14
F.3.2. Our Five Senses /Living Things and Life	Sense Organs and Their Duties	3
F.3.3. Let's Recognize Force/ Physical Phenomena	Movement Characteristics of Entities	5
	Moving and Stopping Objects	5
F.3.4. Let's Know Matter /Matter and Its Nature	Properties Characterizing Matter	8
	States of Matter	9
F.3.5. Light and Sounds / Physical Phenomena in Our Environment	The Role of Light in Vision	3
	Light Sources	3
	Sounds Around Us	1
	The Role of Sound in Hearing	2
F.3.6. Journey to the World of Living Things / Living Things and Life	Recognize the Things Around Us	3
	Me and My Environment	3
F.3.7. Electric Vehicles /Physical Phenomena	Electrical Equipment	4
	Electricity Sources	7
	Safe Use of Electricity	4

According to Table 1, the "Structure of the Earth" subject is seen by teachers as the topic that students have the most difficulty in understanding among the 3rd grade science course topics. Teachers state that students have difficulty in making associations with concepts that they do not encounter in their daily lives, which affects the retention of the information learned. Teachers emphasized that abstract concepts should be supported with concrete materials and 3D displays. In particular, it is stated that explaining topics such as the structure of the Earth with concrete examples will help students understand. The importance of using visual materials and play dough in education is emphasized. It is stated that these materials can contribute to students' permanent learning of both information and visuality.

Table 2 shows the frequency distributions of the 4th grade science course units, and subject areas and the frequency distributions of the responses of the teachers regarding the learning difficulties of these units, and subject areas for students.

Table 2. Frequency Table of the Difficulties Experienced for the Units And Subject Areas for the 4th Science Course

Units	Subject Areas	(f)
F.4.1. Movements of the Earth's crust and our Earth /Earth and the Universe	Structure of the Earth's Crust	17
	Movements of our Earth	10
F.4.2. Our Food / Living Things and Life	Nutrients and Their Properties	13
F.4.3. Effects of Force /Physical Phenomena	Effects of Force on Objects	8
	Force Applied by Magnets	8
F.4.4. Properties of Matter /Matter and Nature	Properties Characterizing Matter	4
	Measurable Properties of Matter	10
	States of Matter	4
	Change of Matter Under the Effect of Heat	6
	Pure Substance and Mixture	9
F.4.5. Lighting and Sound Technologies / Physical Events	Lighting Technologies	3
	Proper Lighting	4
	Light Pollution	4
	Sound Technologies from Past to Present	7
	Sound Pollution	4
F.4.6. Human and Environment / Living Things and Life	Conscious Consumer	6
F.4.7. Simple Electric Circuits/ Physical Phenomena	Simple Electric Circuits	12

According to Table 2, it is seen that students mostly have difficulty in understanding concepts such as the structure of the earth's crust and the movements of the earth.

It was stated by the teachers those students had difficulties especially in the subject of "The Earth's Crust and the Movements of the Earth" due to conceptual and procedural knowledge. Students have difficulty in comprehension because they do not know the concepts and vocabulary sufficiently, cannot make associations with daily life and cannot understand abstract concepts without supporting them with concrete examples. Students confuse topics such as rotational and entanglement motions. While students have fewer problems with layers that can be observed, they cannot fully comprehend layers that cannot be observed. Teachers pointed out that students had difficulty in understanding concepts that they could not observe or hold in their hands and emphasized the importance of using animations and materials to overcome this situation. However, three teachers stated that students did not experience any difficulty in the topic of the "Structure of the Earth's Crust".

3.2. Results of the Second Sub-question

The results of the statistical comparison of the scores obtained from the achievement test applied to 3rd grade students before and after the implementation are given in Table 3.

Table 3. Comparison of the 3rd Grade Students' Achievement Pre-test and Post-test Scores

	N	$\bar{x}$	*sd*	*t*	*p*
Pre-test	31	72.26	16.27	-5.00513	0.00002
Post-test	31	87.10	10.71		

As a result of the comparative t-test, a significant difference was found in favor of the post-test ($t_{(sd)}$=-5.0051; p< .05)

The results of the statistical comparison of the scores obtained from the achievement test

applied to 4th grade students before and after the implementation are given in Table 4.

Table 4. Comparison of the 4th Grade Students' Achievement Pre-test and Post-test Scores

	N	$\bar{x}$	*sd*	*t*	*p*
Pre-test	29	73.79	18.21	-2.8134	0.00886
Post-test	29	81.03	21.44		

As a result of the comparative t-test, a significant difference was found in favor of the post-test ($t_{(sd)}$=-2,813; p<.05).

3.3. Results of the Third Sub-question

After the using 3D models in science courses, the 3rd and 4th grade students were given the interview form containing three questions. In line with the answers given by the students, the answers given to these three questions were put together, and the results are presented in Table 5, Table 6 and Table 7.

The results derived from analyzing the responses to the first open-ended question on the achievement test, which was administered as a post-test following the intervention, are presented below. Here are the codes based on 3rd grade students' expressions of how models or certain teaching methods impacted their learning:

Table 5. Codes and Example 3rd Grade Students' Responses to First Open-Ended Question

Codes	Example Student Responses	Frequency (f)
Conceptual Understanding	"Explained with a model made it better understood." ($S_3$2), "Course dealing with the model helped keep the subject in mind." ($S_3$29)	12
Misconception Correction	"Corrected some misconceptions about the layers of the world." ($S_3$5)	1
Achievement and Success	"I succeeded." ($S_3$6), "My science class made me stronger." ($S_3$20)	2
Prior Knowledge Affirmation	"I already knew." ($S_3$7)	1
Enhanced Engagement	"3D model made me love learning." ($S_3$12), "Learned something new and I learned the lesson." ($S_3$14)	2
Information Acquisition	"3D model provided me a lot of information." ($S_3$25), "Helped me to research and understand more." ($S_3$26)	11
Effective Learning Experience	"Good time to have a good lesson." ($S_3$18), "Better because it was shown on the board and explained with a model." ($S_3$31)	3

Table 5 shows the codes derived from analyzing the responses of 3rd grade students to the first open-ended question on the achievement test administered as a post-test. The table presents various themes such as conceptual understanding, misconception correction, achievement and success, prior knowledge affirmation, enhanced engagement, information acquisition, and effective learning experience. These themes are illustrated with example student responses and their respective frequencies, highlighting the impact of using 3D models on students' learning experiences and understanding of scientific concepts.

The results derived from analyzing the responses to the second open-ended question on the achievement test, which was administered as a post-test following the intervention, are presented below. The codes and sample student responses obtained from the analysis of 31 3rd students' views on how teaching methods (especially models) facilitated their learning are as follows:

Table 6. Codes and Example 3rd Grade Students' Responses to Second Question

Codes	Example Student Responses	Frequency (f)
Enhanced Understanding	"It made it easier because he explained the layers of the world one by one." ($S_3$23), "It was easy because we researched it and because we saw it." ($S_3$26)	17
Learning Reinforcement	"Yes, it made it easier because I repeated the subject and learned new things." ($S_3$4), "It made it easier for me to learn what I didn't know." ($S_3$30)	3
Ease of Learning	"Yes, it made it easier because it is easier to do it with shapes, but it is more difficult to do it by showing it." ($S_3$15), "This lesson was a bit easy for me because we have never had a lesson like this before." ($S_3$29)	8
Success and Achievement	"I succeeded." ($S_3$6)	1
Prior Ease	"It was already easy." ($S_3$7)	1
New Information Acquisition	"Yes, because I have new information in my head." ($S_3$19), "We learned about the Earth's core." ($S_3$22)	2
Attention and Interest	"Models caught our attention at first glance." ($S_3$18)	1
Real-World Connection	"Understood how to recognize the real world made with the model." ($S_3$20)	1

Table 6 presents the analysis of 3rd grade students' responses to the second open-ended question on the post-test. The codes include enhanced understanding, learning reinforcement, ease of learning, success and achievement, prior ease, new information acquisition, attention and interest, and real-world connection. Each code is supported by example student responses, reflecting how the use of 3D models facilitated their learning and comprehension of the lesson topics. The frequency of each code indicates the prevalence of these themes among the student responses.

The frequency values obtained from the analysis of the responses of 3rd grade students to the last open-ended question in the achievement test applied after the implementation are presented in Table 7.

Table 7. Analysis of 3rd Grade Students' Responses to Last Question

Subject Areas	Frequency (f)
The Shape of the Earth	25
Structure of the Earth	27
Sense Organs and Their Tasks	26
Movement Properties of Entities	20
Moving and Stopping Objects	21
Properties Characterizing Matter	16
States of Matter	12
The Role of Light in Vision	16
Light Sources	9
Sounds Around Us	12
The Role of Sound in Hearing	10
Recognize the Things Around Us	16
Me and My Environment	14
Electrical Equipment	17
Electricity Sources	14
Safe Use of Electricity	14

Table 7 summarizes the frequency values obtained from the analysis of 3rd grade students' responses to the last open-ended question on the achievement test conducted after the implementation. The table lists various subject areas and the number of students who expressed interest in being taught these topics using 3D models. The subjects include the shape of the Earth, structure of the Earth, sense organs and their tasks, movement properties of entities, and more. The frequency of responses highlights the students' preferences and perceived benefits of using 3D models for different science topics.

To analyze the opinions of the 31 3rd grade students related to Table 7 and create codes based on their reasons for choosing science courses or topics. The codes created after the students' responses are presented below:

Table 8. Codes and Example 3rd Grade Students' Responses to Last Question

Codes	Example Student Responses	Frequency (f)
Ease and Relevance	"I learn more easily and while I am learning I know things that are relevant to the topic." ($S_3$1), "Because it's easier." ($S_3$28)	2
World Understanding	"I chose it to learn more about the world and other subjects." ($S_3$2), "I didn't know the layers of the earth, and when I did, it was very useful and helpful to me." ($S_3$26)	4
Specific Interests	"For example, I would like to know what harm the layers of the earth can do to people, and I would like to know what the layers of the earth are for." ($S_3$5), "I would like to understand different features, I would like to see different lights, I would like to see different electrical appliances." ($S_3$8)	4
Comprehensive Learning	"I would like to cover all subjects because I am a very curious person." ($S_3$13), "I would like to learn about the shape of the world, the structure of the world, the properties of beings, the states of matter, the sounds in the environment, electricity." ($S_3$30)	5
Teacher Influence	"This is what my own teachers and researcher told me." ($S_3$10)	1
Learning Enjoyment	"Because learning a new subject makes me very happy." ($S_3$14), "Because it would be better and more narrative." ($S_3$31)	3
Personal Preference	"Because I really want to learn what I have marked." ($S_3$15), "Because I like them all and they're all beautiful." ($S_3$19)	5
Novelty and Utility	"I wish our world wasn't round, I wish our sense organs were in charge." ($S_3$23), "The shape of the world, the structure of the world, sense organs and their functions." ($S_3$27)	5
Narrative and Illustration	"I would love to see the topics here in the figure and we would understand everything more easily and it would be a lot of fun." ($S_3$11), "I would like to see all of these issues illustrated." ($S_3$29)	3
Disinterest or Indifference	"None of them." ($S_3$7)	1

Table 8 summarizes the responses of 3rd-grade students regarding their preferred science topics taught using 3D models. The students highlighted that the use of 3D models facilitated easier understanding and engagement, particularly in abstract concepts like the structure of the Earth and the properties of matter. They expressed that visual and tangible representations helped them grasp these concepts better, making learning enjoyable and reinforcing their comprehension. The frequency of responses indicates a strong preference for topics that involve significant visual and spatial understanding, underscoring the effectiveness of 3D models in enhancing learning experiences in science education.

The results derived from analyzing the responses to the first open-ended question on the achievement test, which was administered as a post-test following the intervention, are presented below. Here are the codes based on 4th grade students' expressions of how models or certain teaching methods impacted their learning:

Table 9. Codes and Example 4th Grade Students' Responses to First Open-Ended Question

Codes	Example Student Responses	Frequency (f)
Reinforcement and Recall	"We remembered the topic again because we did it again." ($S_4$1), "So that when the researcher gives a test, we get a high score." ($S_4$12)	3
New Knowledge Acquisition	"I learned how the earth's crust is like and that there are minerals in the core." ($S_4$11), "I learned the subject much better and learned about the hydrosphere lithosphere." ($S_4$22)	9
Enhanced Comprehension	"It gave me a better understanding of the layers of the world because I learned better by modeling." ($S_4$5), "I didn't understand much about the earth's crust, thanks to you, I understood more." ($S_4$21)	9
Enjoyment and Engagement	"It was very fun for me and helped me to reinforce what we know." ($S_4$18), "It gave me fun and curiosity because I am interested in models and Tinkercad." ($S_4$27)	4
No Contribution	"I knew that's why he didn't contribute." ($S_4$14)	1
Learning Strategy Effectiveness	"I understood better, I was happy, I saw the 3D pen." ($S_4$16), "I understood better, I won't be surprised in the exams, we went over it twice and I remembered I better." ($S_4$23)	2

Table 9 presents the responses of 4th-grade students on how 3D models impacted their learning of scientific concepts. The students reported that 3D models significantly improved their comprehension by providing a concrete visual aid to abstract ideas. Many students noted that these models made learning fun and engaging, leading to better retention and understanding of topics such as the Earth's crust and its layers. The frequency of responses highlights the positive impact of hands-on learning tools, with a notable increase in students' enjoyment and interest in science classes.

The results derived from analyzing the responses to the second open-ended question on the achievement test, which was administered as a post-test following the intervention, are presented below. When the responses of 29 4th grade students regarding whether teaching the lesson with models facilitated their learning were analyzed, their opinions were coded thematically as follows:

Table 10. Codes and Example 4th Grade Students' Responses to Second Open-Ended Question

Codes	Example Student Responses	Frequency (f)
Enhanced Learning	"It made it easier because we understand better when there is a model." ($S_4$3), "It made it easier. We hadn't learned many things about that subject and now we have." ($S_4$28)	20
Fun and Engagement	"Yes, because a bit of fun makes us learn better." ($S_4$10), "Yes, it made it easier because the lesson taught with the model instead of paper was very fun and easy for me." ($S_4$18)	5
Repetition and Reinforcement	"Yes, and the more I went over it, the better I understood it." ($S_4$7), "Yes, because we went over it." ($S_4$23)	2
No Significant Effect	"No, because I knew." ($S_4$14), "No, because it doesn't matter whether we work with models or listen to the teacher's explanation, because if we listen, we understand." ($S_4$25)	2
Facilitated Understanding	"It made it easier to see the layers." ($S_4$4), "It made it easier because I learn more easily with the model." ($S_4$24)	11
Educational Accessibility	"It made it easier. We hadn't learned many things about that subject and now we have." ($S_4$28)	2

Table 10 details the 4th-grade students' opinions on whether 3D models facilitated their learning. Many of the students indicated that these models made the lessons easier to understand, emphasizing the effectiveness of visual aids in simplifying complex scientific concepts. The students appreciated the interactive nature of the models, which not only made the lessons more enjoyable but also reinforced their learning through repeated exposure and hands-on engagement. The responses reflect a consensus on the benefits of incorporating 3D models into science education to enhance learning outcomes.

The frequency values obtained from the analysis of the responses of 4th grade students to the last open-ended question in the achievement test applied after the implementation are presented in Table 11.

Table 11. Analysis of 4th Grade Students' Responses to Last Question

Subject Areas	Frequency (f)
Structure of the Earth's Crust	22
Movements of our Earth	18
Nutrients and Properties	13
Effects of Force on Objects	19
Force Applied by Magnets	20
Properties Characterizing Matter	13
Measurable Properties of Matter	15
States of Matter	17
Change of Matter with Heat Effect	15
Pure Substance and Mixture	17
Lighting Technologies	13
Appropriate Lighting	9
Light Pollution	12
Sound Technologies from Past to Present	20
Sound Pollution	10
Conscious Consumer	15
Simple Electric Circuits	15

Table 11 analyzes the 4th-grade students' preferences for science topics to be taught using 3D models. The students showed a strong interest in subjects involving significant visual and spatial elements, such as the structure of the Earth's crust, the effects of force on objects, and the properties of matter. The frequency of responses suggests that students find 3D models particularly useful in understanding and retaining information on these topics. The analysis underscores the potential of 3D models to improve engagement and comprehension in science education, especially for complex and abstract subjects.

To analyze the opinions of the 29 4th grade students related to Table 11 and create codes based on their reasons for choosing science courses or topics. The codes created after the students' responses are presented below:

Table 12. Analysis of 4th Grade Students' Responses to Last Question

Codes	Example Student Responses	Frequency (f)
Curiosity and Interest	"Because I am curious about these issues, and I want to learn." ($S_4$1), "Science is my favorite subject and it interests me." ($S_4$26)	9
Educational Engagement	"I chose these because they are better explained with models." ($S_4$10), "Because with models, it is easier, and I understand it very well and it is very beautiful." ($S_4$19)	5
Improvement and Understanding	"Because I don't know much about those subjects and to learn them in more detail." ($S_4$16), "It confuses me a lot, science is one of my worst subjects." ($S_4$21)	4
Academic Choice	"I chose more science courses because it was fun and beautiful." ($S_4$4), "Because we have two classes a day and because the class is busy." ($S_4$7)	2
Favoritism	"Because it's my favorite subject." ($S_4$12), "Science is my favorite subject and it interests me." ($S_4$26)	2
Educational Necessity	"To learn." ($S_4$6), "Because I want to learn about these things." ($S_4$14)	2
Content Specific	"Light pollution because I would like to learn. I would like to learn the force applied by the magnet because the structure of the earth's crust is fun, I would like to learn the measurable property of matter, I would like to learn how matter can be measured." ($S_4$11), "Because I want to know what pure matter and mixture are." ($S_4$24)	2
Aesthetic or Fun Preference	"I chose more science courses because it was fun and beautiful." ($S_4$4), "It would all be a lot of fun." ($S_4$25)	3

Table 12 categorizes the reasons why 4th-grade students chose specific science topics for 3D model-based learning. The students' responses highlight curiosity and interest in understanding the world around them, as well as the educational engagement and enjoyment derived from interactive learning tools. Many students pointed out that 3D models helped them understand difficult concepts more easily and made learning more fun and engaging. The analysis indicates a strong preference for hands-on, visually stimulating educational methods that enhance students' interest and performance in science subjects.

4. CONCLUSION AND DISCUSSION

Considering the results of the study conducted in two phases, the study indicates that teachers find certain abstract scientific concepts challenging to teach. Teachers observed that students struggle with topics not directly observable or relatable to their daily experiences. The study suggests that teaching methods incorporating visual and tactile elements could significantly enhance understanding. Integrating 3D modeling and printing in classroom instruction can help teach abstract scientific concepts to young learners across elementary, middle, and high school grades [28]. The results indicate a significant improvement in students' comprehension and retention of the structure of the Earth and its layers, when these models are incorporated into the teaching process. 3D printing in education improves students' practical ability, comprehensive quality, observation, concentration, creativity, and learning habits, including autonomous learning and cooperative learning [29]. Teachers noted that students frequently struggle with abstract concepts, finding it challenging to relate these to their daily experiences, ultimately affecting learning retention. Abstract concepts can indeed pose a challenge for students, as they often struggle to relate these concepts to their daily experiences [30] This difficulty can be attributed to various factors, including cognitive development, prior knowledge, and instructional strategies.

According to Piaget's theory of cognitive development, children in the concrete operational stage (ages 7-11) have difficulty understanding abstract concepts because they primarily focus on concrete experiences and struggle with hypothetical and abstract thinking. This developmental stage may explain why students find it challenging to relate abstract concepts to their daily experiences [31]. Furthermore, students' prior knowledge and experiences play a crucial role in their ability to

grasp abstract concepts [32]. When students encounter abstract ideas that are disconnected from their prior experiences, they may struggle to comprehend and internalize these concepts [33-34]. This highlights the importance of building on students' existing knowledge and providing real-world examples to make abstract concepts more tangible and relatable. Instructional strategies also play a significant role in helping students bridge the gap between abstract concepts and their daily experiences. Hmelo-Silver, Duncan, Chinn [34] suggests that incorporating hands-on activities, visual aids, and real-life examples can enhance students' understanding of abstract concepts By providing concrete experiences and tangible connections, educators can help students relate abstract concepts to their daily lives. Educators can enhance the understanding of abstract concepts by relating them to familiar experiences. Moreover, encouraging discussions and critical thinking can help students explore the relevance of abstract concepts in their daily lives, fostering a more meaningful connection to the material [35-36].

In conclusion, the struggle that students face in relating abstract concepts to their daily experiences can be attributed to cognitive development, prior knowledge, and instructional strategies. Understanding these factors is crucial for educators in developing effective teaching methods that support students in comprehending and applying abstract concepts in their daily lives.

The use of 3D models in science lessons shows a positive impact on student achievement. The results suggest that these models make abstract concepts more tangible, aiding in better comprehension and retention. There's a noticeable improvement in students' test scores and conceptual understanding when 3D models are integrated into lessons. The use of 3D models as part of a more interactive and experiential approach in education effectively bridges this gap. By allowing students to handle and explore tangible representations of scientific concepts, these models facilitate a deeper understanding and increased student engagement [37]. The positive shift in students' academic achievements, as evidenced by pre-test and post-test results, underscores the potential of 3D models to enhance educational outcomes [38]. Students responded positively to the use of 3D models. They found these models engaging and helpful in visualizing complex scientific concepts. The hands-on experience provided by these models enhanced their interest in science and facilitated a deeper understanding of the subject matter. Students reported a newfound interest in science subjects, suggesting that the engaging nature of 3D models contributes to a more positive attitude towards learning. This finding is consistent with research indicating that interactive learning tools can significantly impact students' attitudes and interest in science [39]. Additionally, both teachers and students noted the potential of these models to correct misconceptions and reinforce content previously taught, thereby improving overall science literacy [40].

It is possible to say that 3D models can make important contributions in concertizing the subjects and concepts by enabling the transition from virtual objects to physical objects, verifying the theoretical knowledge learned by making applications, recognizing, and eliminating possible misconceptions in this process, and providing students with learning experiences by doing [41]. Many researchers argue that learning environments should be production and application-oriented to raise individuals who can keep up with the needs of the age and have these skills [42]. In this context, teachers and students can use 3D printing technologies in the design and production process of models suitable for the subject or problem situation, for example, in project-based learning activities Pinger [19] highlighted that students can choose what to print and how to print it, creating a platform for constructivist teaching, where educators encourage students to teach themselves how to use the technology. Additionally, Ishutov et al. [43] emphasized that the use of 3D printing in the K-12 environment could better prepare students for careers in emerging fields of technology, including STEM disciplines. Trust and Maloy [44] found that using 3D printing technologies in the teaching process is effective in the development of student skills such as 3D modelling skills, creativity, technology literacy, problem solving, self-learning and critical thinking, which are called 21st century skills.

The use of 3D printing technologies has been shown to have a positive impact on students'

skill development, including cooperation, problem-solving, communication, responsibility, and leadership. For instance, studies have demonstrated that 3D printing technology can be effectively utilized to enhance project-based learning activities, providing students with opportunities to engage in hands-on, experiential learning and fostering interdisciplinary connections across various subjects [19], [41], [45-51]. Furthermore, the use of 3D printing in education has been reported to promote active student involvement in the teaching-learning process and better communication, which are essential skills for collaboration and cooperation [47]. On the other hand, the use of 3D printed models has been found to be directly applicable to students' intended careers, providing them with opportunities to develop leadership skills in their respective fields [51]. The findings show significant improvements in students' understanding of science topics using 3D models. However, the novelty effect is thought to have the potential to influence these results. The increased engagement and enthusiasm often associated with new educational tools may improve performance, a factor that should be considered when interpreting these results. Nevertheless, the integration of 3D models into science education addresses key challenges in teaching abstract concepts, improves academic performance and is well received by students, suggesting a useful approach to primary science education

The design thinking model, which constitutes the main framework of the study, has emerged as an effective method for concretizing abstract concepts in primary school science education and increasing students' academic achievement. By providing students with active learning experiences, this model enabled them to better understand and retain scientific concepts. The results of this study can be an important resource for educators and policy makers in developing teaching methods that support active learning processes and promote conceptual understanding.

5. RECOMMENDATIONS

The following suggestions can be made considering the study's findings regarding the implementation of 3D models in the teaching of science in elementary schools:

- Using 3D models to teach other complex scientific concepts in primary education is a good idea, since it improves student understanding and engagement.
- Give educators the tools and resources they need to successfully integrate 3D models into their lessons. Training on the creation and implementation of these models is part of this.
- More methodically incorporate 3D model-based learning into the science curriculum, making sure that it supports traditional teaching techniques and is in line with learning objectives.
- Encourage more studies examining the usefulness of 3D models for a range of age groups and other subjects. It is important to pursue innovation in technology and model design.
- Emphasize student-centered methods that allow students to actively interact with 3D models to develop their analytical and problem-solving abilities.
- Ensure that sufficient funds are set aside for the acquisition or development of 3D models as well as for the infrastructure required by technology to enable their use.
- Provide a feedback system so that students can voice their thoughts about the implementation of 3D models. This will help shape future modifications and enhancements.
- Future research could benefit from larger, more diverse samples that would enable a more comprehensive examination of these educational tools' impact across different demographic and educational settings.
- Future studies may aim to distinguish between the long-term educational benefits of 3D models and short-term increases in engagement and performance due to their novelty. This distinction is crucial for educators considering integrating innovative tools into their teaching practice.

ACKNOWLEDGES

A part of this study was presented as an oral presentation at the ASES VI. International Scientific Research Conference held in Ankara between 22-24 December 2023. In addition, this study was not published as an article but was published as a pre-print in "Research Square".

REFERENCES

1. Denessen, E., Vos, N., Hasselman, F., & Louws, M. "The relationship between primary school teacher and student attitudes towards science and technology", Education Research International, Vol. 1, Pages 1-7, 2015.

2. Fleer, M. "Supporting scientific conceptual consciousness or learning in 'a roundabout way' in play-based contexts", International Journal of Science Education, Vol. 3, Issue 8, Pages 1069-1089, 2009.

3. Ndjangala, M., Abah, J., & Mashebe, P. "Teachers' views on challenges affecting learners' performance in natural science", International Journal of Evaluation and Research in Education (IJERE), Vol. 10, Issue 1, Pages 48-56, 2021.

4. Jarvis, T. and Pell, A. "Primary teachers' changing attitudes and cognition during a two-year science in-service programme and their effect on pupils", International Journal of Science Education, Vol. 26, Issue 14, Pages 1787-1811, 2004.

5. Doğru, M. S., & Demirbaş, İ. "The relationship between perceptions of multicultural competence and democratic values: Examining science teachers working with international students", Journal of International Students, Vol. 11, Issue 1, Pages 24-40, 2021.

6. Kazeni, M. "Early primary school teachers' perceptions about science and science process skills: A case study in South Africa", Education and New Developments, Pages 18-22, 2021.

7. Yildiz, Z. "Science teaching self-efficacy beliefs of pre-service teachers: context of technological pedagogical content knowledge and visual metaphors", Journal of Baltic Science Education, Vol. 21, Issue 6, Pages 989-1003, 2022.

8. Sulaiman, T., Subramaniam, P., & Kamarudin, N. "The influence of higher order thinking and metacognitive skills towards hands-on teaching among primary school science teachers", International Journal of Academic Research in Progressive Education and Development, Vol. 8, Issue 4, Pages 245-258, 2019.

9. Arthur, J., Beni, S., & Stears, M. "Teaching science in the foundation phase: where are the gaps and how are they accounted for?", South African Journal of Childhood Education, Vol. 9, Issue 1, Pages 1-9, 2019.

10. Vasylenko, S. "Experience using multimedia boards for visualization, conducting pedagogical discussions, developing interactive exercises for primary school", Open Educational E-Environment of Modern University, Vol. 3, Pages 173-185, 2017.

11. 馬漢煊, H. "Teaching about science teaching and learning through an experimental inquiry approach", Australian Journal of Education, Vol. 48, Issue 2, Pages 182-198, 2004.

12. Mtsi, N. and Maphosa, C. "Challenges encountered in the teaching and learning of the natural sciences in rural schools in South Africa", Journal of Social Sciences, Vol. 47, Issue 1, Pages 58-67, 2016.

13. Deehan, J., MacDonald, A. "Examining the Metropolitan and Non-metropolitan Educational Divide: Science Teaching Efficacy Beliefs and Teaching Practices of Australian Primary Science Educators", Res Sci Educ Vol. 53, Pages 889-917, 2023.

14. Lee, E., & Hannafin, M. J. "A design framework for enhancing engagement in student-centered learning: own it, learn it, and share it", Educational Technology Research and Development, Vol. 64, Issue 4, Pages 707-734, 2016.

15. Morel, G. "Student-centered learning: context needed", Educational Technology Research and Development, Vol. 69, Issue 1, Pages 91-92, 2021.

16. Beligatamulla, G., Rieger, J., Franz, J., & Strickfaden, M. "Making pedagogic sense of design thinking in the higher education context", Open Education Studies, Vol. 1, Issue 1, Pages 91-105, 2019.

17. Sawant, S. and Rizvi, S. "Study of passive didactic teacher centered approach and an active student centered approach in teaching anatomy", International Journal of Anatomy and Research, Vol. 3, Issue 3, Pages 1192-1197, 2015.

18. Scalfani, V. and Vaid, T. "3d printed molecules and extended solid models for teaching symmetry and point groups", Journal of Chemical Education, Vol. 91, Issue 8, Pages 1174-1180, 2014.

19. Pinger, C., Geiger, M., & Spence, D. "Applications of 3d-printing for improving chemistry education", Journal of Chemical Education, Vol. 97, Issue 1, Pages 112-117, 2019.

20. Smith, D., Lampley, S., Dolan, B., Williams, G., Schleppenbach, D., & Blair, M. "Effect of 3d manipulatives on students with visual impairments who are learning chemistry constructs: a pilot study", Journal of Visual Impairment & Blindness, Vol. 114, Issue 5, Pages 370-381, 2020.

21. Canabrava, S., Diniz-Filho, A., Schor, P., Fagundes, D., Lopes, A., & Batista, W. "Production of an intraocular device using 3d printing: an innovative technology for ophthalmology", Arquivos Brasileiros De Oftalmologia, Vol. 78, Issue 6, Pages 393-394, 2015.

22. Groenendyk, M. "Cataloging the 3d web: the availability of educational 3d models on the internet", Library Hi Tech, Vol. 34, Issue 2, Pages 239-258, 2016.

23. Chatzikyrkou, M., Manavis, A., Minaoglou, P., & Efkolidis, N. "A pedagogical methodology for introducing cad modeling tools and 3d printing technologies to adult trainees". Matec Web of Conferences, 318, 01032, 2020.

24. Teplá, M., Teplý, P. & Šmejkal, P. "Influence of 3D models and animations on students in natural subjects", IJ STEM Ed, Vol. 9, Issue 65, Pages 1-20, 2022.

25. Anđić, B., Lavicza, Z., Ulbrich, E., Cvjetićanin, S., Petrović, F. & Maričić, M. "Contribution of 3D modelling and printing to learning in primary schools: a case study with visually impaired students from an inclusive Biology classroom", Journal of Biological Education, Pages 1-17, 2022.

26. Doğru, M. S., & Özsevgeç, L. C. "Comparison of effects of computer-based instructional support on academic achievement of university students regarding meiosis", The American Biology Teacher, Vol. 85, Issue 5, Pages 259-264, 2023.

27. Baki, A., & Gökçek, T. "Karma yöntem araştırmalarına genel bir bakış", Elektronik Sosyal Bilimler Dergisi, Vol. 11, Issue 42, Pages 1-21, 2012.

28. Wan, A., & Ivy, J. "Providing access by integrating computer aided design in mathematics teacher education courses", Journal of Digital Learning in Teacher Education, Vol. 37, Pages 234-246, 2021.

29. Chen, J., & Cheng, L. "The influence of 3D printing on the education of primary and secondary school students", Journal of Physics: Conference Series, 1976, 2021.

30. Dove, G. "The Challenges of Abstract Concepts". In: Robinson, M.D., Thomas, L.E. (eds) Handbook of Embodied Psychology. Springer, Cham., 2021

31. McLeod, S. "Piaget's theory and stages of cognitive development", Developmental Psychology, Simply Psychology, 2018.

32. Bransford, J. D., Brown, A. L., & Cocking, R. R. (Eds.). "How people learn: Brain, mind, experience, and school." This seminal work explores the interplay between prior knowledge, cognitive processes, and educational experiences in shaping students' understanding and learning of complex concepts, Pages 1-374, 2000.

33. Vosniadou, S. "Human learning and the understanding of knowledge." In S. Vosniadou (Ed.), International handbook of research on conceptual change, Pages 39-63, Routledge, New York, 2013.

34. Hmelo-Silver, C. E., Duncan, R. G., & Chinn, C. A. "Scaffolding and achievement in problem-based and inquiry learning", Educational Psychologist, Vol. 42, Issue 2, Pages 99-107, 2007.

35. Bereiter, C., & Scardamalia, M. "Education for the knowledge age: Design-centered models of teaching and instruction." In K. Sawyer (Ed.), The Cambridge handbook of the learning sciences, Pages 695-704, Cambridge University Press, Cambridge, UK, 2006.

36. Doğru, M. S., & Kurnaz, M. A. "Students' contextualizing knowledge on the mirage incident, reflection and refraction: a case study", Physics Education, Vol. 58, Issue 6, Pages 1-14, 2023.

37. Marshall, J. A., & Young, E. S. "Preservice teachers' theory development in physical and simulated environments", Journal of Research in Science Teaching: The Official Journal of the National Association for Research in Science Teaching, Vol. 43, Issue 9, Pages 907-937, 2006.

38. Kern, E. & Carpenter, J. "Enhancement of student values, interests, and attitudes in earth science through a field-oriented approach", Journal of Geological Education, Vol. 32, Pages 299-305, 1984.

39. Rennie, L. J., & Johnston, D. J. "The nature of learning and its implications for research on learning

from museums", Science Education, Vol. 88, Issue 1, Pages 4-16, 2004.

40. Schneider, I., & Ohadi, M. M. "Unraveling students' misconceptions about the Earth's shape and gravity", Science Education, Vol. 82, Issue 2, Pages 265-284, 1998.

41. Griffith, K., Cataldo, R., & Fogarty, K. "Do-it-yourself: 3d models of hydrogenic orbitals through 3d printing", Journal of Chemical Education, Vol. 93, Issue 9, Pages 1586-1590, 2016.

42. Resnick, M., Silverman, B. "Some reflections on designing construction kits for kids", In Proceedings of the Conference on Interaction Design and Children, Pages 117-122, 2005.

43. Ishutov, S., Hodder, K., Chalaturnyk, R., & Zambrano-Narvaez, G. "A 3d printing short course: a case study for applications in the geoscience teaching and communication for specialists and non-experts" Frontiers in Earth Science, 9, Pages 1-12, 2021.

44. Trust, T., Maloy, R. W. "Why 3D print? The 21st-century skills students develop while engaging in 3D printing projects", Computers in the Schools, Vol. 34, Issue 4, Pages 253-266, 2017.

45. Davis, E., Jones, M., Thiel, D., & Pauls, S. "Using open-source, 3d printable optical hardware to enhance student learning in the instrumental analysis laboratory", Journal of Chemical Education, Vol. 95, Issue 4, Pages 672-677, 2018.

46. Vangunten, M., Walker, U., Han, G., & Knust, K. "3d-printed microfluidics for hands-on undergraduate laboratory experiments", Journal of Chemical Education, Vol. 97, Issue 1, Pages 178-183, 2019.

47. Lemu, H. and Mikkelsen, O. "Experience in use of 3d printing in engineering education at university of stavanger", Nordic Journal of Stem Education, Vol. 5, Issue 1, Pages 1-5, 2021.

48. Pernaa, J. and Wiedmer, S. "A systematic review of 3d printing in chemistry education – analysis of earlier research and educational use through technological pedagogical content knowledge framework", Chemistry Teacher International, Vol. 2, Issue 2, Pages 1-16, 2019.

49. Higman, C., Situ, H., Blacklin, P., & Hein, J. "Hands-on data analysis: using 3d printing to visualize reaction progress surfaces", Journal of Chemical Education, Vol. 94, Issue 9, Pages 1367-1371, 2017.

50. Zhang, T., Cummings, M., & Dulay, M. "An outreach/learning activity for steam education via the design and 3d printing of an accessible periodic table", Journal of Chemical Education, Vol. 99, Issue 10, Pages 3355-3359, 2022.

51. Harmon, D., Klein, B., Im, C., & Romero, D. "Development and implementation of a three-dimensional (3d) printing elective course for health science students", Anatomical Sciences Education, Vol. 15, Issue 3, Pages 620-627, 2022.

ULUSLARARASI 3B YAZICI TEKNOLOJİLERİ
VE DİJİTAL ENDÜSTRİ DERGİSİ

INTERNATIONAL JOURNAL OF 3D PRINTING
TECHNOLOGIES AND DIGITAL INDUSTRY

ISSN:2602-3350 (Online)

URL: https://dergipark.org.tr/ij3dptdi

UNMANNED GROUND VEHICLE SELECTION WITH ARTIFICIAL NEURAL NETWORKS

Yazarlar (Authors): Cüneyd Demir, Cengiz Eldem, Mustafa Bozdemir

Bu makaleye şu şekilde atıfta bulunabilirsiniz (To cite to this article): *Demir C., Eldem C., Bozdemir M., "Unmanned Ground Vehicle Selection with Artificial Neural Networks" Int. J. of 3D Printing Tech. Dig. Ind., 8(2): 255-265, (2024).*

DOI: 10.46519/ij3dptdi.1482087

Araştırma Makale/ Research Article

Erişim Linki: (To link to this article): https://dergipark.org.tr/en/pub/ij3dptdi/archive

UNMANNED GROUND VEHICLE SELECTION WITH ARTIFICIAL NEURAL NETWORKS

Cüneyd Demir[a]*, Cengiz Eldem[b], Mustafa Bozdemir[c]

[a*]Kırşehir Ahi Evran University, Mucur Vocational School, Computer Technologies Department, TÜRKİYE
[b]Gazi University, Technology Faculty, Industrial Design Engineering Department, TÜRKİYE
[c]Kırıkkale University, Kırıkkale Vocational School, Machinery and Metal Technologies Department, TÜRKİYE

* *Corresponding Author:* cuneyd.demir@ahievran.edu.tr

(**Received:** 10.05.2024; **Revised:** 20.06.2024; **Accepted:** 06.07.2024)

ABSTRACT

In recent years, significant advancements have been made in defense systems in response to the increasing demands of countries. The importance of unmanned ground vehicles, a highly critical technology, is becoming more evident with each passing year.

In this study, a selection program is intended to be developed to determine the mission purposes for which military unmanned ground vehicles will be used. In line with the operating principles, the basic mechanical systems have been identified. Subsequently, a design catalog containing these basic mechanical systems was created. The desired features for use in the field were asked to the customer. Based on the received responses, the best alternative unmanned ground vehicles were identified using an artificial neural network algorithm.

In the artificial neural network model, a feedforward neural network architecture was used. Stochastic Gradient Descent was utilized in the network training function to minimize the model's loss function. The activation functions tanh and softmax were used, and the model has four hidden layers. The model was trained for 150 epochs. Results were obtained for the metrics of accuracy, precision, recall, and F1-score. The model's accuracy rate was found to be %99,63. Such a high accuracy rate indicates that the model has well understood the data in the dataset and provides accurate predictions.

Keywords: Defense Technology, Unmanned Ground Vehicle, Artificial Neural Networks

1. INTRODUCTION

Thanks to their nonlinear structures, artificial neural networks have been used in a wide range of fields, from engineering to data analysis. Additionally, they have found applications in various sectors such as defense, economy, industry, sports, gaming, energy, environment, and finance. Today, numerous studies have been conducted on applications of artificial neural networks.

Urgan and Tamgöz (2020) used artificial neural networks to predict the active user numbers of games on the Steam platform [1]. Özkurt (2020) demonstrated that digital transformation and artificial intelligence applications can be used to model the future position and production methods of the defense and manufacturing industries by training with artificial neural networks [2].

Ayyıldız and Demirci (2022) examined the relationship between the budget allocated for R&D activities from the central government budget and economic growth in Turkey between 2008 and 2035 using artificial neural networks [3]. Aka and colleagues (2020) predicted the end-of-season team rankings, goals scored, and goals conceded in the Turkish Super League using artificial neural networks based on input variables [4].

Köse (2021) made exchange rate predictions using artificial neural networks and grey prediction models based on exchange rate data obtained from the Central Bank of the Republic

of Turkey [5]. Burçin (2023) predicted the size of vehicle loans using artificial neural networks based on monthly data from Turkey between 2006 and 2022 [6]. Şahin (2023) predicted the natural gas consumption of a house in Isparta using an artificial neural network model [7].

Ertem (2022) accurately predicted which warehouse section stored spare parts belong to by using data mining and artificial neural networks to optimize the warehouse zone assignment process [8].

Tütüncü (2022) predicted the evaporation amount using artificial neural networks based on the daily meteorological data from a station at the Atatürk Dam [9]. Karakul (2020) modeled the relationships between the Borsa Istanbul (BIST) 100 Index, overnight interest rates, and the dollar exchange rate using artificial neural networks and accurately predicted the BIST 100 Index value [10].

Buyrul (2022) modeled the mechanical properties of TiB2-added aramid fiber-reinforced composites with different orientations using artificial neural networks and statistical analyses, successfully identifying the composites with the best ballistic performance [11]. Kaya (2022) modeled the water quality parameters of Lake Iznik using artificial neural networks and accurately predicted the values of total nitrogen, total phosphorus, and dissolved oxygen [12].

Baylan and Salepçioğlu (2023) predicted the impact of strategic management tools on organizational DNA using artificial neural networks [13]. Süleymanlı (2021) predicted the gross foreign exchange reserves of the Central Bank of the Republic of Turkey using artificial neural network techniques based on data from 2013 to 2021 [14].

In recent years, studies on unmanned ground vehicles have focused on various areas such as autonomous movement, obstacle detection, route planning, agricultural applications, and various industrial uses.

Topal and Yiğit (2021) developed a low-cost and ergonomic system that enables unmanned ground vehicles to move autonomously and recognize their surroundings using a LIDAR laser scanner sensor, night vision camera, and Arduino microcontroller [15].

Kırçıl and Tepe (2024) designed a portable, low-cost, cross-platform supported, and user-friendly telemetry system that displays real-time status information and camera images of unmanned ground vehicles [16]. Sonugür (2016) developed a low-cost and highly successful auxiliary system, supported by image processing and GPS-based artificial neural networks, for unmanned ground vehicles to detect and recognize moving obstacles [17].

Kıvanç (2020) developed a specially designed outer rotor brushless DC motor that provides high torque and efficiency at low speeds, tailored for unmanned ground vehicles with omnidirectional movement capability, low friction, and high vibration. This motor is also easy to manufacture [18].

Hülako and Kapucu (2018) developed and tested a system for a microcontroller-controlled unmanned ground vehicle that reaches designated destinations using a low-cost GPS and electronic compass sensor, applying a guidance algorithm with a Kalman filter [19]. Vardin and colleagues (2022) developed a compact, remotely controlled unmanned ground vehicle prototype with four-wheel drive, operating at low speeds (<1 m/s), a carrying capacity of 5 kg, and structural strength verified by the finite element method [20].

Akdan and colleagues (2023) developed an autonomous and solar-powered agricultural unmanned ground vehicle equipped with a depth camera, convolutional neural network-based detection algorithm, and an innovative suspension system, capable of locally treating harmful plants in agricultural fields with 90% accuracy [21]. Bayram and colleagues (2022) successfully implemented path-following control based on position and orientation error feedback using an unmanned ground vehicle equipped with RTK-GPS, IMU, and absolute encoder sensors, utilizing a successively linearized and discretized kinematic model predictive control [22].

Gökçe and Sonugür (2018) compared the performance of two image processing-based auxiliary systems for detecting moving objects on the routes of unmanned ground vehicles

using geographic location data and artificial neural networks [23]. Naglak and colleagues (2021) designed a low-cost, compact, and adjustable cable management mechanism to facilitate the distribution of electrical cables by unmanned ground vehicles in mobile microgrid systems, and explained how to recreate this mechanism [24].

Patel and colleagues (2022) developed an asphalt layer change classifier to automatically monitor road construction progress using sensors mounted on unmanned ground vehicles, achieving a 97.88% accuracy rate with the ConvLSTM algorithm, demonstrating the potential to increase efficiency in road construction projects [25]. Zhou and colleagues (2020) presented a strategy for global and local trajectory planning using an artificial fish swarm algorithm and a Markov chain-based trial-and-error search algorithm to ensure unmanned ground vehicles reach their targets safely in dynamic environments [26]. Mei and colleagues (2022) introduced the ROADS prototype, a multi-sensor unmanned ground vehicle for monitoring road degradation, showing that road condition assessments can be conducted with 74.2% accuracy using an image-based method [27].

Chung and colleagues (2021) provided information on an unmanned ground vehicle designed and developed to detect crevasses in Antarctica and prevent accidents. This vehicle can adapt to harsh terrain conditions and operate at a speed of 2.5 m/s for over two hours [28]. Liu and colleagues (2022) presented a path planner for multiple unmanned ground vehicles that uses continuous ant colony optimization for path planning and coordination, demonstrating superior performance in complex and high-dimensional problems [29]. Wang and colleagues (2020) designed a new modeling and path planning framework for unmanned ground vehicles with specific sensing capabilities, enabling them to continuously monitor events occurring at unknown locations and probabilities by moving through a road network with different priorities [30]. Hassan and colleagues (2023) designed a control system using the double deep Q-network (DDQN) algorithm to ensure unmanned ground vehicles follow the desired path. Simulation results demonstrate that this system operates with high accuracy even under noisy conditions [31].

With advancing technology, unmanned ground vehicles find applications in various fields such as defense, agriculture, logistics, and exploration. The correct selection and configuration of these vehicles are crucial for their effective and efficient performance. Today, advanced artificial intelligence techniques like artificial neural networks play a critical role in the processes of selecting and optimizing UGVs according to environmental conditions and mission requirements. This study examines the methods, advantages, and research gaps in the selection of UGVs using ANNs. The aim is to enhance the operational success of UGVs by determining an appropriate ANN model. The absence of a selection program specifically for military-purpose UGVs and its lack of integration with artificial intelligence make this study unique.

2. MATERIAL AND METHOD

A selection program has been developed to determine the tasks for which military unmanned ground vehicles will be used. Within this program, the fundamental mechanical systems of UGVs have been identified based on their operating principles. Subsequently, a design catalog containing these fundamental mechanical systems was prepared. The desired features of the UGV to be used in the field were gathered from customers, and based on the responses, the most suitable UGV was developed using an artificial neural networks algorithm.

2.1. Unmanned Ground Vehicle

The development of unmanned ground vehicles began in the 1970s with research examining the feasibility of legged machines. These studies revealed that before producing a walking machine, it was necessary to develop a robot equipped with specific equipment to perform the targeted tasks. Over time, this research was particularly adapted for military applications, leading to concrete steps in the development of UGVs [32].

Unmanned ground vehicles are among the autonomous systems expected to play a significant role in the future armies. These vehicles are designed to minimize battlefield risks and neutralize threats using their electronic vision systems, various sensors, and remotely controlled weapon systems. These sensors enable the vehicle to perceive its surroundings,

map the terrain, and navigate effectively. Additionally, these vehicles often utilize artificial intelligence (AI) and machine learning algorithms to process environmental data and make decisions [33].

According to current definitions, UGVs are described as vehicles with high mobility and adaptable platforms that can integrate mission-specific modules. These vehicles, which can be remotely controlled with adjustable levels of autonomy and modular control consoles, are referred to as next-generation unmanned systems that advance by maintaining contact with the ground [34].

Unmanned ground vehicles are used in the military for tasks such as infiltrating enemy lines, armed attacks, bomb disposal, logistics, mine detection, and surveillance. In the civilian sector, they are effectively utilized in agriculture, firefighting, environmental monitoring, and infrastructure inspection. UGVs play a crucial role, especially in disaster management and emergency response [35].

Unmanned ground vehicles in the defense sector are distinguished by their capacity to operate in dangerous and hard-to-reach areas. These vehicles can undertake reconnaissance, surveillance, and direct combat missions during military operations without risking human lives. Equipped with advanced sensor packages and autonomous navigation systems, they can maneuver effectively even in complex battlefield environments. These features make them critical assets that enhance strategic advantages on the battlefield. As technological advancements make UGVs increasingly indispensable, they also underscore the need for ethical and legal regulations. The use of UGVs brings new debates in the realms of the laws of war and military ethics. Their operational capabilities are reshaping the role of unmanned systems in military disciplines, leading to significant changes in defense strategies [36].

Unmanned ground vehicles are being developed for armed forces worldwide and have the potential to replace traditional tanks as dominant combat vehicles. Over the past decade, UGV technology has made significant advances in the defense sector. Countries such as the United States, the United Kingdom, China, Europe, and Turkey are among those heavily investing in the development of robotic combat vehicles. The global unmanned ground vehicles market, valued at an estimated USD 2.54 billion in 2020, is expected to grow at a compound annual growth rate of 6.5% from 2022 to 2029, reaching USD 3.91 billion by 2029. This growth is driven by the strategic and operational advantages of UGVs, as well as increases in defense budgets [37].

The general design of unmanned ground vehicles involves numerous subsystems and a complex network of relationships among them that directly influence the design. Design-related requirements are evaluated based on these existing system relationships, and a data set has been created to determine the most optimal solution. This data set consists of 15 parameters included in the design catalog: autonomous structure, control system, payload, body material, motor, energy system, power transmission system, braking system, thermal management system, electrical system, guidance system, suspension system, mobility configuration, chassis, and electronic units (Table 1).

Artificial neural networks with decision-making structures require some responses from the designer or customer to generate suitable alternatives. The questions to be used in inference development for the decision-making structure are listed below.

1. What should be the cost of the unmanned ground vehicle? *(Low, Medium, High)*
2. What should be the dimensional classification of the unmanned ground vehicle? *(Light, Small, Medium, Heavy)*
3. What should be the autonomy level of the unmanned ground vehicle? *(Level 1, Level 2, Level 3)*
4. What should be the coverage area of the unmanned ground vehicle? *($x<2$ km², $x<5$ km², x km²)*
5. What tasks is the unmanned ground vehicle expected to perform? *(Reconnaissance, surveillance and intelligence, bomb disposal, attack and rear security, logistics, mine and obstacle clearance)*
6. What type of motor should be used in the unmanned ground vehicle?
   (0-20 kW, 20-75 kW, 75-300 kW, 300+ kW, 25-100 Hp, 100-400 Hp, 400+ Hp, 25-100 Hp + 0-20 kW,

100-400 Hp + 20-75 kW,
400+ Hp + 75+ kW)

7. On what types of terrain will the unmanned ground vehicle be used? *(Flat hard ground, flat soft ground, rough hard ground, and rough soft ground)*
8. What level of maneuverability should the unmanned ground vehicle have? *(Large turning radius, medium turning radius, and small turning radius)*

The alternatives in the solution space created with the design catalog parameters have been evaluated using the questions mentioned above. Out of 907.200.000 alternatives, the ones that will ensure the system's functionality have been identified (Figure 1).

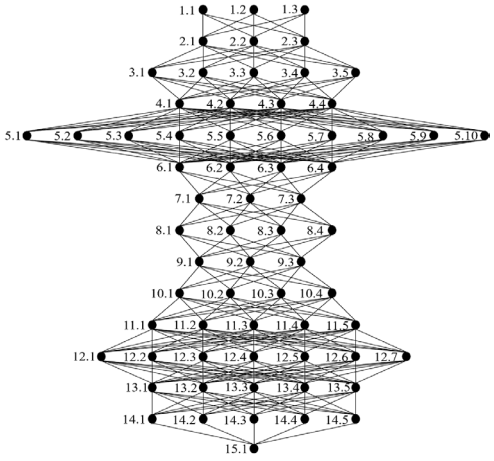

Figure 1. Solution space

2.2. Artificial Neural Network

Artificial neural networks (ANNs) are systems designed to mimic the working principles of neurons in the human brain. These systems consist of simple processors interconnected at varying levels of influence, forming a decision-making mechanism based on learning capability. Early studies focused on the mathematical modeling of biological cells (neurons) in the brain. These studies demonstrated that each neuron transforms information received from neighboring neurons into an output in a manner consistent with the dynamics of biological neurons [38].

Figure 2 illustrates a neuron model as a basic element. Data from the external environment are connected to the neuron via weights, which determine the influence of the input. The result obtained from the multiplication of inputs and their respective weights forms the net input. This process is carried out through the summation function. The activation function computes the net output during the processing phase, which also constitutes the neuron's output. The activation function is usually a nonlinear function. The constant "b" represents the bias or the threshold value of the activation function. The "w" represents the weights, "x" represents the inputs, and "f" represents the activation function. Variables x_1, x_2, x_3, ..., x_m represent the n number of inputs to the neuron, and variables w_1, w_2, w_3, ..., wm represent the weights associated with these inputs. A basic artificial neural network cell is much simpler than a real neuron, consisting primarily of components like the input vector (x) and the weight vector (w). In the multilayer perceptron and backpropagation model, (w) is used as a matrix instead of a vector [39].

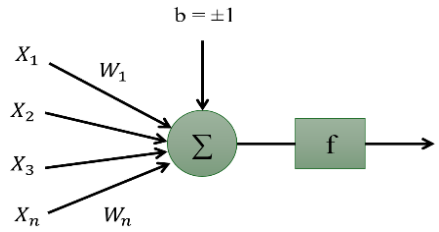

Figure 2. Artificial neural network cell [40]

The initial element compares the total value obtained by summing the products of the inputs and their respective weights with a given initial value. When this total is compared to the initial value, if the total is higher, the output value is calculated using a nonlinear function (F). The output signal y is the result of the nonlinear function (F) of the difference between the total and the initial value. Here, x_i is the input signal, w_i is the weight associated with x_i, and (F) is the nonlinear function, as expressed in Equation 1. The nonlinear function F is determined based on the modeling choice and the desired output type of the artificial neural network model.

$$y = F\left(\sum w_i x_i + b\right) \quad (1)$$

An artificial neural network consists of three layers: input, hidden, and output layers (Figure 2). The first layer, the input layer, allows data to enter the neural network. Data from this layer is processed and sent to the output layer. The hidden layer, which performs the main function of the network, transmits signals from the input layer to the output layer. The number of hidden layers can vary in different networks depending

on the application's purpose [41]. The final layer, the output layer, processes data from the hidden layer and produces results based on the data received from the input layer.
Additionally, an artificial neural network consists of three fundamental components: the architecture, the learning algorithm, and the activation function [42]. The architecture includes the layers, neurons, and the connections between neurons. The learning algorithm calculates probabilities based on input data and determines the likely outcomes. The activation function processes the input data to generate the results.

A neuron is located in a network with numerous feedback connections. Many networks consist of simple processor elements, and their basic structures are typically single-layered. Applications in various fields have demonstrated the limited capabilities of single-layer networks. However, these types of networks later led to the development of multilayer networks, which are formed by integrating two or more neural layers. In the multilayer networks shown in Figure 3, the number of neurons in each layer can vary, and the output of each layer is created as a weighted sum of the outputs from the previous layer. Researchers have developed algorithms for the systematic training of multilayer networks. The application of these algorithms to multilayer networks has yielded superior results compared to single-layer networks [43].

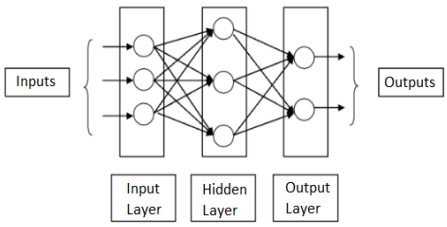

Figure 3. Multilayer neural network [40]

Activation functions used in artificial neural networks are mathematical functions employed to process input signals to produce outputs for the neural networks. These functions determine the output of each neuron in every layer of the neural network. The functions of activation functions significantly influence the learning rate and the training process of the model. Table 2 provides the most common activation functions and their mathematical formulas.

Hyperbolic Tangent Function (Tanh): The Tanh function transforms the input into a value between -1 and 1, providing more symmetric output. Since the gradient of the Tanh function is larger, the vanishing gradient problem is less pronounced during training [44]. However, the vanishing gradient problem can still occur in deep neural networks, especially with very large values.

Softmax Function: Normalizes the elements of a vector to be between 0 and 1. It is used in multi-class classification problems and its outputs can be interpreted as a probability distribution. The Softmax function is specifically tailored for classification problems.

Table 2. Activation functions

Activation Function	Formulas	
Sigmoid	$\sigma(x) = {}^{1}/_{(1+e^{-x})}$	0,1
Relu	$f(x) = \max(0, x)$	0, ∞
Tanh	$\tanh(x) = \frac{(e^{x} - e^{-x})}{(e^{x} + e^{-x})}$	-1,1
Softmax	$\text{softmax}(x_i) = \frac{e^{x_i}}{\sum_{j=1}^{K} e^{x_j}}$	0,1

3. EXPERIMENTAL FINDINGS

The created model features a feedforward backpropagation neural network architecture. To minimize the model's loss function, the SGD (Stochastic Gradient Descent) algorithm, one of the most commonly used optimization algorithms in neural networks and machine learning models, has been utilized in the network training function. The activation functions used are Tanh and Softmax. The model comprises four hidden layers with 64, 128, 64, and 16 neurons, respectively. The model was trained for 150 epochs, with 60% of the dataset used for training, 20% for testing, and 20% for validation. Table 3 and Figure 4 provide information and visual representations related to the model.

Table 3. Model of network architecture

Network Type	Feed Forward Backprop
Training Function	Stochastic Gradient Descent
Activation Function	Tanh-Softmax
Hidden Layer	4 (64, 128, 64, 16)
Epoch	150
Training Data	%60
Test Data	%20
Validation Data	%20

Table 1. Unmanned ground vehicles design catalog

		DESIGN CATALOG									
		1	**2**	**3**	**4**	**5**	**6**	**7**	**8**	**9**	**10**
1	**Autonomous Structure**	Manuel	Semi-Autonomous	Autonomous							
2	**Control System**	RF Control	Remote Control Module	Satellite							
3	**Payload**	Surveillance System	Manipulator System	Carrier System	Weapon System	Mine and Obstacle Clearing System					
4	**Body Material**	Polymer Materials	Composite Materials	Aluminum Alloys	Steel Alloys						
5	**Engine**	0-20 kw	20-75 kw	75-300 kw	300+ kw	25-100 Hp	100-400 Hp	400+ Hp	25-100 Hp + 0-20 kw	100-400 Hp + 20-75 kw	400+ Hp + 75+ kw
6	**Energy System**	Cell Battery	Battery	Fuel Cell	Fuel Tank						
7	**Powertrain System**	Fixed Ratio Transmission	Electric Transmission	Variable Ratio Transmission							
8	**Brake System**	Dynamic Braking	EBS	ABS	Regenerative Braking						
9	**Thermal Management System**	Air Cooled	Oil Cooled	Water Cooled							
10	**Electrical System**	Accumulator Free	12V Accumulator	24V Accumulator	28V Accumulator						
11	**Steering System**	Ackerman	Differential	4WS	Skid-Steer	Independent Steering					
12	**Suspension System**	Rubber-Elastomeric	Spring and Shock Absorber Systems	MacPherson Strut	Double Wishbone	Torsion Beam	Solid Axle	Hydropneumatic			
13	**Mobility Configuration**	2-Wheeled	4-Wheeled	6-Wheeled	8-Wheeled	Tracked					
14	**Chassis**	2-Wheeled Chassis	4-Wheeled Chassis	6-Wheeled Chassis	8-Wheeled Chassis	Tracked Chassis					
15	**Electronic Units**	Sensors-Cameras-Processors-Power Distribution Units-Cables									

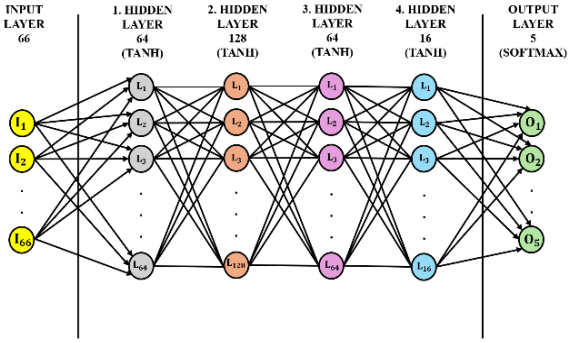

Figure 4. ANN model

The table shows the performance metrics of the model for different classes. The overall model accuracy is %99.6, indicating a very high performance across all classes. For the 2-wheeled class, the model has perfect precision and recall, with a recall of %93. The 4-wheeled class performance is nearly perfect, with a recall of %98 and an F1 score of %99. The 6-wheeled class demonstrates flawless performance with 100% in all metrics. For the 8-wheeled class, precision is slightly lower at %97, but recall remains perfect at %100, resulting in an F1 score of %98. In the tracked class, the model shows near-perfect precision and recall, with an F1 score of %100. Overall, the model exhibits excellent accuracy and reliability in classifying all classes, proving its high general performance.

Table 4. Model performance metrics

Class	Accuracy	Precision	Recall	F1 Score
2 Wheeled	0.996	1.00	0.93	0.96
4 Wheeled		1.00	0.98	0.99
6 Wheeled		1.00	1.00	1.00
8 Wheeled		0.97	1.00	0.98
Tracked		0.99	1.00	1.00

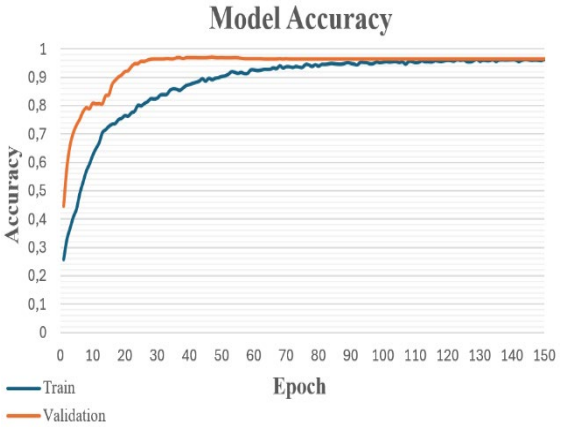

Figure 5. Model accuracy graph

The model quickly achieves a high level of accuracy on the validation data and maintains this accuracy. The loss on the training data steadily decreases and continues to decline throughout the learning process. This indicates that the model is successful in its learning process and optimizes its performance on both validation and training data (Figure 5).

The model consistently reduces the loss during training, indicating that the learning process is effective. The validation loss decreases rapidly during the initial epochs and then stabilizes at a certain value. This demonstrates that the model performs steadily on the validation data. The overall view of the loss values in Figure 6 shows that the model progresses well during training, the learning process occurs in an orderly manner, and signs of overfitting are not very pronounced.

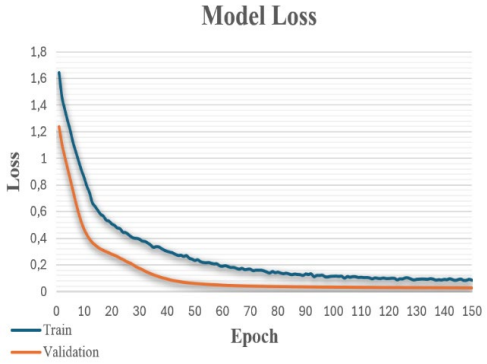

Figure 6. Model loss graph

The classification performance of the model is displayed on a confusion matrix graph. Out of thousands of designs, it does not appear to be an external error factor in mistakenly learning 12 tracked vehicles as 4-wheeled vehicles (Figure 7).

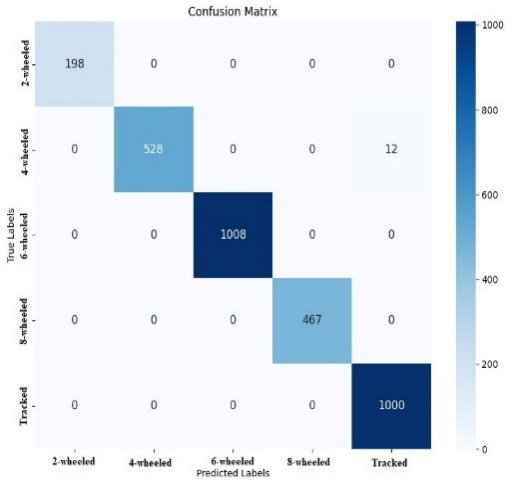

Figure 7. Confusion matrix graph

4. RESULTS

Artificial neural networks have been applied to various fields such as defense, economy, industry, sports, gaming, energy, environment, and finance. Unmanned ground vehicles, on the other hand, have been used in autonomous movement, obstacle detection, route planning, agricultural, and various industrial applications. In light of all this information, it has been observed that no study has been conducted on the selection of unmanned ground vehicles using artificial neural networks.

Artificial neural networks have been applied in various fields such as defense, economy, industry, sports, gaming, energy, environment, and finance. Unmanned ground vehicles, on the other hand, have been used in autonomous movement, obstacle detection, route planning, agricultural, and various industrial applications. In light of all this information, it is evident that no study has been conducted on the selection of unmanned ground vehicles using artificial neural networks.

In this study, an innovative selection program has been developed using artificial neural networks to determine the optimal choice for unmanned ground vehicles. By processing multidimensional data and leveraging their learning capabilities, artificial neural networks can make highly accurate decisions in selecting unmanned ground vehicles. Based on feedback received within the framework of eight specified questions, the design catalog and the system have quickly and effectively identified the best alternatives.

These results expand the potential application areas of neural network-based decision support systems in the defense industry and other critical sectors. The unmanned ground vehicle selection process demonstrates that similar methods can be applied to other unmanned systems as well. The flexible and adaptable structure of the developed model proves that it can quickly adjust to different future conditions and requirements.

This study has revealed that all parameters in unmanned ground vehicles are interrelated. It has been determined that creating a mobility system capable of operating in all types of terrain conditions is quite challenging. In a traditional design process, it is known that the design of an unmanned ground vehicle begins with the selection of the mobility system. Thanks to the answered questions and the data set used, the most suitable mobility system has been identified using artificial neural networks.

With this method, the time required for the designer to evaluate alternatives according to all criteria has been shortened, and the design costs have been reduced. In the event of the commercialization of the unmanned ground vehicle selection program, it has been clearly demonstrated that various unmanned ground vehicle designs can be realized according to customer demands.

REFERENCES

1. Urgan, N. N., Tamgöz, M. “Yapay Sinir Ağları ile Aktif Kullanıcı Sayısı Tahmini Üzerine Bir Uygulama”, European Journal of Engineering and Applied Sciences, Vol3 Issue 2, Pages 8-14, 2020.

2. Özkurt, C., “Savunma sanayinde dijitalleşmenin kurumsal niteliklere etkisinin yapay zeka yöntemleri ile öngörülmesi: Sakarya ili örneği”, Doktora Tezi, [Foreseeing the impact of digitalization on institutional qualities by artificial intelligence methods in the defense industry: an application in Sakarya] [Thesis in Turkish], Sakarya Üniversitesi, Sakarya, Pages 55-60, 2020.

3. Ayyıldız, F.V., Demirci, O., “Ar-Ge harcama gruplarının ekonomik büyüme üzerindeki etkileri: Türkiye örneğinde yapay sinir ağları ile ARDL analizi”, Trends in Business and Economics, Vol 36 Issue 4, Pages 346-358, 2022.

4. Aka, H., Aktuğ, Z. B., Kılıç, F., “Türkiye Süper Lig Sezon Sonu Takım Sıralamasının Geliştirilen Yapay Sinir Ağları Modeli ile Tahmin Edilmesi”, Spor ve Performans Araştırmaları Dergisi, Vol 11, Issue 3, Pages 258-268, 2020.

5. Köse, Ü. B. (2021). Yapay Sinir Ağlari ve Gri Model ile Döviz Kuru Tahmini (Doctoral dissertation, Marmara Universitesi (Turkey)).

6. Burçin, T., “Taşıt Kredileri Talep Tahmininin Yapay Sinir Ağları Kullanılarak Analiz Edilmesi”, Dumlupınar Üniversitesi Sosyal Bilimler Dergisi, Vol 1, Issue 78, Pages, 102-110, 2023.

7. Şahin, M. E., “Gaz Yakıtlı Kombi Sisteminin Yapay Sinir Ağı ile Yakıt Miktarı Tahmini Isparta Örneği”, Uluslararası Teknolojik Bilimler Dergisi, Vol 15 Issue 1, Pages 11-18, 2023.

8. Ertem, M., “Bir Savunma Sanayi Firmasında Depo Bölgesi Atama Sisteminin Veri Madenciliği ve

Makine Öğrenme Yaklaşımlarıyla İyileştirilmesi", Avrupa Bilim ve Teknoloji Dergisi, Vol 1, Issue 34, Pages 501-506, 2022.

9. Tütüncü, Ö. (2022). "Yapay sinir ağları (YSA) modeli ile su yüzeyinden buharlaşma tahmini: Atatürk barajı örneği", Yüksek Lisans Tezi, [Forecasting water surface evaporation with artificial neural networks (ann) model: example of Ataturk Dam][Thesis in Turkish],Bilecik Şeyh Edebali Üniversitesi, Bilecik, Pages 40-45, 2022.

10. Karakul, A. K., "Yapay Sinir Ağları ile Borsa Endeksi Tahmini", Mehmet Akif Ersoy Üniversitesi İktisadi ve İdari Bilimler Fakültesi Dergisi, Vol 7, Issue 2, Pages 497-509, 2020.

11. Buyrul, F., "Aramid Elyaf Takviyeli Polimer Matris Kompozitlerin Mekanik Deney Sonuçlarının Yapay Sinir Ağlarıyla Tahminleri ve Istatistiksel Analizleri", International Journal of Engineering Research and Development, Vol 14 Issue 1, Pages 271-281, 2022.

12. Kaya, E., "İznik Gölü su kalite parametrelerinin yapay sinir ağları yöntemi ile değerlendirilmesi", Yüksek Lisans Tezi, [Evaluation of İznik Lake water quality parameters by artificial neural networks method] [Thesis in Turkish], Sakarya Üniversitesi, Sakarya, Pages 25-35, 2022

13. Baylan, H. K., Salepçioğlu, M. A., "Yapay Sinir Ağları Ile Stratejik Yönetim Araçlarının Kullanımının Örgütsel DNA'ya Etkisinin Tahmin Edilmesi: İstanbul'da Özel Hastanelerde Bir Araştırma", İşletme Araştırmaları Dergisi, Vol 15, Issue 4, Pages 2724-2745, 2023.

14. Süleymanlı, C., "Yapay sinir ağları ile türkiyenin brüt döviz rezervlerinin tahmini", Finans Ekonomi ve Sosyal Araştırmalar Dergisi, Vol 6, Issue 4, Pages 612-624, 2021.

15. Topal, A., Yiğit, T., "İnsansız Kara Araçları için Lidar Teknolojisi Kullanılarak 3B Ortam Haritalama Sistemi", International Journal of 3D Printing Technologies and Digital Industry, Vol 5, Issue 2, Pages 171-186, 2021.

16. Kırçıl, U., Tepe, C., "İnsansız Kara Araçları İçin Çapraz Platform Destekli Telemetri Sistemi Tasarımı", Afyon Kocatepe Üniversitesi Fen ve Mühendislik Bilimleri Dergisi, Vol 24, Issue 1, Pages 53-60, 2024.

17. Sonugür, G., "İnsansız kara araçları için dinamik nesnelerin tanınması amacıyla görüntü işleme tabanlı bir sistem geliştirilmesi", Doktora Tezi, [Development of a computer vision-based system to detect dynamic objects for unmanned ground vehicles] [Thesis in Turkish], Pages 63-65, 2016.

18. Kıvanç, Ö. C., "Bir İnsansız Kara Aracı İçin Yüksek Verimli Fırçasız Doğru Akım Motoru Tasarımı", Süleyman Demirel Üniversitesi Fen Bilimleri Enstitüsü Dergisi, Vol 24 Issue 2, Pages 494-501, 2020.

19. Hülako, H., Kapucu, S., "Düşük Maliyetli GPS Tabanlı Otonom Bir İnsansız Kara Aracının Tasarımı ve Yapılması", Gazi Üniversitesi Fen Bilimleri Dergisi Part C: Tasarım ve Teknoloji, Vol 6, Issue 4, Pages 834-850, 2018.

20. Vardin, S., Demircioğlu, P., Böğrekci, İ., "Arazi Uygulamaları İçin İnsansız Yer Aracı Geliştirilmesi", Uluborlu Mesleki Bilimler Dergisi, Vol 5 Issue 1, Pages 1-13, 2022.

21. Akdan, S., Öner, İ., Akdeniz, N., Bingöl, A., Şimşek, S. E., Yavşan, E., "Zararlı bitkilerin ilaçlanması için tarımsal bir insansız kara aracı", Interdisciplinary Studies on Contemporary Research Pratices in Engineering in the 21st Century-III, Özgür Yayınları, Gaziantep, Pages 251-265, 2023.

22. Bayram, A., Almalı, M. N., Al-Naqshbandı, F. M., "Bir insansız kara aracının model öngörü kontrol metodu ile GPS tabanlı yol takibi", Gazi Üniversitesi Mühendislik Mimarlık Fakültesi Dergisi, Vol 38, Issue 1, Pages 345-356, 2022.

23. Gökçe, B., Sonugür, G., (2018). İnsansız Kara Araçlarından Kamera ile Görüntülenen Hareketli Nesnelerin Sınıflandırılması Amacıyla Geliştirilen Görüntü İşleme Tabanlı Yöntemlerin Karşılaştırılması. Afyon Kocatepe Üniversitesi Fen ve Mühendislik Bilimleri Dergisi, Vol 18, Issue 3, Pages 1118-1129, 2018.

24. Naglak, J. E., Kase, C., McGinty, M., Majhor, C. D., Greene, C. S., Bos, J. P., Weaver, W. W., "Cable deployment system for unmanned ground vehicle (UGV) mobile microgrids", HardwareX, Vol 10, Issue e00205, 2021.

25. Patel, T., Guo, B. H., van der Walt, J. D., Zou, Y., "Effective motion sensors and deep learning techniques for unmanned ground vehicle (UGV)-based automated pavement layer change detection in road construction", Buildings, Vol 13, Issue 1, Pages 5, 2022.

26. Zhou, X., Yu, X., Zhang, Y., Luo, Y., & Peng, X., "Trajectory planning and tracking strategy applied to an unmanned ground vehicle in the presence of obstacles", IEEE Transactions on Automation Science and Engineering, Vol 18, Issue 4, Pages 1575-1589, 2020.

27. Mei, A., Zampetti, E., Di Mascio, P., Fontinovo, G., Papa, P., D'Andrea, A., "ROADS—Rover for Bituminous Pavement Distress Survey: An Unmanned Ground Vehicle (UGV) Prototype for Pavement Distress Evaluation", Sensors, Vol 22, Issue 9, Pages 3414, 2022.

28. Chung, C., Kim, H. K., Yoon, D. J., Lee, J., "Development of unmanned ground vehicle (UGV) for detecting crevasses in glaciers", Journal of Institute of Control Robotics and Systems Vol 27, Issue 1, Pages 61-68, 2021.

29. Liu, J., Anavatti, S., Garratt, M., Abbass, H. A., "Modified continuous ant colony optimisation for multiple unmanned ground vehicle path planning", Expert Systems with Applications, Vol 196, Issue 116605, 2022.

30. Wang, T., Huang, P., Dong, G., "Modeling and path planning for persistent surveillance by unmanned ground vehicle", IEEE Transactions on Automation Science and Engineering, Vol 18, Issue 4, Pages 1615-1625, 2020.

31. Hassan, I. A., Attia, T., Ragheb, H., Sharaf, A., M., "Design of unmanned ground vehicle (UGV) path tracking controller based on reinforcement learning", International Journal of Heavy Vehicle Systems, Vol 30, Issue 5, Pages 577-587, 2023.

32. Demir, C., "İnsansız kara araçlarının hareket sistemlerinin kavramsal tasarımı", Yüksek Lisans Tezi, [Conceptual design of unmanned ground vehicles's motion systems] [Thesis in Turkish], Kırıkkale Üniversitesi, Kırıkkale, Pages 18-25, 2017.

33. Demir, C., Bozdemir, M., "Mili Savunma Sanayimiz Açısından İnsansız Kara Araçlarının Önemi", Uluslararası Taşköprü Pompeiopolis Bilim Kültür Sanat Araştırmaları Sempozyumu, Pages 616-632, Kastamonu, 2018.

34. Demir, C., Bozdemir, M., "İnsansız Kara Aracı Tasarımında Ağırlık Oranı Metodu Kullanımı", Gazi Mühendislik Bilimleri Dergisi, Vol 5, Issue 1, Pages 32-45, 2019.

35. Demir, C., Bozdemir, M, "İnsansız Kara Araçlarında Tekerlek ve Palet Tahrik Sistemlerinin İncelenmesi" II. Uluslararası Savunma Sanayi Sempozyumu, Kırıkkale, Pages 378-387, 2017.

36. Yoon, S. and Bostelman, R., "Analysis of automatic through autonomous-unmanned ground vehicles (A-UGVs) towards performance standards", IEEE International Symposium on Robotic and Sensors Environments, Ottowa, Pages 1-7, 2019.

37. Exactitude Consultancy, "Global Unmanned Ground Vehicles Market By Application Global Trends And Forecast From 2022 To 2029".https://exactitudeconsultancy.com/tr/reports/18995/unmanned-ground-vehicles-ugv-market/#request-a-sample April 19, 2024.

38. Efe, Ö., Kaynak, O., "Yapay Sinir Ağları ve Uygulamaları", Pages, 48-50, Boğaziçi Üniversitesi Yayınevi, İstanbul 2000.

39. Karanfil, S., "Fuzzy lojik problemlerinde üyelik fonksiyonunun belirlenmesinde deneysel verilere dayanarak bir yöntem geliştirme", [Developing a method based on experimental data to determine the membership function in fuzzy logic problems] [Thesis in Turkish], Doktora Tezi, Yıldız Teknik Üniversitesi, İstanbul, Pages 110, 1997.

40. Karakoyun, M., Hacıbeyoğlu, M., "Biyomedikal veri kümeleri ile makine öğrenmesi sınıflandırma algoritmalarının istatistiksel olarak karşılaştırılması", Dokuz Eylül Üniversitesi Mühendislik Fakültesi Fen ve Mühendislik Dergisi, Vol 16 Issue 48, Pages, 30-42, 2014.

41. Akyüz, A. Ö., Kumaş, K., Ayan, M., Güngör, A., "Antalya ili meteorolojik verileri yardımıyla hava sıcaklığının yapay sinir ağları metodu ile tahmini", Gümüşhane Üniversitesi Fen Bilimleri Dergisi, Vol 10 Issue 1, Pages 146-154 2020.

42. Altun, Ö., "Yapay zekâ yöntemleriyle hazine taşınmazlarının değerlemesi: Yapay sinir ağları ile kamu konutları üzerine bir uygulama", Türkiye Arazi Yönetimi Dergisi, Vol 4 Issue 2, Pages 62-73, 2022.

43. Akkaş, N., "Tozaltı köşe kaynağında yapay zeka teknolojileri kullanılarak dikiş geometrisinin modellenmesi", Yüksek Lisans Tezi, [Modeling of seam geometry using artificial intelligence technologies in submerged fillet welding] [Thesis in Turkish], Sakarya Üniversitesi, Sakarya, Pages 20-23, 2006.

44. Nwankpa, C., Ijomah, W., Gachagan, A. and Marshall, S., "Activation Functions: Comparison of trends in Practice and Research for Deep Learning", arXiv. Pages 25-26, 2018.

ULUSLARARASI 3B YAZICI TEKNOLOJİLERİ
VE DİJİTAL ENDÜSTRİ DERGİSİ
INTERNATIONAL JOURNAL OF 3D PRINTING
TECHNOLOGIES AND DIGITAL INDUSTRY

ISSN:2602-3350 (Online)
URL: https://dergipark.org.tr/ij3dptdi

ANALYSIS OF DIFFERENT POOLING FUNCTIONS ON A CONVOLUTION NEURAL NETWORK BASED MODEL

Yazarlar (Authors): Halit Çetiner*, Sedat Metlek

Bu makaleye şu şekilde atıfta bulunabilirsiniz (To cite to this article): *Çetiner H., Metlek S., "Analysis of Different Pooling Functions on A Convolution Neural Network Based Model" Int. J. of 3D Printing Tech. Dig. Ind., 8(2): 266-276, (2024).*

DOI: 10.46519/ij3dptdi.1484354

Araştırma Makale/ Research Article

Erişim Linki: (To link to this article): https://dergipark.org.tr/en/pub/ij3dptdi/archive

ANALYSIS OF DIFFERENT POOLING FUNCTIONS ON A CONVOLUTION NEURAL NETWORK BASED MODEL

Halit Çetiner[a]*, Sedat Metlek[b]

[a]Isparta Applied Sciences of University, Vocational School of Technical Sciences, Computer Technology, TÜRKİYE
[b]Burdur Mehmet Akif Ersoy University, Vocational School of Technical Sciences, Mechatronic Program, TÜRKİYE

* *Corresponding Author: halitcetiner@isparta.edu.tr*

(**Received:** 15.05.2024; **Revised:** 13.08.2024; **Accepted:** 14.08.2024)

ABSTRACT

The common denominator of deep learning models used in many different fields today is the pooling functions used in their internal architecture. These functions not only directly affect the performance of the study, but also directly affect the training time. For this reason, it is extremely important to measure the performance of different pooling functions and share their success values. In this study, the performances of commonly used soft pooling, max pooling, spatial pyramid pooling and average pooling functions were measured on a dataset used as benchmarking in the literature. For this purpose, a new CNN based architecture was developed. Accuracy, F1 score, precision, recall and categorical cross entropy metrics used in many studies in the literature were used to measure the performance of the developed architecture. As a result of the performance metrics obtained, 97.79, 92.50, 91.60 and 89.09 values from best to worst for accuracy were obtained from soft pooling, max pooling, spatial pyramid pooling and average pooling functions, respectively. In the light of these results, the pooling functions used in this study have provided a better conceptual and comparative understanding of the impact of a CNN-based model.

Keywords: Pooling, Artificial Intelligence, Convolution Neural Network, Classification.

1. INTRODUCTION

Convolutional neural networks (CNN) are used in many artificial intelligence algorithms, especially image classification and segmentation [1-3]. Image classification applications using CNN architectures are one of today's important research topics [4-7]. The underlying problem of this research topic is that CNN architectures are high-cost algorithms. For this reason, it is aimed that newly developed CNN architectures will be advantageous in terms of time, cost and complexity, especially in image classification applications. At the same time, it is critical that these algorithms are competitive with their competitors in terms of performance. For this reason, many researchers working in the field of artificial intelligence are trying to develop new algorithms for image classification applications. They often aim to solve these problems by using CNN layers in different combinations. However, new solutions to these problems can be brought from a different perspective by focusing on layer structures that are commonly used in many architectures. For this reason, the study focused on the pooling layer. Generally, two types of pooling are used in CNN architectures: local and global. In the local pooling method, feature maps are obtained from local regions in window size with the help of windows hovering over the images. The second type of pooling, the global pooling type, is a pooling that creates a scalar value for each feature in the feature map. Pooling, which has a non-linear process, collects the outputs in layers by reducing them [8].One of the most important features that distinguishes the pooling layer from other layers is that it reduces input sizes to minimize memory consumption in order to maintain statistical performance [9-11]. Pooling layer is used to obtain semantic information and reduce the spatial resolution of feature maps, known as

subsampling [12]. When performing subsampling, maximum pooling preserves the most distinctive, distinct features in the feature map, while average pooling creates a smooth transition effect [12]. Pooling also partially solves the overfitting problem, which is a significant disadvantage in deep learning models.

CNN-based architectures generally consist of multiple convolutional layers to extract distinctive features and subsequent layers such as Batch Normalization, Pooling, and Fully connected. In the Pool-SH model proposed in this article, while the layers other than the pooling layer remain constant, the max pooling, average pooling, soft pooling and spatial pyramid pooling methods are used separately and compared in the pooling layer. The main purposes of pooling layers that form the architectures in deep learning are to learn features despite changes such as subsampling feature maps and scaling and rotation [4]. Pooling reduces computational complexity and memory requirements by reducing the feature map size while preserving important features. In the Pool-SH model proposed in this article, it has been proven on a benchmark dataset which of the max pooling, average pooling, soft pooling, spatial pyramid pooling methods will give better performance values. For this purpose, the natural image data set, which is frequently used in the literature, was used.

The main contributions of the study to the literature are presented below.

- The proposed Pool-SH model provides a structure that can compare popular pooling functions that operate in very critical tasks such as computational cost, complexity and data size reduction.
- The proposed Pool-SH model tries to compete with its unique structure consisting of 16 layers instead of the high-weight structures of transfer learning-based architectures.
- The soft pooling function outperforms the other pooling functions on the proposed Pool-SH model.
- As a result of the performance results obtained on the proposed Pool-SH model, values were obtained from soft pooling, max pooling, spatial pyramid pooling and average pooling functions, from highest to lowest.

The rest of the study consists of 4 sections. Section 2 presents the related work in the literature. Section 3 introduces the materials and methods used. Section 4 presents the performance results obtained from the experimental studies. In the last section, the findings obtained are evaluated in general.

2. RELATED WORKS

In this chapter, A literature review was conducted to cover maximum pooling and average pooling, as well as soft pooling and spatial pyramid pooling methods, which are frequently mentioned in the literature. At the same time, studies using natural images [13], which is the benchmarking dataset used in this article, are also analyzed in this section.

The pooling layer is a layer that reduces the feature map from the previous convolution layer to smaller sizes, which is often used in CNN and transfer learning based architectures. In CNN and transfer learning based architectures, the pooling layers used are among the important factors affecting the performance of the model. Pooling layers greatly reduce the computational cost and learning process of the model by reducing the spatial dimension of the model in transfer learning and CNN models. Among the most widely used pooling layers in the literature are maximum and average pooling layers [14]. The main shortcoming of the maximum pooling layer is that it only takes the largest value in the area where it is used, and therefore ignores other values. The main shortcoming of the average pooling method is that it takes the average of the values in the area where it is applied. Thus, the minimum and maximum values, which are extreme values, are ignored. Due to these disadvantages, there are many studies in the literature where these methods are used and tested [4,8]. A brief analysis of the applications that use the Natural images dataset as a dataset in their work is also shared below.

Dogo et al. [15] compared Adamax, AdaDelta, Nadam, SGD, vSGD, Adam, SGDm, RMSProp and SGDm+n methods, which are stochastic gradient-based optimization techniques frequently used in CNN-based architecture setup. They obtained performance graphs by training the architectural models used on the benchmark dataset used in the article with the relevant optimization technique. As a result of the performance results, it is stated that the

Nadam optimization technique gives better results than other optimization techniques.

Sikandar et al. [16] developed a hybrid machine learning method consisting of ResNet50, VGG16 and KNN algorithms. In the method they developed, first the features from the ResNet50 and VGG16 methods are given as input to the GlobalMaxPooling2D layer and converted into a one-dimensional array. Secondly, the features converted into a one-dimensional array are clustered by determining the Euclidean distances with the KNN method. After the clustering process, the distance between image clusters was determined. Prabavathi and Sakthi [17], carry out a new study, different from the studies in the literature, to obtain a higher compression ratio. First, the noise of the image is removed. It then performed image compression to achieve storage efficiency and transmission.

Praveenkumar and Nagaraj developed a new model consisting of many layers of nodes in deep neural networks. They aimed to increase classification performance and reduce training time with the model they developed [18]. A brief summary of studies using maximum and average pooling methods commonly used in the literature is presented below.

Özdemir et al. [14] takes the average of the K number of highest pixels inspired by the maximum and average pooling layers. It is stated that the Avg-TopK method, which is the pooling method they developed, gives better results in transfer learning-based models. Within the scope of the study, the effects of maximum, average and Avg-TopK methods were tried to be measured not only on color images but also on gray images. The Avg-TopK method is reported to be better than other classical pooling methods in terms of computational cost, speed and performance.

Muhammed et al. [19] implemented designs for a block called vector pooling block for the pooling layer, which is not widely studied in the literature. The developed pooling method consists of two data paths focusing on the extraction of features on vertical and horizontal paths. Here, instead of collecting features using a fixed square filter, CNN architectures can collect both local and global features by using long and narrow filters.

Vigneron et al. [20] developed a new pooling method based on Zeckendorf's number series. It is stated that their newly developed Z pooling layer is better adapted to partitioning tasks than other pooling methods.

Sharma et al. [21], tried to improve the performance of CNN architecture by trying a hybrid pooling method for image classification. The hybrid pooling method they developed is a method that can be thought of as a mixture of fuzzy and maximum pooling with the help of using pixel intensity values such as maximum and average pooling. The fuzzy and maximum pooling layer is combined with the learning parameter α. The study tries to prove that the hybrid pooling method they developed is better than the traditional pooling method in their performance.

Bhattacharjee et al. [22] designs a trainable pooling process that determines the instance-to-bag relationship based on the genetic algorithm. It is reported that the initialization of random weights is achieved by optimizing the attention weights thanks to the genetic algorithm.

3. MATERIAL AND METHODS

Deep learning methods are current algorithms developed especially for problems that cannot be solved with a certain formulation. One of the basic building blocks of these algorithms is pooling methods. Pooling methods are special methods developed to use a certain fraction of many features. Therefore, pooling methods improve the learning performance of CNN-based models by reducing computational complexity [4]. Pooling methods are used for different purposes such as reducing overfitting, capturing high-level information between features, and increasing the impact of the most important features. For this reason, soft pooling, SPM, max pooling, average pooling and max pooling methods, which are frequently used in the literature, are used in this study. SPM method is preferred because it extends the fully connected layer feed with multi-level pooling to alleviate the shortcomings of traditional pooling methods.

The main reason for choosing the soft pooling method is that it aims to smooth the maximum activation values in the kernel values used in deep learning methods. Max pooling method is chosen because it is simpler and more

understandable than many pooling functions. The average pooling method is generally similar to the max pooling method. The difference is that if the values in the region where the pooling method is applied are zero or close to zero, it presents values close to zero in the output. As a result, dominant features may be lost. In this study, the average pooling method was preferred to examine the effect of this disadvantage on the situation.

3.1. Materials

The natural image dataset used within the scope of the article consists of 727 airplanes, 968 cars, 885 cats, 702 dogs, 843 flowers, 1000 fruits, 788 motorcycles, and 986 person images. The dataset consists of a total of 6899 images belonging to 8 different classes: airplane, dog, flower, fruit, car, cat, motorbike, person [13].

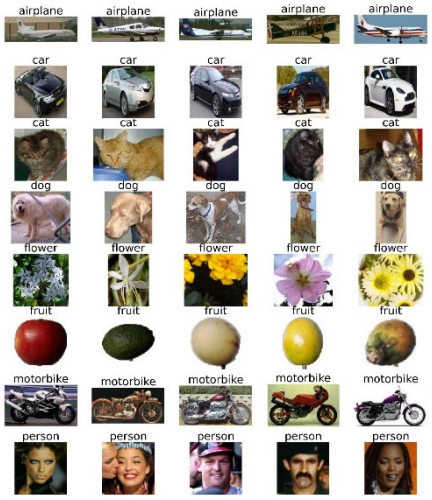

Figure 1. Sample dataset

Figure 1 shows image examples of each class in the dataset.

3.2. Max Pooling Method

In many CNN models in the literature, the maximum pooling method is preferred. The main reason for this is that its structure is simpler and more understandable than many pooling functions. Max pooling is based on the largest value within the kxk neighborhood when optimizing the spatial size of a feature map [23-25]. The general structure of max pooling is presented in Eq. 1.

$$f_{max}(x) = max\{x_i\}_{i=0}^{N} \quad (1)$$

The expression x in Eq. 1 refers to the pooling region in the input image. Given sparse codes and simple linear classifiers, max pooling performs better [14]. The disadvantage of the max pooling function is that it takes the largest value in the relevant region and ignores other values. For this reason, in some cases, distinctive features may be lost. As a result, the performance of applications may be negatively affected.

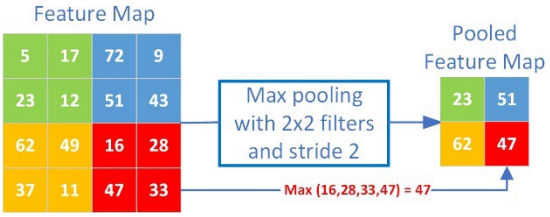

Figure 2. Max pooling

The situation in question can be seen in Figure 2. In the feature map in Figure2, the stride value was selected as 1 and a 2x2 pooling function was applied. As can be seen from here, only the largest values in the relevant area were taken. This may cause unacceptable results in some applications.

3.3. Average Pooling Method

As can be seen in Figure 3, the average pooling method takes the average of the values in the pooling region. This situation is mathematically illustrated by Eq. 2.

$$f_{avg}(x) = \frac{1}{N}\sum_{i=1}^{N} x_i \quad (2)$$

While the x_i value in Eq. 2 shows the data in the area where the pooling process is applied, the N value represents the total number of these data. In addition, the general working principle of the Average pooling method is similar to the max pooling method. The disadvantage is that if the values in the region where the pooling method is applied are zero or close to zero, it presents zero or close to zero values in parallel with these values at the output. As a result, dominant features may be lost.

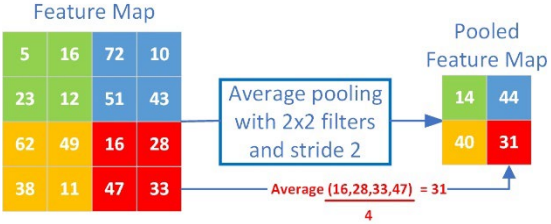

Figure 3. Average pooling

3.4. Soft Pooling Method

The general logic of the soft pooling method developed by Riesenhuber and Poggio [26] is based on the natural exponent (e), which ensures that larger activation values have a greater effect on the output. This can be done with a gradient value proportional to at least the minimum value during backpropagation to all activations within the local core neighborhood [27]. As a result, this process is the opposite of the methods presented in Sections 3.2 and 3.3. The soft pooling method aims to soften maximum activation approaches within the kernel region. For this, Eq. 3 is used first.

$$w_i = \frac{e^{a_i}}{\sum_{j \in \mathbf{R}} e^{a_j}} \tag{3}$$

While the weight applied to the ith index in Eq. 3 is expressed with w_i, the applied activation is expressed with a_i. Nonlinear transformations can be performed with weights corresponding to the activation values. Thus, higher activations are made more dominant than lower ones. Since most pooling operations are performed in high-dimensional feature spaces, highlighting activations with higher impact is a more logical approach than simply selecting the mean or maximum value [27]. While in the max pooling and average pooling approaches, discarding some information means discarding important features, in this approach, the equal contribution of activations may correspond to local density reductions by taking the overall regional feature density equally into account. In the soft pooling method, the output value is generated via a standard sum of all weighted activations within the R core neighborhood as in Eq. 4.

$$\tilde{a} = \sum_{i \in \mathbf{R}} w_i * a_i \tag{4}$$

Compared to traditional maximum and average pooling methods, using softmax of regions of interest allows each activation to be normalized relative to neighboring activations for the core region with a probability distribution proportional to their values. This is in contrast to the popular choice of maximum or average value, or averaging all activations over the core region, where the output activations are not regularized [27].

3.5. Spatial Pyramid Matching Method

Spatial pyramid matching (SPM) method is a new pooling method that eliminates the need for fixed-size images in CNNs. This method is applied as fixed-size constraints to fully connected layers instead of convolution layers. In general, before pyramid pooling functions, it was necessary to crop and warp images in order to fit the images into the dimensions in the CNN layers. However, operations such as cropping and warping could lead to content loss and geometric distortions [28,29]. SPM, a popular pooling method today, is designed to match the size of feature maps. The sizes of the contents may vary. For example, let's say you have an image of size 128x128. If the four container number is used under this image, a patch of 32x32 dimensions can be created. In this way, a total of 16 boxes (thousand) are formed. The highest value in each box (bin) is considered the activation value of the next level of the pyramid. As a result, the SPM technique can produce a fixed-length output without taking into account the size of the input. Moreover, it allows adaptation to input image scales during the testing and training phases of SPM, which strengthens the scale invariance feature and eliminates the problem of overfitting in the network [30]. The SPM method is primarily designed to deal with images of variable size. It also has a more complex learning procedure. As a result, it is sometimes less efficient. For example, in the CIFAR10 dataset, it caused an error of 16:89 percent [31].

3.6. Proposed Model (Pool-SH)

Pool-SH, a new CNN-based model, was proposed to analyze the pooling functions used in the study. The Pool-SH model aims to use layers similar to those commonly used in CNN-based architectures.

Thus, a more realistic comparison with the models in the literature was enabled. In the input layer of the model developed in the study, first thresholding is applied to the image, and in the cabin the images are resized to 240x240. These dimensions are again very close to the dimensions used in many transfers learning models in the literature. In the layers following the entry layer, convolution and pooling operations are performed sequentially.

Although ReLU activation functions were used in the convolution layers used in the study, the dimensions of the tested pooling layers were

determined as 2x2. This situation is shown in detail in Figure4. Flatten and Fully Connected Layer, which have become standards in many deep learning models in the literature, were added to the model proposed in the study. In the last stage of the proposed model, the classification layer was added. Since there are 8 outputs in the added classification layer, the softmax activation function was used. The content of the softmax activation function is also presented in Eq. 5.

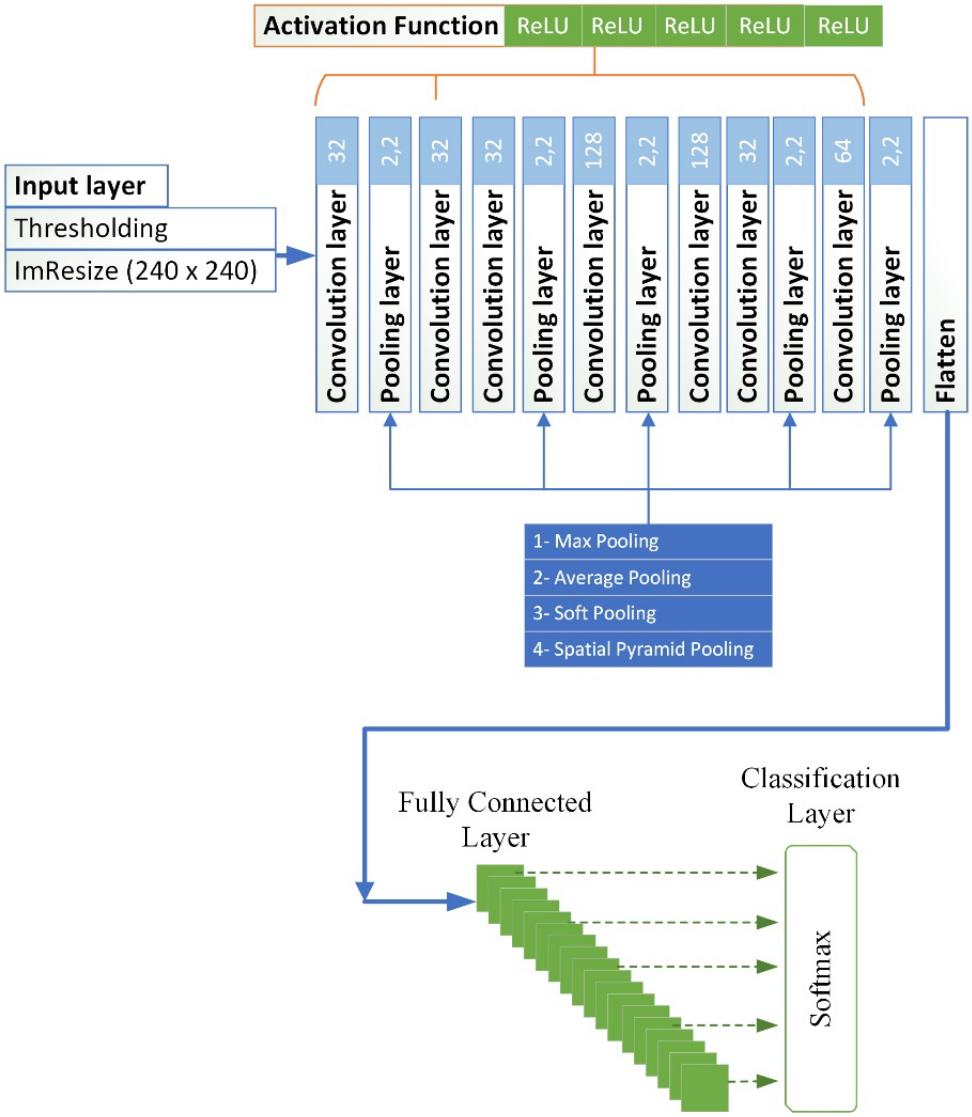

Figure 4. Proposed Pool-SH model.

$$softmax(z_j) = \frac{e^{z_j}}{\sum_{j=1}^{N} e^{z_j}} \quad for\ j = 1, \ldots, N \tag{5}$$

The softmax function is a variant of the sigmoid function. Although the term N used in Eq. 5 refers to N classes, the softmax function allows the calculation of which class each output of these classes belongs to by adding their exponential values. The z_j value in Eq. 5 represents the jth value in the classification layer. The model designed in this way consists of 16 layers in total and includes four pooling layers. Soft pooling, max pooling, spatial pyramid pooling and average pooling functions were used in these pooling layers, respectively. In this case it is shown in detail in Figure 4.

3.7. Execution of the Pooling Methods

In the execution of pooling methods, the max pooling method was preferred first. In this method, using only the largest number in the filter used provides ease of operation and has an effective role in highlighting only the dominant features on the image. However, local features

in the data are lost. In the average pooling method, sharp features are lost and more localized images can be obtained. In parallel with the literature, it was found that soft pooling gives higher performance than max pooling and average pooling when the size of the features representing the class is smaller than the image size [8]. SPM is a pooling method that provides multi-level input by removing the fixed constraints associated with the fully connected layer. Due to its inherent computational complexity, it is found to be less efficient than other methods, in accordance with the literature [31].

If it is necessary to evaluate the pooling methods used in terms of computational complexity, SPM, soft pooling, average pooling, and max pooling methods are found to be the highest to the lowest. It is noteworthy that while the computational complexity of average pooling and max pooling methods are close to each other, it is seen that the SPM method offers a considerably higher computational complexity compared to other methods.

4. EXPERIMENTAL RESULTS AND DISCUSSION

The 6899 images in the natural image dataset used in the study were divided into two groups: training and validation, according to the cross-validation value of 5. While the number of images in the test group was determined as 1380, the number of images in the training group was determined as 5519. In the study, experimental studies were carried out on a computer with a 64-bit operating system with NVIDIA RTX 3060 graphics card, AMD Ryzen 7 5800H branded processor with a capacity of 3.2 GHz, 16 GB RAM and hardware features. Training the system takes approximately 48 minutes. For performance measurement in training and testing, we used the commonly used metrics of accuracy, F1 score, precision, recall and categorical cross entropy (CELoss), which are presented in Eqs. 6-10 respectively [32-36,37].

$$Accuracy = \frac{TP + TN}{TP + TN + FN + FP} \quad (6)$$

$$Recall = \frac{TP}{TP + FN} \quad (7)$$

$$Precision = \frac{TP}{TP + FP} \quad (8)$$

$$F1\ Score = \frac{2 * Recall * Precision}{Recall + Precision} \quad (9)$$

$$CE_{Loss} = -\frac{1}{N}\sum_{i=1}^{N}\sum_{c=1}^{C}(y_{ic}\log(\widehat{y_{ic}})) \quad (10)$$

The terms TP, TN, FP and FN used in Eqs. 6-8 refer to true-positive, true-negative, false-positive and false-negative respectively. The training results obtained with these metrics are detailed in Table 1. In Eq. 10, $\widehat{\boldsymbol{y_{ic}}}$ denotes the probabilistic prediction result, while $\boldsymbol{y_{ic}}$ denotes the classification result at the end of $\boldsymbol{i}$. training for the $\boldsymbol{c_{th}}$ category

As can be seen from Table 1, the soft pooling function performs the best, followed by max-pooling. These are followed by spatial pyramid-pooling and average pooling. It is noteworthy that the results of max-pooling and spatial pooling are close to each other, while average pooling has the lowest performance.

The main reason behind the high performance of the soft pooling method preferred in the study is the natural upper bound that allows larger activation values to have a greater impact on the output. It can be said that the high performance of the max pooling method after the soft pooling method is due to the high discriminative power of the maximum numbers in the extracted features. In SPM, the multilevel expansion process of feeding the fully connected layer did not have as high performance impact as soft pooling and max pooling. Average pooling, on the other hand, often results in a loss of performance in terms of information in terms of contrast. When calculating the average, all values in the filter are taken into account. As a result, if the values of all activation outputs are low, the average is also low. This situation is obtained in parallel with the literature [38]. Unlike in the literature, if most of the activation results are zero, the performance values decrease even more.

Table 1. Training performance results.

Pooling Type	Accuracy	F1 score	Precision	Recall	CE_{Loss}
Soft	98.25	98.40	98.25	98.25	0.001
Spatial pyramid	93.37	92.15	94.63	94.40	0.016
Max	95.50	94.72	95.61	95.60	0.015
Average	90.72	90.03	90.25	90.17	0.054

Table 2. Validation performance results.

Pooling Type	Accuracy	F1 score	Precision	Recall	CE_{Loss}
Soft	97.79	97.80	97.79	97.79	0.095
Spatial pyramid	91.60	90.87	91.68	91.50	0.776
Max	92.50	91.82	92.59	92.50	0.628
Average	89.09	88.05	89.82	88.30	0.386

In the study, the same metrics were used to measure the performance of the data allocated for testing. The results obtained here are shared in detail in Table 2.

When the performance results presented in Table 2 are analyzed, it is seen that they are in parallel with the training data. However, the test results were about 1% lower than the training results. The graphs of accuracy, F1 score, precision, recall and CE_{Loss} obtained from four different pooling functions as a result of the test are presented in Figures 5-9, respectively.

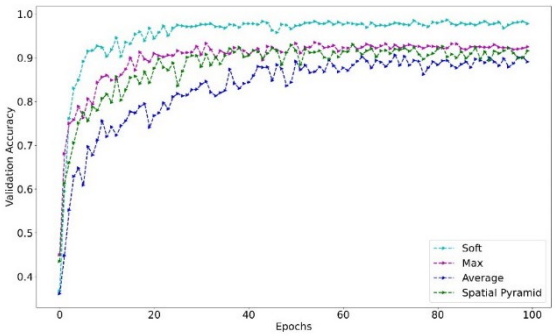

Figure 5. Validation accuracy performance graphics of proposed model for different pooling types

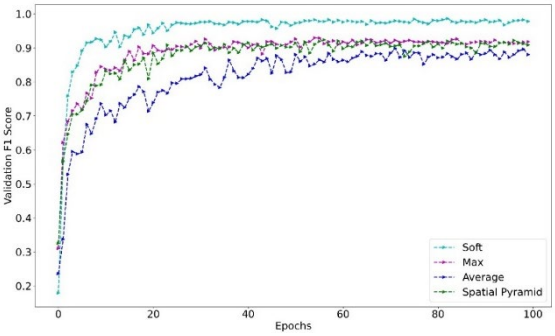

Figure 6. Validation F1 score performance graphics of proposed model for different pooling types

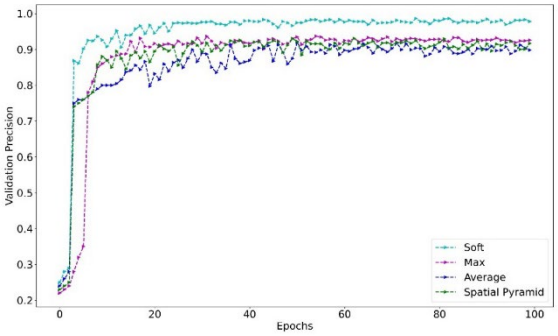

Figure 7. Validation precision performance graphics of proposed model for different pooling types

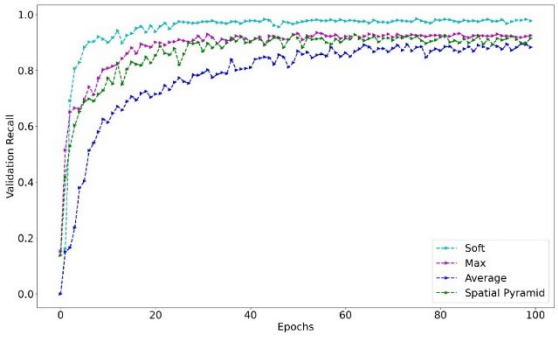

Figure 8. Validation recall performance graphics of proposed model for different pooling types

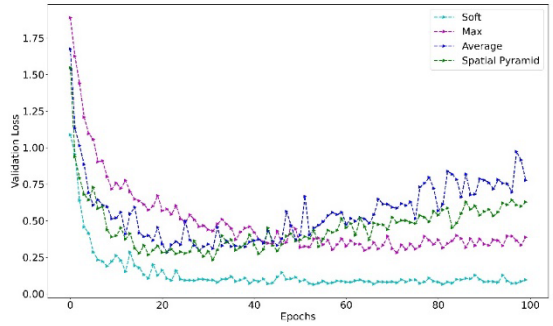

Figure 9. Validation loss performance graphics of proposed model for different pooling types

As can be seen in Figure 6, the lowest CE_{Loss} value is obtained from the soft pooling function, while the highest CE_{Loss} value is obtained from the average pooling function. This also confirms the accuracy values.

5. CONCLUSION

In this study, a study-specific convolutional deep learning model with four different pooling layers is used. The main purpose of the designed model is to measure the performance of soft pooling, max pooling, spatial pyramid pooling, and average pooling functions which are widely used in the literature. For this purpose, the natural images dataset used as benchmarking in the literature is used. On this dataset, accuracy, F1 score, precision, recall and CELoss metrics commonly used in the literature were used. The dataset used in the study was divided into two groups as training and test according to the cross validation 5 value.

In the light of the results obtained, the accuracy values of 0.9779 for soft pooling function, 0.9250 for max pooling function, 0.9160 for spatial pyramid pooling and 0.8909 for average pooling were obtained on the same dataset and deep learning model. As it can be seen from these results, the soft pooling function gave very good performance results compared to the other pooling functions used in the study. The main objective of this study is to measure the performance of the pooling functions comparatively.

It is seen that many CNN-based applications have been developed in autonomous systems and medical imaging systems, and the pooling methods tested in this study are also used in these applications [39-40]. It is seen that the performance results of the proposed method on the test set used in the study are quite good compared to other methods. In parallel with this, it is obvious that it will increase the success performance in CNN-based medical imaging and autonomous systems. When the pooling methods tested comparatively on the model proposed in the study are analysed, it is found that the computational complexity of the soft pooling method is higher than the other methods. However, the computational performance is quite high. If there are no hardware constraints, it is obvious that the soft pooling method will improve the performance of the study. On the other hand, if there are any hardware constraints, max pooling or average pooling can be preferred, respectively. Although the complexity of SPM is higher than max pooling, its performance is lower than max pooling. In the presence of hardware constraints, it would not be a reasonable solution to choose SPM. It is recommended that future research should take this situation into consideration.

At the same time, it is aimed to improve performance by developing different pooling functions with low computational cost with a new study on the dataset used in the study.

REFERENCES

1. Çetiner, H. and Metlek, S., "DenseUNet+: A novel hybrid segmentation approach based on multi-modality images for brain tumor segmentation,", J. King Saud Univ. - Comput. Inf. Sci., Vol. 35, Issue 8, Pages 101663, 2023.

2. Metlek, S., "CellSegUNet: an improved deep segmentation model for the cell segmentation based on UNet++ and residual UNet models,", Neural Comput. Appl., Vol. 36, Issue 11, Pages 5799–5825, 2024.

3. Çetiner, H., "Citrus disease detection and classification using based on convolution deep neural network,", Microprocess. Microsyst., Vol. 95, Issue 104687, Pages 1–10, 2022.

4. Nirthika, R., Manivannan, S., Ramanan, A., and Wang, R., "Pooling in convolutional neural networks for medical image analysis: a survey and an empirical study,", Neural Comput. Appl., Vol. 34, Issue 7, Pages 5321–5347, 2022.

5. Jena, B., Saxena, S., Nayak, G. K., Saba, L., Sharma, N., and Suri, J. S., "Artificial intelligence-based hybrid deep learning models for image classification: The first narrative review,", Comput. Biol. Med., Vol. 137, Pages 104803, 2021.

6. Mai, Z., Li, R., Jeong, J., Quispe, D., Kim, H., and Sanner, S., "Online continual learning in image classification: An empirical survey,", Neurocomputing, Vol. 469, Pages. 28–51, 2022.

7. Schmarje, L., Santarossa, M., Schröder, S.-M., and Koch, R., "A survey on semi-, self-and unsupervised learning for image classification,", IEEE Access, Vol. 9, Pages. 82146–82168, 2021.

8. Zafar, A., Aamir, M., Nawi, N. M., Arshad, A., Riaz, S., Alruban, A., Dutta, A. K., and Almotairi, S. "A Comparison of Pooling Methods for Convolutional Neural Networks,", Applied Sciences, Vol. 12, Issue 17, 2022.

9. Zhao, R., Song, W., Zhang, W., Xing, T., Lin, J, and Srivastava, M., "Accelerating binarized convolutional neural networks with software-programmable FPGAs,", in Proceedings of the 2017 ACM/SIGDA International Symposium on Field-Programmable Gate Arrays, Pages 15–24, 2017.

10. Yildirim, O., Baloglu, U. B., Tan, R.-S., Ciaccio, E. J. and Acharya, U. R., "A new approach for arrhythmia classification using deep coded features and LSTM networks,", Comput. Methods Programs Biomed., Vol. 176, Pages 121–133, 2019.

11. Cai, H., Gan, C., Wang, T., Zhang, Z., and Han, S., "Once-for-all: Train one network and specialize it for efficient deployment,", arXiv Prepr. arXiv1908.09791, 2019.

12. Murray, N. and Perronnin, F., "Generalized max pooling,", in Proceedings of the IEEE conference on computer vision and pattern recognition, Pages 2473–2480, 2014.

13. Roy, P., Ghosh, S., Bhattacharya, S., and Pal, U., "Effects of degradations on deep neural network architectures," arXiv Prepr. arXiv1807.10108, 2018.

14. Özdemir, C., "Avg-topk: A new pooling method for convolutional neural networks,", Expert Syst. Appl., Vol. 223, Pages 119892, 2023.

15. Dogo, E. M., Afolabi, O. J., Nwulu, N. I., Twala, B. and Aigbavboa, C. O., "A Comparative Analysis of Gradient Descent-Based Optimization Algorithms on Convolutional Neural Networks,", in 2018 International Conference on Computational Techniques, Electronics and Mechanical Systems (CTEMS), Pages 92–99, 2018.

16. Sikandar, S., Mahum, R. and Alsalman, A., "A Novel Hybrid Approach for a Content-Based Image Retrieval Using Feature Fusion,", Applied Sciences, Vol. 13, Issue 7, 2023.

17. Prabavathi, M. V and Sakthi, M., "Poisson Wavelet Quantized Piecewise Regressive Distributed Coding for Image Compression and Transmission,", Tuijin Jishu/Journal Propuls. Technol., Vol. 44, Issue 6, 2023.

18. Praveenkumar, G. D. and Nagaraj, R., "Regularized Anisotropic Filtered Tanimoto Indexive Deep Multilayer Perceptive Neural Network learning for effective image classification,", Neurosci. Informatics, Vol. 2, Issue 2, Pages 100063, 2022.

19. Mohamed, E. A., Gaber, T., Karam, O. and Rashed, E. A., "A Novel CNN pooling layer for breast cancer segmentation and classification from thermograms,", PLoS One, Vol. 17, Issue 10, Pages e0276523, 2022.

20. Vigneron, V., Maaref, H. and Syed, T. Q., "A New Pooling Approach Based on Zeckendorf's Theorem for Texture Transfer Information,", Entropy, Vol. 23, Issue 3. 2021.

21. Sharma, T., Verma, N. K. and Masood, S. "Mixed fuzzy pooling in convolutional neural networks for image classification,", Multimed. Tools Appl., Vol. 82, Issue 6, Pages 8405–8421, 2023.

22. Bhattacharjee, K., Pant, M., Zhang, Y.-D. and Satapathy, S. C., "Multiple Instance Learning with Genetic Pooling for medical data analysis,", Pattern Recognit. Lett., Vol. 133, Pages 247–255, 2020.

23. Boureau, Y.-L., Ponce, J., and LeCun, Y., "A theoretical analysis of feature pooling in visual recognition,", in Proceedings of the 27th international conference on machine learning (ICML-10), Pages 111–118, 2010.

24. Singh, P., Chaudhury, S., and Panigrahi, B. K., "Hybrid MPSO-CNN: Multi-level Particle Swarm optimized hyperparameters of Convolutional Neural Network,", Swarm Evol. Comput., Vol. 63, Pages 100863, 2021.

25. He, Z., Shao, H., Zhong, X., and Zhao, X., "Ensemble transfer CNNs driven by multi-channel signals for fault diagnosis of rotating machinery cross working conditions,", Knowledge-Based Syst., Vol. 207, Pages 106396, 2020.

26. Riesenhuber, M. and Poggio, T., "Hierarchical models of object recognition in cortex,", Nat. Neurosci., Vol. 2, Issue 11, Pages 1019–1025, 1999.

27. Stergiou, A., Poppe, R., and Kalliatakis, G., "Refining activation downsampling with SoftPool,", in Proceedings of the IEEE/CVF international conference on computer vision, Pages 10357–10366, 2021.

28. Zeiler, M. D. and Fergus, R., "Visualizing and understanding convolutional networks,", in Computer Vision–ECCV 2014: 13th European Conference, Zurich, Switzerland, September 6-12, Springer, Pages 818–833, 2014.

29. Girshick, R., Donahue, J., Darrell, T., and Malik, J., "Rich feature hierarchies for accurate object

detection and semantic segmentation,", in Proceedings of the IEEE conference on computer vision and pattern recognition, Pages 580–587, 2014.

30. Mumuni, A. and Mumuni, F., "CNN Architectures for Geometric Transformation-Invariant Feature Representation in Computer Vision: A Review,", SN Comput. Sci., Vol. 2, Issue 5, Pages 340, 2021.

31. Cao, Z., Xu, X., Hu, B. and Zhou, M., "Rapid Detection of Blind Roads and Crosswalks by Using a Lightweight Semantic Segmentation Network,", IEEE Trans. Intell. Transp. Syst., Vol. 22, Issue 10, Pages 6188–6197, 2021.

32. Ghosh, P., Azam, S., Jonkman, M., Karim, A., Shamrat, F. J. M., Ignatious, E., and De Boer, F. , "Efficient prediction of cardiovascular disease using machine learning algorithms with relief and LASSO feature selection techniques,", IEEE Access, Vol. 9, Pages 19304–19326, 2021.

33. Gupta, A., Kumar, R., Arora, H. S., and Raman, B., "MIFH: A machine intelligence framework for heart disease diagnosis,", IEEE access, Vol. 8, Pages 14659–14674, 2019.

34. Wang, L., Zhou, W., Chang, Q., Chen, J., and Zhou, X., "Deep ensemble detection of congestive heart failure using short-term RR intervals,", IEEE Access, Vol. 7, Pages 69559–69574, 2019.

35. Miao, F., Cai, Y. P., Zhang, Y. X., Fan, X. M., and Li, Y., "Predictive modeling of hospital mortality for patients with heart failure by using an improved random survival forest,", IEEE Access, Vol. 6, Pages 7244–7253, 2018.

36. Mohan, S., Thirumalai, C., and Srivastava, G., "Effective heart disease prediction using hybrid machine learning techniques,", IEEE access, Vol. 7, Pages 81542–81554, 2019.

37. Çelebi, S. B. and Emiroğlu, B. G., "A Novel Deep Dense Block-Based Model for Detecting Alzheimer's Disease,", Applied Sciences, Vol. 13, Issue 15, 2023.

38. Zhang, W., Li, C., Peng, G., Chen, Y., and Zhang, Z., "A deep convolutional neural network with new training methods for bearing fault diagnosis under noisy environment and different working load,", Mech. Syst. Signal Process., Vol. 100, Pages 439–453, 2018.

39. Metlek, S. and Çetiner, H., "ResUNet+: A New Convolutional and Attention Block-Based Approach for Brain Tumor Segmentation," IEEE Access, Vol. 11, Pages. 69884–69902, 2023.

40.Metlek, S. and Çetiner, H., "Inception SH: A New CNN Model Based on Inception Module for Classifying Scene Images,", Mühendislik Bilim. ve Tasarım Dergisi, Vol. 12, Issue 2, Pages 328–344, 2024.

ULUSLARARASI 3B YAZICI TEKNOLOJİLERİ
VE DİJİTAL ENDÜSTRİ DERGİSİ

INTERNATIONAL JOURNAL OF 3D PRINTING TECHNOLOGIES AND DIGITAL INDUSTRY

ISSN:2602-3350 (Online)

URL: https://dergipark.org.tr/ij3dptdi

3B YAZICILAR IÇIN SÜREKLI TAKVIYELI FILAMENT ÜRETIMINE UYGUN KALIP TASARIMI

SUITABLE MOLD DESIGN FOR CONTINUOUS REINFORCED FILAMENT PRODUCTION FOR 3D PRINTERS

Yazarlar (Authors): Mohamad Diaa Taleb, Özkan Öz, Fatih Huzeyfe Öztürk

Bu makaleye şu şekilde atıfta bulunabilirsiniz (To cite to this article): *Taleb M. D.,Öz Ö., Öztürk F. H., "3B Yazıcılar İçin Sürekli Takviyeli Filament Üretimine Uygun Kalıp Tasarımı" Int. J. of 3D Printing Tech. Dig. Ind., 8(2): 277-286, (2024).*

DOI: 10.46519/ij3dptdi.1490399

Araştırma Makale/ Research Article

Erişim Linki: (To link to this article): https://dergipark.org.tr/en/pub/ij3dptdi/archive

3B YAZICILAR IÇIN SÜREKLI TAKVIYELI FILAMENT ÜRETIMINE UYGUN KALIP TASARIMI

Mohamad Diaa Taleb*, Özkan Öz, Fatih Huzeyfe Öztürk

Karabük Üniversitesi, Teknoloji Fakültesi, Endüstriyel Tasarım Mühendisliği Bölümü, Türkiye

* *Sorumlu Yazar: ooz@karabuk.edu.tr*

(**Geliş/Received:** 28.05.2024; **Düzeltme/Revised:** 18.07.2024; **Kabul/Accepted:** 12.08.2024)

ÖZ

Üç boyutlu (3B) yazdırma teknolojisi sahip olduğu esnek imalat kabiliyetlerinden dolayı, günümüzde farklı endüstri alanlarında alternatif imalat metodu olarak kullanılmaktadır. Bu yöntemde, geleneksel imalat yöntemlerinden farklı olarak, parçalar katmanlar halinde üretilmektedir. Geleneksel imalat yöntemleri ile üretimi oldukça zor olan karmaşık geometrilere sahip parçalar 3B yazıcılar ile üretilebilmektedir. Bu imalat yönteminde karşılaşılan en büyük dezavantaj son ürün mekanik özelliklerinin polimer kalıplama yöntemleri ile karşılaştırıldığında düşük olmasıdır. Ancak, sürekli veya süreksiz fiber takviyeli filamentlerin geliştirilmesi ile son ürün mekanik özelliklerinin belirgin oranda iyileştirilmesi mümkün olmaktadır. Bu çalışmada, sürekli takviye elemanı ile güçlendirilmiş termoplastik matrisli filament üretiminde kullanılabilecek kalıp tasarımı ve üretimi amaçlanmıştır. Takviye ve matris elemanları olarak sırasıyla, tel ve Polilaktik Asit (PLA) tercih edilmiştir. Çalışmanın deneysel kısmında, tel takviyeli kompozit filament kullanılarak yazdırılan çekme test numunelerinin dayanımları ile saf PLA filament kullanılarak yazdırılan numune dayanımları karşılaştırılmıştır. Deneysel sonuçlar, yazdırmanın kompozit filament ile yapılması durumunda parça dayanımının belirgin şekilde iyileştirilebileceğini göstermiştir.

Anahtar Kelimeler: 3B Yazdırma, Sürekli Metal Takviyeli Filament, Kompozit Malzemeler, Mekanik Özellikler.

SUITABLE MOLD DESIGN FOR CONTINUOUS REINFORCED FILAMENT PRODUCTION FOR 3D PRINTERS

ABSTRACT

Three-dimensional (3D) printing technology is now being used as an alternative manufacturing method in various industries due to its flexible manufacturing capabilities. Unlike traditional manufacturing methods, 3D printing builds parts in layers. Parts with complex geometry that are difficult to produce with traditional manufacturing methods can be produced with 3D printers. The main disadvantage of this manufacturing method is that the mechanical properties of the final product are low compared to polymer molding techniques. However, by developing continuous or discontinuous fiber reinforced filaments, it is possible to significantly improve the mechanical properties of the final product. The objective of this study is to design and fabricate mold that can be used to produce thermoplastic matrix filament reinforced with continuous reinforcing elements. Wire and polylactic acid (PLA) were preferred as reinforcement and matrix elements, respectively. In the experimental part of the study, the strength of tensile test specimens printed with wire-reinforced composite filament was compared with the strength of specimens printed with pure PLA filament. The experimental results showed that part strength can be significantly improved when printing with composite filament.

Keywords: 3D Printing, Continuous Metal Reinforced Filament, Composite Materials, Mechanical Properties.

1. GİRİŞ

Eklemeli imalat yöntemlerinden olan termoplastiklerin 3B yazıcılar kullanılarak imal edilmesi araştırmacıların en fazla ilgi duyduğu ve gelişimine devam eden güncel üretim metodudur. Bu yöntemde, geleneksel imalat yöntemlerinden farklı olarak, parçalar katmanlar halinde üretilmektedir. Katmanlı üretim karmaşık geometriye sahip parçaların üretiminde malzeme sarfiyatını ve imalat süresini önemli oranda düşürmektedir [1]. Ancak, bu yöntemin en büyük dezavantajı plastik kalıplama yöntemleri ile karşılaştırıldığında son ürün mekanik özelliklerinin düşük olmasıdır. Katmanlar arası arayüzey etkileşimi, yapı içerisindeki boşluklar ve uygun olmayan yazdırma parametreleri (yazdırma hızı, yazdırma sıcaklığı vb.) yazdırılan parçaların mekanik özelliklerinde meydana gelen düşüşlerin başlıca nedenleridir [2,3]. Günümüzde yazdırma parametreleri ve prosesin iyileştirilmesi üzerine yapılan çalışmalar son ürün kalitesinin belirgin şekilde artmasına katkıda bulunmuş ve plastik kalıplama yöntemleri ile üretilen ürünler ile rekabet edebilir seviyeye getirmiştir [4]. Ayrıca, sürekli veya süreksiz fiber takviyeli kompozit parçaların yazdırılması amacıyla geliştirilen tasarımlar son ürün mekanik özelliklerinin geliştirilmesine olanak sağlamıştır [5–8]. Farklı takviye elemanları ile güçlendirilen polimerler, kompozitlerin yoğun olarak tercih edildiği havacılık, otomotiv ve denizcilik sanayilerinde temel malzeme grupları arasında önemli bir yere sahiptir. Bunun en önemli nedeni, düşük ağırlık-yüksek dayanım oranına sahip olmalarıdır [9,10]. Günümüzde, polimer kompozitlerin üretiminin yetişmiş elemana ihtiyaç duyması ve çok aşamalı bir üretim sürecini barındırması nedeniyle yüksek maliyetlidir. Enjeksiyonlu kalıplama, basınçlı kalıplama ve reçine enjeksiyonlu kalıplama yöntemlerinin uygulanabilmesi bu alanlarda yetişmiş teknik elemanlara ihtiyaç duymaktadır [11]. 3B yazdırma teknolojisinin kompozit parça üretimine uyarlanması kompozit ürün maliyetlerini düşürebilir ve endüstriyel uygulama alanlarını arttırabilir. Şekil 1'de termoplastik kompozit üretiminde 3B yazıcıların avantajlarından faydalanabilmek amacıyla araştırmacılar tarafından geliştirilen farklı tasarımlar gösterilmektedir.

Şekil 1'de gösterilen tasarımları uygulayan çalışmalar ve elde edilen sonuçlar aşağıda tartışılmıştır.

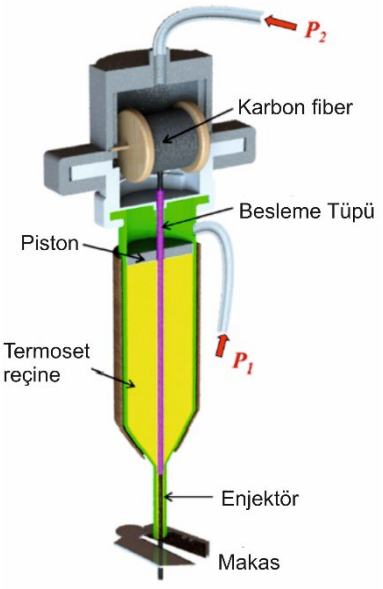

(a) Doğrudan mürekkepli yazdırma şırınga tasarımı [12]

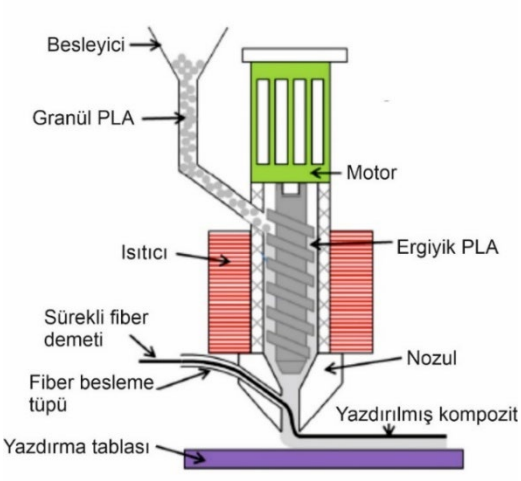

(b) Ekstrüderle kompozit parça yazdırma tasarımı [13]

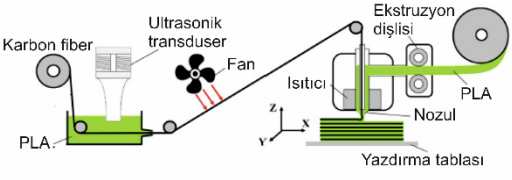

(c) Ultrasonik transdüser destekli fiber ön emprenye hazırlama ve yazıcı tasarımı [14]

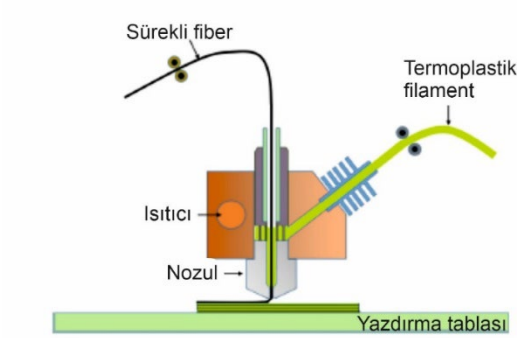

(d) Sürekli fiberin yerinde emprenye edildiği 3B yazıcı tasarımı [15]

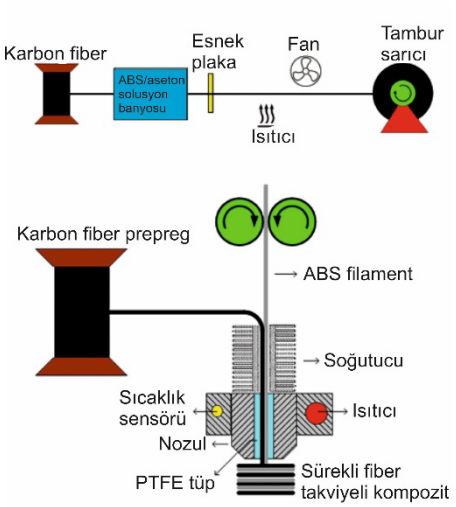

(e) Fiber ön emprenye hazırlama ve yazdırma entegre yazıcı tasarımı [16]

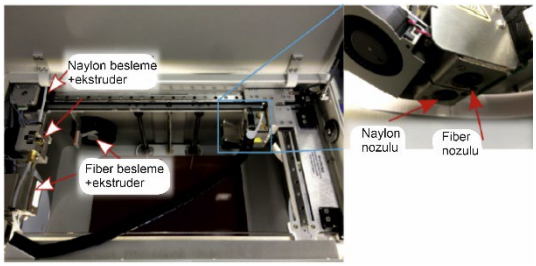

(f) MarkOne yazıcı nozul detay görüntüsü [17]

Şekil 1. Sürekli fiber takviyeli parça yazdırma sistemleri.

He vd. [12], çalışmalarında Şekil 1.a'da gösterilen fiber besleme tüpü ve fiberin içerisinden geçirildiği termoset reçine (mürekkep) ile doldurulmuş enjektörden meydana gelen tasarımı kullanmışlardır. Kompozit parçanın yazdırılması amacıyla içerisinde termoset reçine bulunan enjektöre fiber demeti besleme tüpü yardımıyla iletilmektedir. Tasarlanan yazıcıda reçinenin ilerletilmesi P1 piston basıncı ile sağlanmaktadır. P2 basıncı ise fiber besleme tüpü ucundaki basıncı dengeleyerek termoset reçinenin boru içerisine akışını engellemek için uygulanmaktadır. P1 basıncı altında çalışan enjektör içerisindeki fiber demeti kesme gerilimi ile yazdırma tablasına iletilerek kompozit parça yazdırılmaktadır. Önerilen bu tasarım hem termal olarak hem de UV ile kürlenebilen reçinelerin kullanımına uygundur. Termal olarak kürlenebilen reçineler ile yazdırılan kompozitlerin, tüm yazdırma yönlerinde doğrudan kalıplanmış numunelerin mekanik özelliklerine yakın değerler elde ettiklerini belirtmişlerdir.

Pappas vd. [13], çalışmalarında ekstrüder prensibi ile kompozit parça yazdırılması amacıyla Şekil 1.b'de gösterilen 3B yazıcıyı tasarlanmıştır. Bu tasarımda besleme hunisinden vida içerisine iletilen granül formundaki polimer ergitilerek, vida ucuna bağlı fiber besleme tüpünden iletilen fiber demetinin eriyik polimer ile kaplanması sağlanmaktadır. Çalışmalarında eriyik polimer ile kaplanan fiberin tabla üzerine yazdırılması ile parçanın imalatı gerçekleştirilir. Nozul eğim açısının arttırılması ile akışın daha rahat sağlandığını, elyaf kırılmalarının azaldığını ve bunlara bağlı olarak mekanik özelliklerinin arttığını belirtmişlerdir. Ancak, bu durumun yazdırma basıncını düşürdüğünü ve boşluk oluşumunu arttırdığını vurgulamışlardır.

Qiao vd. [14], Şekil 1.c'de detayları gösterilen bütünleşmiş sistemi kullanarak kompozit parça yazdırmışlardır. Bu tasarımda fiber, çözündürülmüş reçine içerisinden geçirilirken kullanılan transdüserin oluşturduğu kavitasyon etkisi ile fiber demetinin reçine ile etkili şekilde kaplanması sağlanmıştır. Sistemin devamında fiber üzerindeki diklorometan çözücü sıcak hava altında buharlaştırılarak uzaklaştırılmıştır. Bu sistemde elde edilen emprenye edilmiş fiber demeti 3B yazıcıda kullanmak üzere makarada sarılarak biriktirilmiştir. Kullanılan 3B yazıcının yazdırma kafası iki adet koaksiyel nozuldan oluşmaktadır. Emprenye edilmiş fiber demeti ve PLA filament yazdırma nozulunun alt kısmında karıştırılarak tablaya yapışması sağlanmıştır. Yapışmanın gerçekleşmesi ile fiberin sürekli olarak iletilmesi çekme kuvveti ile sağlanmaktadır. Yazdırılan parçalardan elde edilen sonuçlar, eğilme mukavemeti, eğilme modülü, çekme mukavemeti ve elastisite modülünün ultrasonik genliğin artmasıyla arttığını, ancak ultrasonik işlem hızının artmasıyla azaldığını göstermiştir. Kompozit malzemelerin çekme ve bükülme mukavemetlerinin işlenmemiş malzemeye kıyasla sırasıyla, %34 ve %29 oranında arttığı bulunmuştur.

Zhang vd. [15], fiberin ve eriyik polimerin nozul ucuna aynı anda beslendiği Şekil 1.d'de gösterilen tasarımı kullanmışlardır. Eriyik polimer, nozul ile entegre edilmiş yarıklar yoluyla fiberlerin üzerine polimer ile kaplanmaktadır. Polimer kaplı fiber yazdırılarak kompozit parça üretimini gerçekleştirmişlerdir. Deneysel sonuçlar, daha ince yazdırma kalınlığının daha büyük baskı kuvveti oluşturduğunu ve boşluk oluşumunu en aza indirdiğini ve buna bağlı olarak kompozit parçaların mekanik özelliklerini ve yüzey kalitesini iyileştirdiğini göstermiştir. Yazdırma işlem parametrelerini optimize ederken boyut doğruluğu ile mekanik özellikler arasında denge kurulması gerektiğini açıklamışlardır.

Mosleh vd. [16], Şekil 1.e'de gösterilen tasarımlarında polimer matris ile fiber ara-yüzey etkileşimini geliştirmek için sürekli fiberi aseton içinde çözündürülen ABS solüsyonu içerisinden geçirmişlerdir. Saf ABS ve kompozit parçaların mekanik özelliklerinin karşılaştırılması için numunelere çekme ve eğilme testleri uygulanmıştır. Deneysel sonuçlar, kompozitlerin eğilme ve çekme mukavemetinin, ABS numunelere göre arttığını gösterdi. Fiberlerin ABS çözelti içinden geçirilmesi ve düşük yazdırma hızının kompozit numune dayanım artışında önemli parametreler olduğunu belirtmişlerdir. Ayrıca, fiberlerin çözelti ile kaplanmasının kompozit parçaların yazdırılmasını kolaylaştırdığını belirtmişlerdir.

Blok vd. [17], çalışmalarında kompozit parça yazdırılmasında ise ticari olarak üretimi gerçekleştirilen MarkOne 3B yazıcıyı kullanmışlardır (Şekil 1-f). MarkOne 3B yazıcıda iki farklı nozul yardımıyla naylon matrise gömülü sürekli karbon fiber parça yazdırılabilmektedir. Kapalı kaynak kodlu yazılım kullanılan bu yazıcıda yazdırma parametrelerinin kullanıcı tarafından belirlenmesine izin verilmemektedir. Çalışmada kısa fiberler kullanılarak yazdırılan kompozit parça mekanik özellikleri MarkOne 3B yazıcı ile yazdırılan kompozit parça mekanik özellikleri ile karşılaştırılmıştır. Kısa fiberli kompozit parçaların yazdırılmasında açık kaynak kodlu 3B yazıcı kullanmışlardır. Sürekli fiber ile yazdırılan parçalarda dayanım ve rijitlik sırasıyla, 986 MPa ve 64 GPa olarak elde edilirken, kısa fiberle güçlendirilmiş naylon baskılı parçalarda bu değerler belirgin şekilde düşerek sırasıyla, 33 MPa ve 1.9 GPa olarak elde edilmiştir. Yazarlar, sürekli fiber yazıcının en büyük dezavantajının, fiberin yerleştirilmesi üzerindeki sınırlı kontrol ve daha karmaşık şekilleri yazdırırken meydana gelen parça içindeki boşluklar olarak sıralamıştır.

Yukarıda belirtilen sistemler, fiberin emprenye ile ön hazırlığının yapıldığı, nozul içerisinde fiber ve matrisin eş zamanlı karıştırıldığı veya fiber ve matrisin farklı nozullardan iletilerek kompozit parça yazdırma işlemi için tasarlanan yazıcı sistemleridir. Bu çalışmada literatürde yapılan çalışmalardan farklı olarak, sürekli fiber takviye elemanına sahip filament üretimi amaçlanmıştır. Sürekli fiber takviyesinin filament yapısı içerisine eklenmesi amacıyla kalıp tasarlanmış ve üretilmiştir. PLA matrisli filament takviye elemanı olarak kolay şekil alabilen 0.25 mm çapa sahip pirinç tel kullanılmıştır. Üretilen kompozit filament ile çekme test numuneleri yazdırılarak kompozit parça dayanımları belirlenmiş ve saf PLA ile üretilen parça dayanımları ile karşılaştırılmıştır.

2. MATERYAL VE METOD

2.1. Malzemeler

Kompozit filament üretiminde sürekli takviye malzemesi olarak 1040 MPa çekme dayanımına sahip pirinç tel ile PLA kullanılmıştır. Pirinç tel nispeten yumuşak, kolay şekil değiştirebilir ve iyi mekanik özelliklere sahip olduğu için seçilmiştir. PLA'nın fiziksel özellikleri Tablo 1'de gösterilmiştir.

Tablo 1. PLA fiziksel özellikleri [18].

Özellik	Değer
Elastisite modülü	3500 MPa
Çekme dayanımı	50 MPa
Kopmada uzama yüzdesi	≤ 5%
Ergime sıcaklığı	175°C
Camsı geçiş sıcaklığı	60°C

2.2. Kompozit Filament Üretim Kalıbı

Şekil 2'de sürekli tel takviyeli kompozit filament üretimi amacıyla tasarlanan kalıbın detay resimleri ve ölçüleri gösterilmektedir. Kalıbın ölçülendirilmesinde ve tasarımında tek vidalı ekstrüder ile uyumlu çalışması amaçlanmıştır. Kalıp gövdesi, eriyik termoplastik matrisin ilerletildiği gövde, takviye elemanın sürüldüğü yolluk ve kompozit filamentin şekillendirildiği nozzul kısımlarından oluşmaktadır.

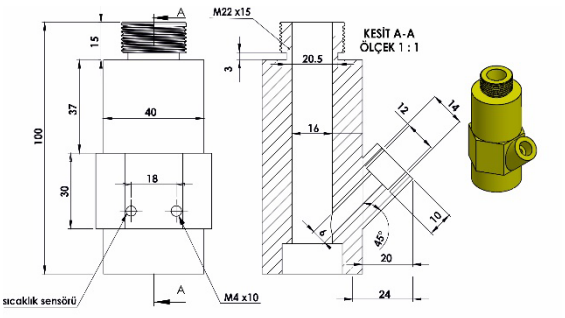

Şekil 2. Kalıp ölçüleri.

Şekil 3, kalıp yolluğu detay resmini göstermektedir. Takviye elemanının matris içerisine ilerletilmesi için tasarlanan yolluğun filament kesit merkezinde hassas şekilde konumlanabilmesi için vida adımı ile hareket ettirilmesi sağlanmıştır. Ayrıca, yolluğun gövde içerisine açılı şekilde yerleştirilmesi ile yolluğun içerisine eriyik polimer akışının engellemesi amaçlanmıştır. Eriyik polimer ile takviye elemanının gövde içerisinde teması başladığı anda takviye elemanı ile polimer matris arasında oluşan kesme kuvveti ile kesintisiz şekilde nozul içerisinde herhangi bir iticiye ihtiyaç duyulmadan takviye elemanı ilerleyebilmektedir.

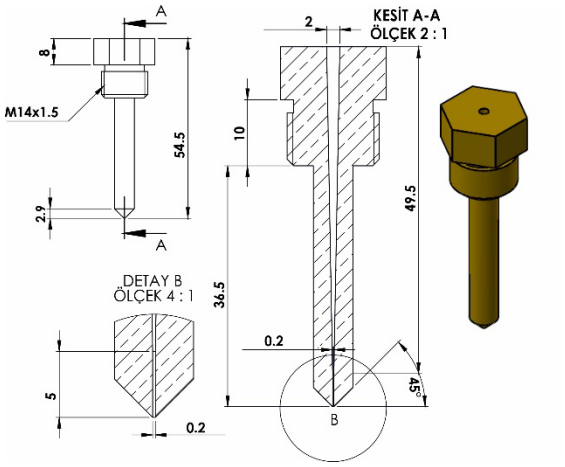

Şekil 3. Takviye elemanı giriş yolluğu ve ölçüleri.

Şekil 4, kalıbın çıkış ucuna bağlı filament çıkış nozulunu göstermektedir. Nozul kalıp gövdesi içerisinde birleştirilen matris ve takviye elemanının filament formunda çekilmesini sağlamaktadır. Kalıbın ısıtılmasından önce, tel yolluktan ve nozuldan geçirilmektedir. Başlangıçta telin geçirilmesi için kalıptan ayrılan nozul, kalıp ucuna tekrar bağlanarak kalıbın kovan ısısına ulaşması beklenmektedir.

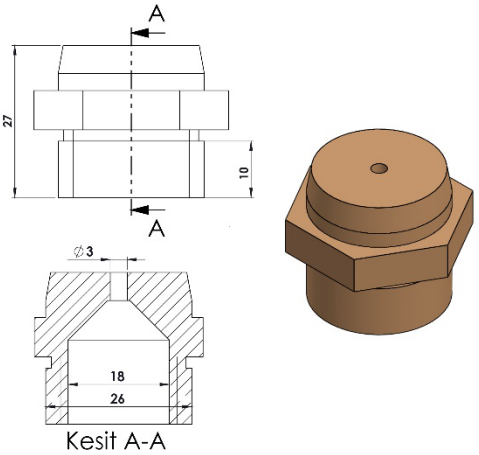

Şekil 4. Kalıp nozul ölçüleri.

Şekil 5, üretimi yapılan kalıbın tek vidalı ekstrüdere bağlantısını göstermektedir. Kalıp tek vidalı ekstrüderin vida sonuna konumlandırılmıştır. Eriyik termoplastik ekstrüder içerisinden kalıp gövdesine iletilmektedir. Kalıp gövdesi içerisine önceden konumlanan tel, eriyik polimer ile temas ettiği anda matris ile kaplanmakta ve kesme kuvveti vasıtası ile nozul dışına herhangi itici kullanılmadan sürülmektedir.

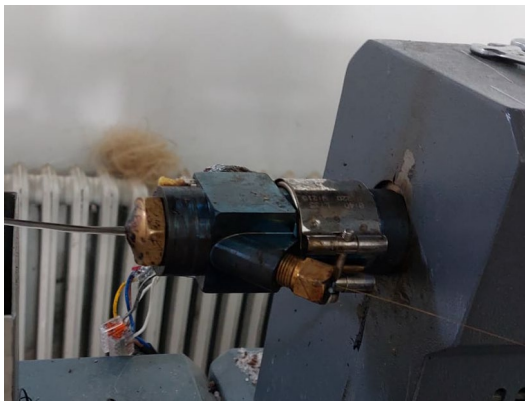

Şekil 5. Kalıp montajı.

2.3. Kompozit Filament Üretimi

Kompozit filament üretiminde matris olarak kullanılan PLA, hidrofilik yapıda olduğundan, neminin giderilerek kurutulması amacıyla 24 saat boyunca, 60°C sıcaklıktaki etüv içerisinde bekletilmiştir. Nem giderme işlemi yapılan granül formdaki PLA, 200°C sıcaklığa ayarlanan ekstrüder kovanı içerisine besleme hunisi vasıtasıyla dökülmüş ve eriyik formda kalıp nozulundan çıkması beklenmiştir. Kalıp nozulundan çıkan eriyik PLA teli sürüklemeye başladı anda, ekstrüderin sarma ünitesindeki filament makarasına bağlanarak sarım işlemine başlanmıştır. Sarım işleminde, filament çapı 1.75 mm olacak şekilde sarım hızı kademeli olarak arttırılmıştır. Şekil 6, sarım işlemi tamamlanmış ve 3B yazıcıda kullanıma hazır filament makarasını göstermektedir. Kompozit filament ortam koşullarından etkilenmemesi için yazdırılma işlemine kadar etüv fırın içerisinde bekletilmiştir.

Şekil 6. Filament makarası.

Şekil 7'de telin PLA matrisli filament içerisindeki konumlanması gösterilmektedir. Vida adımı ile hareket ettirilen yolluk tasarımının, teli filament kesiti ortasında konumlandırılabildiği Şekil 7'de net olarak görülmektedir.

2.4. Test Numunelerinin Yazdırılması ve Hazırlanması

Üretilen kompozit filamentlerin yazdırılmasında açık kaynak kodlu 3B yazıcı kullanılmıştır. Yazıcı tablası tek yönde (y ekseni doğrultusu), yazdırma nozulu iki yönde (x ve z eksen doğrultuları) harekete sahiptir. Tablo 2 kompozit filament ve PLA filament ile üretilen parçaların yazdırma parametrelerini göstermektedir. Çekme test numuneleri ASTM D3039/D3039M-00 standardı ile uyumlu 200x15x1,2 mm ölçülerinde yazdırılmıştır. Bütün numunelerde yazdırma yönü yük yönüne paralel olacak şekilde seçilmiştir. Yazdırma işlemi süresince, 1.2 mm çapa sahip nozul kullanılmış ve yazdırma hızı ile filament besleme hızı eşitlenmiştir.

Tablo 2. Yazdırma parametreleri

Parametre	Değer
Yazdırma hızı (mm/s)	50
Katman yüksekliği (mm)	0.6
Yazdırma sıcaklığı (ºC)	200
Nozul çapı (mm)	1.2
Yazdırma deseni	Doğrusal
Doluluk oranı	100%

Şekil 8 kompozit numunelerin 3B yazıcı ile yazdırılmasını göstermektedir.

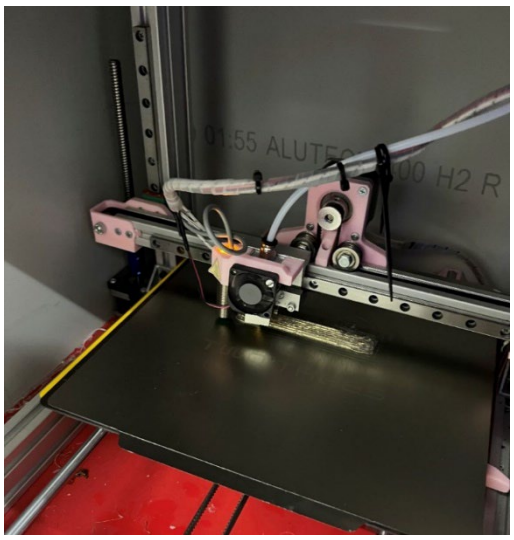

Şekil 8. Numunelerin yazdırılması.

(a) Filament uzunluğu doğrultusunda tel konumu. (b) Filament kesitinde tel konumu.

Şekil 7. Kompozit filament içerinde telin konumlanması.

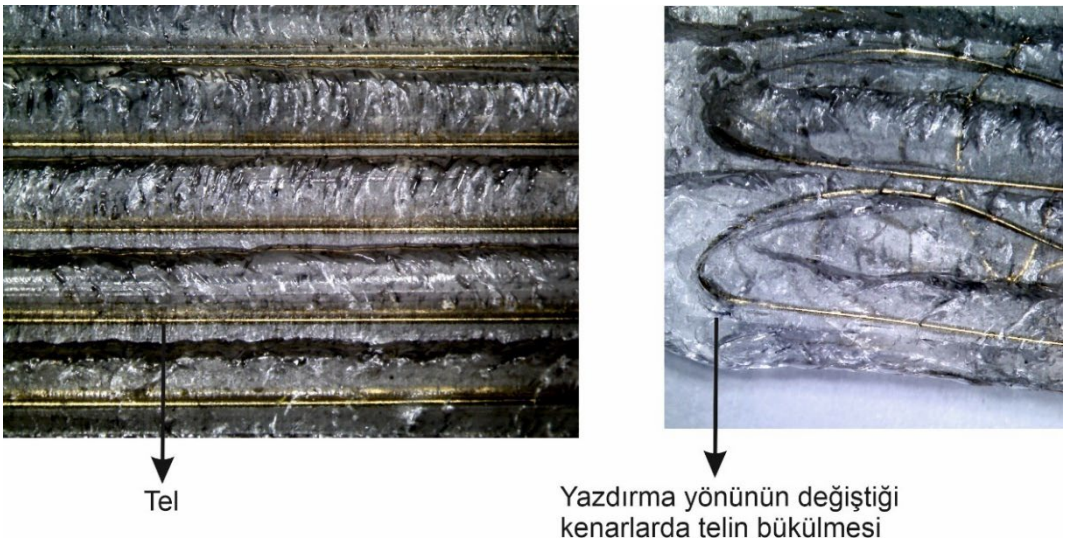

Şekil 9. Yazdırılan Numune içerisinde tel detay görüntüleri.

Şekil 9'da yazdırılan katmanların doğrultusunda tel detay görüntüleri gösterilmektedir. Şekil 9 incelendiğinde, tel takviyesinin katmanların içerisinde numune uzunluğu boyunca hatasız şekilde konumlandığı görülmektedir. Ayrıca, katmanların yön değiştirdiği numune uç kısımlarında telde herhangi bir deformasyon ya da kopma meydana gelmemesi kullanılan yazdırma parametrelerinin *(yazdırma ve besleme hızı)* uygun olarak seçildiğini göstermektedir.

Şekil 10'da çekme testi için hazırlanan numuneler gösterilmektedir. Numunelerin çekme test cihazı çenesi tarafından tutulan uç kısımlarına tablar yapıştırılmış ve kürlenmesi beklenmiştir.

Şekil 10. Çekme test numuneleri.

Çekme testlerinde Shimadzu marka elektro-mekanik 50 kN çekme test cihazı kullanılmıştır (Şekil 11). 2 mm/dk sabit çene hızında numuneler hasara uğrayana kadar yük uygulanmıştır. Deneyler süresince yük-yer değiştirme eğrileri kaydedilerek hasar yükleri belirlenmiştir. Numunelerin ulaştığı pik yük değerleri hasar yükü olarak kabul edilmiştir.

Şekil 11. Çekme test cihazı.

3. DENEYSEL SONUÇLAR

Şekil 12, kompozit ve PLA numune yük yer-değiştirme eğrilerini göstermektedir. Şekil 12 incelendiğinde, tel takviyeli kompozit numunenin saf PLA numuneye göre daha yüksek hasar yükü değerine ulaştığı görülmektedir. Ayrıca, kompozit filament kullanılması durumunda parça rijitliğini de önemli ölçüde artığı gözlemlenmiştir.

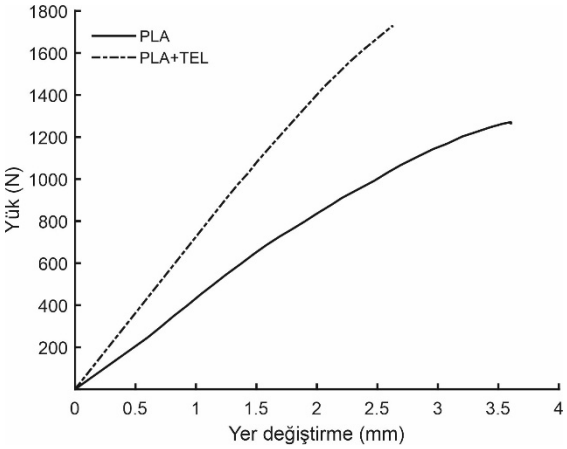

Şekil 12. Numunelerin yük-yer değiştirme eğrileri.

Şekil 13 numunelerin hasar yükü ve maksimum yer değiştirme değerlerini göstermektedir. Kompozit filament kullanımı parça hasar yükünü %39.53 oranında arttırmış ve rijitlik artışına bağlı olarak yer değiştirme değerini % 27.82 oranında düşürmüştür.

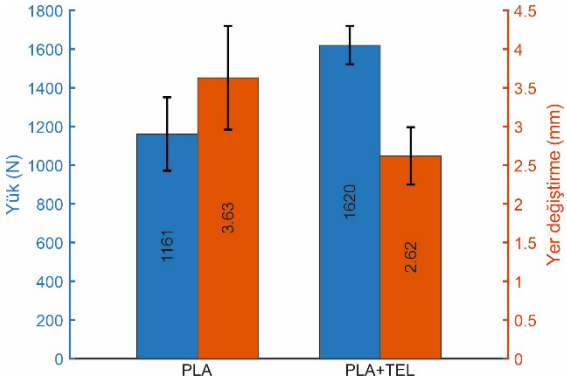

Şekil 13. Numunelerin yük-yer değiştirme diyagramı.

Parça yazdırılmasında sürekli fiberin kullanıldığı önceki çalışmalarda da benzer dayanım artışlarına ulaşılmıştır. Heidari-Rarani vd. [10], sürekli karbon fiber takviyeli PLA'nın çekme ve eğilme dayanımlarının saf PLA'ya göre sırasıyla, %35 ve %108'e kadar arttırdığını belirtmişlerdir. Ibrahim vd. [19], kompozit parça yazdırma işlemi için filament ve takviye elemanın nozul içerisine iletildiği çift girişli tasarımlarında tel takviyeli PLA matrisli kompozit yazdırmışlardır. Tel takviyesi olarak nikel krom ve bakır kullanmışlardır. Nikel krom ve bakır tel kullanılan kompozit parçaların dayanımındaki artışın PLA parçaya göre sırasıyla, %9 ve %30 oranlarında olduğunu belirtmişlerdir. Yapılan bu çalışmalar sürekli fiber kullanımının dayanım değerlerini belirgin şekilde geliştirdiğini göstermektedir. Düzenli fiber yönlenmesi dayanım artışının temel sebebidir. Ayrıca, fiber ve matris arasında arayüzey etkileşiminin yüksek olması matris fiber yük transferini önemli oranda arttırır. Bu çalışmada tel için özel bir yüzey hazırlama işlemi yapılmamasına rağmen, PLA ve takviye elemanlarının yazıcı içerisinde karıştırıldıkları yukarıdaki çalışmalara göre dayanım değerlerinin daha fazla geliştirilebildiği sonucuna ulaşılmıştır. Kalıp yardımı ile kompozit filament üretiminin dayanımda sağladığı avantajlar ile beraber kullanım kolaylığı açısından literatürde yapılan çalışmalara göre önemli avantajlar sağladığının vurgulanması önemlidir. Üretilen filamentin yazdırılmasında herhangi bir açık kaynak kodlu yazıcının kullanımında sınır olmaması ve özel tasarımlı yüksek maliyetli yazıcılara ihtiyaç duyulmaması bu yöntemin üstünlüğü olarak belirtilebilir.

4. SONUÇ VE TARTIŞMA

Bu çalışmanın temel amacı sürekli takviye elemanı kullanılarak kompozit filament üretiminde kullanılacak kalıp tasarımı ve üretiminin yapılmasıdır. Elde edilen sonuçlar, tasarlanan kalıbın sürekli takviyeli filament üretim kabiliyetine sahip olduğunu göstermiştir. Kompozit filament üretim sürecinde kullanılan tel takviye elemanının 1.75 mm çapa sahip filament kesitinin orta noktasında konumlanması sağlanmış ve makara sarımı süresince telin konumunun değişmediği belirlenmiştir. Kalıp yardımıyla başarılı şekilde üretilen kompozit filamentin yazdırılması çalışmanın numune üretim aşamasını içermektedir. Bu aşamada yazdırma işlemi çekme test numuneleri için tekrarlanmış ve üretimin hatasız bir şekilde gerçekleştirilebildiği görülmüştür. Çalışmanın son aşamasında üretilen numuneler çekme yükü altında test edilmiş ve kompozit filamentin hasar yükünün önemli oranda arttırdığı belirlenmiştir. Yazdırılacak parçaların geometrisi bu çalışmanın sınırlarını belirlemektedir. Hazırlanan kompozit filament kesintili olarak yazdırılan karmaşık numunelerin üretilmesi için uygun olmamakla beraber kesintisiz yazdırmanın mümkün olduğu levha veya silindirik parça imalatında başarılı bir şekilde uygulanabilir. Kesintili üretim yapılabilmesi filamentin belli aşamalarda kesilmesi ile mümkün olabilir. İlerleyen çalışmalarda filamentin kesilmesi için tasarlanacak eklentilerin kullanılması ile farklı geometrilerin yazdırılması mümkün olacaktır. Ayrıca, tasarlanan ekstrüzyon kalıbında, farklı takviye elemanları kullanılarak kompozit filament çeşitliliğinin arttırılması mümkündür. Son olarak bu kalıp yardımıyla üretilen filamentler kırpılarak enjeksiyon kalıplama sistemlerinde hammadde olarak da kullanılabilir. Bu sayede belirlenen karışım oranları garanti edilmiş granül elde edilmesine olanak sağlanabilir.

KAYNAKLAR

1. Anaç, N., Koçar, O., and Altuok, C., “Investigation of The Weldability of PLA Plus Sheets with Different Infill Ratios by Friction Stir Welding”, Gazi Üniversitesi Fen Bilimleri Dergisi Part C: Tasarım ve Teknoloji, Vol. 12, No. 1, Pages. 282–296 (2024).

2. Temiz, A., “The effect of build orientation on the mechanical properties of a variety of polymer AM-created triply periodic minimal surface structures”, J Braz. Soc. Mech. Sci. Eng., Vol. 46, No. 2, Pages. 121, 2024.

3. Öz, Ö. and Öztürk, F. H., “Yazdırma Açısının 3B Yazıcıda Üretilen PLA Numunenin Mekanik Özellikleri Üzerine Etkisinin Deneysel ve Sonlu Elemanlar Metodu ile İncelenmesi”, Politeknik Dergisi, Cilt. 26, Sayı. 2, Sayfa. 529–540, 2023.

4. Rouf, S., Malik, A., Singh, N., Raina, A., Naveed, N., Siddiqui, M. I. H., and Haq, M. I. U., “Additive manufacturing technologies: Industrial and medical applications”, Sustainable Operations and Computers, Vol. 3, Pages. 258–274, 2022.

5. Zhuo, P., Li, S., Ashcroft, I. A., and Jones, A. I., “Material extrusion additive manufacturing of continuous fibre reinforced polymer matrix composites: A review and outlook”, Composites Part B: Engineering, Vol. 224, Pages. 109143, 2021.

6. Öz, Ö., Öztürk, F. H., and Güleç, C., “Effect of fiber content and plasticizer on mechanical and joint properties of carbon fiber powder reinforced PLA manufactured by 3D printing process”, Journal of Adhesion Science and Technology, Vol. 37, No. 15, Pages. 2208–2231, 2023.

7. Sezer, H., Eren, O., Börklü, H., and Özdemir, V., “Karbon fiber takviyeli polimer kompozitlerin ergiyik biriktirme yöntemi ile eklemeli imalatı: fiber oranı ve yazdırma parametrelerinin mekanik özelliklere etkisi”, Journal Of The Faculty Of Engıneerıng And Archıtecture of Gazı Unıversıty, Cilt. 34, Sayı. 2, 2019.

8. Parmaksız, F., Anaç, N., Koçar, O., and Erdogan, B., “Investigation of mechanical properties and thermal conductivity coefficients of 3D printer materials”, Int. Adv. Res. Eng. J., Vol. 7, No. 3, Pages. 146–156 (2023).

9. Mortazavian, S. and Fatemi, A., “Fatigue behavior and modeling of short fiber reinforced polymer composites: A literature review”, International Journal of Fatigue, Vol. 70, Pages. 297–321, 2015.

10. Heidari-Rarani, M., Rafiee-Afarani, M., and Zahedi, A. M., “Mechanical characterization of FDM 3D printing of continuous carbon fiber reinforced PLA composites”, Composites Part B: Engineering, Vol. 175, Pages. 107147, 2019.

11. Rajak, D. K., Wagh, P. H., and Linul, E., “Manufacturing Technologies of Carbon/Glass Fiber-Reinforced Polymer Composites and Their Properties: A Review”, Polymers, Vol. 13, No. 21, Pages. 3721, 2021.

12. He, X., Ding, Y., Lei, Z., Welch, S., Zhang, W., Dunn, M., and Yu, K., "3D printing of continuous fiber-reinforced thermoset composites", Additive Manufacturing, Vol. 40, Pages. 101921, 2021.

13. Pappas, J. M., Thakur, A. R., Leu, M. C., and Dong, X., "A parametric study and characterization of additively manufactured continuous carbon fiber reinforced composites for high-speed 3D printing", Int J Adv Manuf Technol, Vol. 113, No. 7, Pages. 2137–2151, 2021.

14. Qiao, J., Li, Y., and Li, L., "Ultrasound-assisted 3D printing of continuous fiber-reinforced thermoplastic (FRTP) composites", Additive Manufacturing, Vol. 30, Pages. 100926, 2019.

15. Zhang, Z., Long, Y., Yang, Z., Fu, K., and Li, Y., "An investigation into printing pressure of 3D printed continuous carbon fiber reinforced composites", Composites Part A: Applied Science and Manufacturing, Vol. 162, Pages. 107162, 2022.

16. Mosleh, N., Rezadoust, A. M., and Dariushi, S., "Determining process-window for manufacturing of continuous carbon fiber-reinforced composite Using 3D-printing", Materials and Manufacturing Processes, Vol. 36, No. 4, Pages. 409–418, 2021.

17. Blok, L. G., Longana, M. L., Yu, H., and Woods, B. K. S., "An investigation into 3D printing of fibre reinforced thermoplastic composites", Additive Manufacturing, Vol. 22, Pages. 176–186, 2018.

18. Luminy® "Product Data Sheet L175", https://www.totalenergies-corbion.com/media/eushodia/pds-luminy-l175-190507.pdf, April 20, 2024.

19. Ibrahim, Y., Melenka, G. W., and Kempers, R., "Fabrication and tensile testing of 3D printed continuous wire polymer composites", Rapid Prototyping Journal, Vol. 24, No. 7, Pages. 1131–1141, 2018.

ULUSLARARASI 3B YAZICI TEKNOLOJİLERİ
VE DİJİTAL ENDÜSTRİ DERGİSİ
INTERNATIONAL JOURNAL OF 3D PRINTING
TECHNOLOGIES AND DIGITAL INDUSTRY

ISSN:2602-3350 (Online)
URL: https://dergipark.org.tr/ij3dptdi

MONITORING PEI PRODUCTION PARAMETERS ON A CUSTOM-MADE 3D PRINTER: AN INSIGHT INTO PHYSICAL AND MECHANICAL PROPERTIES

Yazarlar (Authors): Alptekin Yıldız

Bu makaleye şu şekilde atıfta bulunabilirsiniz (To cite to this article): *Yıldız A., "Monitoring PEI Production Parameters On A Custom-Made 3D Printer: An Insight Into Physical And Mechanical Properties" Int. J. of 3D Printing Tech. Dig. Ind., 8(2): 287-302, (2024).*

DOI: 10.46519/ij3dptdi.1493819

Araştırma Makale/ Research Article

Erişim Linki: (To link to this article): https://dergipark.org.tr/en/pub/ij3dptdi/archive

MONITORING PEI PRODUCTION PARAMETERS ON A CUSTOM-MADE 3D PRINTER: AN INSIGHT INTO PHYSICAL AND MECHANICAL PROPERTIES

Alptekin Yıldız[a,b]*

[a] Istanbul Technical University, Aviation Institute, Türkiye
[b] Istanbul Technical University, Aerospace Research Center, Türkiye

* *Corresponding Author: alptekin.yildiz@itu.edu.tr*

(**Received:** 01.06.2024; **Revised:** 12.08.2024; **Accepted:** 15.08.2024)

ABSTRACT

This study investigates the impact of production parameters on the quality of 3D-printed polyetherimide (PEI) samples using a custom-made 3D printer. In contrast to traditional optimization approaches, this research emphasizes the variability of outcomes despite maintaining fixed parameters such as nozzle and bed temperatures and slicer options. The study involves real-time monitoring of factors including nozzle, bed, and chamber temperatures, as well as relative humidity during the production process. Each layer was photographed individually to analyze its impact on the final product. Detailed physical and mechanical analyses revealed significant deviations in dimensions and flexural modulus, with a 10% loss in density and nearly 25% loss in flexural modulus in lower-performing samples compared to the best results. Results show correlations between critical parameters and product quality, underscoring the necessity for proper preparation and precise control. Furthermore, the research proposes a new method to geometrically represent the manufacturing process in a time-independent way using collected sensor data in 3D printing. This approach provides valuable insights for future studies aimed at optimizing additive manufacturing processes and enhancing the application of high-performance thermoplastics in high-tech fields such as aerospace and defense industries.

Keywords: Additive Manufacturing, Material Extrusion, Fused Filament Fabrication, Polyetherimide, DMA.

1. INTRODUCTION

Additive manufacturing (AM) has revolutionized industrial production processes in recent years, providing flexibility and cost savings in both the design and production stages. The advantages of AM technologies are not only evident in prototyping but also extend to final product manufacturing. In particular, AM methods enable the rapid and precise production of parts with complex geometries, thereby making production processes more adaptable and economical [1-3]. Among the various AM technologies, Fused Filament Fabrication (FFF), classified under Material Extrusion (MEX), has struggled to gain traction in high-tech sectors due to disadvantages such as limited material diversity and lower mechanical strengths compared to traditional manufacturing techniques. However, recent advancements have begun to address these challenges. The advent of high-performance thermoplastics like polyetherimide (PEI) and polyether ether ketone (PEEK), along with composites enhanced with various nano- and micro-additives, has paved the way for the application of FFF technology in high-tech areas, including aerospace and defense industries. These materials offer superior thermal stability, mechanical strength, chemical resistance, and multifunctional properties, making them suitable for demanding applications [4-6]. In sectors with stringent requirements, maintaining consistent quality control and physical and mechanical properties throughout the additive manufacturing process is crucial [7-8]. Consequently, monitoring and controlling relevant parameters during the production of high-performance thermoplastics has become vital for both production efficiency and product reliability.

In FFF, extensive analytical, numerical, and experimental studies have examined the fundamental production parameters, general characteristics, and limitations of all production stages [9-12]. Additionally, optimization studies employing parametric and statistical approaches for various additive manufacturing technologies are well-documented in the literature [13,14]. On the other hand, research focused on high-performance materials such as PEI and PEEK has consistently demonstrated their superior thermal stability and mechanical strength, particularly under optimal printing conditions [15]. The influence of nozzle temperature and structural orientation on the performance of PEEK and PEI is well-documented, showing significant improvements in mechanical properties when these parameters are carefully controlled [16]. Additionally, it has been shown that optimal infill parameters play a minimal role in the mechanical performance of PEI parts, which is particularly beneficial for weight-sensitive applications in the aerospace industry [17]. Furthermore, detailed investigations into process parameters that enhance print quality by optimizing the thermal and mechanical properties of PEEK and PEI blends have provided valuable insights into the production of high-quality components using FFF [18-20]. These studies underscore the critical role of temperature control, structural orientation, and material blends in achieving superior part quality in additive manufacturing.

Several studies have emphasized the importance of monitoring and controlling key parameters that influence the quality and physical properties of the final product. For instance, Vanaei et al. [21] highlighted the critical role of temperature control in optimizing the crystallinity and mechanical integrity of 3D prints produced via the FFF process. Their research demonstrated that monitoring filament temperature profiles is essential for enhancing interlayer adhesion and overall print quality. Similarly, Sgrulletti et al. [22] investigated the effects of bed temperature on the microstructure and tensile properties of FFF prints made from polyamide 6, utilizing thermal and optical live monitoring techniques. Their findings revealed that precise control of bed temperature significantly improves mechanical properties and morphology, with the use of integrated live monitoring systems resulting in a 70% increase in Young's modulus and a 79% improvement in tensile strength. Alatefi et al. [23] assessed the benefits of multivariate statistical quality monitoring in additive manufacturing. Their research demonstrated that the MEWMA (Multivariate Exponentially Weighted Moving Average) control chart reduces production defects, thereby improving the quality and stability of the FFF process. A transformation algorithm was employed to normalize data distribution, and MEWMA parameters were optimized using a novel heuristic technique, proving effective in maintaining process stability. Özsoy and Aksoy [24] investigated the effectiveness of artificial intelligence and image processing techniques in FFF printing. Their study showed that these techniques substantially enhanced the accuracy and quality control of the printing process, achieving a prediction accuracy of 92.5% for process parameters. By employing AI algorithms and image processing techniques, defects were swiftly identified, thereby increasing process efficiency.

Researchers investigating the critical effects of production parameters on the final product naturally aim to identify the optimal settings. The general assumption is that end users will apply these optimal parameters to achieve the best possible results. However, the production mechanism in AM is highly complex, influenced by multiple factors, many of which are non-linear. Parameters that are expected to remain constant may vary for various reasons, leading to deviations from the expected outcomes. As highlighted in the literature, real-time monitoring during production enhances the understanding and control of these complex processes. Therefore, further research is essential to optimize quality in the additive manufacturing of high-performance thermoplastics such as PEI. This includes developing systematic approaches for monitoring and controlling these parameters throughout the production process to ensure consistent and high-quality outputs.

This study intends to contribute to both academic literature and industrial practices by critically examining the FFF production process for high-performance thermoplastics, specifically PEI, under controlled yet naturally fluctuating environmental conditions. Unlike previous research that focuses primarily on

optimizing fixed production parameters, this work addresses the complexities that arise from variable chamber conditions, such as temperature and relative humidity, which inherently impact the production process. By systematically tracking and analyzing these parameters throughout the 3D printing process, this study provides a novel perspective on how real-time environmental monitoring influences the physical and mechanical properties of the final product. The adoption of ASTM D790 standard sample geometry, combined with advanced data collection techniques, enhances the robustness and applicability of this approach. This study not only deepens the understanding of FFF technology in the context of high-performance materials but also lays the foundation for future research aimed at improving the reliability and quality control of additive manufacturing processes in highly demanding sectors such as aerospace and defense.

2. MATERIAL AND METHODS

2.1. Filament Production

The polyetherimide (PEI - ULTEM™ RESIN 1010) granules was sourced from Sabic. The chemical formula of PEI is $C_{37}H_{24}O_6N_2$, with a density of 1.27 g/cm³ and a molecular weight of 592 g/mol. The glass transition temperature (T_g) of this material is 217 °C.

The PEI granules were subjected to a drying process in an oven at a temperature of 150 °C for a duration of eight hours. This was done to remove any residual moisture present, thereby preventing any undesirable conditions from occurring during the extrusion process. A lab-scale co-rotating twin-screw extruder was utilized to fabricate neat PEI filaments with a diameter of 1.75 mm. The extruder, manufactured by Kökbir Import & Export, features a screw diameter of 12 mm and a length-to-diameter (L/D) ratio of 22 [5]. The temperature gradient from the feed to the nozzle was meticulously controlled within the range of 310–360 °C, with a maintained screw speed of 210 rpm.

2.2. Custom-Made 3D Printer

The 3D printer (ARC-Beta) developed at the ITU Aerospace Research Center was designed to handle high-performance thermoplastics and includes several advanced features. Controlled by Marlin firmware on RAMPS 1.4, the printer employs a direct drive extruder, DyzEND-X & DyzeXtruder GT 1.75 mm kit with high-temperature sensors, compatible with a range of thermoplastic filaments, including PLA, ABS, nylon, PEEK, and PEI. Its Core-XY motion system enables precise extruder positioning. The printer is constructed with all-metal components and 3D-printed PEI parts, allowing it to reach print nozzle temperatures of up to 500 °C and bed temperatures of up to 200 °C. The device offers a print area of 25 × 25 cm and a print volume of 25 × 25 × 30 cm, housed within an 80 × 80 × 80 cm enclosed chamber. The chamber can reach temperatures up to 85K °C while maintaining a relative humidity of 10% or lower. Furthermore, the printer is equipped with remote control capabilities via OctoPrint software and integrated cabin temperature and humidity measurement. The design of the 3D printer can be seen in Figure 1.

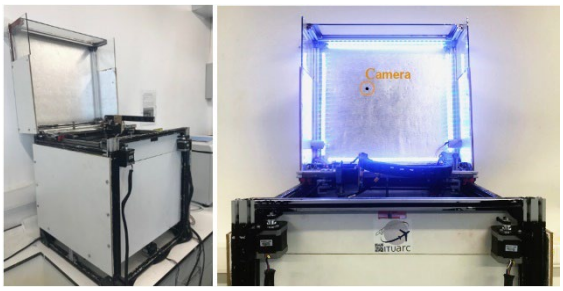

Figure 1. The custom-made 3D Printer ready for high-performance thermoplastics.

To understand the effects of production parameters on the printed product, the objective was to collect visual and real-time signal data during printing. Consequently, additional features were incorporated into the 3D printer cabinet. One key enhancement is a camera mounted above the printing bed, allowing it to capture images of each entire layer during printing. The Raspberry Pi Camera Module V2 was selected for this purpose and integrated with the 3D printer using a Raspberry Pi 3 control board, which enables remote control of the printer and the incorporation of mechanisms to capture images. To ensure optimal layer imaging, LED strips were installed for in-cabinet lighting. Another feature added to the 3D printer is the BME280 sensor. This sensor complements the monitoring of bed and nozzle temperatures by measuring the instantaneous chamber temperature and humidity, considering the bed temperature and cabinet insulation. This setup allows for the simultaneous capture of each layer's image and real-time recording of

nozzle, bed, and chamber temperatures, as well as chamber humidity, throughout the printing process.

2.3. 3D Printed Sample Production

For the test specimens printed using a 3D printer, the ASTM D790 standard was adopted. Specimens measuring 65 × 13 × 3 mm were produced in accordance with this standard, which is designed to determine dynamic mechanical properties (Dynamic Mechanical Analysis - DMA) by the three-point bending method for plastics. Based on experience [25], the optimal parameters for printing the test specimens are as follows:

- Nozzle diameter: 0.4 mm
- Nozzle temperature: 375°C
- Bed temperature: 160°C.
- Layer height: 0.2 mm
- Number of layers: 15
- Number of perimeter lines: 3
- Infill: 100% with a ±45° rectangle pattern
- Outline overlap:15%
- Skirt (First layer): 10 outlines without offset
- Speed: 30 mm/ s, %50 reduced for 1st layer

Figure 2 illustrates the sample dimensions and the specimen prepared for 3D printing using the slicing program.

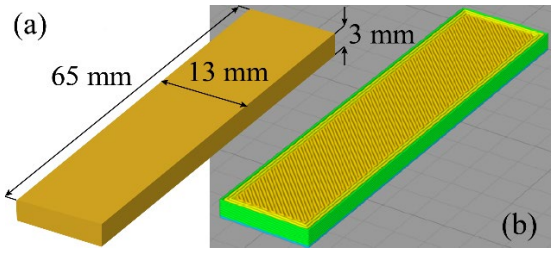

Figure 2. (a) Dimensions and (b) layered (sliced) view of a DMA specimen conforming to ASTM D790 Standard prepared for 3D printing using the Simplify3D slicing program.

Each printing process followed a specific protocol. First, the glass surface on the bed was thoroughly cleaned with alcohol. The bed was then carefully aligned to be exactly perpendicular to the nozzle plane (or parallel to the ground). The distance between the nozzle and the bed was checked at a minimum of three points using a feeler gauge for the z-end point to ensure precise positioning. A very thin layer of Nano Polymer Adhesive from Vision Miner was applied to the surface using a brush. Both the nozzle and the bed were preheated, and after a designated waiting period, the print-specific protocol (gcode) prepared with Simplify3D software was initiated. During printing, at the end of each layer, the extruder was moved to the side using a command added to the gcode, and photographs with a resolution of 3280 × 2464 were taken using the camera module, capturing the entire sample. Upon completion of the printing process, the bed and chamber were allowed to cool, and the sample was carefully removed. The production steps described were then repeated for the next print.

2.4. Characterization

Geometric measurements of the samples included width, thickness, and length. Using precision calipers, measurements were taken at three different points: the center and near both edges of the relevant surfaces (Figure 3). These values were then averaged with standard deviations to obtain the final dimensions.

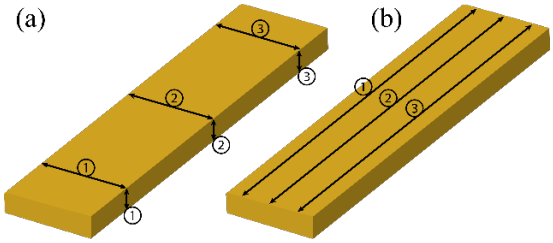

Figure 3. Measurement points for (a) width, thickness and (b) length on each specimen.

The mass of the samples was measured using an analytical balance. Density calculations were then performed using the mass data and the averages of the dimensions of the relevant sample.

Flexural modulus measurements were performed using a TA Instruments DMA 850 (New Castle, DE) following the ASTM D790 standard. The test utilized a 3-point bending fixture with a span of 50 mm. The measurement parameters included a crosshead speed of 0.05 mm/min and an initial force of 0.1 N.

2.5. Collecting Sensor Data from 3D Printer

In the study, in addition to the photographs taken during the production of each layer, a data processing algorithm was developed in Python to collect and organize data by processing log files generated by the OctoPrint and Marlin Control software. The algorithm, written in Python, reads data from two different log files

(octoprint.log and serial.log), parses the information, and structures it into a pandas DataFrame. The resulting data is then made available for analysis.

The contents of the log files are as follows:
Octoprint.log:
- This log file, generated by OctaPrint software, contains information about the printer's state changes (e.g., 'Starting', 'Printing'), events and enclosure temperature and humidity readings from the BME280 sensor.
- Each line includes a timestamp, the type and detailed information about the event.

Example Lines:
2024-01-10 07:58:17,267 –
octoprint.util.comm - INFO - Changing monitoring state from 'Starting' to 'Printing'
2024-01-10 07:58:17,276 –
octoprint.filemanager.analysis - DEBUG - Pausing analysis
2024-01-10 08:10:15,387 –
octoprint.plugins.enclosure - DEBUG - BME280 result: 79.2 | 4.6

Serial.log:
- This log file, generated by Marlin firmware, contains serial communication commands and feedback between the printer and the software.
- It includes sent and received commands, temperature readings, layer and coordinate information, and sensor data (e.g., nozzle and bed temperature).

Example Lines:
2024-01-10 07:58:17,257 –
Changing monitoring state from 'Starting' to 'Printing'

2024-01-10 07:58:17,309 –
Send: N1 G90*17
2024-01-10 07:58:17,377 –
Recv: ok T:375.1 /375.0 B:160.0 /160.0 @:87 B@:55
2024-01-10 07:58:19,285 –
Recv: X:0.00 Y:220.00 Z:0.00 E:3663.27 Count A: 17600 B:-17600 Z:0

The algorithm designed to systematically retrieve data from these two documents works through the following steps:

1. The log files are read line by line using the command ‘with open(filepath, 'rt') as in_file:’ and each line is appended to a list. This process is performed separately for both `octoprint.log` and `serial.log` files.

2. Regular expressions (regex) are used to extract the necessary data from each line. For example, timestamps are parsed using the ‘pd.to_datetime()’ function. The ‘re.compile()’ and ‘re.search()’ functions are used to find lines that match specific patterns.

3. Sensor data in "serial.log" and "Octoprint.log" are extracted from specific command and feedback lines in two separate locations.

4. The timestamps are converted to seconds and normalized, enabling the seamless integration of data from different sensors for comprehensive analysis.

5. The parsed data is converted into a pandas DataFrame and then exported as a csv file.

As a result, X-Y position of extruder, nozzle, bed and chamber temperatures, and relative humidity data were collected for 10 different samples, with 3,375 data points each.

2.6. Data Analysis Methodology
Python was employed extensively for data preparation, visualization, and statistical analyses, including correlation and ANOVA in this study. The data processing workflow utilized a combination of Python libraries to ensure thorough and accurate analysis. The pandas library was used for data manipulation, cleaning, and structuring, while numpy facilitated numerical operations and data array management. The scipy library provided tools for statistical computations, including correlation and ANOVA, whereas the statsmodels library was used for advanced statistical modeling and hypothesis testing. For visualization, matplotlib and seaborn libraries were used for initial data visualization and exploratory analysis, although these figures are not included in the article to save space. All final graphs presented in this article were generated using Origin Pro to ensure publication-quality figures.

3. RESULTS AND DISCUSSION

3.1. Dimensional Analysis of 3D-Printed Samples

The results of the geometric measurements of PEI samples produced with the 3D printer using the same parameters can be seen in the Figure 4 with deviation values.

The average dimensions of the 65×13×3 mm samples were 64.51 ± 0.10 mm for length, 12.87 ± 0.09 mm for width, and 2.91 ± 0.04 mm for thickness. Although the differences are at the micron level, the targeted dimensions were not fully achieved, resulting in slightly smaller product sizes than expected. On the other hand, considering the density value of 1.27 g/cm³ for PEI, mass values of 2.68 ± 0.15 g were measured, whereas the expected mass is approximately 3.22 g (Figure 4d). The average density value, calculated based on all relevant measurements, was determined to be 1.11 ± 0.06 g/cm³ (Figure 4e).

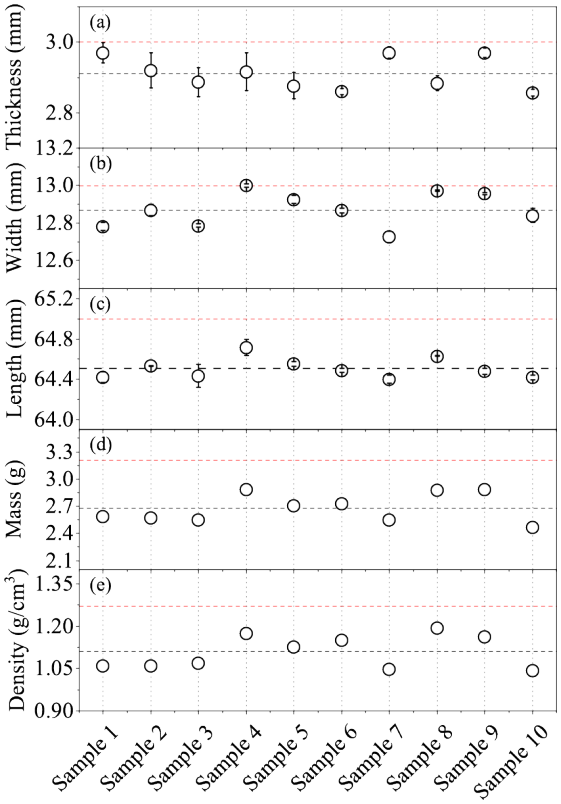

Figure 4. (a) Thickness, (b) Width, (c) Length, (d) Mass values, and (e) Density calculations of 3D-printed samples. The dimensional plots (a-c) present values with deviation lines. In all plots, the target values (red) and average values (black) of all samples are indicated by horizontal dashed lines.

The slightly lower than expected average values can be attributed to the *Extrusion Multiplier*, a production parameter that can vary for each filament type. This parameter addresses the issue where the filament is not extruded to the correct length due to various physical properties such as diameter and viscosity. For instance, if 10 mm of thermoplastic is expected to be extruded from the nozzle by feeding a certain amount of filament into the extruder, but the actual extrusion falls short, a simple multiplier value (e.g., 1.05) can be applied to push the filament further, achieving the required 10 mm. This adjustment allows the average dimensions of the produced parts, whether above or below the target, to be brought to the desired specifications. Although achieving these targeted values was confirmed in additional studies, the focus of this study is not on the absolute values themselves, but rather on examining the reasons for the deviations observed around the average values.

3.2. Flexural Moduli Results

The flexural moduli of the 3D-printed specimens were determined from the slope of the stress (σ_E) and strain (ε) curves. After applying linear curve fitting, moduli values were obtained for all specimens. It should be noted that these values are independent of the specimen geometry. In the measurements, the geometric dimensions of each specimen were entered into the TA Instrument's TRIOS software and the specimen lengths were fixed at 50 mm due to the span value of the fixture.

Table 1. The flexural moduli of 3D-Printed PEI samples.

Sample #	Flexural Modulus (MPa)
Sample 1	1808.8
Sample 2	1797.4
Sample 3	1967.1
Sample 4	2387.6
Sample 5	2381.6
Sample 6	2530.4
Sample 7	1816.2
Sample 8	2550.0
Sample 9	2328.9
Sample 10	1941.4

The flexural moduli values with an average value of 2150.93 ± 295.97 MPa are presented in Table 1 for the samples. The distribution of

relatively low, geometry-independent values clearly highlights the anisotropic and complex nature of additive manufacturing and underscores the motivation for this study.

3.3. Relationship Between Flexural Moduli and Physical Properties

Pearson, Spearman, and Kendall correlation analyses were employed to investigate the relationships between Flexural Moduli (FM) and other physical properties, including Thickness, Width, Length, Mass, and Density. Prior to the analysis, the data distribution and adherence to normal distribution were assessed through histograms and Q-Q Plots. However, these visualizations were omitted from the article to conserve space. The distribution of FM, Width, Mass, and Density variables closely approximated a normal distribution, while Thickness and Length variables exhibited some deviations. Scatter plots (Figure 5) were used to visually represent the relationships between FM and other physical characteristics, revealing negative correlations between FM and Thickness and positive correlations between FM and Width, Length, Mass, and Density.

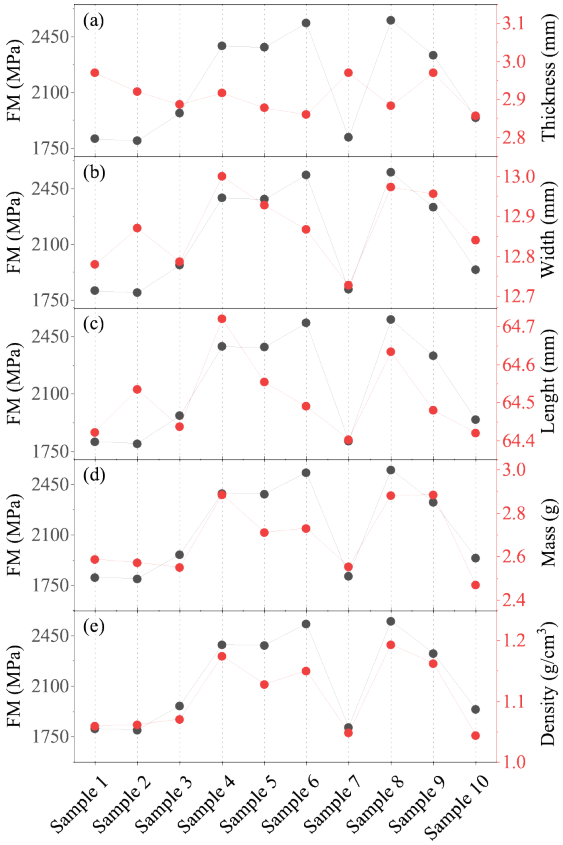

Figure 5. Flexural Moduli plots vs (a) Thickness, (b) Width, (c) Length, (d) Mass and (e) Density.

The correlation analysis results, conducted using three different methods, are presented in Table 2, with corresponding p-values in parentheses.

Table 2. Results of correlation analysis between flexural moduli (FM) and physical properties using Pearson, Spearman, and Kendall methods, with p-values in parentheses.

Variable	Pearson	Spearman	Kendall
Thickness	-0.4346 (0.2095)	-0.5079 (0.1340)	-0.3581 (0.1679)
Width	0.7853 (0.0071)	0.6991 (0.0245)	0.4944 (0.0482)
Length	0.6455 (0.0438)	0.6383 (0.0470)	0.5394 (0.0311)
Mass	0.8346 (0.0027)	0.6485 (0.0425)	0.4222 (0.1083)
Density	0.9428 (4.36e-5)	0.8268 (0.0032)	0.6293 (0.0119)

Pearson's correlation, which measures linear relationships between FM and other physical characteristics, showed a negative relationship between FM and Thickness, and positive relationships with Width, Length, Mass, and Density, with strong positive correlations for Density (0.942811) and Mass (0.834605). Spearman correlation, less sensitive to outliers of data, mirrored these results, with significant relationships for Width, Length, Mass, and Density ($p < 0.05$), but not Thickness ($p > 0.05$). Kendall correlation, robust to outliers, also showed positive relationships, with significant results for Width, Length, and Density ($p < 0.05$), but not for Thickness and Mass ($p > 0.05$). Overall, the strongest associations between FM and other physical properties were observed with Density and Mass. Given that the data were mostly normally distributed and exhibit linear relationships, Pearson analyses were more appropriate for revealing the relationships between variables. However, Spearman and Kendall correlations should also be considered, particularly for non-linear relationships or those deviating from normal distribution, such as Thickness and Length.

The observed relationships between physical properties and FM provide valuable insights into the additive manufacturing process. The positive correlation between FM and width, alongside the negative correlation between FM and thickness, suggests that specimens tend to

be relatively flattened and edge-spread. These characteristics indicate denser specimens with better interlayer adhesion when fully filled. Such findings imply that the pre-production distance between the nozzle and the bed may not have been uniformly adjusted across all samples, and/or the bed was not aligned perpendicularly (or parallel to the ground) to the nozzle plane. Additionally, the adhesive used to fix the samples to the bed might contribute to this issue. Uneven application of the adhesive with a brush after cleaning the surface with alcohol before each production can lead to adhesion problems to the bed and varying thicknesses.

These problems were particularly evident in the thickness measurements of the first five samples, where the thickness decreased toward one end, albeit by microns. The variations in thickness values shown in Figure 4 represent this observation. Furthermore, improperly set nozzle-to-bed spacing exacerbates anisotropy in printed products by causing *road distortion*, as noted by Turner et al [9]. In some cases, this can also lead to blockages, interrupting material flow and compromising print quality.

On the other hand, the relationship between FM and densities, along with the varying mass distributions, raises questions about the amount of polymer extruded. Two scenarios can lead to this situation: insufficient material being extruded or completely cutoff. The lower material output could result from a localized reduction in filament diameter used in the feed and/or fluctuations in production parameters that are expected to remain constant (such as the sensors monitored in this study), affecting the extrusion flow. Layer photographs were examined to identify these issues in the products.

3.4. Analysis of Layer Photographs

A total of 150-layer photographs, 15 from each sample, were collected at the end of production. Each layer was meticulously examined to check for proper production. Particular attention was paid to any deficiencies in layer production and the specific areas where they occurred. The FM values were considered during the examination of the layers, using the segregation observed in the FM values provided in Table 1 as a basis for analysis. The FM values of the samples exhibited a clear division, with values above and below 2000 MPa. Samples 1, 2, 3, 7, and 10 belonged to the low-FM class, averaging 1866.15 ± 72.16 MPa, while Samples 4, 5, 6, 8, and 9 belonged to the high-FM class, averaging 2435.70 ± 87.94 MPa. Layer photographs were categorized and analyzed based on these low and high-value FM groups, respectively.

In all but one of the low-FM specimens, deformations and deficiencies incurred during layer production were evident. With an average density of 1.06 ± 0.01 g/cm³, these defects, typically observed across multiple layers, were most noticeable in the middle and edge regions of the samples. Examples of these defective layers are illustrated in the Figure 6.

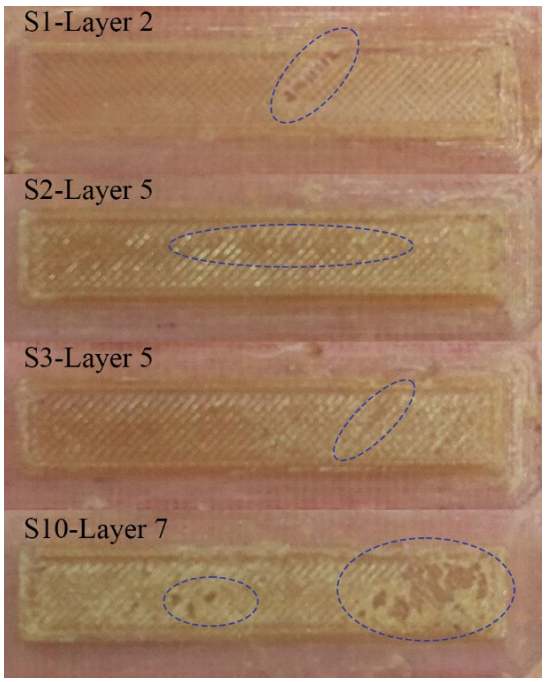

Figure 6. Examples of defective layers in low-FM samples. In the upper left corner of each image, the specific layer number of the sample (S) is indicated.

The most notable sample in this cluster is Sample 7, which exhibits no issues across any of its layers. Remarkably, this nearly flawless specimen has the lowest density and an above-average thickness. This anomaly can be attributed to a relatively high nozzle-to-bed distance and a consistent reduction in filament diameter during printing. Consequently, despite the production process being executed correctly, the low density and weak interlayer adhesion of this sample likely result in a lower FM value.

The samples in the High-FM cluster either exhibit very minor defects or are entirely flawless. Samples 8 and 9 show no issues at all. Sample 4 has only small imperfections in the last layer, and Sample 6 displays a slight mark in the tenth layer. Sample 5 is distinct from the others as it has defects in a few layers; however, these imperfections are located near the edges, well outside the 50 mm span used for FM measurements. Figure 7 illustrates the layer photographs of these High-FM samples, highlighting the minor defects where present.

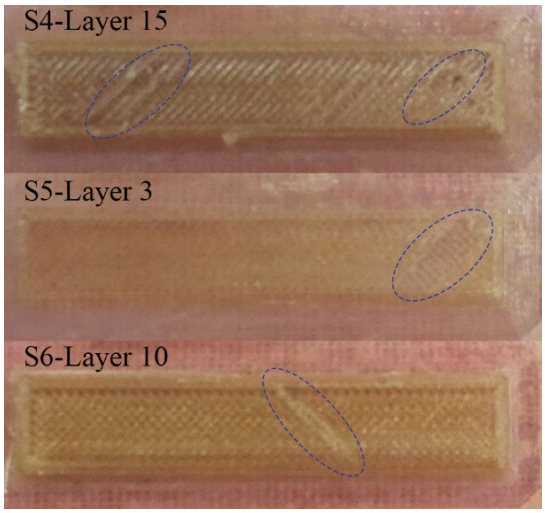

Figure 7. Defective layers in High-FM samples. In the upper left corner of each image, the specific layer number of the sample (S) is indicated.

The case observed in Sample 5 underscores that anisotropy resulting from additive manufacturing can lead to varying mechanical properties depending on the specific use and purpose of the fabricated product. This observation further emphasizes the critical importance of maintaining high production quality. In this context, the next section discussed the impact of production parameters, monitored via sensors, on the final products.

3.5. Sensor Data Analysis

Sensor data was collected for four different physical quantities. Two of these are the nozzle temperature and bed temperature, which were obtained from the log records of Marlin, the 3D printer's control software, and were entered as fixed values. The other two measurements are the chamber temperature and relative humidity, recorded by the BME280 sensor and collected from the log records of the OctoPrint software. Unlike the fixed nozzle and bed temperatures, these values vary and reflect the in-cabinet conditions during printing, particularly in relation to the bed temperature.

For the four monitored quantities, the mean values obtained across all samples were 375.062 ± 0.203 °C for nozzle temperature, 160.004 ± 0.009 °C for bed temperature, 80.544 ± 0.937 °C for chamber temperature, and 3.952 ± 0.106 % for relative humidity.

Sensor data from the production of 3D printed PEI samples can be seen in the Figure 8 as box charts. The graphs in the figure visualize the distributions of nozzle temperature, bed temperature, chamber temperature, and relative humidity data. Each plot displays the median, quartile values (25%-75%), mean values, and outliers identified according to the 1.5 IQR method. The green boxes represent the central tendency and spread of each sample, circle symbols denote the mean values, and the whiskers indicate the range of the data, including outliers.

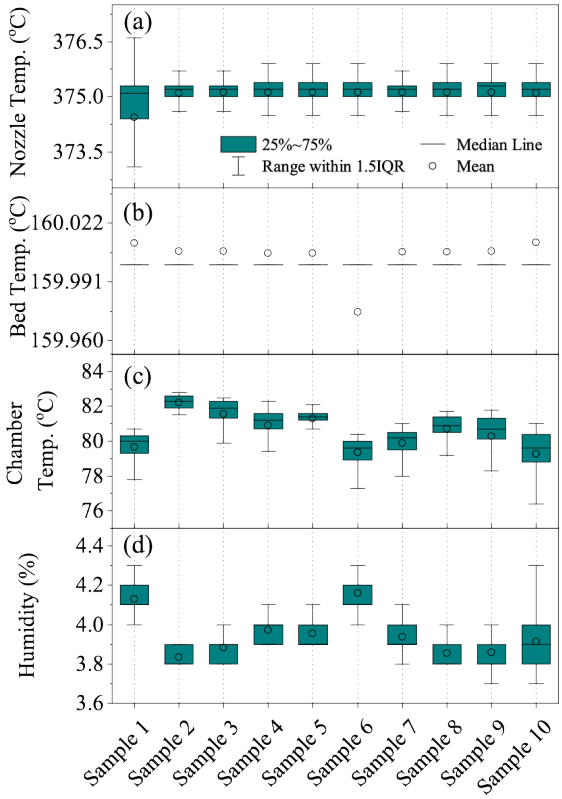

Figure 8. Box charts of sensor data from the production of 3D printed PEI samples: (a) Nozzle temperature, (b) Bed temperature, (c) Chamber temperature and (d) Relative Humidity.

When analyzing the nozzle temperature data, it was observed that the temperature remained stable around the target value of 375 °C. Both

the median and mean values were remarkably close to 375 °C, with the data distribution concentrated within a narrow range. This indicates that the Nozzle temperature was well-maintained. However, some samples contained outliers, identified using the 1.5 IQR method, suggesting occasional temperature fluctuations.

For the bed temperature data, the values were centered around the target temperature of 160°C. The median and mean values were generally close to 160°C, with minor deviations. Outliers in some samples indicated unexpected fluctuations in temperature control.

Analysis of the chamber temperature data revealed a range of 70 – 80 °C across samples. Differences between the median and mean values suggested potential asymmetries in the data distribution. The data spread over a wide range, with outliers indicating that chamber temperature might fluctuate due to environmental factors or equipment condition during the production process.

Relative humidity data showed variation between 3.9% and 4.8% among samples. The median and mean values were remarkably close, with a narrow distribution range, indicating general stability in moisture levels. However, outliers were detected in certain samples according to the 1.5 IQR method, indicating occasional unexpected fluctuations in humidity levels. In conclusion, the analyzed physical quantities were generally stable, but certain samples exhibited unexpected fluctuations and outliers.

3.6. Relationship Between Sensor Data, Physical Properties and Flexural Moduli

For the correlation analysis between sensor data and physical measurements, the distribution and relationships of the data were first assessed to determine the most appropriate correlation methods. A preliminary examination using scatter plots, which were not included here to save space, revealed mostly non-linear relationships and the presence of some outliers. Consequently, Pearson correlation was deemed unsuitable due to its assumption of linearity. Instead, Spearman and Kendall correlations were identified as more appropriate for this analysis.

The results of the Spearman and Kendall correlation analyses are presented in Table 3, which includes both correlation values and p-values for each pair. The Spearman correlation analysis showed significant results for the variable pairs nozzle temperature and width, and nozzle temperature and length, suggesting potential monotonic relationships between these pairs. Both Spearman and Kendall correlations indicated significant results for bed temperature and mass, and bed temperature and density, implying consistent order-based relationships in these pairs. Additionally, the Spearman correlation revealed a significant result for the enclosure temperature and length pair, indicating a potential monotonic relationship.

Table 3. Correlation Analysis Results between Sensor Data and Physical Dimensions with p-values in parentheses.

Coor.	Feature	Nozzle Temp.	Bed Temp.	Cham. Temp.	Hum.
Spearman Correlation	Thickness	-0.204 (0.571)	0.215 (0.551)	0.180 (0.620)	-0.099 (0.785)
	Width	0.498 (0.143)	-0.471 (0.169)	0.298 (0.403)	-0.182 (0.614)
	Length	0.559 (0.093)	-0.550 (0.099)	0.517 (0.126)	-0.116 (0.751)
	Mass	0.539 (0.108)	-0.622 (0.055)	0.103 (0.777)	0.152 (0.676)
	Density	0.552 (0.098)	-0.634 (0.049)	0.309 (0.385)	-0.079 (0.829)
Kendall Correlation	Thickness	-0.167 (0.520)	0.220 (0.405)	0.119 (0.646)	-0.072 (0.783)
	Width	0.405 (0.106)	-0.322 (0.205)	0.180 (0.473)	-0.135 (0.590)
	Length	0.449 (0.072)	-0.414 (0.103)	0.315 (0.209)	-0.135 (0.590)
	Mass	0.333 (0.216)	-0.432 (0.087)	0.067 (0.862)	0.156 (0.601)
	Density	0.422 (0.108)	-0.523 (0.038)	0.156 (0.601)	-0.022 (1.000)

To accurately evaluate the relationship between sensor data and flexural modulus (FM), an appropriate method must be employed. FM, an intrinsic property of the material, was measured individually for each sample, independent of physical dimensions. However, the analyses revealed that FM values were distributed into two distinct clusters, which were strongly correlated with the density of the samples. Defects such as filament diameter fluctuations,

bed and nozzle misalignment, and incomplete layer production were identified as contributing factors. To address this issue, although not a complete solution, the relationship between sensor data and FM was analyzed using normalized FM values, obtained by dividing the FMs by the density values.

For the correlation analysis between the sensor data and FM_{Norm} (normalized flexural moduli), the distribution and relationships of the data were first analyzed using scatter plots, which are not presented here. Preliminary examination showed that the data showed mostly non-linear relationships and some outliers were present. This once again showed that Pearson's correlation may not be suitable due to the linearity assumption, whereas Spearman and Kendall correlations may give more meaningful results.

Table 4 presents Spearman and Kendall correlation coefficients alongside their respective p-values for the relationships between sensor data (nozzle, bed and chamber temperatures, and humidity) and FM_{Norm}. Significant monotonic relationships were identified between the nozzle and bed temperatures and FM_{Norm}. The Spearman correlation for nozzle temperature is 0.685 ($p = 0.029$), and for bed temperature, it is -0.744 ($p = 0.014$), indicating medium strength and significant correlations.

Table 4. Spearman and Kendall Correlation Analysis between sensor data and normalized flexural moduli (FM_{Norm}) with p-values in parentheses.

Sensor	Spearman Correlation	Kendall Correlation
Nozzle Temp.	0.685 (0.029)	0.511 (0.047)
Bed Temp.	-0.744 (0.014)	-0.568 (0.024)
Chamber Temp.	-0.200 (0.580)	-0.111 (0.727)
Humidity	0.285 (0.425)	0.156 (0.601)

Similarly, the Kendall correlation analysis shows significant relationships for nozzle and bed temperatures. The Kendall correlation for nozzle temperature is 0.511 ($p = 0.047$), and for bed temperature, it is -0.568 ($p = 0.024$). These findings confirm that nozzle and bed temperatures are significantly correlated with FM_{Norm} in terms of ranking consistency. No significant correlations were found for chamber temperature and humidity data, as both Spearman and Kendall correlations and p-values indicate no significant relationships with FM_{Norm}.

In addition to correlation analyses, ANOVA was performed to investigate the relationships between the FM_{Norm} and the sensor data. Despite the lack of strong correlations, one-way and several multivariate ANOVA models were examined, the models of which are given below:

1) $FM_{Norm} \sim$ Nozzle
2) $FM_{Norm} \sim$ Bed
3) $FM_{Norm} \sim$ Chamber
4) $FM_{Norm} \sim$ Humidity
5) $FM_{Norm} \sim$ Nozzle + Bed + Chamber + Humidity
6) $FM_{Norm} \sim$ Nozzle × Bed × Chamber × Humidity
7) $FM_{Norm} \sim$ Nozzle × Bed × Chamber
8) $FM_{Norm} \sim$ Nozzle × Bed × Humidity
9) $FM_{Norm} \sim$ Nozzle × Bed
10) $FM_{Norm} \sim$ Nozzle + Bed + Chamber + Humidity + $Nozzle^2$ + Bed^2 + $Chamber^2$ + $Humidity^2$

ANOVA results were obtained for all models except the sixth model, which produced infinite values and could not be analyzed. To save space, only the key findings are presented here, as many results were not statistically significant.

The one-way ANOVA analyses (models 1-4) examined the effects of nozzle, bed and chamber temperatures, and humidity on FM_{Norm} individually. The effect of nozzle temperature on FM_{Norm} ($F=1.887653$, $p=0.206729$) was not statistically significant. Similarly, the effects of bed temperature ($F=3.866159$, $p=0.084834$), chamber temperature ($F=0.124862$, $p=0.732950$), and humidity ($F=0.233881$, $p=0.641621$) were also found to be non-significant.

In the multivariate model (model 5), which included all sensor variables, none of the variables exhibited a significant effect on FM_{Norm}: nozzle temperature ($F=1.044978$, $p=0.346102$), bed temperature ($F=1.714087$, $p=0.238357$), chamber temperature ($F=0.078238$, $p=0.789092$), and humidity ($F=0.147595$, $p=0.720394$).

When analyzing the interaction between nozzle, bed, and chamber temperatures (model 7), the interaction term Nozzle:Bed (F=1.805673, p=0.250190) and other main effects remained non-significant.
However, in the model examining the interaction between nozzle and bed temperatures, and humidity (model 8), a significant interaction was found for the temperature term (F=9.576104, p=0.036414), while the other interaction terms were not significant.

Further analysis of the interaction between nozzle and bed temperatures (model 9) also revealed no significant results for the nozzle temperature interaction term (F=2.418823, p=0.170884).

Finally, the relationship between FM_{Norm} and the variables nozzle, bed and chamber temperatures, and humidity, along with their squared terms (model 10), was analyzed. None of these variables were found to have a statistically significant effect in this model.

In summary, while some individual and interaction terms approached significance, most of the ANOVA results did not indicate statistically significant relationships between FM_{Norm} and the sensor data. This suggests that other factors or more complex interactions may influence FM, or that the variability in the measurements was too high to detect significant effects with the current dataset. The lack of significance in many results underscores the complexity of additive manufacturing processes and the need for further investigation into other potential influencing factors.

The most significant challenge encountered in these analyses is that the average values of the sensors do not accurately represent the production process. In fact, for a sample production that takes an average of 14.6 minutes, sensor data comprising 3,375 values each are more meaningful when analyzed on a layer-by-layer basis. For a layer that takes an average of 52.3 seconds to complete (excluding the first layers, which take an average of 144 seconds, about 2 and a half minutes, due to the inclusion of skirts and 50% speed reduction), each sensor records approximately 200 different values (an average of 554 values for the first layers). Therefore, an accurate representation of the sensor data must be provided on a per-layer basis.
Within the scope of this study, conclusive results based on mathematical models were not obtained from analyzing sensor data on a layer-by-layer basis to uncover their relationships in physical specifications or production quality. However, a novel method was developed that can geometrically represent a layer's production using sensor data and completely independent of time constraints, which could lead to more precise results with more extensive studies in the future.

3.7. Representative Layer Figures by Sensor Data

A method was developed to correlate the sensor data with the extruder positions (X and Y) and to compare the layer photographs taken during printing for each layer. The algorithm, utilizing the numpy and svgwrite libraries, processes the collected data and generates SVG visualizations that illustrate sensor values across different layers. The primary steps of the algorithm are as follows:

1. The algorithm reads the dataset containing X-Y coordinate data along with sensor values such as nozzle temperature, bed temperature, enclosure temperature, and humidity created by the log files.

2. A function maps the sensor values to RGB color values, which are used to visually represent the different sensor readings in the SVG. For instance, nozzle temperature, with minimum and maximum values of 363.3 °C and 379.3 °C respectively, 379.3 °C is defined as full red (RGB: 255, 0, 0) and 363.3 °C as full black (RGB: 0, 0, 0). For intermediate values, the corresponding red value is determined by linear interpolation between 0 and 255 (e.g., 370°C → RGB: 107, 0, 0).

3. For each layer in the dataset, an SVG file is created. The X and Y coordinates are used to draw lines representing the movements of the 3D printer nozzle, with the line colors indicating the sensor values at those points.

4. The code iterates through all layers, generating individual SVG files for each layer and sensor type. These individual SVGs are then combined into a comprehensive SVG file,

providing a visual representation for a single sample.

An example of the visualization of data collected from a single sensor during the production of a layer is shown in Figure 9. For Sample 1, this visualization clarifies the significant deviation in nozzle temperature observed in Figure 8a. The deviation was a momentary issue during the printing of the first layer, causing the temperature to drop to 363.3 °C and rise to a maximum of 376.3 °C. In fact, this fluctuation occurred only in specific parts of the layer and did not impact the entire layer.

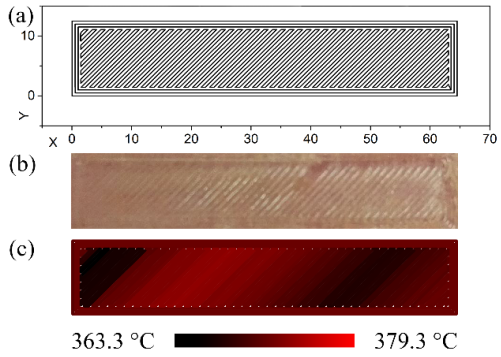

Figure 9. (a) Extruder paths generated from the X-Y coordinates of the first layer without skirt lines, with (b) photograph belongs to the relevant layer and (c) nozzle temperature values along these paths during the production of Sample 1.

The optimal approach for further research involves examining the representative layer figures produced using sensor data alongside the layer photographs. **Figure 10** presents the layer photographs and corresponding sensor data layers for Sample 6, which exhibited the lower flexural modulus (Low-FM) value.

Figure 10 clearly demonstrates that the nozzle temperature, a critical parameter, deviated from the target value during the production of the first and fifth layers. Correspondingly, the layer photographs exhibit printing defects within this range. It appears that the initial defect originates from a gap in the first layer, subsequently affecting the layers above it. This imperfection may be related to the temperature variation, although conclusive evidence is lacking. Additionally, faded surfaces on the left side of the first five-layer photographs can exist because of the temperature drop in the first layer. This temperature variation could have resulted in weaker adhesion to the bed, causing the observed color difference. Alternatively, the bed may not have been perfectly parallel to the nozzle. In both scenarios, thickness variation across the sample is evident, as shown by the standard deviation plots in Figure 4a.

On the other hand, instantaneous fluctuations in humidity are particularly significant for PEI, a thermoplastic highly sensitive to moisture. Notably, a marked decrease in humidity is observed in the fifth layer. This reduction may contribute to the production of relatively higher-quality layers following this point.

Although these interpretations can be made through straightforward observation, the high resolution of the images and the narrow oscillation range of the fixed parameters make these conclusions highly speculative. To establish such relationships with greater precision, a larger number of samples is required. Comprehensive studies with parameters taking multiple values, similar to classical optimization approaches, are essential. By employing advanced data analysis methods such as machine learning and neural networks, these relationships can be more robustly determined.

Finally, to facilitate a comparison between specimens in the Low-FM and High-FM clusters, Figure 11 presents the layer photographs of Sample 8 alongside their corresponding representative layers.

4. CONCLUSION

In this study, a comprehensive critique of the 3D printing process for PEI filament produced in a domestically developed extrusion park using a custom-made 3D printer were conducted. The investigation focused on the diverse outcomes produced by fixed printing parameters under complex influences, without eliminating or selecting specific samples.

The results clearly demonstrated the significant impact of production parameters on the final product quality. In addition to examining physical attributes such as dimensions and density, the study also evaluated the mechanical properties of each specimen through flexural modulus tests, as determined by the chosen specimen geometry. The findings revealed the formation of two distinct clusters (Low- and High-FM). The Low-FM cluster exhibited a 10% reduction in density and a 25% reduction

in flexural modulus compared to the High-FM cluster. These results underscore the necessity for precise control of production parameters, considering the complex and anisotropic nature of additive manufacturing. Correlation analyses between sensor data collected during production and mechanical properties highlighted the critical role of nozzle and bed temperatures in determining product quality. However, none of the variance analyses (ANOVA) models yielded significant results.

The main findings of this study highlight several critical considerations that differentiate this research from previous works in the field. Unlike many studies that focus on parameter optimization by eliminating outliers or selecting specific conditions, this study uniquely explores the variability in outcomes when parameters are kept constant yet subjected to complex and uncontrolled influences. This approach provides a more realistic insight into the challenges of maintaining consistency in additive manufacturing. The detailed analysis of each layer, including photographing and examining potential defects, further distinguishes this study by providing practical methods for improving quality control. Moreover, while some studies have not fully explored the subtle impacts of the nozzle and bed temperature adjustments and fluctuations, this research highlights their role in determining product quality, providing new insights into the importance of these parameters. In addition to temperature control, precise alignment of the nozzle and bed, along with proper surface preparation, especially when using adhesives, has also been identified as essential for achieving optimal production outcomes.

The findings from this study will form the basis for more extensive future research. Further exploration into real-time monitoring with more precise sensors and control of production parameters promises to enhance process efficiency. The use of machine learning and advanced data analysis techniques, supported by the representative layer algorithm, has the potential to reveal complex relationships within manufacturing processes. These innovative approaches will be instrumental in enhancing the consistency of additive manufacturing processes. By demonstrating that varying outcomes can arise in manufacturing processes, even with fixed parameters, this study opens up new avenues for quality control and optimization in additive manufacturing technologies. Future research will build on these findings to enable more effective use of high-performance thermoplastics in industrial applications.

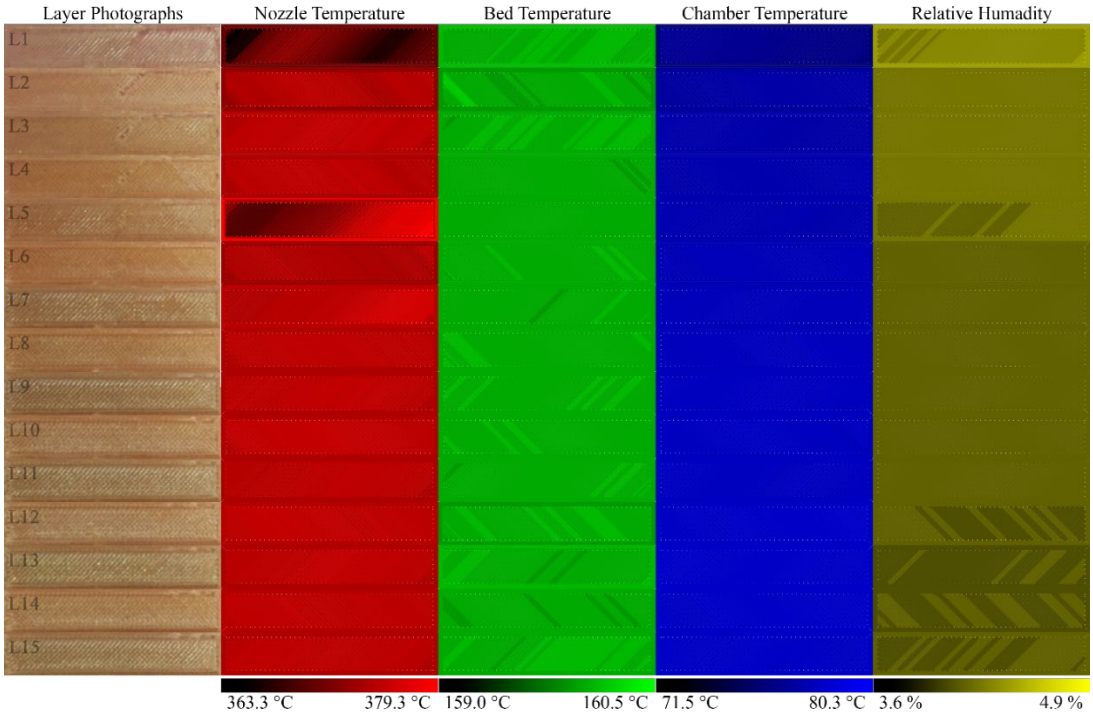

Figure 10. Layer photographs and corresponding sensor data-generated representative layers for Sample 1. The color scale for each sensor is provided below the respective representative layers.

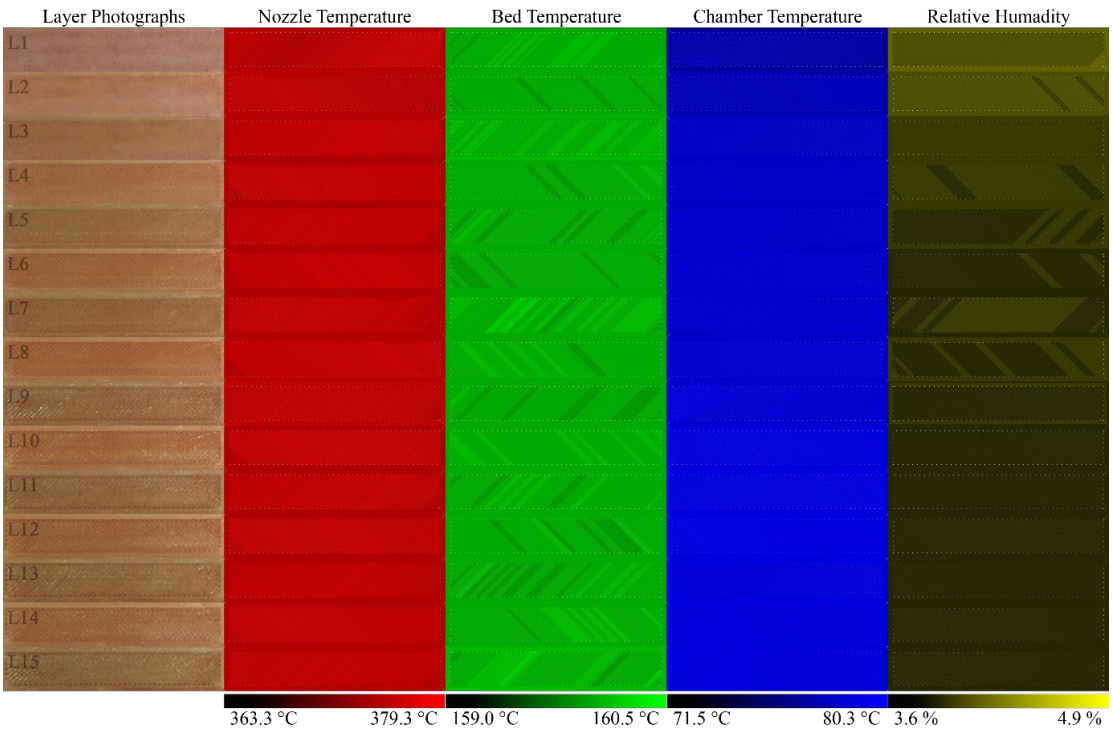

Figure 11. Layer photographs and corresponding sensor data-generated representative layers for Sample 8. The color scale for each sensor is provided below the respective representative layers.

ACKNOWLEDGES

The author would like to thank Uğur Emanetoğlu for his help with 3D printing, Merve Karabal for her help with DMA tests, and Dr. Emre Koyuncu for a thought-provoking discussion on the algorithm of representative layer figures. Special thanks are extended to Dr. Hülya Cebeci for providing access to laboratory facilities and other resources. The study was supported by the ITU BAP Division with project number MAB-2019-42010.

REFERENCES

1. Gao, W., Zhang, Y., Ramanujan, D., Ramani, K., Chen, Y., Williams, C. B., Zavattieri, P. D., "The status, challenges, and future of additive manufacturing in engineering", Computer-Aided Design, Vol. 69, Issue 1, Pages 65-89, 2015.

2. Baumers, M., Dickens, P., Tuck, C., Hague, R., "The cost of additive manufacturing: machine productivity, economies of scale and technology-push", Technological Forecasting and Social Change, Vol. 102, Issue 1, Pages 193-201, 2016.

3. Ford, S., Despeisse, M., "Additive manufacturing and sustainability: an exploratory study of the advantages and challenges", Journal of Cleaner Production, Vol. 137, Issue 1, Pages 1573-1587, 2016.

4. Vakharia, V. S., Leonard, H., Singh, M., Halbig, M. C., "Multi-Material Additive Manufacturing of High Temperature Polyetherimide (PEI)–Based Polymer Systems for Lightweight Aerospace Applications", Polymers, Vol. 15, Issue 3, Pages 561, 2023.

5. Kaynan, O., Yıldız, A., Bozkurt, Y.E., Yenigun, E.O., Cebeci, H., "Electrically conductive high-performance thermoplastic filaments for fused filament fabrication", Composite Structures, Vol. 237, Issue 1, Pages 111930, 2020.

6. Bozkurt, Y.E., Emanetoğlu, U., Yıldız, A., Türkarslan, Ö., Şaşal, F.N., Cebeci, H., "3D printable CNTs and BN hybridized PEEK composites for thermal management applications", Journal of Materials Science, Vol. 58, Issue 38, Pages 15086-15099, 2023.

7. Kim, H., Lin, Y., Tseng, T.-L. B., "A review on quality control in additive manufacturing", Rapid Prototyping Journal, Vol. 24, Issue 3, Pages 645-669, 2018.

8. Strano, M., Farioli, D., Giberti, H., "Extrusion Additive Manufacturing of PEI Pellets", Journal of Manufacturing and Materials Processing, Vol. 6, Issue 6, Pages 157, 2022.

9. Turner, B.N., Strong, R., Gold, S.A., "A review of melt extrusion additive manufacturing processes: I.

Process design and modeling", Rapid Prototyping Journal, Vol. 20, Issue 3, Pages 192-204, 2014.

10. Turner, B.N., Gold, S.A., "A review of melt extrusion additive manufacturing processes: II. Materials, dimensional accuracy, and surface roughness", Rapid Prototyping Journal, Vol. 21, Issue 3, Pages 250-261, 2015.

11. Go, J., Schiffres, S.N., Stevens, A.G., Hart, A.J., "Rate limits of additive manufacturing by fused filament fabrication and guidelines for high-throughput system design", Additive Manufacturing, Vol. 16, Issue 1, Pages 1-11, 2017.

12. Sun, X., Mazur, M., Cheng, C.-T., "A review of void reduction strategies in material extrusion-based additive manufacturing", Additive Manufacturing, Vol. 67, Issue 1, Pages 103463, 2023.

13. Kuruoğlu, Y., Akgün, M., Demir, H., "FDM Yöntemiyle Üretilen ABS, PLA ve PETG Numunelerin Yüzey Pürüzlülüğü ve Çekme Dayanımının Modellenmesi ve Optimizasyonu" [Modelling and Optimization of Surface Roughness and Tensile Strength of ABS, PLA and PETG Samples Produced by FDM Method] [article in Turkish], International Journal of 3D Printing Technologies and Digital Industry, Vol. 6, Issue 3, Pages 358-369, 2022.

14. Albaşkara, M., Türkyılmaz, S., "Optimization of Accuracy and Surface Roughness of 3D SLA Printed Materials with Response Surface Method", International Journal of 3D Printing Technologies and Digital Industry, Vol. 7, Issue 3, Pages 403-414, 2023.

15. Jiang, S.; Liao, G.; Xu, D.; Liu, F.; Li, W.; Cheng, Y.; Li, Z.; Xu, G., "Mechanical properties analysis of polyetherimide parts fabricated by fused deposition modeling", High Performance Polymer, Vol. 31, Issue 1, Pages 97–106, 2019.

16. Ding, S.; Zou, B.; Wang, P.; Ding, H., "Effects of nozzle temperature and building orientation on mechanical properties and microstructure of PEEK and PEI printed by 3D-FDM", Polymer Testing, Vol. 78, Issue 1, Pages 105948, 2019.

17. Forés-Garriga, A.; Pérez, M.A.; Gómez-Gras, G.; Pozo, G.R., "Role of infill parameters on the mechanical performance and weight reduction of PEI Ultem processed by FFF", Materials and Design, Vol. 193, Issue 1, Pages 108810, 2020.

18. Bozkurt, Y.E., Kincal, C., Yüksel, R., Yildiz, A., Solak, N., Cebeci, H., "3D Printable BN/PEEK/PEI Polymer Blend Composites for Thermal Management Applications", AIAA SCITECH 2024 Forum, Pages 0368, 2024.

19. El Magri, A.; Vanaei, S.; Vaudreuil, S., "An overview on the influence of process parameters through the characteristic of 3D-printed PEEK and PEI parts", High Performance Polymers, Vol. 33, Issue 1, Pages 862–880, 2021.

20. El Magri, A.; Mabrouk, K.E.; Vaudreuil, S., "Preparation and characterization of poly (ether ether ketone)/poly (ether imide) [PEEK/PEI] blends for fused filament fabrication", Journal of Materials Science, Vol. 56, Issue 1, Pages 14348–14367, 2021.

21. Vanaei, H.R., Shirinbayan, M., Deligant, M., Khelladi, S., Tcharkhtchi, A., "In-Process Monitoring of Temperature Evolution during Fused Filament Fabrication: A Journey from Numerical to Experimental Approaches", Thermo, Vol. 1, Issue 3, Pages 332-360, 2021.

22. Sgrulletti, M., Bragaglia, M., Giarnetti, S., et al., "Understanding the Impact of Fused Filament Fabrication Conditions on the Microstructure and Tensile Properties of Polyamide 6 by Thermal and Optical Live Monitoring", Materials Today Communications, Vol. 28, Issue 1, Pages 102679, 2021.

23. Alatefi, M., Al-Ahmari, A.M., AlFaify, A.Y., Saleh, M., "A Framework for Multivariate Statistical Quality Monitoring of Additive Manufacturing: Fused Filament Fabrication Process", Processes, Vol. 11, Issue 4, Pages 1216, 2023.

24. Özsoy, K., Aksoy, B., "Real-Time Data Analysis with Artificial Intelligence in Parts Manufactured by FDM Printer Using Image Processing Method", Journal of Testing and Evaluation, Vol. 50, Issue 1, Pages 629-645, 2022.

25. Yıldız, A., Emanetoğlu, U., Yenigun, E.O., Cebeci, H., "Towards optimized carbon nanotubes (CNTs) reinforced polyetherimide (PEI) 3D printed structures: A comparative study on testing standards", Composite Structures, Vol. 296, Issue 1, Pages 115853, 2022.